



ELSEVIER

Contents lists available at ScienceDirect

## Materials Science &amp; Engineering R

journal homepage: [www.elsevier.com/locate/mser](http://www.elsevier.com/locate/mser)

## Structural evolutions of metallic materials processed by severe plastic deformation

Yang Cao<sup>a,\*</sup>, Song Ni<sup>b,\*</sup>, Xiaozhou Liao<sup>c</sup>, Min Song<sup>b</sup>, Yuntian Zhu<sup>a,d</sup><sup>a</sup> School of Materials Science and Engineering, Nanjing University of Science and Technology, Nanjing 210094, China<sup>b</sup> State Key Laboratory of Powder Metallurgy, Central South University, Changsha 410083, China<sup>c</sup> School of Aerospace, Mechanical and Mechatronic Engineering, The University of Sydney, Sydney, NSW 2006, Australia<sup>d</sup> Department of Materials Science and Engineering, North Carolina State University, Raleigh, NC 27695, USA

## ARTICLE INFO

## Keywords:

Severe plastic deformation  
 Nanostructured metallic materials  
 Grain refinement  
 Grain growth  
 Dislocations  
 Deformation twinning  
 Phase transformation  
 Mechanical properties

## ABSTRACT

Bulk nanostructured (ns)/ultrafine-grained (UFG) metallic materials possess very high strength, making them attractive for high strength, lightweight and energy efficient applications. The most effective approach to produce bulk ns/UFG metallic materials is severe plastic deformation (SPD). In the last 30 years, significant research efforts have been made to explore SPD processing of materials, SPD-induced microstructural evolutions, and the resulting mechanical properties. There have been a few comprehensive reviews focusing mainly on SPD processing and the mechanical properties of the resulting materials. Yet no such a review on SPD-induced microstructural evolutions is available. This paper aims to provide a comprehensive review on important microstructural evolutions and major microstructural features induced by SPD processing in single-phase metallic materials with face-centered cubic structures, body-centered cubic structures, and hexagonal close-packed structures, as well as in multi-phase alloys. The corresponding deformation mechanisms and structural evolutions during SPD processing are discussed, including dislocation slip, deformation twinning, phase transformation, grain refinement, grain growth, and the evolution of dislocation density. A brief review on the mechanical properties of SPD-processed materials is also provided to correlate the structure with mechanical properties of SPD-processed materials, which is important for guiding structural design for optimum mechanical properties of materials.

## 1. Introduction

Tremendous efforts have been devoted in the history of mankind to develop structural materials with optimized mechanical properties for applications in areas including civil, medical, transportation, oil, aerospace, and energy industries. Strength and ductility are two of the most fundamental mechanical properties for structural materials. Research over a century on metallic materials revealed a dilemma of strength–ductility trade-off that seemed to be intrinsic [1–4]. In 1989, Gleiter [5] made the visionary argument that significant change of physical and mechanical properties of materials could be realized when the grain size of materials is reduced to the nanoscale regime. Nanostructured (ns) materials usually have very high strength, but ductility is typically low. Recent researches revealed that some ns materials can be designed to have improved ductility without sacrificing their strength [1,6–15]. This triggered unprecedented innovation in the field of ns materials [16] including processing techniques, knowledge of nano/

microstructural evolution and knowledge of structure-property relationships. Nanocrystalline (nc) materials have grain sizes smaller than 100 nm. The terminology “ns materials” has often been used to describe materials having structural features, e.g., sub-grains and dislocation cells, smaller than 100 nm but their grain sizes may be larger than 100 nm [17]. It should be noted that the grain size measured by X-ray diffraction (XRD) is actually the crystalline domain size, which makes it consistent with the definition of ns materials. In addition, the term “ultrafine-grained (UFG) materials” has been extensively used for materials processed by severe plastic deformation (SPD), an approach that can produce bulk materials without porosity and large enough for structural applications. UFG materials are defined as materials with grains smaller than 1000 nm, and they are often referred to as ns materials when they have structural features smaller than 100 nm [17].

After decades of development, many methods have been established to synthesize UFG and ns materials. These methods can be classified into two major approaches – “bottom-up” and “top-down” [18]. In the

\* Corresponding authors.

E-mail addresses: [y.cao@njust.edu.cn](mailto:y.cao@njust.edu.cn) (Y. Cao), [song.ni@csu.edu.cn](mailto:song.ni@csu.edu.cn) (S. Ni).<https://doi.org/10.1016/j.mser.2018.06.001>

Received 12 May 2018; Accepted 25 June 2018

Available online 25 August 2018

0927-796X/ © 2018 Elsevier B.V. All rights reserved.

### Nomenclature

BCC	Body-centered cubic	LD	Longitudinal direction
BDT	Brittle-to-ductile transition	MD	Molecular dynamic
CG	Coarse-grained	nc	Nanocrystalline
CLS	Confined layer slip	ND	Normal direction
CRSS	Critical resolved shear stress	ns	Nanostructured
EBSD	Electron backscatter diffraction	SAED	Selected-area electron diffraction
ECAP	Equal channel angular pressing	SFE	Stacking fault energy
FCC	Face-centered cubic	SMGT	Surface mechanical grinding treatment
GB	Grain boundary	SPD	Severe plastic deformation
GNB	Geometrically necessary boundary	T/M	Twin/matrix
GND	Geometrically necessary dislocation	TB	Twin boundary
HCP	Hexagonal close-packed	TD	Transverse direction
HPT	High-pressure torsion	TEM	Transmission electron microscopy
HRTEM	High-resolution transmission electron microscopy	UFG	Ultrafine-grained
L-C	Lomer-Cottrell	UTS	Ultimate tensile strength
		XRD	X-ray diffraction

“bottom-up” approach, atoms or nanoparticulate solids are bonded together to form ns bulk solids. Electro-deposition [19], inert gas condensation [20] and ball milling with subsequent consolidation [21] are typical examples of these “bottom-up” methods. In the “bottom-up” approach, the grain sizes, types of boundary and textures of the product materials can be manipulated to a certain extent. Fig. 1 shows transmission electron microscopy (TEM) images of two typical examples of materials synthesized by electro-deposition. Presented in Fig. 1(a) is a nc Ni with an average grain size of  $\sim 30$  nm and a narrow grain size distribution [22]. The corresponding selected-area electron diffraction (SAED) pattern indicates small grain sizes and random grain orientations. Fig. 1(b) presents a coarse-grained (CG) Cu containing a high density of nano-twins (the strip-like structures) [23]. However, some “bottom-up” methods are very time consuming and expensive. Materials synthesized by the “bottom-up” methods always have one or more of the following issues: (1) unwanted impurity contents, (2) texture and (3) porosity or incomplete densification [24–26]. Thus, the ns materials synthesized by “bottom-up” methods are often very limited in sizes, and the high impurity and/or porosity content may deteriorate the mechanical properties of the materials [27].

In the “top-down” approach, bulk CG materials are effectively refined by heavily imposed shear strain to form UFG and/or nc materials, by comparing the electron backscatter diffraction (EBSD) images in Fig. 2. The resultant UFG or nc materials are free of porosity and

contamination [28,29]. Nowadays, the most successful and popular “top-down” grain refinement approach is SPD. SPD can be achieved by mechanically imposing an extensive hydrostatic pressure and a very high strain to a bulk metallic material. SPD normally does not alter much the shape of the work piece while the grain size can be significantly refined [17]. The most developed SPD techniques include equal channel angular pressing (ECAP) [30], high-pressure torsion (HPT) [29,31], multi-axial forging [32], rotary swaging [33], and accumulative roll bonding [34,35]. Detailed description of these techniques and their development history have been well reported in the literatures [28,31,36–38].

The high strain level that is attainable by SPD is far beyond that of conventional plastic deformation methods such as rolling and extrusion. As a result, SPD induced structural evolution processes can be very complex, and may involve various deformation mechanisms including dislocation slip, deformation twinning, elemental redistribution, phase transformation, grain rotation and even grain growth. Each of these deformation mechanisms may contribute or affect the grain refinement to a certain extent. The activation of various deformation mechanisms and the resultant overall microstructural evolution are determined by the processing history and the intrinsic properties of materials such as stacking fault energy (SFE). Microstructures determine the way by which the materials respond to imposed stress; therefore, ultimately microstructures determine the mechanical properties of SPD-processed

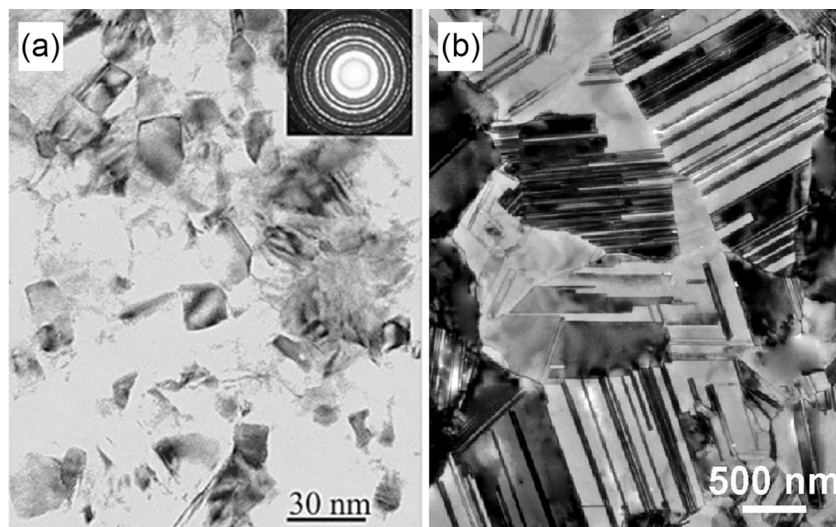


Fig. 1. (a) A TEM image showing the microstructure of an electro-deposited nc Ni [22]. The inset is a corresponding SAED pattern; (b) a TEM image showing the microstructure of an electro-deposited CG Cu containing a high density of nano-twins [23].

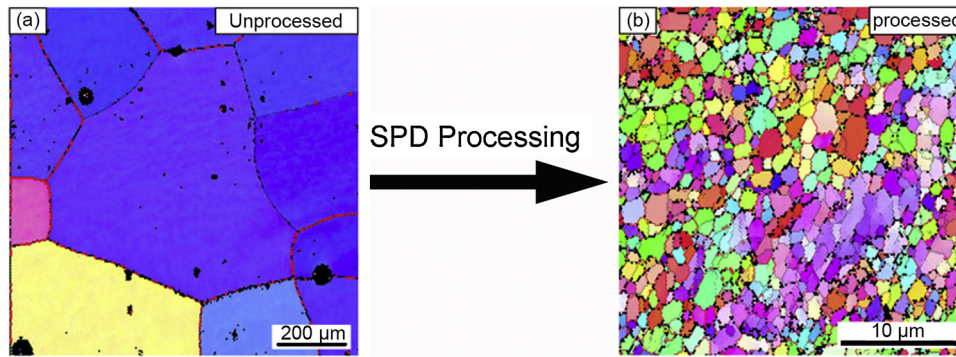


Fig. 2. (a) An EBSD image showing the CG structure of an Al sample before SPD (ECAP) processing; (b) an EBSD image showing the refined grain structure of the Al sample after eight ECAP passes [54].

ns materials. It is of interest and critical importance to understand the evolution of microstructures so that SPD parameters can be tuned to produce microstructures for optimum mechanical properties.

Although there have been a few influential SPD-related review articles [3,17,28–31,36–44], they mainly focused on SPD techniques [28–31,36] and the properties of processed materials [3,37]. No systematic review on SPD-induced microstructural evolutions has been published. On the other hand, a large number of research papers on SPD-induced microstructural evolutions has been published, and many interesting micro/nanostructures have been revealed in detail, thanks to the fast development of materials and microstructural characterization techniques [45–49]. It is worth to mention that SPD is applicable to a huge variety of materials including both metallic materials and non-metallic materials [50–53]. Considering majority of the SPD-processed materials are metallic materials, this review will focus on SPD-induced microstructural evolutions of metallic materials, including grain refinement (Section 3), grain growth (Section 4), dislocation density evolution (Section 5), phase transformation (Section 6), structural evolutions in dual-phase and multi-phase materials (Section 7). The effect of SPD-induced structural evolution on the mechanical properties will also be briefly reviewed in Section 8 to correlate microstructure with mechanical properties. At last, concluding remarks and outstanding issues in the field of SPD-induced microstructural evolution are provided in Section 9.

## 2. Major deformation modes in coarse grains

Dislocation slip and deformation twinning are the two major deformation mechanisms in CG metallic materials. Dislocations are line

defects, which can nucleate and slip under stress to accommodate the applied plastic deformation. In crystalline solids, atoms are arranged in ordered lattice structures. A single dislocation line can glide on a densely packed atomic plane called slip plane along any direction but the resulting crystalline slip is along a particular direction called slip direction. The relative displacement of a set of atoms caused by a single dislocation slip is the Burgers vector of the dislocation [55–57]. Depending on the orientation relationships between dislocation lines and their Burgers vectors, dislocations can be classified into three basic types: edge dislocations (dislocation lines is perpendicular to their Burgers vectors), screw dislocations (dislocation lines is parallel to their Burgers vectors) and mixed dislocations (dislocation lines is neither perpendicular nor parallel to their Burgers vectors). The microscopic appearance, motion and interaction of dislocations are very complicated [55,58]. Fig. 3 shows dislocation structures observed in a Cu-10 at.%Al alloy, a Ni sample and a Al sample. Twinning occurs when the crystalline lattice is re-orientated by atomic displacements that are equivalent to a simple shear of the crystal lattice to form mirror symmetry with the matrix lattice [59]. A twinned lattice structure is schematically illustrated in Fig. 4(a).  $K_1$  is the invariant twinning plane. Atoms on  $K_1$  are sheared along  $\eta_1$ , which is the twinning shear direction to form a twin relationship with respect to the matrix. Therefore, the coherent twin boundary (TB) is parallel to  $K_1$ .  $K_2$  is the conjugate twinning plane which is from the same crystalline plane family of  $K_1$  and intersects with  $K_1$  in a line normal to the plane of shear,  $P$ .  $\eta_2$  is the conjugate shear direction on  $K_2$  [59]. Fig. 4(b) presents a high-resolution TEM (HRTEM) image showing the twin–matrix lattice structure observed in a CG austenitic steel. The atomic arrangement above the marked coherent TB is symmetrical to that of the matrix.

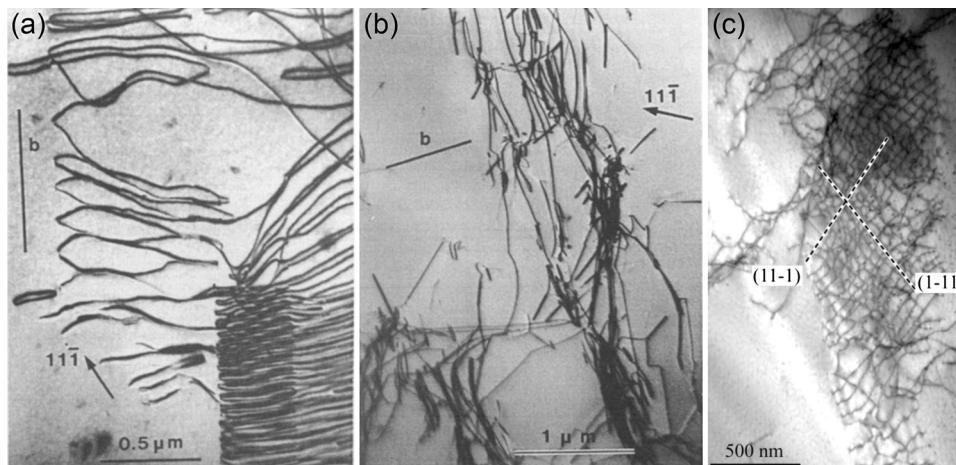
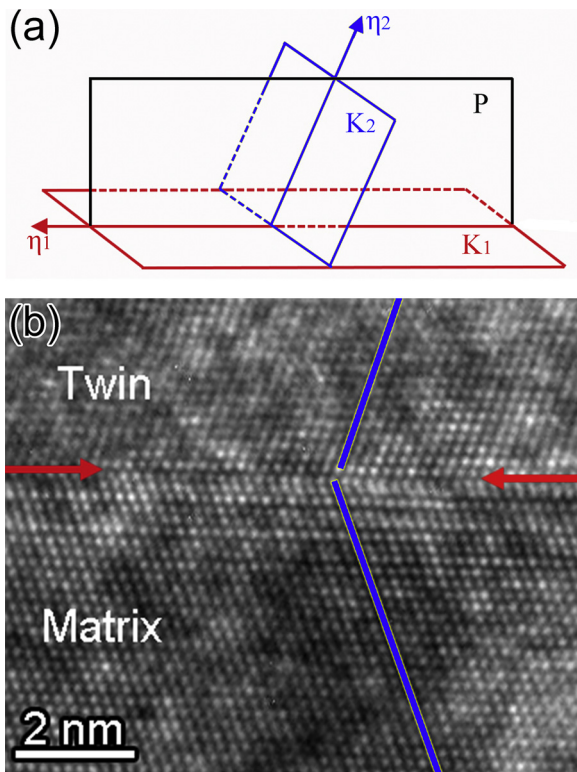


Fig. 3. (a) Dislocation arrays in a Cu-10 at.%Al alloy [60]; (b) dislocation bundles observed in a single crystal Ni deformed at a low strain ( $g = 11\bar{1}$ ) [60] (The Burgers vector is denoted by a letter “b”); (c) a dislocation net observed in a CG Al deformed by cold rolling to a thickness reduction of 10% [61].



**Fig. 4.** (a) A schematic diagram showing the four twinning elements: the invariant twinning plane  $K_1$ , the twinning shear direction  $\eta_1$ , the conjugate twinning plane  $K_2$  and the conjugate shear direction  $\eta_2$ . P represents the plane of shear [59]; (b) an HRTEM image of a typical twin–matrix atomic arrangement in an FCC steel. Two red arrows mark the coherent TB which clearly separates the twin structure on the top from the matrix at the bottom. Blue lines trace the  $\{111\}$  planes that form the twin–matrix relationship.

The combination of a slip plane and a slip direction forms a slip system in which the dislocation motion is confined. Slip systems depend on the crystal structure of the material in a way that the atomic distortion that accompanies the motion of a dislocation is kept to a minimum. Therefore, the slip plane is normally the most densely packed plane and the slip direction is the most closely packed direction. Available slip systems in the three most important metallic crystal structures, comprising face-centered cubic (FCC), body-centered cubic (BCC), and hexagonal close-packed (HCP) structures, are summarized in Table 1.

Deformation twinning can occur in different modes depending on crystal structures and deformation conditions. It is convenient to represent the twinning mode in the form of  $\{K_i\}\langle\eta_i\rangle$ , and the commonly observed twinning modes in FCC, BCC and HCP structures are also shown in Table 1. The twinning mode shown in Fig. 4(b) is the typical  $\{111\}\langle11\bar{2}\rangle$  mode observed in FCC materials. In BCC materials, the  $\{112\}\langle1\bar{1}\bar{1}\rangle$  twinning mode has been frequently observed experimentally, and seven other twinning modes have been theoretically predicted but seldom observed [59]. HCP materials have four common twinning modes as listed in Table 1. More than 10 twinning modes have been proposed in HCP structures while some debates are yet to be resolved [64–68].

The nucleation of either a dislocation or twin requires a resolved shear stress higher than a critical value. Dislocation nucleation is a thermally activated process with a high activation energy [69,70]. Homogeneous dislocation nucleation requires stresses that are much higher than the values observed in experiments, indicating that most dislocations formed via inhomogeneous nucleation processes [59,71–73]. Once a dislocation or a twin is nucleated, the glide of the dislocation or the growth of the twin can occur at stresses that are a

fraction of the nucleation stress [60,73]. The critical resolved shear stress (CRSS) for dislocation slip and deformation twinning are affected by grain size, temperature and SFE [73,74].

According to von Mises criterion [75,76] for strain accommodation, strain compatibility in a CG metal requires the operation of at least five independent slip systems [62,77]. A slip system is activated only when the resolved shear stress for the system is larger than its CRSS [55]. This leads to the activation of multiple slip systems on different slip planes. The interactions of dislocations from different slip systems lead to dislocation entanglement and accumulation, which consequently leads to strain hardening, i.e., increases in flow stress. According to the low-energy dislocation structure concept [78], dislocation tangling into various microstructures such as bundles (Fig. 3(a)) and nets (Fig. 3(b)) is an important deformation mechanism that naturally reduces the free energy of dislocations and increases the flow stress [60,61]. Under sufficient stress, dislocation sources may keep emitting dislocations, which may travel and eventually encounter an obstacle such as a dislocation with a different Burgers vector, a precipitate or a grain boundary (GB), as shown in Fig. 5 [79]. Those dislocations can form extended pile-ups against obstacles [80], or dislocation multiplication may occur at the obstacles.

The dislocation structures shown in Figs. 3 and 5 are also affected by the SFE of the materials. High SFE confines the separation of partial dislocations, which facilitates cross-slip. As such, dislocations show irregular wavy shapes (Fig. 3(b–c)) and easily tangle together to form three-dimensional dislocation cells. In contrast, low SFE leads to the formation of extended partial dislocations which are difficult to cross-slip. Therefore, large amounts of planar arrays dominate the plastic deformation of the low SFE materials, as exemplified in Fig. 5.

Deformation twinning can be a result of dislocation interactions and motion in a highly restricted manner [81–85] or atomic shuffling [59], and often occurs in materials with low SFEs. Deformation twinning is stress driven and normally requires much higher stress than conventional dislocation slip [73,86]. If the flow stress is sufficiently high due to strain accumulation [29,30,86] and/or high strain rate [87,88] competition between twinning and dislocation slip may become evident. Twinning is very important for strain accommodation, especially in HCP materials in which slip mainly occurs on the basal planes; therefore, deformation twinning is often activated to provide additional deformation systems in order to comply with the von Mises criterion for strain accommodation [64–68].

Overall, dislocation slip and deformation twinning are the two most common deformation mechanisms in CG materials. Under SPD processing conditions where the flow stress of the materials can be

**Table 1**

Common slip systems and twinning systems in FCC, BCC and HCP crystal structures [55,59,62–64].

Crystal Structures	Slip systems	Twinning modes
Face-Centered Cubic (FCC)	$\{111\}\langle1\bar{1}0\rangle$	$\{111\}\langle11\bar{2}\rangle$
	$\{001\}\langle1\bar{1}0\rangle$	
	$\{110\}\langle1\bar{1}0\rangle$	
Body-Centered Cubic (BCC)	$\{110\}\langle\bar{1}11\rangle$	
	$\{211\}\langle\bar{1}11\rangle$	$\{112\}\langle1\bar{1}\bar{1}\rangle$
	$\{321\}\langle\bar{1}11\rangle$	
	$\{hkl\}\langle111\rangle$ any of the plane with the maximum resolved shear stress	
Hexagonal Close-Packed (HCP)	$\{0001\}\langle11\bar{2}0\rangle$	$\{10\bar{1}2\}\langle10\bar{1}\bar{1}\rangle$
	$\{10\bar{1}0\}\langle11\bar{2}0\rangle$	$\{10\bar{1}1\}\langle10\bar{1}\bar{2}\rangle$
	$\{10\bar{1}1\}\langle11\bar{2}0\rangle$	$\{11\bar{2}2\}\langle11\bar{2}\bar{3}\rangle$
	$\{11\bar{2}2\}\langle11\bar{2}\bar{3}\rangle$	$\{11\bar{2}1\}\langle\bar{1}\bar{1}26\rangle$



Fig. 5. Dislocation structures observed in a CoCrFeMnNi high-entropy alloy deformed at a low strain. A  $\{111\}$  slip plane trace is marked by a double-arrow line [79].

significantly increased, dislocation and twinning activities are often very extensive. Deformation twinning produces microstructures that are very different from those produced by dislocation slip [87,89–91]. Therefore, extensive efforts have been devoted to investigate the effect of twinning on the microstructures evolution in materials processed by SPD. Extensive observations suggest that the CRSS for twinning is affected by temperature [87], grain size [92,93] and SFE [89,94–96]. These three factors will be often considered when discussing twinning related deformation mechanisms and microstructural evolution processes in the following sections of this review article. Interestingly, it was found that there is an optimum grain size for twinning in ns FCC metals, which was both predicted theoretically [97,98] and observed experimentally [99,100].

### 3. SPD-induced grain refinement

Dislocation slip and deformation twinning are two major competing plastic deformation mechanisms during the SPD-induced grain refinement processes. The crystalline structures and SFEs of materials play critical roles in determining their deformation modes and therefore SPD-induced grain refinement mechanisms [35,87,89–91,94,101–105]. Therefore, this review is organized based on the crystalline structures of materials. For FCC materials, because the grain refinement mechanism varies dramatically with their SFEs, the review is further grouped into three parts: 3.1 Grain refinement of FCC materials with high SFEs, 3.2 Grain refinement of FCC materials with medium SFEs, and 3.3 Grain refinement of FCC materials with low SFEs. As twinning does not play an important role in the deformation processes of most BCC materials [106–108], the discussion of SPD-induced grain refinement of BCC materials in Section 3.4 does not include SFE. In contrast, because twinning plays a critical role in accommodating the c-axis component of the plastic deformation of HCP materials, both dislocation slip and deformation twinning are always involved in the SPD-induced

microstructural evolution [64,109]. Issues related to the effect of SFE on deformation in HCP materials are very complicated and have not been well understood [110–117]. Therefore, Section 3.5 focuses more on the SPD-induced microstructural evolution in HCP materials with limited discussion on the effect of SFE.

#### 3.1. Grain refinement of FCC materials with high SFEs

Al and Ni are typical materials with high SFEs with reported SFEs in the ranges of  $\sim 135$ – $220$  mJ/m<sup>2</sup> [118] and  $\sim 137$ – $278$  mJ/m<sup>2</sup> [119–121], respectively. Note that the discrepancy in the reported SFE values for the same materials is attributed to the different models and methods used for determining SFEs [110,117,122,123]. Plastic deformation and grain refinement in materials with high SFEs occur mainly via dislocation activities. Their SPD-induced microstructural evolution is categorized into 5 stages according to the dominant microstructural features at each stage [57,78,80,124–127].

At deformation stage 1, individual grains are quickly subdivided into many volume elements delineated by dense dislocation walls [128]. These dense dislocation walls are named geometrically necessary boundaries (GNBs) [124] across which there is a misorientation that is controlled by the difference in dislocation-slip-induced lattice rotation in neighboring volumes [57]. These volume elements are defined as cell blocks [80]. The active slip systems in these cell blocks are different from each other and can operate collectively to fulfil the von Mises criterion for strain accommodation [62,75,76,129]. Dislocations from neighboring cell blocks meet at a GNB, leading to dislocation interactions, entanglement and rearrangement [57,130,131]. Since dislocations from neighboring cell blocks are from different slip systems, the cell blocks will rotate in different ways, leading to increasing misorientation across the GNB. Meanwhile, a large number of dislocation cells formed at the interior of each cell block. A cell wall may look similar to a dense dislocation wall, but it is formed primarily by the mutual and statistical trapping of incidental glide dislocations, and thereby named as incidental dislocation boundary [57,124,132].

A typical microstructure of dislocation cells and cell walls in an Al sample rolled to 10% thickness reduction is presented in Fig. 6 [61,133], in which dislocation-free and dislocation tangled areas co-exist in coarse grains. It was observed that during deformation, dislocation-free regions emerge and vanish dynamically in local areas [133], reflecting the underlying stochastic dynamics of the dislocation activities proposed by Hahn in 1996 [134]. The cell walls are all low-angle dislocation boundaries [133]. Some Net-like dislocation entanglements that are marked by ovals in Fig. 6 formed one type of cell walls that are commonly observed in CG FCC materials deformed at low strain levels [80,135]. With increasing shear strain, diffused cell walls

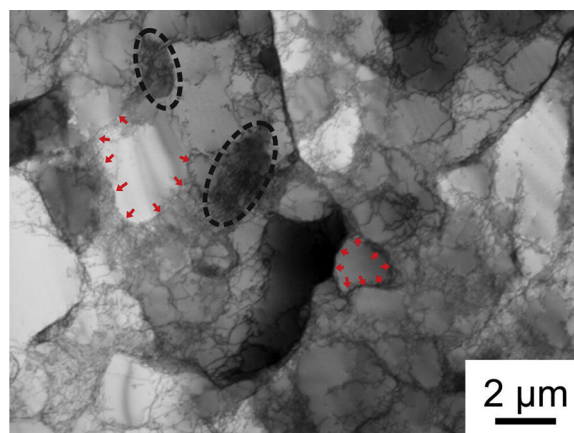


Fig. 6. A typical microstructure of a high-purity Al deformed by rolling to a thickness reduction of 10%. Some cell walls are marked by red arrows. Two typical net-like dislocation entanglements are marked by ovals [61].

gradually sharpen into narrow string-like dislocation boundaries [61,124]. Therefore, the emerging and subsequent sharpen-up of the cell walls is a major part of the stochastic dislocation dynamics [134]. The formation mechanism of these cell walls can be explained by the low-energy dislocation structures theory: dislocations are trapped into positions of local energy minima in which stress-screening between dislocations occurs [136,137]. The contribution to work hardening by the formation of dislocation cells can be explained by dislocation pile-ups and the forest hardening mechanism [138,139]. Some details about work hardening will be given in Section 8, when the correlation between microstructures and materials strength are discussed.

As the imposed strain increases, significant amounts of dislocations accumulate at cell walls and dense dislocation walls, resulting in higher misorientation across these cell walls. Eventually, cell walls may transform into dense dislocation walls. Meanwhile, some early formed dense dislocation walls may split into new dense dislocation walls that are roughly parallel. The regions enclosed by these parallel walls are called microbands, as shown in Fig. 7(a). As a result, large amounts of cell blocks and microbands with reduced sizes are formed, as exemplified in Fig. 7, featuring deformation stage 2. In addition, dense dislocation walls have a tendency to align with the macroscopically most stressed planes (the shear direction) to delineate comparatively long and regularly spaced slip bands [140,141], despite of different plastic deformation processes such as cold rolling, ECAP and HPT. It is worth to mention that when long slip bands interact with a parallel group of dense dislocation walls and microbands, localized shear deformation could cause slip bands to evolve (offset) from a straight line and become S-shaped bands (S-bands) as shown in Fig. 7(b). The S-band formation is temperature sensitive, that it could be suppressed or even avoided at very low processing temperatures close to the liquid nitrogen temperature [142].

At deformation stage 3, large amounts of lamellar sub-grains enclosed by lamellar boundaries form, as a result of continuous reduction of cell block sizes and significant increase of misorientation angles across dense dislocation walls. These lamellar sub-grains therefore tend to align parallel to the shear strain direction as shown in Fig. 8(a). Within these lamellar sub-grains are interconnecting boundaries, dislocation clusters and individual dislocations. Some typical interconnecting boundaries, which are marked by white arrows in Fig. 8(b), could create easily detectable misorientation (contrast difference in TEM) within the lamellar sub-grains.

Fig. 9 shows that as the imposed strain further increases, increasing numbers of lamellar boundaries and interconnecting boundaries gradually sharpen and become thinner. The increase in boundary sharpness is a reflection of dislocation annihilation (dislocation density reduction) at the boundary [124]. As a result, the misorientation across

the boundary increases [80,144,145]. While interconnecting boundaries and dislocation clusters are still apparent, lamellar structures become finer and clearly some equiaxed grains start to form, as marked by red triangles in Fig. 9(a). The microstructural evolution process has entered into deformation stage 4.

Eventually, overall grain refinement reaches a steady state at deformation stage 5, or the steady state stage. In general, at the steady state, grains are mostly equiaxed. Directional appearance of grains is less evident than that at early stages of deformation. A small fraction of deformation twins may form, as a result of extremely high strain and very small grain size [126].

The microstructures observed at deformation stage 5 can differ significantly among different materials. Even for the same material, different processing conditions can alter the microstructures at the steady state [143,146]. For example, an SPD processed Ni sample has an average grain size of  $\sim 170$  nm [146] and the majority of the GBs are non-equilibrium GBs [135,147–149]. In contrast a SPD processed Al sample has an average grain size is  $\sim 800$  nm and the majority of the GBs are well developed [143]. Both low melting temperature [150,151] and high SFE [95,152–154] of Al assisted dynamic recovery, which counteracts the grain refinement process, and therefore increases the steady-state grain size of Al processed by SPD. For another example, as a result of high hydrostatic pressure, an HPT processed Ni may attain an average grain size [146] that is about half of the average grain size of ECAP processed Ni [29,146,155–157]. A detailed discussion about the steady state grain size processed by SPD will be provided in Section 3.6.

Fig. 10 presents schematic diagrams summarizing the SPD-induced microstructural evolution of materials with high SFEs. Dislocation slip is the dominant deformation mechanism in materials with high SFEs. Therefore, grain subdivision mechanisms and corresponding development of dislocation structures govern the microstructural evolution of the materials under SPD processing, and five grain refinement stages are involved in the process. Despite of different strain paths of various SPD processing techniques [29,158], the five grain refinement stages are generally the same for materials with high SFEs.

Deformation stage 1 is featured with large size cell blocks containing pronounced dislocations and dislocation cell structures which drastically strengthen the material [57,61,80,124,130,131,133,135,159–161]. Deformation stage 2 is featured mainly with an increased number of cell blocks with smaller sizes, due to the formation of microbands and reorientation of early formed dislocation cells. The misorientation angles between cell block boundaries increase, some of which become high-angle boundaries at deformation stage 2 [126,136,150,162]. At deformation stage 3, lamellar sub-grains are widely observed throughout the materials. Interconnecting boundaries within lamellar grains begin to form due to pronounced dislocation accumulation [80,125,126,143,162]. Deformation stage 4 is

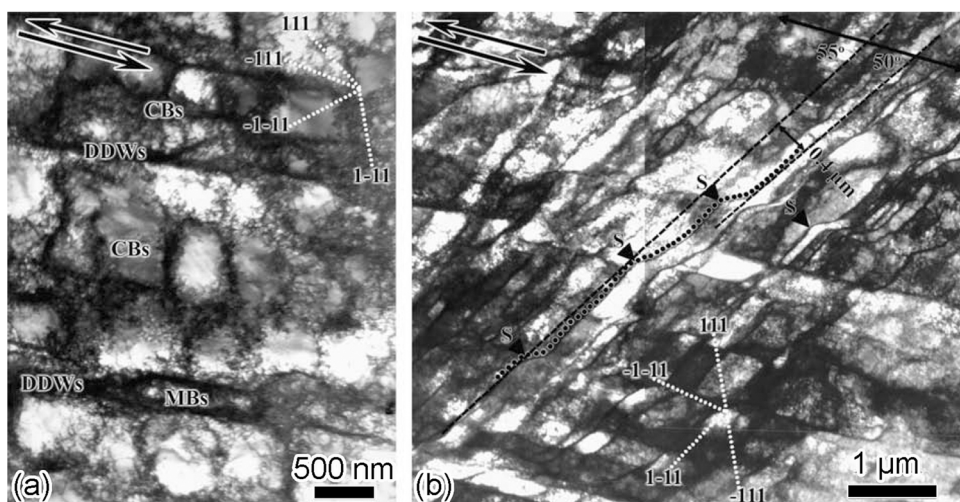
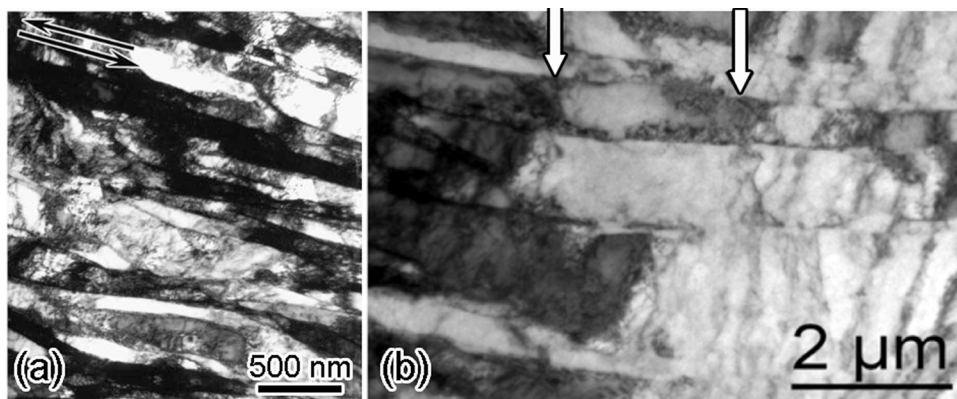


Fig. 7. Typical microstructures in a Ni processed by HPT to a strain of 0.9 (a) and 1.7 (b). Double arrows indicate the shear direction. In (b), a solid black line at the top right corner traces a set of dense dislocation walls and microbands which is nearly parallel to the shear direction and a dash line traces the other set which is inclined to the shear direction at an angle of  $\sim 55^\circ$ . An S-band is marked by a dotted line; “S” and “▼” mark the shear localization points on the S-band [126].



**Fig. 8.** (a) Lamellar dislocation structures in a Ni sample deformed by HPT to a strain of  $\sim 9$ . The black double arrows indicate the shear direction [126]; (b) lamellar dislocation structures in an Al sample deformed by ECAP at low temperature to a strain above 1 (low temperature may increase the effectiveness of the deformation process) [143]. White arrows point to some typical interconnecting boundaries inside lamellar-shaped sub-grains.

featured with ultrafine and/or ns lamellar grains. Some equiaxed grains start to form at this stage. The limited space between lamellar boundaries makes further dislocation generation and accumulation very difficult [127,163,164]. Deformation stage 5 is also called the steady state [165,166] or the equilibrium stage [167–169] of SPD processing. Deformation stage 5 is reached when SPD induced grain refinement is balanced by dynamic recrystallization [170–173] and dislocation generation is balanced by dynamic recovery [16,150,174]. Homogeneous distribution of equiaxed ultrafine grains or nano-grains is the characteristic microstructure of this stage.

### 3.2. Grain refinement of FCC materials with medium SFEs

The microstructural evolutions of FCC materials with medium SFEs are very sensitive to external deformation conditions [87,175,176]. Under conventional deformation conditions such as low stress, low strain, low strain rate and room temperature, the materials tend to deform by dislocation slip. However, if the flow stress of the material is increased to a critical high level by high imposed pressure and high strain, and/or if the deformation temperature is lowered, deformation twinning tends to dominate certain stages of the microstructural evolution.

Copper (Cu) is a widely used model material with a medium SFE of  $\sim 45 \text{ mJ/m}^2$  [87,104,119,177–179]. When CG Cu is processed by SPD at room temperature and a quasistatic strain rate, dislocation sub-structures such as dislocation cells, dense dislocation walls and lamellar sub-grains are the characteristic microstructures observed during the microstructural evolution process [92,133,180]. For example, lamellar

structures/sub-grains containing large amounts of interconnecting boundaries, dislocation clusters and individual dislocations are found in a Cu sample deformed by ECAP to a strain of  $\sim 8$  [180]. These microstructures resemble the microstructures formed in materials with high SFEs at deformation stage 3 (Figs. 8 and 10). As the shear strain increases to  $\sim 18$ , the microstructure of Cu can be refined to below 300 nm [181]. At this deformation stage, the grains are mostly equiaxed, dislocation clusters and stacking faults are randomly found at the interior of some grains (the microstructures resemble the microstructures formed in materials with high SFEs at deformation stage 5) [181,182]. Further deformation by ECAP or cold rolling at room temperature does not noticeably alter the microstructure. Although, deformation twins may be randomly found in ECAP Cu samples at medium to high strain levels due to local stress concentration, the number of deformation twins is still very small [183]. Therefore, one can conclude that the microstructural evolution of the materials with medium SFEs processed by SPD at room temperature, a quasistatic strain rate and low hydrostatic pressure is similar to the microstructural evolution of materials with high SFEs [127,184].

If a high hydrostatic pressure is added during SPD processing, e.g. by means of HPT, further grain refinement to materials with medium SFEs is achievable [92,146,185,186]. For example, when a Cu sample was processed by HPT for five revolutions under a pressure of 7 GPa, the microstructure could be featured with UFGs containing a high density of inhomogeneously distributed dislocations. HRTEM analysis reveals that each ultrafine grain is subdivided by agglomerated dislocations into many nanodomains with similar orientations, as shown in Fig. 11. At the interior of the nanodomains, there is a high density of

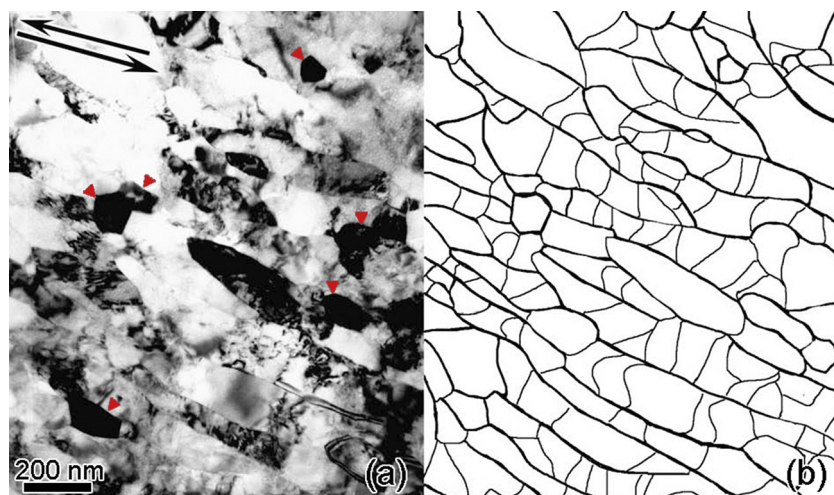


**Fig. 9.** (a) A typical microstructure in a Ni sample deformed by HPT to a strain of  $\sim 12$ ; Some typical equiaxed grains are marked by red triangles; (b) a sketch of the lamellar boundaries and interconnecting boundaries in (a) [126].

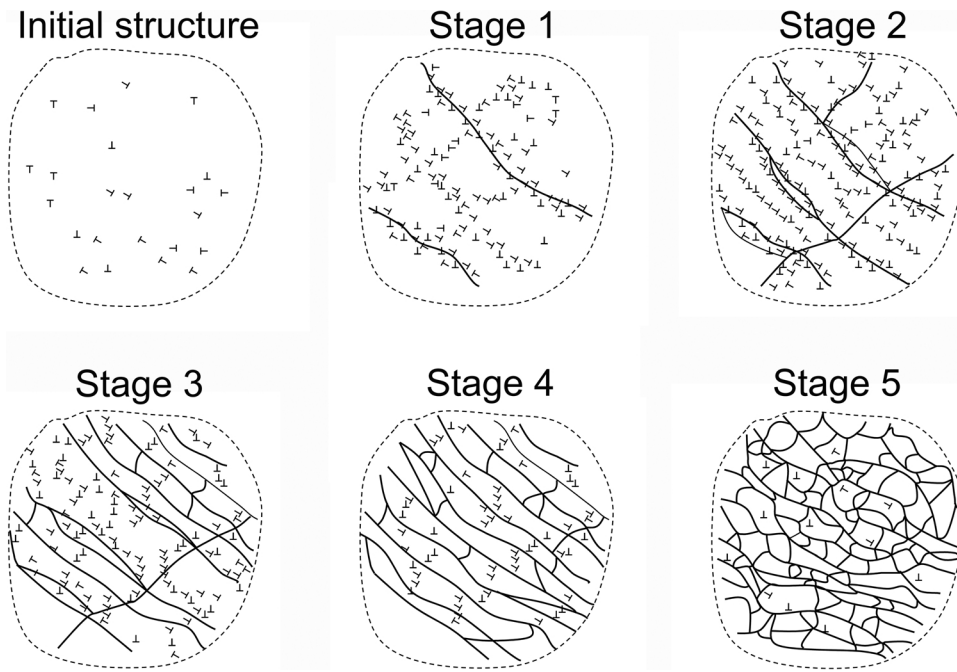


Fig. 10. Schematic illustration of the five grain refinement stages, formed sequentially throughout the microstructural evolution, during SPD of materials with high SFEs. “T” denotes dislocations. GBs and dense dislocation walls are GNBs and are represented by solid lines. Stage 1: Formation of large size dislocation cell blocks containing dislocations and dislocation cell structures. Stage 2: Formation of microbands and transformation of some early dislocation cells into cell blocks. Stage 3: Formation of lamellar sub-grains containing large quantities of dislocations. Stage 4: Formation of well-developed lamellar sub-grains and some equiaxed sub-grains. Stage 5: Homogeneous distribution of equiaxed ultrafine grains or nano-grains.

nano-twins evidenced by the many straight lines at the interior of the nanodomains in Fig. 11(a) and by the Fourier transformation image in Fig. 11(b). Lattice dislocations are mainly located along the boundaries of the nanodomains as shown in Fig. 11(c–d). Only a few lattice

dislocations are observed in the interior of the nanodomains marked by “A” in Fig. 11(c). This indicates that dislocation slip is in dominance until the formation of the nanodomains, then twinning becomes a major deformation mechanism.

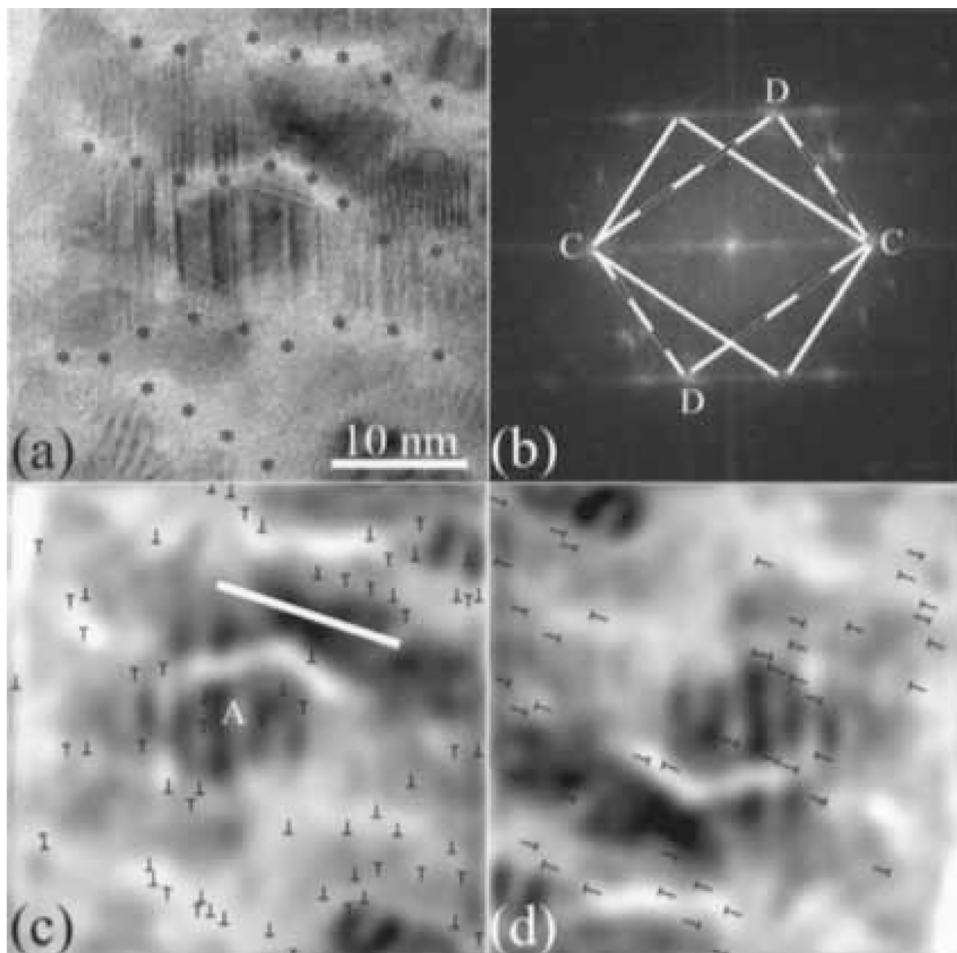


Fig. 11. (a) A TEM image showing nanodomains formed in a Cu processed by HPT for five revolutions under 7 GPa pressure. Black asterisks delineate domain boundaries; (b) Fourier transformation of (a). Two rectangles mark the two sets of lattice forming a twin relationship; (c) an image obtained by inverse Fourier transformation of the (000) and “C” spots in (b). Dislocation cores and slip plane are marked with black “T” and indicated using a white straight line, respectively. Some dislocations are located within a nanodomain at the area marked “A”; (d) an image obtained by inverse Fourier transformation of the (000) and “D” spots in (b) [92].

A systematic investigation suggested that deformation twins in Cu prefer to form in nc grains [92]. This is contradictory to the conventional observations in CG metals and alloys that smaller grain size impedes deformation twinning [3,73,187–189]. For CG metals, the critical stress for activating twinning increases much faster with decreasing grain size than the critical stress for lattice dislocation slip, as revealed by the Hall–Petch slopes shown in Fig. 12 [43,190]. Therefore, smaller grain size makes the deformation twinning more difficult in CG metals irrespective of lattice structure of the metals [73].

When the grain size is reduced to the nc regime, the twinning mechanisms in CG materials cease to operate [191]. Therefore, the Hall–Petch relationship shown in Fig. 12 is no longer valid. An alternative mechanism involving the nucleation of Shockley partials from GBs begins to operate. In nc materials, abundant partial dislocation sources are available from the enormous amount of non-equilibrium GBs, and partial dislocations from GBs need low stresses to move than full dislocations [43,98,192]. Therefore, twinning becomes a major deformation mechanism when the grain size is sufficiently small. This is also true for materials with high SFEs, such as Al and Ni [193–195]. However, it is difficult to refine Al and Ni down below the critical grain size, even with SPD. On the other hand, when the grain becomes too small, twinning becomes more difficult although partial dislocations continue to be emitted to form stacking faults. This leads to an optimum grain size for twinning [43,97,99].

Eventually materials with medium SFEs can be processed by SPD with high pressure (e.g. HPT), into nc structures as exemplified in Fig. 13. Both deformation twins and dislocation slip facilitate the grain refinement from the UFG regime into the nc regime [92]. The steady state grain size is already reached in the nc regime, further straining may be accommodated by deformation twinning [43,196] and GB mediated deformation mechanisms [197–202] owing to high accumulated stress and the grain size effect [99,203]. As a result, deformation twins (Fig. 13(b)) including even multiple or multifold twins (Fig. 13(c)) are often observed at the ns steady state [204,205]. Thus, the high imposed hydrostatic pressure could activate additional deformation mechanisms, extend the deformation stage and further reduce the steady state grain size of materials with medium SFEs.

### 3.3. Grain refinement of FCC materials with low SFEs

SPD-processing of FCC materials with low SFEs presents two important characteristics: (1) deformation twinning; and (2) comparatively effective grain refinement. Overall, deformation twinning is an essential part of the grain refinement process of FCC materials with low SFEs, and the smallest grain size attainable by SPD processing has a close relationship with deformation twinning. However, twinning is very sensitive to processing conditions including temperature [105,206], strain [126,186,205], strain rate [87,88,186,207–209] and stress [86,183,210]. Thus, the actual participation of twinning in the SPD induced grain refinement process is very complicated and “case-dependent”.

Cu–30 wt.% Zn alloys with a very low SFE of  $\sim 7$  mJ/m<sup>2</sup> have been taken as model materials to study the SPD-induced grain refinement process [103,211]. The material was processed by HPT under 5 GPa applied pressure for 5 revolutions. Detailed TEM analysis was conducted from the center to the edge of the HPT disk. TEM images of the characteristic microstructures are shown in Fig. 14 [211]. It is found that, at the disk center where the shear strain is comparatively low [146], equiaxed ultrafine grains containing some twins and SFs are the major microstructural features [95,103], as depicted in Fig. 14(a). The grain sizes at the disk center span over a large range of  $\sim 40$  nm to 400 nm. With increasing shear strain, the twin density increased and the average thickness of the Twin/Matrix (T/M) lamellae decreased to  $\sim 13$  nm as illustrated in Fig. 14(b) [211]. Meanwhile some SFs inclined to the primary TBs formed (marked by white arrows in Fig. 14(b)), and these SFs could be the precursor of the secondary twins.

Primary deformation twins gradually bent as a result of dislocation accumulation on the originally coherent TBs, which would eventually lose coherency and become conventional GBs as shown in Fig. 14(b–c). Fig. 14(c) shows the transitional microstructure consisting of both bent primary twins and lamellar grains. The long boundaries of lamellar grains (marked by black arrows) are nearly parallel to the TBs (marked by white arrows) indicating that the long lamellar GBs were transformed from the coherent TBs. Fig. 14(d) shows a typical TEM image of a bundle of long lamellar grains and the corresponding diffraction pattern indicating a strong texture. Further increase in shear strain increased the amount of secondary SFs and twins, which further subdivided the previously elongated grains into many equiaxed parts (Fig. 14(e)) and thereby transformed the elongated structure into an equiaxed nc structure. The homogeneously distributed equiaxed nano-grains, featuring the final steady state, have an average grain size of  $\sim 10$  nm, which is comparable to the minimum average TB spacing of  $\sim 10$ – $13$  nm, as shown in Fig. 14(f).

Moreover, the GBs of the nano-grains are of an amorphous structure. The formation of the amorphous structure is a result of the collapse of the crystallinity due to the accumulation of a high density of dislocations [212–214]. In contrast, localized amorphisation of GBs was not observed in ECAP processed Cu–16 at.% Al alloys, which also have a low SFE. This is perhaps due to insufficient strain and pressure by ECAP [169]. It is suspected that the constrained nature and the high pressure of HPT are the main factors to cause localized GB amorphisation of materials with low SFEs.

The grain refinement process of Cu–30 wt.% Zn alloy from UFG regime to the nc regime under HPT processing can be schematically described by five steps, as illustrated in Fig. 15. At step 1, equiaxed ultrafine grains are divided into twin lamellae. With increasing shear strain, the densities of dislocations, stacking faults and twins increase. Some of these dislocations pile up at TBs because TBs are strong obstacles for dislocation slip [215,216], as evidenced by Fig. 16 [211]. At step 2, continuous accumulation of dislocations at the TBs gradually bends the originally atomically flat coherent TBs and transforms the TBs into semi-coherent TBs. At step 3, under further straining the semi-coherent TBs completely lose the coherency and transform into high-angle GBs. As a result, long parallel lamellar grains formed. It is known that the interaction between TBs and dislocations not only transforms the TBs into high-angle GBs but also generates new dislocation sources at the GBs [216]. Thus, partial dislocations are emitted from the new GBs to form SFs with further deformation and secondary deformation twins are also formed by twinning partial multiplication. At step 4, secondary SFs and twins subdivide the lamellar grains into rhombic

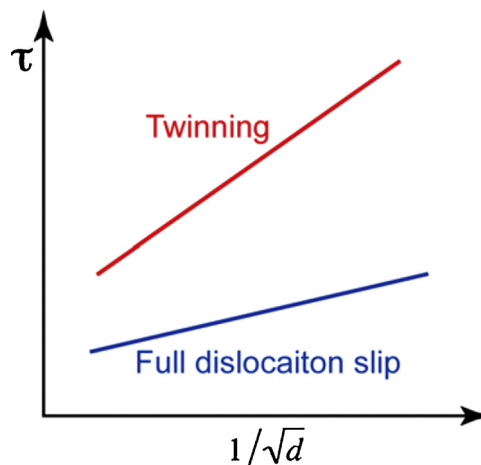


Fig. 12. Schematic of Hall–Petch relationships for twinning and full dislocation slip in CG metals and alloys. Critical stresses ( $\tau$ ) for twinning and for dislocation slip increase with decreasing grain size ( $d$ ) [43].

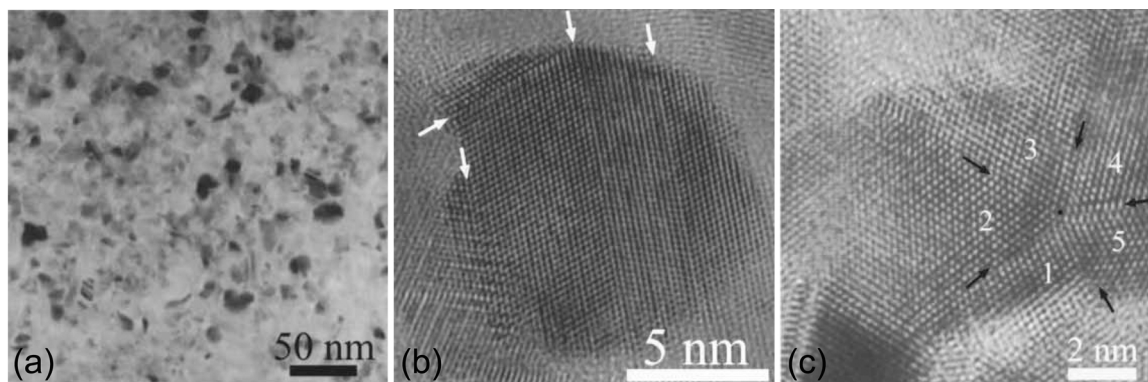


Fig. 13. (a) A typical bright-field TEM image showing nc structure in an HPT processed Cu [92]; (b) a typical HRTEM image of an equiaxed grain containing nano-twins; (c) a fivefold twin observed in a ns copper processed by HPT [186].

domains. At step 5, the secondary TBs transform into incoherent high-angle GBs as noted earlier for the primary TBs, and equiaxed nanograins are formed. In this grain size range, GB mediated mechanisms such as grain rotation, GB-sliding may play significant roles in plastic deformation [198,200,217–219], thereby producing a final steady state nc structure having a random grain orientation. In fact, grain subdivision and refinement via TBs and stacking faults illustrated in Fig. 15 is very common in materials with low SFEs [87,176]. The steady state grain size formed by this grain refinement mechanism is comparable to the TB spacing formed at early steps [175,211]. Because the TB spacing decreases with decreasing SFEs [96], the steady state grain size also decreases with decreasing SFEs [103,104].

The steady state grain size in materials with low SFEs can be larger than the TB-spacing if de-twinning occurred during the deformation process. In recent years, deformation induced de-twinning has received significant attention. De-twinning mechanisms may involve twin-twin interactions [101,220], twin-dislocation interactions [221–224] and partial dislocation slip [225–227]. While the coexistence of high-density deformation twins and dislocations are common in SPD processed materials [86,222], it makes people wonder if de-twinning also plays a role in the grain refinement process and imposes an impact on the steady state grain size. Answers can be found from the systematic research work conducted on HPT processing of the austenitic phase [86,101,228] in steels. At early stages of the deformation, a very high density of nano-twins formed in coarse grains as shown in Fig. 17(a).

The T/M lamellae spacing had a range from  $\sim 1$  nm to  $\sim 25$  nm and an average value of  $\sim 7$  nm. Secondary nano-twins and SFs within the primary T/M lamellae were seldom found as shown in Fig. 17(b). The nano-twinning structure is nearly identical to those observed in one-pass ECAP processed Cu–8 at.% Al alloy according to TEM images [89,169,184], although accurate data of the grain size and TB-spacing were not provided.

As the shear strain increased, a large number of secondary SFs and secondary nano-twins formed, as shown in Fig. 18(a). However, it was noted that neither secondary SF nor secondary nano-twin were found within narrow lamellae with widths smaller than 7 nm [220]. Some of the narrow SF-free lamellae are marked with white arrows. At this strain level, the primary T/M lamellae spacing increased up to 70 nm, indicating the occurrence of de-twinning.

Fig. 18(b) provides a clue of the de-twinning mechanism [101]. There is a primary twin with TBs indicated by 2 TB1 lines and a secondary twin with the TBs specified by 2 TB2 lines. The secondary twinning process occurred via successive partial dislocation emissions from primary TBs. It can be seen that the TB spacing of the primary twin on the left of TB2 is thinner than that on the right by seven  $\{111\}$  atomic layers, which is equivalent to the TB spacing of the secondary twin. This indicates that the reactions between the leading partials of the secondary twin and the primary twin have caused de-twinning by seven consecutive  $\{111\}$  atomic layers to the primary twin. Obviously, the thin twins, mostly less than 7 nm in thickness, were the major target

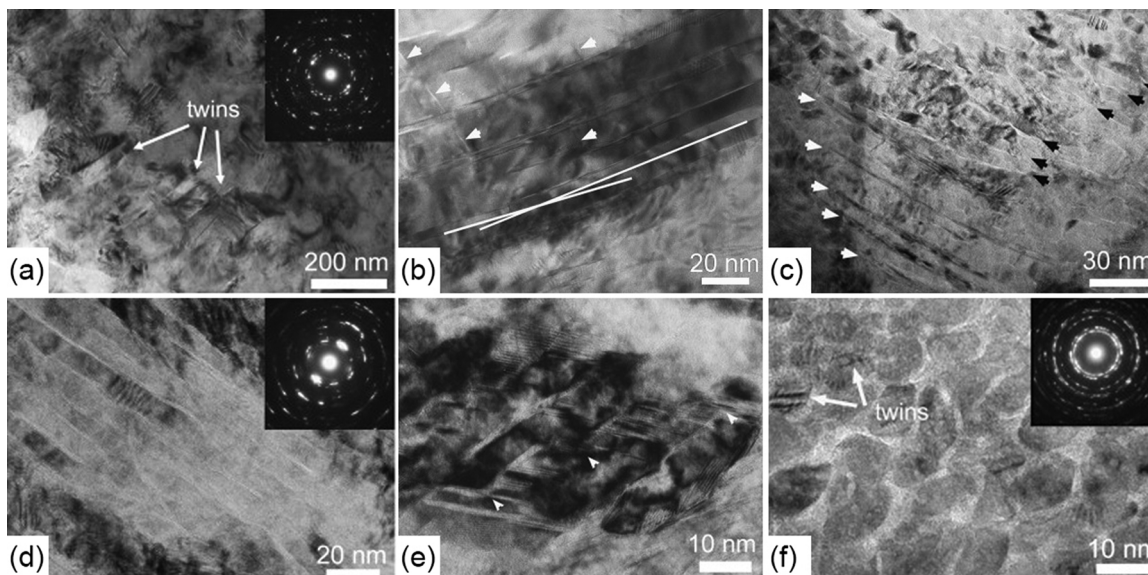
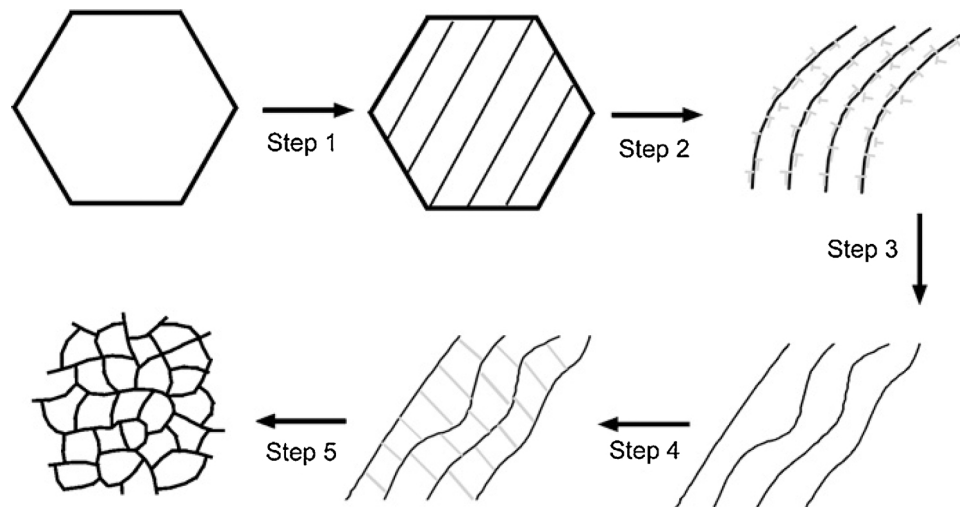
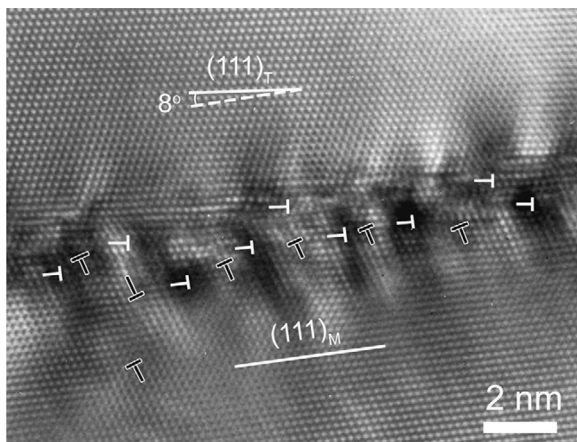


Fig. 14. TEM images showing the characteristic microstructures at locations of incremental strain along the HPT disk radius [211].



**Fig. 15.** Schematic illustration of the grain refinement mechanism by transforming coherent TBs into conventional GBs in materials with low SFEs under SPD processing [211].



**Fig. 16.** An HRTEM image showing a large amount of dislocations blocked by a TB [211]. (Image were taken from a Cu-30 wt.% Zn alloy processed by HPT. “T” indicates dislocations. Two white solid lines trace a {111} plane at each side of the TB, respectively. One dash line traces  $(111)_M$  to indicate the misorientation between the {111} planes across the TB.).

for de-twinning, because thin twins were less likely to trap dislocations but having dislocations slipping along the coherent TB to cause de-twinning [91,229–231]. The detailed explanation about the de-twinning process can be found in literatures [101,220,229]. As a result, significant amount of primary nano-twins were de-twinning. The remaining primary TBs could later transform into high-angle GBs after absorbing a large amount of dislocations [176].

Interestingly, there were also significant amount of low-angle boundaries formed after the de-twinning process as shown in Fig. 19(a). As shown by Fig. 19(b–c), the low-angle boundary is actually a dislocation wall that is nearly parallel to the GB. Systematic investigation showed that the dislocation wall was formed by the remnant dislocations from the de-twinning of thin nano-twins [101]. The microstructure formed by this mechanism has a distinct characteristic of elongated grains divided by low-angle GBs as shown in Fig. 19(a). Similar microstructures have also been observed in many other SPD processed low SFE materials [11,169,211,228].

With further shear straining, the primary twins in the coarse grains were either de-twinning by interacting with secondary twins and SFs, or transformed to conventional GBs [101,220]. As a result, elongated ultrafine grains with non-equilibrium GBs formed as shown in Fig. 20(a) [228]. There are high densities of extrinsic (extra) dislocations at non-

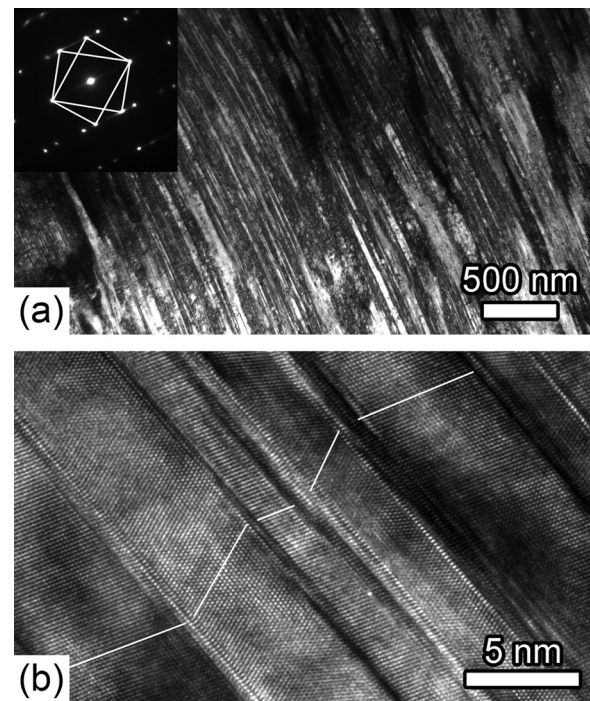


**Fig. 17.** (a) A TEM image showing a high density of deformation twins (the inset SAED confirms the twin relationship); (b) an HRTEM image of the deformation twins (white lines tracing the {111} planes forming the twin relationship) [228].

equilibrium GBs owing to the formation mechanisms of the GBs [17,101,135,147,148]. These extrinsic dislocations are readily available sources of partial dislocations and twin embryos [149]. Meanwhile, as the grain size is in the lower UFG regime, GB mediated twinning mechanisms began to operate. It is noted that the optimum grain size to activate GB mediated twinning mechanisms increases with decreasing SFE [102,184,205]. Thus, an extremely high density of SFs and nano-twins could form within these grains, as exemplified by Fig. 20(a–b) (an average TB spacing of 1.7 nm have been reported) [228].

TBs are usually very strong obstacles to dislocation motion [232]. However, when the TB spacing is extremely small, the classical Hall–Petch type of strengthening due to dislocation pile-up at TBs switches to

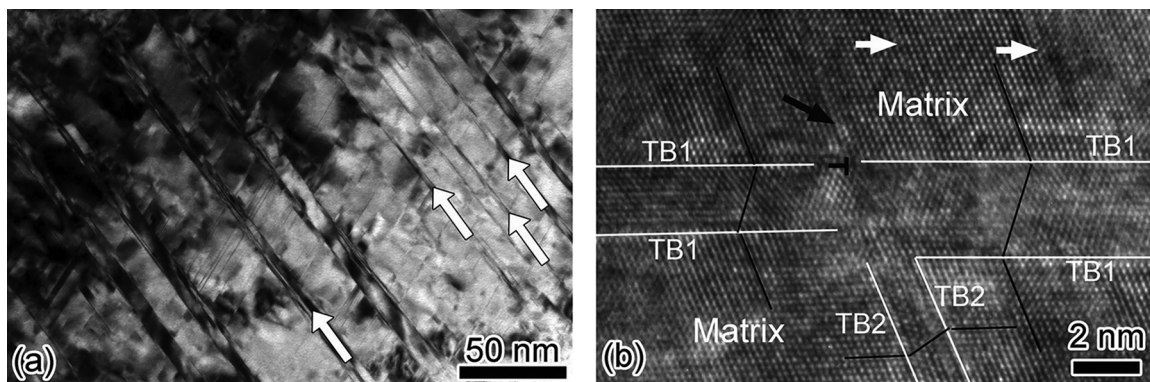


**Fig. 18.** (a) A typical TEM micrograph showing secondary twinning within primary T/M lamellae; (b) a typical HRTEM image illustrating the de-twinning to the primary twins via the interactions with secondary nano-twins/SFs [101].

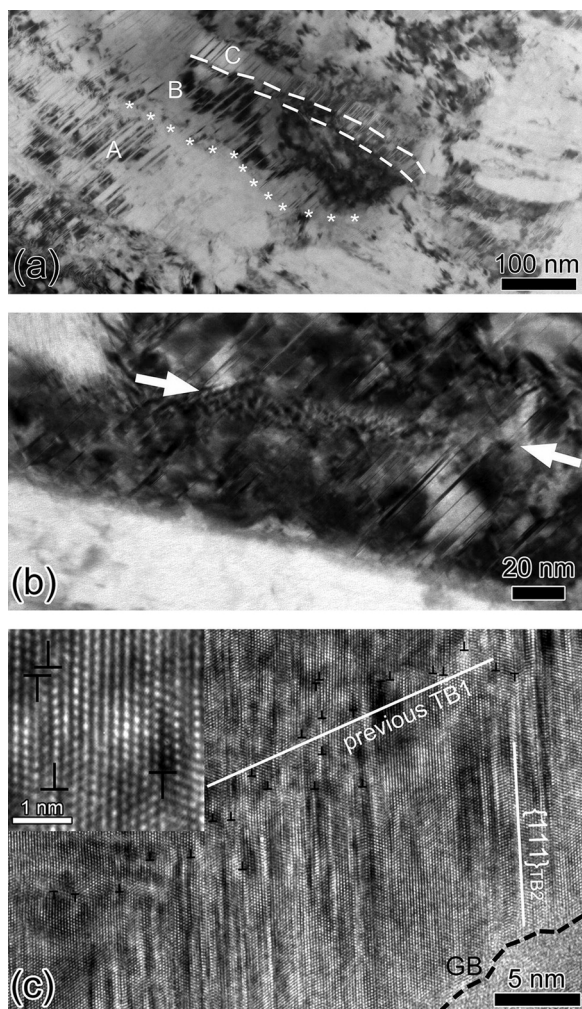


**Fig. 19.** (a) A low magnification TEM micrograph showing the microstructures of elongated grains formed after the de-twinning of primary twins; (b) a high magnification TEM micrograph showing a dislocation wall within an elongated grain; (c) an HRTEM image showing a high density of dislocations aligned along the previous TB1 which is roughly parallel to the elongated GB. The inset shows a magnified image of an area with dislocations [101].

a dislocation-nucleation controlled softening mechanism with TB migration resulting from nucleation and motion of partial dislocations parallel to the twin planes [233]. Thus, the TBs lose their ability to trap dislocations and therefore lower the strength of the material when the TB spacing is too small [234]. There exists a critical TB spacing for

softening and this critical spacing is a function of grain size [233]. An estimation based on the theory proposed in the literature [233] indicates that the TB spacing of 1.7 nm is below the critical TB spacing for grains larger than 100 nm, implying that the high density nano-twins no longer contributed to the strengthening of the material. To further increase the flow stress with increasing strain, de-twinning through nucleation and slip of partial dislocations from GB and GB–TB junctions is the only choice [229,230,233,235]. With decreasing twin density, the remaining TBs regained the capability to trap dislocations and further grain refinement by TBs was activated again, as shown in Fig. 20(c–d).

The grain refinement process involving pronounced twinning and de-twinning can be described in four stages, as illustrated schematically in Fig. 21. At step 1, a high density of primary deformation twins formed in the coarse grains. One or two twinning systems can be activated in each grain depending on the relative orientation of individual grains that affects the resolved shear stresses on different twinning systems, as illustrated in Fig. 21(b). At step 2, a de-twinning process occurred through the formation of secondary SFs/nano-twins on inclined slip planes and the interaction between the secondary SFs/nano-twins and the primary twins. The de-twinning process increased the TB spacing of the primary twins from a few nanometers to a few tens or even hundreds nanometers, transformed the remaining TBs into non-equilibrium GBs through dislocation–TB interactions. The average grain size is then reduced to the UFG regime. The large amount of dislocations residing on the non-equilibrium GBs becomes the source of SFs and nano-twins, leading to an extremely high density of nano-twins under the effect of high stress, as illustrated in Fig. 21(c). At step 3, the resulting highly twinned UFG structure underwent immediately through the second de-twinning process that occurs via partial dislocation emissions from TB and GB junctions [49,54]. The reduced twin density caused by the second de-twinning process enables dislocation activities on the inclined slip planes [54] that leads to significant dislocation–TB interactions and consequently transformed the remaining TBs into conventional GBs to further subdivide the grains, as presented in Fig. 21(d). At step 4, SFs and nano-twins were continuously formed through partial dislocation emission from GBs in the nano-crystallites. Thus, further grain refinement was through the interactions between newly formed dislocations and nano-twins [222]. The average grain size at the steady state (Fig. 21(e)) is only slightly smaller than that of the previous stage (Fig. 21(d)) [228].

In summary, imposed high shear strain and shear stress by SPD promote the formation of nano-twins in FCC materials with low SFEs [86,210]. TBs are effective obstacles for dislocation slip, thus dislocations may quickly accumulate at the TBs and transform coherent TBs into conventional GBs upon further straining by SPD. As a result, the steady state grain sizes of many SPD processed FCC materials with low SFEs are comparable to the TB-spacing found at the early stage of deformation. However, de-twinning may participate in the SPD induced

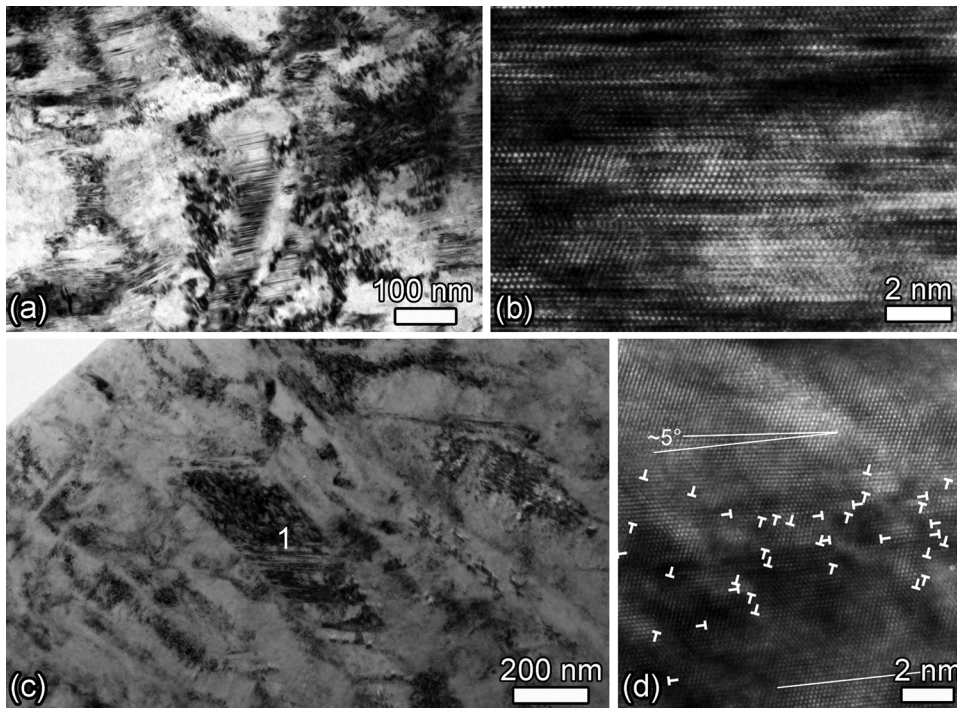


**Fig. 20.** (a) A TEM image of ultrafine austenite grains containing a high density of nano-twins; (b) an HRTEM image showing a high density of SFs/nano-twins within a grain; (c) a TEM image of an ultrafine austenite grain containing a high density of dislocations and some nano-twins; (d) an HRTEM image of area 1 in (c) where the white “T” denote dislocation cores and the misorientation between the top and bottom areas is  $\sim 5^\circ$  [228].

microstructural evolution, if the nano-twins formed at the early stage of deformation are thinner than a critical thickness [230,233–235]. Detwinning may occur due to interactions between primary coherent TB and inclined nano-twins/SFs [101,220] or due to partial dislocation emission from GBs [226,228,233]. Most importantly, if any type of detwinning occurs in any stage of the grain refinement process, the steady state grain size will be larger than the average TB-spacing [87,89,101,184,220,228,236,237].

### 3.4. Grain refinement of BCC materials

Unlike FCC materials, literatures about SPD processing of BCC materials are comparatively limited. This is possibly due to two reasons: (1) researchers are more interested in strain rate sensitivity and temperature sensitivity of BCC materials [238–243] and (2) it is difficult to have a general description about SPD processing of BCC materials because of the large variation of plasticity among BCC materials

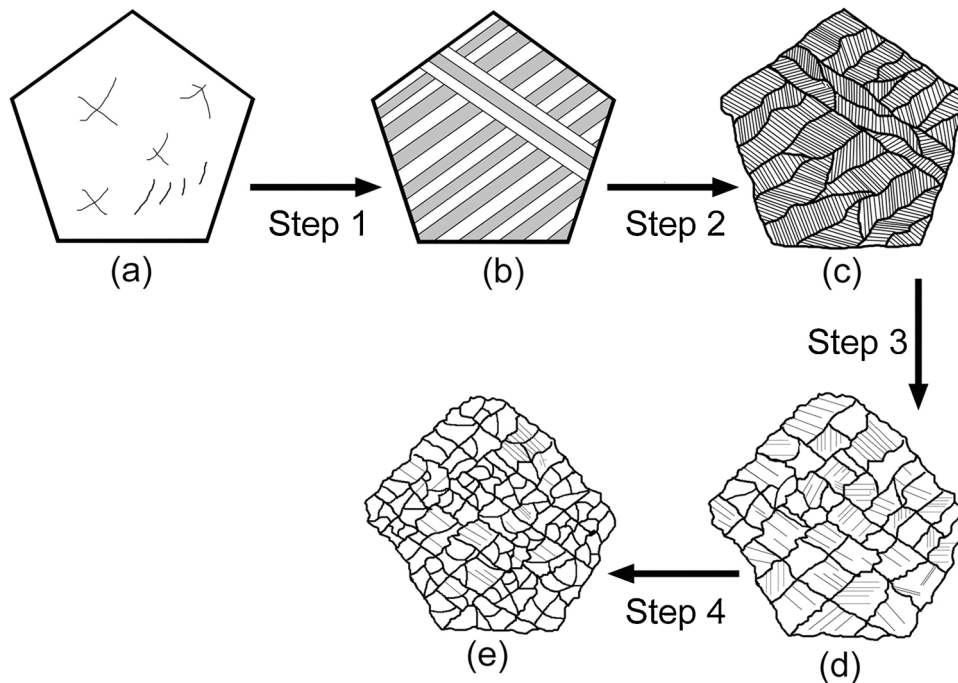


**Fig. 21.** A schematic diagram of the grain refinement process involving twinning and de-twinning in FCC materials with low SFEs [228].

[244–246]. Typical BCC materials processed by SPD include Vanadium (V) [247–249], Chromium (Cr) [107,250], Iron (Fe) [241,251–253] and ferritic steel [228,254–256], Niobium (Nb) [246,257], Molybdenum (Mo) [258,259], Tantalum (Ta) [244,260,261], and Tungsten (W) [108,262,263]. Among these materials, Ta (Group VB) has a brittle-to-ductile transition (BDT) temperature of  $\sim 10$  K and stands out to be the most ductile metal at low temperatures [243]. In contrast, W (Group VIB) has the highest melting point among all metals and a high BDT temperature of above  $\sim 370$  K [264]. The BDT temperature of polycrystalline W spreads a wide range due to variation in grain size, impurity concentration, and tensile strain rate [265]. On the other hand, W has negligible ductility at temperatures below 423 K in any case [266]. Therefore, while other BCC materials could be SPD processed at room temperature, W has to be deformed at high temperatures above 873 K [245] to avoid brittle failure before substantial grain refinement.

Plastic deformation of BCC materials is fundamentally governed by dislocation slip along the close-packed  $\langle 111 \rangle$  directions and dislocation activities have been observed on  $\{110\}$ ,  $\{112\}$  and  $\{123\}$  planes in the

order of increasing rarity [63,267,268]. Experimental observations and atomistic simulations suggested that edge dislocations in BCC materials possess planar cores, low lattice friction, and consequently high mobility [268–272], while screw dislocations possess non-planar cores, strong lattice friction and consequently low mobility [273], but they can cross-slip as shown in Fig. 22 [274].

In Fig. 22(a–b), the dislocation source was pinned at point S. During dislocation emission process, the dislocation loop (in the form of curved trails) expanded into a straight screw part and a curved non-screw part, spiralling around the source pinning point S. Fig. 22(c–f) shows the continuous dislocation emission process (the original movie is available in the reference [268]). When the curved non-screw part reaches its critical position (white colour trace) at  $t = 2.32$  s in Fig. 22(d), the curved part escaped suddenly to touch the top ( $\bar{1}23$ ) plane as shown in Fig. 22(e), creating a dipole of two opposite screw segments (two parallel white lines). Two straight screw dislocations with opposite Burgers vectors slip away from the source, that one screw dislocation slip toward top left in Fig. 22(a and f) and the other screw dislocation

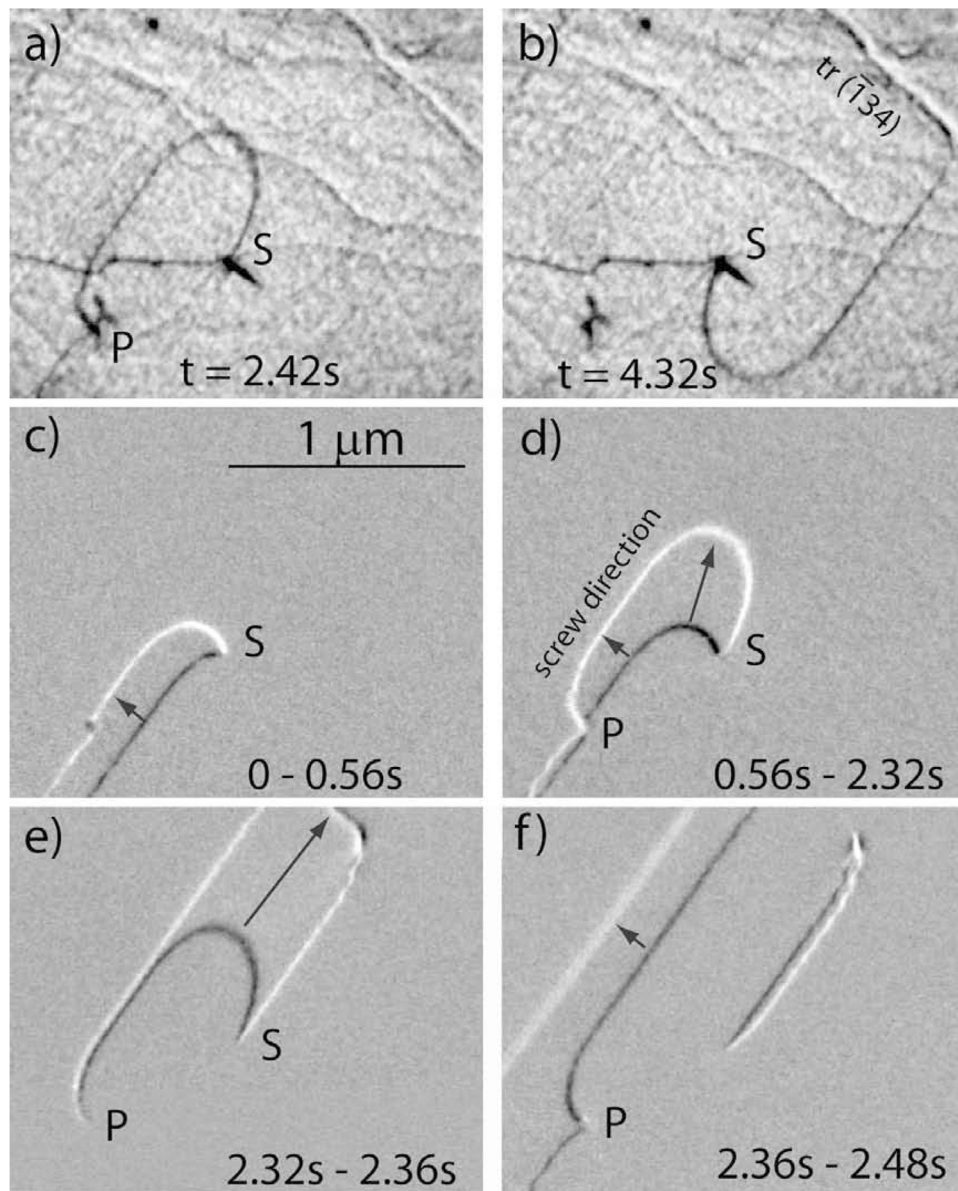


**Fig. 22.** Emission and subsequent cross-slip of dislocations observed in a high purity Fe sample; Point S is the source pinning point. Point P is a pinning point for incoming screw dislocation. (a) and (b) snapshots of dislocation motion at 2.42 s and 4.32 s, respectively; (c–f) successive images showing the trace of dislocation slip within the period of 0 s to 2.48 s [268].

slip toward bottom right in Fig. 22(b and f). The slip plane of the second screw dislocation is close to  $(\bar{1}23)$  as shown in Fig. 22(b).

To complicate matters further, the core structures of  $\frac{1}{2}\langle 111 \rangle$  screw dislocations are very different among BCC materials, due to different characteristic properties such as the cohesive energy and the elastic constants [239,273]. For group VIB metals, a dislocation core may spread asymmetrically into three intersecting planes, creating one fractional dislocation with a Burgers vector  $1/6 [111]$  on each plane. For group VB metals, a dislocation core may spread symmetrically into three planes, creating two fractional dislocations with Burgers vectors  $1/12 [111]$  on each plane [239,260,264]. It should be noted that fractional dislocations delimit a region of an unstable generalized stacking fault. In contrast, partial dislocations terminate metastable stacking faults [273]. Under plastic deformation, the shear stress perpendicular to the dislocation slip direction alters the symmetry of the dislocation core such that it could either promote or impede the slip on the most highly stressed slip plane. As a result, these screw dislocations have to move (to cross slip) by kink-pair nucleation and slip on fundamental slip planes [63], creating net slip on either  $\{110\}$  or  $\{112\}$  planes [239,275]. The unique dislocation core structures and frequent cross slip of  $\frac{1}{2}\langle 111 \rangle$  screw dislocations are responsible for the plastic anisotropy [239] and the widely observed non-Schmid effect (slip on non-close-packed planes) in BCC materials [239,276–283].

Although, BCC materials possess unique dislocation core structures [278,279,281,284–287], the SPD-induced grain refinement process for BCC materials is somehow similar to that observed in FCC materials with high SFEs [243,246,257,288–292]. The grain refinement of BCC materials is governed by the development of dislocation structures, in such way that incidental dislocation boundaries and GNBs continuously form and increase in quantities by trapping dislocations with increasing strain. As shown in Fig. 23, dislocation walls and sub-grain boundaries are evident in SPD processed Fe (Fig. 23(a)) and W (Fig. 23(b)). In the latter case, the W sample was processed at  $\sim 600^\circ\text{C}$ , which corresponds to a homologous temperature of  $\sim 0.24$ . Therefore, W was able to deform plastically while significant dynamic recovery was suppressed [293]. Increasing the shear strain leads to the formation of typical lamellar dislocation structures and interconnecting boundaries (short dislocation walls inside lamellar grains) as shown in Fig. 24, which are similar to those observed in FCC materials. As the shear strain increases to a sufficiently high level, the microstructures of BCC materials eventually reach a steady state where the average grain size is not further reduced. The strain required to reach the steady state for a BCC material is positively related to the shear modulus of the material, this is also the same as for FCC materials [107,252,294].

Similar to the cases in FCC materials processed by SPD, dislocation

densities of  $> 10^{16} \text{ m}^{-2}$  can be easily achieved in BCC materials processed by SPD. Local dislocation density variation caused by dislocation interactions and re-arrangement is also noticed during the microstructural evolutions of BCC materials processed by SPD [244,260]. Series of TEM works have shown that in the very tiny sub-grains (a few tens of nanometers), a high density of dislocations with edge components can be found at the interior [243,246,260,262], such as these shown in Fig. 25 of HPT processed Mo samples [295]. Two-beam conditions were used for imaging dislocations with enhanced contrast. The segments of both edge and mixed dislocations in the grain of  $\sim 140 \text{ nm}$  are visible in Fig. 25(a). In a larger grain of  $\sim 300 \text{ nm}$  shown in Fig. 25(b), the dislocations are mostly of the screw type. It has been proven experimentally that the dominant type of dislocations tends to change from the screw type to the edge and mixed types when the grain size is reduced to the nc regime [260,262,295], as shown by the statistical data in Fig. 26.

In BCC materials, it is well-known that deformation twinning may occur via the propagation of  $\frac{1}{6}\langle 111 \rangle$  partial dislocations on  $\{112\}$  planes [59,278]. However, the SFEs of BCC materials are usually very high, and the critical twinning stress in BCC metals and alloys does not vary significantly in a large temperature range of 4–300 K. [73,106,297–299]. Thus, deformation twinning has been rare in SPD-processed BCC materials. To date deformation twinning in polycrystalline BCC materials has only been experimentally achieved under extremely high stress induced by shock loading [279–281,300–302], or at the crack tip [303]. There are also simulation results showing deformation twinning in nc BCC materials at high strain rate, but the extremely small grain size and extremely high strain rate adopted in the simulations are hardly achievable in experiments [304,305]. Moreover, recent experimental results showed that twinning in nano scale BCC materials could be pseudo-type and de-twinning is likely to occur upon unloading [278]. Therefore, deformation twinning is rarely observed or involved in SPD-induced grain refinement of BCC materials. Gapontseva et al. performed SPD processing of Nb at cryogenic temperature (80 K) to achieve an average grain size as small as 40 nm, but no deformation twin was found in the material [306].

### 3.5. Grain refinement of HCP materials

In contrast to materials with cubic structures, materials with HCP structures possess lower crystallographic symmetry and fewer independent slip systems. Fig. 27 illustrates schematically the HCP structure and its slip systems. All easy slip systems having the shortest perfect dislocation Burgers vectors of  $1/3 \langle 11\bar{2}0 \rangle$  or  $\langle a \rangle$  are on the basal plane or prismatic planes, which are perpendicular to the  $c$ -axis. To accommodate strain along the  $c$ -axis, slip systems with a  $c$ -component

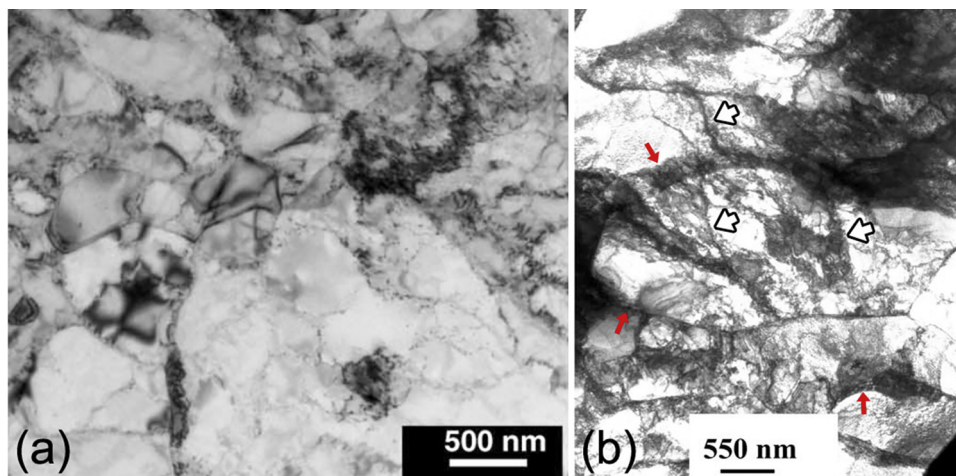


Fig. 23. TEM micrographs of (a) polycrystalline iron processed by HPT to an equivalent strain of  $\sim 210$  [296]; (b) polycrystalline W processed by ECAP + rolling at high temperatures [293]. White arrows and red arrows indicate some dislocation walls and sub-grain boundaries, respectively.

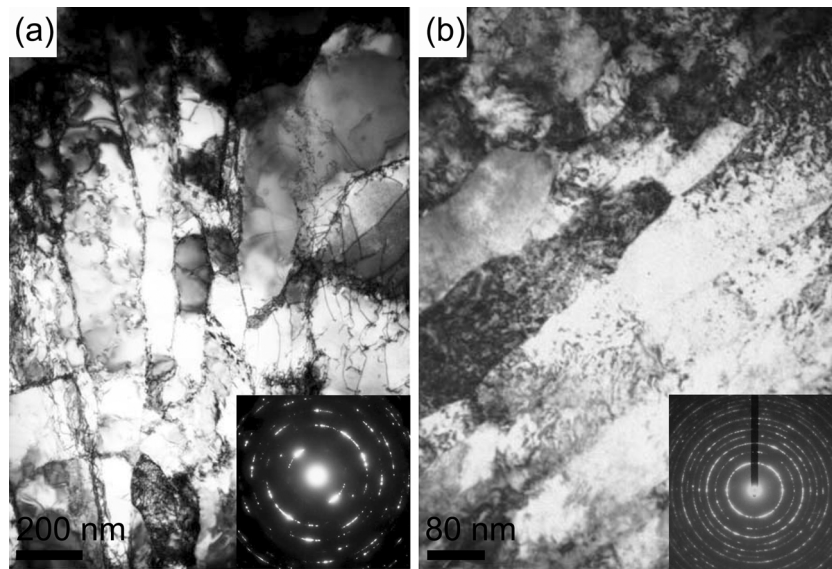


Fig. 24. TEM micrographs of (a) commercially pure (99.98%) Ta processed by ECAP to an equivalent strain of  $\sim 4.64$  [291]; (b) commercially pure W processed by high temperature HPT to an equivalent strain of  $\sim 70$  [262].

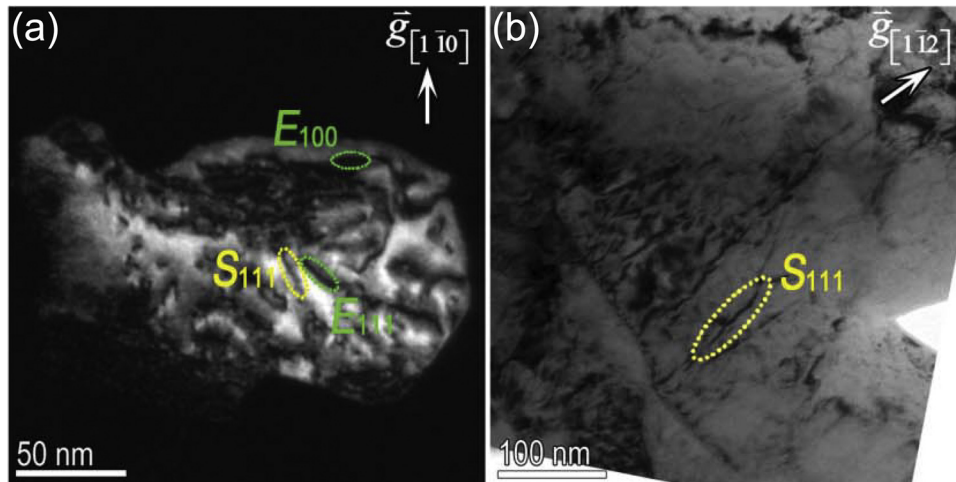


Fig. 25. TEM images taken at two-beam conditions showing dislocations in grains with different sizes in HPT-processed Mo samples. (a) A dark field image of a  $\sim 140$  nm grain, and (b) a bright field image of a  $\sim 300$  nm grain. The  $\bar{g}$  vectors used for imaging are provided on the images.  $S_{111}$ ,  $E_{111}$  and  $E_{100}$  symbolize the  $\frac{1}{2}\langle 111 \rangle$  screw,  $\frac{1}{2}\langle 111 \rangle$  and  $\langle 100 \rangle$  edge dislocations, respectively [295].

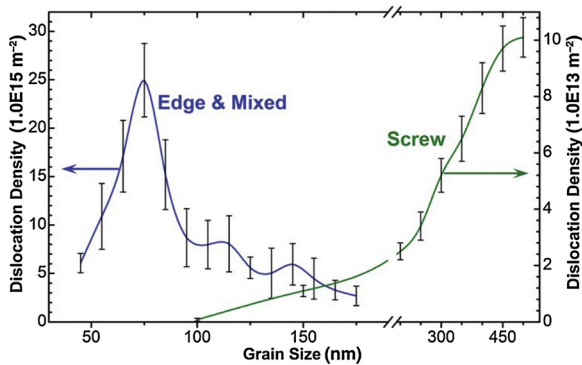


Fig. 26. Statistical analysis of the dislocation density evolution with respect to grain size for  $\frac{1}{2}\langle 111 \rangle$  screw dislocations and for  $\frac{1}{2}\langle 111 \rangle$  edge and mixed dislocations [295].

are necessary [67,109,307–311]. This can be achieved by the nucleation and slip of  $\langle c + a \rangle$  dislocations [312–314]. Thus,  $\langle c + a \rangle$  slip systems are recognized the common secondary slip systems.

The ideal  $c/a$  ratio in a HCP unit cell is 1.633 [315]. In fact, HCP materials may have different  $c/a$  ratios, thus the choice of principle slip planes and the tendency for phase transformation are often different among HCP materials [316]. The principal  $\langle a \rangle$  slip plane is usually either basal plane (0001) or prismatic planes  $\{1\bar{1}00\}$ , depending on whether  $c/a$  is above [317] or below  $\sim 1.6$  [318–323]. An exception is Be, which has a  $c/a$  ratio of 1.568, but its principal slip plane is the (0001) basal plane, which is still puzzling, and may be related to dislocation core structure [324–326].

The preference for active slip systems can be reflected by their CRSS. As illustrated in Table 2, for those with a  $c/a$  ratio above 1.6 (e.g. Mg), the preferred slip system is the  $\langle a \rangle$  basal slip systems. In contrast, for those with a  $c/a$  ratio below 1.6 (e.g. Ti), the preferred slip system is

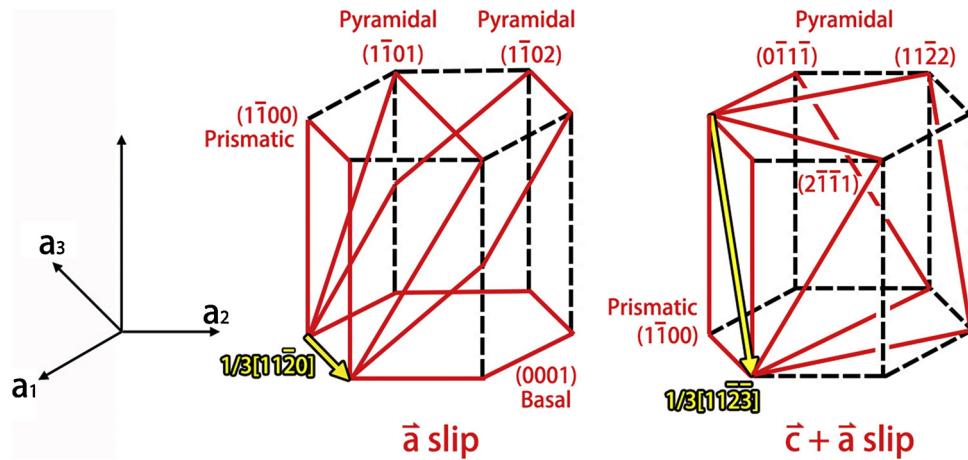


Fig. 27. A schematic illustration of the theoretical slip systems in the HCP lattice structure.

the  $\langle a \rangle$  prismatic slip systems. In addition, some HCP metals have  $\{1\bar{1}01\}\langle a \rangle$  pyramidal slip systems. The strain accommodated by  $\{1\bar{1}01\}\langle a \rangle$  slip is equivalent to the strain produced by simultaneous and independent operation of  $(0001)\langle a \rangle$  slip and  $\{1\bar{1}00\}\langle a \rangle$  slip [62]. However, there are no more than four independent slip systems with  $\langle a \rangle$  Burgers vectors in HCP materials. Therefore,  $\langle a \rangle$  dislocations alone are insufficient to fulfill the von Mises criterion for strain accommodation [62,64], and  $\langle a \rangle$  dislocations are incapable of accommodating the strain perpendicular to the basal plane. Thus,  $\langle c + a \rangle$  dislocations and/or deformation twinning are necessary for a general homogeneous deformation of HCP materials without cracking or forming voids (common twinning systems in HCP materials are listed in Table 1, Section 2).

As shown in Table 2, the CRSS of  $\langle c + a \rangle$  slip and twinning are significantly higher than  $\langle a \rangle$  slip, resulting in significant flow stress anisotropy in HCP materials. Note that the principal  $\langle c + a \rangle$  glide plane is  $\{11\bar{2}2\}$  for Be, Cd, Mg and Zn, but  $\{1\bar{1}01\}$  for Ti and Zr. In addition, the CRSS for slip in HCP materials are sensitive to temperature. For example, CRSS values for  $\langle a \rangle$  prism slip in Ti and Zr are radically lower than for  $\langle a \rangle$  basal slip at low temperatures but becoming more similar at high temperatures. Please refer to the relevant literatures [64,327–335] for more details of CRSS of slip systems in HCP materials.

There are also reports about phase transformation from HCP structures to BCC structures at elevated temperatures or under high pressures. The HCP materials prone to phase transformation are those with small  $c/a$  ratios [316,336–340]. Further discussion about phase transformation in HCP materials is provided in Section 6. SPD-induced phase transformation.

The abovementioned characteristics of HCP materials make them obviously different from FCC and BCC materials in terms of SPD-induced structural evolution. Thereby, many interesting and unique deformation mechanisms and microstructures were found in SPD processed HCP materials.

### 3.5.1. Microstructural inhomogeneity and strain localization in plastically deformed HCP materials

As shown in Table 2, the CRSSs for pyramidal slip and for

deformation twinning are much higher than that for  $\langle a \rangle$  slip [341–343]. When an HCP crystallite has its  $c$ -axis aligned nearly parallel to the imposed stress, the crystallite is therefore in the “hard orientation” [66,311,344]. The existence of the “hard orientation” together with the asymmetric natures of twinning and pyramidal slip in polycrystalline HCP materials leads to significant microstructural inhomogeneity under plastic deformation [343,345–349]. For example, as shown in Fig. 28(a), there is obvious grain size inhomogeneity in Mg processed by one pass ECAP. The large grains are as big as a few hundred micrometers and the small grains are as small as a few micrometers. Similar microstructural inhomogeneity is also exemplified in an ECAP processed polycrystalline Mg shown in Fig. 28(b), although the difference between large and small grains is slightly smaller comparing to that in Fig. 28(a). Such microstructural inhomogeneity has also been observed in an HPT processed Zr alloy with a smaller  $c/a$  ratio than Mg [349]. Therefore, it is concluded that microstructural inhomogeneity induced at the early stages of SPD processing is a common phenomenon in HCP materials.

During SPD processing of an HCP material, microstructural inhomogeneity and microscale flow stress anisotropy may prevent basal dislocations from slipping in grains with certain orientations, and rapidly increase stress concentration at GBs and/or TBs. The highly concentrated stress will eventually lead to shear banding and cracking [334,344,350–352]. Plastic instability and shear banding have been frequently encountered during plastic deformation of HCP materials, but in-depth explanation about shear banding was seldom provided.

Fig. 29(a) shows interconnecting microbands dividing a coarse grain in an ECAP processed Mg–3Al–1Zn alloy. The microbands contain large amounts of recrystallized fine grains. Fig. 29(b) presents a corresponding EBSD–Kikuchi band contrast map, where specific GBs are highlighted in different colors, indicating that different twinning modes accommodated the deformation. It was found that these microbands were originally compression twins [353]. The twinned regions were more favorably oriented for basal slip than the matrix [350]. Because basal slip systems are the softest slip systems in HCP structures, further straining was localized within the compression twins and accommodated by pronounced twinning and basal slip. This non-uniform

Table 2

Estimated CRSS (MPa) for five common deformation systems in Mg and Ti. (CRSS data for Mg and Ti were obtained for the temperature ranges of 500–600 K and 200–600 K, respectively) [64,328–335].

Materials	Basal $\langle a \rangle$ slip	Prismatic $\langle a \rangle$ slip	Pyramidal $\langle c + a \rangle$ slip	$\{10\bar{1}2\}\langle 10\bar{1}1 \rangle$ tension twinning	$\{10\bar{1}1\}\langle 10\bar{1}2 \rangle$ compression twinning
Mg [328,329,330]	2.7–13	12–20	24–45	10–18	~100
Ti [64,331,332,333,334,335]	49–150	37–98	120–224	125–213	N/A

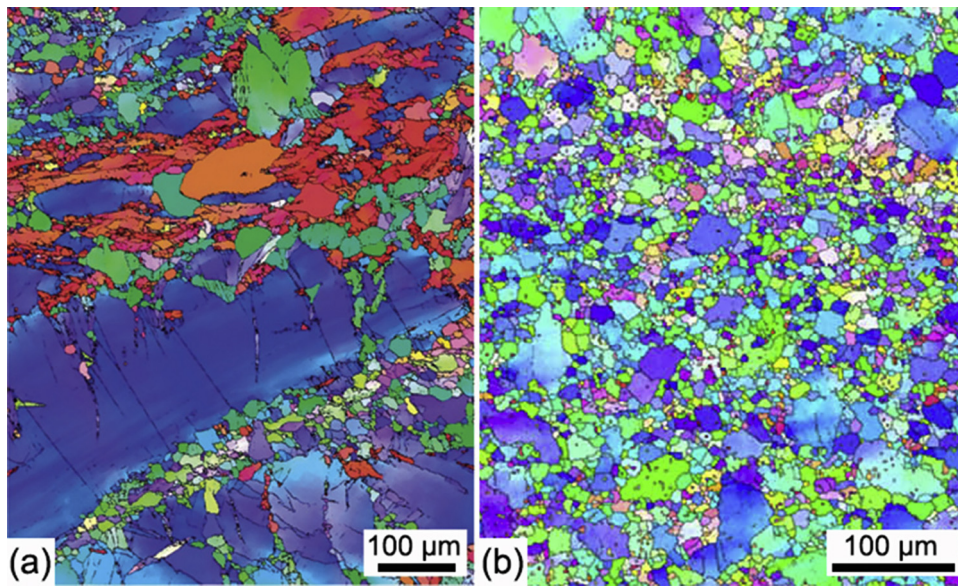


Fig. 28. EBSD images showing the microstructures of (a) a single crystal Mg after one ECAP pass [347] and (b) a polycrystalline Mg after four ECAP passes [343].

deformation triggered earlier dynamic recrystallization inside compression twins than in the surrounding regions, and transformed the previously formed large twin bands into microbands.

Fig. 29(c) presents a low magnification image showing a large number of microbands (the thin lines with light contrast) agglomerated into a macro shear band in an ECAP processed AZ31 (Mg–3Al–1Zn) alloy at 150 °C [353]. Similar microstructures have also been observed in ECAP processed commercially pure titanium [354,355]. At the vicinity of the shear band, there are also pronounced intersecting microbands. Accordingly, Dogan et al. proposed a shear banding mechanism as depicted in Fig. 29(d). Large amounts of twin bands firstly form within coarse grains; then localized deformation proceeds within the twin bands in the form of basal slip and twinning. Vigorous dislocation activities and double twinning within the twin bands lead to

high stress concentration causing dynamic recrystallization and transform the twin bands into microbands. Eventually, a large number of microbands agglomerates into a macro shear band. In addition, this macro shear band formation mechanism has also been observed in ZK60 (Mg–6Zn–0.5 Zr) Mg alloys processed by a high strain-rate rolling process at different strain rates [356,357].

It was found that as the strain rate increased from 1 to 50 s<sup>-1</sup>, the tendency for twinning increased significantly. This in turn provided more nucleation sites for dynamic recrystallization, resulting in smaller average grains. Therefore, the primary macro shear banding mechanism becomes increasing vigorous with increasing strain rate, at least up to 50 s<sup>-1</sup>. What is remarkable about this macro shear banding mechanism is that further deformation results in repeated twinning and the subsequent dynamic recrystallization within the shear band to

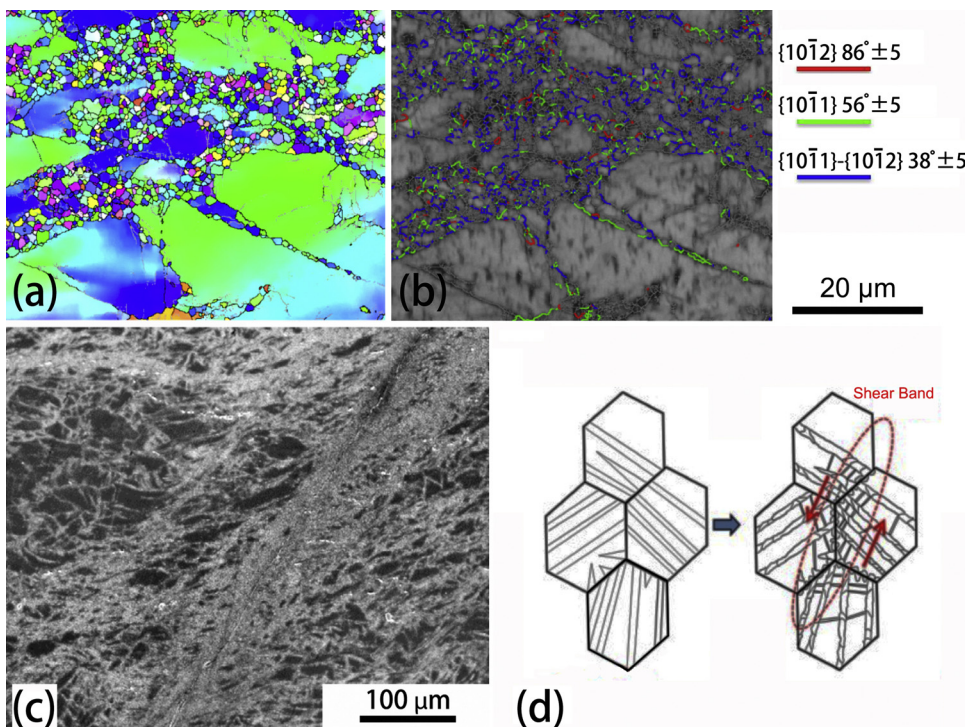


Fig. 29. (a) An EBSD image showing microbands dividing a coarse grain in an ECAP processed Mg–3Al–1Zn alloy; (b) a corresponding EBSD image showing the TBs in (a); (c) a low magnification micrograph showing a shear band observed in an ECAP processed Mg–3Al–1Zn alloy; (d) schematic illustration of a proposed shear-banding mechanism [353].

produce an increasingly fine scale microstructure with increased strain. Meanwhile, dynamic recrystallization is very helpful for randomizing orientations of the refined grains. Thus, the operation of this macro shear banding mechanism substantially refines the grain structure and results in the development of a truly UFG microstructure with reduced texture in HCP materials [356,357].

This shear banding mechanism is different from the conventional adiabatic shear banding mechanism which requires much higher strain rate and producing significantly different microstructures [358–360]. However, further experiments are required to further explore the strain rate sensitivity of the proposed macro shear banding mechanism and to verify if there is a transition between different shear banding mechanisms at the strain rate increases to a very high level [241].

Fig. 30(a) shows the inhomogeneous microstructure at the vicinity of a crack in a room temperature ECAP-processed AZ31 Mg alloy, indicating that microstructural inhomogeneity and flow localization have led to failure [361]. In contrast, Ti and Zr tend to possess better ductility than many other HCP materials, because both tension and compression twins are likely to form in CG Ti and Zr [64]. However, Ti and Zr can still fracture easily just like other HCP materials when processed by unconstrained SPD methods at a low homologous temperature [354,362], exemplified by the image showing in Fig. 30(b). In order to prevent or delay the failure of HCP materials during SPD processing, several strategies can be used independently or collaboratively: (i) tailor the initial orientation of the specimen to maximize the probability of basal slip (prolong the stage II hardening) [363]; (ii) carry out deformation at elevated temperature to promote basal slip [364], to promote recovery and to reduce the effect of strain hardening [65,347,365,366]; (iii) tailor the grain size by pre-deformation at an elevated temperature (homogeneously fine grains with an average size of  $\sim 1 \mu\text{m}$ , can provide an enormous amount of GBs and reduce the chance for twinning, therefore to delay strain localization) [359,367–370]; (iv) apply a strong back pressure with a constraint or semi-constraint deformation setup (HPT and ECAP with a back plunger) [338,349,371,372]. Strong back pressure can help keeping the specimen intact during deformation [373,374]; (v) reduce stress concentration by reducing the strain rate, or in a particular case of ECAP by increasing the channel angle and reducing the ram speed [30,354,375,376].

### 3.5.2. Dislocation slip and deformation twinning in HCP materials

Grain refinement by dislocation activities may be dominant during SPD processing of HCP materials [377–380]. Fig. 31(a) shows lamellar sub-grains containing interconnecting boundaries and dislocation

clusters in a commercially pure Ti sample processed by ECAP to an equivalent strain of  $\sim 1.2$ . Fig. 31(b) shows UFG structures with curved and ill-defined (blurred) GBs. Similar sub-grain structures were commonly found in HCP materials processed by SPD. The sub-grain size may be much bigger when the materials were processed at elevated temperatures, but the curved and ill-defined GBs are always observed [338,381–383]. As the shear strain increases, the grain size decreases and the GBs become sharper as depicted in Fig. 31(c). Dynamic recrystallization may become evident at high strain levels resulting in increased amount of equiaxed grains with sharp GBs [375,383].

Deformation twinning is an essential grain refinement mechanism in HCP materials, because it is necessary for accommodating shear strain along the c-axis [59,330]. While both FCC and BCC materials have only one twinning mode, 18 twinning modes have been predicted including 6 modes verified experimentally in HCP materials. The activation of different twinning modes is material dependent. For instance, twinning on the  $\{10\bar{1}2\}$  plane is favored in Be, Mg, Zn and Cd, while twinning on  $\{10\bar{1}2\}$ ,  $\{11\bar{2}1\}$  and  $\{11\bar{2}2\}$  planes is favored in Ti and Zr. The activation of a particular twinning system also depends on the magnitude of the shear stress and the sense of shear (compression or tension) in relation to the applied stress. For example [384], when an HCP crystal is stressed along the c-axis,  $\{10\bar{1}2\}$  twinning operates under tension if the c/a ratio is less than  $\sqrt{3}$  (Mg, Be), whereas it operates under compression if the c/a ratio is greater than  $\sqrt{3}$  (Zn, Cd). This is because the shear direction reverses as the c/a ratio passes through the value of  $\sqrt{3}$ .

Different twinning modes are related to different twinning mechanisms and different states of core configuration, resulting in different strain accommodation [365,385]. Thus, the participation of deformation twinning in the SPD-induced grain refinement process of HCP materials is very complicated and has only been investigated to a limited extent. Therefore, the following part of this section will provide only a limited picture about the effect of deformation twinning on the SPD-induced grain refinement in HCP materials.

The propensity for deformation twinning is high in CG HCP materials at early deformation stages beyond a certain critical strain [330,386,387], unless the material is deliberately oriented to favor  $\langle a \rangle$  slip [343]. On the other hand, attributed to the microscale flow stress anisotropy and the low CRSS of basal slip, dislocation slip always compete vigorously with deformation twinning [65,353,388]. However, similar to FCC materials, grain refinement by deformation twinning is more effective than that by dislocation activities in HCP materials. For instance, at low to medium strain levels, deformation twins with thicknesses between 500 nm and 80 nm can form in ECAP processed HCP Ti samples [362,365]. According to literatures, the lamellar

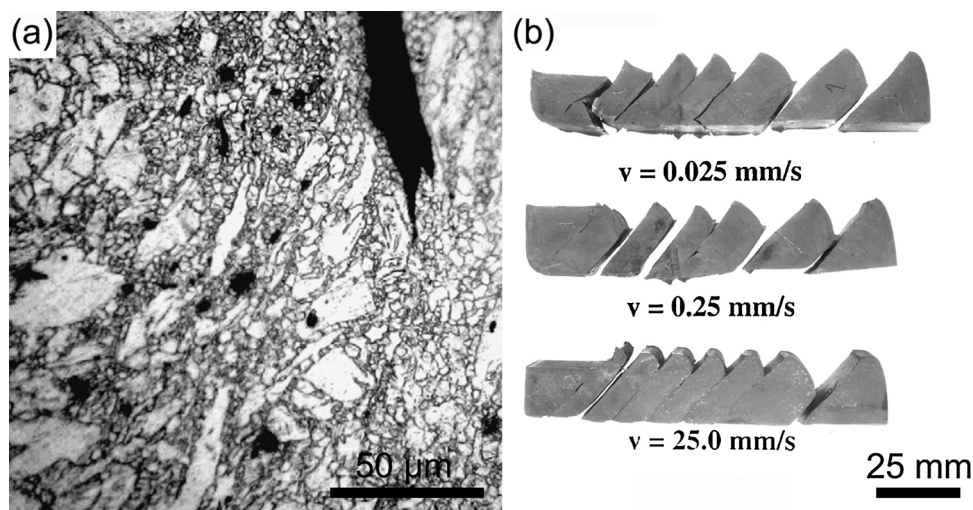


Fig. 30. (a) An optical image showing the microstructures around the crack in an AZ31 Mg alloy processed by ECAP at room temperature [361]; (b) commercially pure Ti samples processed by room temperature ECAP at different ram speeds [354].

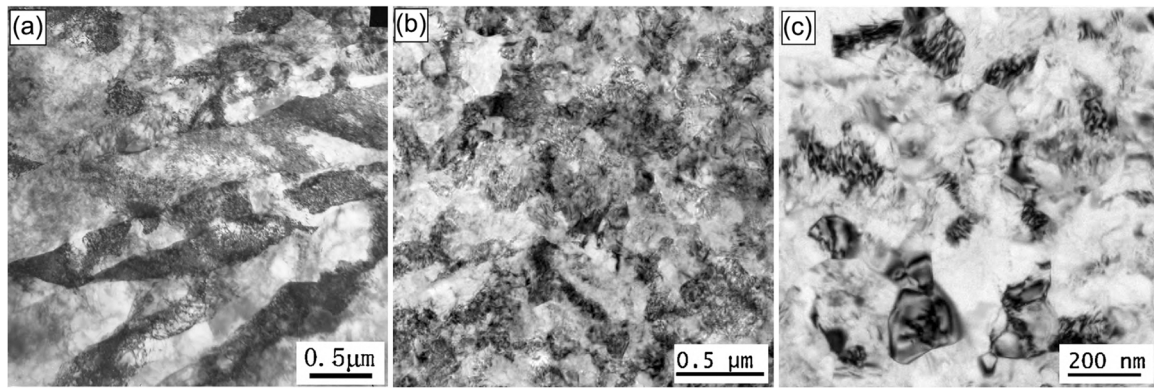


Fig. 31. TEM images of a Ti sample processed by ECAP (channel angle = 120°) through (a) 2 passes, (b) 6 passes and (c) 8 passes at room temperature [375].

sub-grains (widths > 400 nm) formed by dislocation rearrangement are significantly larger than the average thickness of deformation twins at the same strain level [362].

As mentioned earlier, many different types of deformation twins may form in HCP materials, depend on the temperature [65,389], strain rate [390], microscopic stress state [330,391] and  $c/a$  ratio [64,109]. Even for the same type of twins, several crystallographically equivalent variants may be active. For example, the  $\{10\bar{1}2\}\langle\bar{1}011\rangle$  twins in hcp structures possessing six crystallographically equivalent variants can theoretically form three pairs of crystallographically different twin–twin intersections [392–394]. Thus, twinning intersections often facilitate grain refinement to an appreciable extent as shown in Fig. 32(a).

In addition, twin length was found to be strongly dependent on the grain size, stress state, and the intrinsic properties of materials. Thus, for random cases, twins do not extend to the full extent of the perimeter of their parent grains as exemplified in Fig. 32(b–c) [390]. If the twinning dislocations are pinned by other dislocations at the interior of the parent grains, further straining may cause the twinned region transform into sub-grains with irregular shapes and wavy boundaries (e.g. area B in Fig. 32(b)) [390,395]. Otherwise, de-twinning may occur as a reversal of the twinning process when the local stress state is changed [311,396–398]. Although different types of deformation twins may participate in the grain refinement as the processing temperature and/or the stress state are changed, (e.g. the dominant twinning mode changes from  $\{10\bar{1}1\}\langle 10\bar{1}2\rangle$  at temperature above 600 K [365] to  $\{10\bar{1}2\}\langle\bar{1}011\rangle$  and  $\{11\bar{2}2\}\langle\bar{1}\bar{1}23\rangle$  at ambient temperature (Fig. 32), the general effect of deformation twinning facilitating grain refinement is the same.

Similar to FCC materials, grain size also has a strong effect on twinning in HCP materials [400–402]. Although different HCP materials may have different sensitivities to the grain size effect [387], the general trend is that the twinning propensity decreases with decreasing grain size [403]. As shown in Fig. 33, the fraction of twinned grains decreases dramatically as the grain size is reduced to the UFG regime. As the participation of deformation twinning decreases, dislocation slip shall play a bigger role in the grain refinement process. Especially, the dislocations with  $\langle c \rangle$  components that can accommodate the strain along to the  $c$ -axis of the HCP structure, and tend to significantly increase in density in SPD processed ultrafine grains and nano-grains [399].

Zhu et al. proposed a hypothesis for the observed grain size effect on the deformation twinning in HCP metals [43,404]. Deformation twinning in HCP metals requires much higher applied stress than  $\langle a \rangle$  dislocation slip. The HCP metals lack five independent slip systems to coordinate the plastic strain as required by the von Mises criterion [64,75,76], which leads to stress concentration at GBs where the dislocations piled up. For CG HCP metals, this stress concentration could be high enough to activate the twinning to relieve the stress

concentration. However, when the grain size becomes very small (e.g.

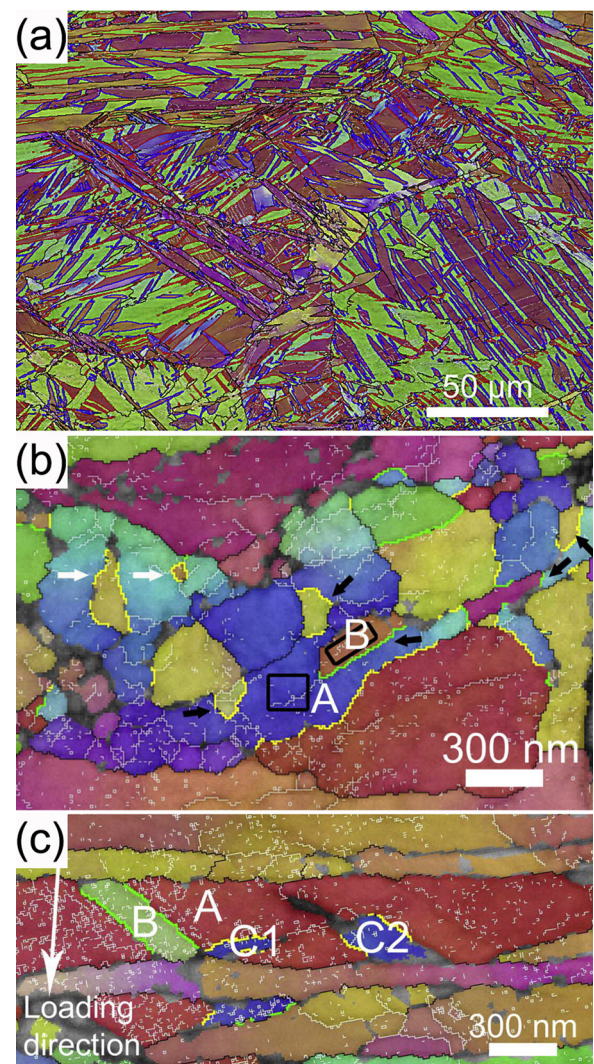


Fig. 32. EBSD images showing (a) pronounced twinning intersections in a plastically deformed Ti (the white, black, blue and red lines delineate low-angle GBs, high-angle GBs,  $\{10\bar{1}2\}\langle\bar{1}011\rangle$  and  $\{11\bar{2}2\}\langle\bar{1}\bar{1}23\rangle$  TBs, respectively.) [399]; (b) twin fragments (marked by black arrows) in ultrafine grains (the yellow and green lines delineate TBs of  $\{10\bar{1}2\}$  tension twins and  $\{11\bar{2}2\}$  compression twins, respectively); (c) a  $\{11\bar{2}2\}$  compression twin marked “B” and two  $\{10\bar{1}2\}$  tension twins marked “C1” and “C2” coexist in an ultrafine grain [390] (For interpretation of the references to colour in this figure legend, the reader is referred to the web version of this article.).

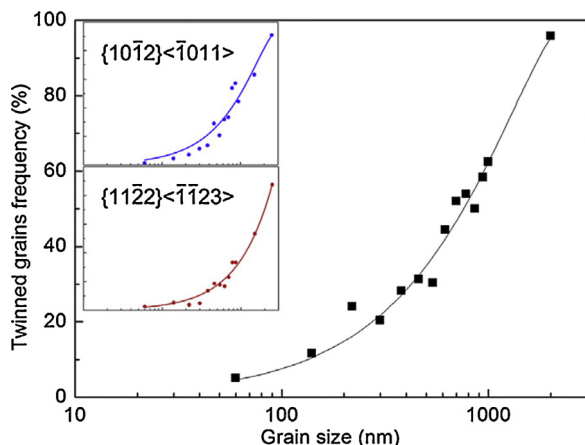


Fig. 33. Grain size effect on the fraction of overall twinned grains. The grain size dependency of  $\{10\bar{1}2\}\langle\bar{1}011\rangle$  and  $\{11\bar{2}2\}\langle\bar{1}\bar{1}23\rangle$  twins is presented separately in the insets [399].

below a few hundred nanometers), no effective dislocation pileup can be established in such small grains to overcome the required high critical stress for twinning, making twinning more difficult. Furthermore, when the grain sizes become very small, GB sliding may become active to help with relieving the stress concentration, making twinning even more difficult. The above hypothesis is supported by the report that some plastic strain by dislocation slip has to take place first before twinning occurs in CG Ti [308], which is needed to build up the stress concentration. Further research is needed to verify the validity of the hypothesis.

### 3.6. The minimum average grain size achievable by SPD

Despite of complicated deformation mechanisms operating in the SPD-induced grain refinement processes, the microstructure of each processed material will eventually reach a steady state at which further deformation does not change the overall microstructure, i.e., the average grain size remains unchanged with further straining. The minimum average grain size achievable depends on intrinsic material properties such as SFE [106,180,405] and external SPD conditions including processing temperature [142,170], the SPD technique [127,406], applied pressure [86,146,407], and strain rate [105,408].

Table 3

Melting temperature  $T_m$ , shear modulus  $G$ , Burgers vector  $b$ , atomic bond energy  $\Delta H$ , specific heat capacity  $Q_s$ , activation energy for self-diffusion  $Q_{SD}$ , stacking fault energy  $\gamma_{SFE}$ , of common model materials [106].

Metal	Structure	$T_m$ (K)	$G$ (GPa)	$b$ (nm)	$\Delta H$ (GJ/m <sup>3</sup> )	$Q_s$ (GJ/m <sup>3</sup> )	$Q_{SD}$ (kJ/mol)	$\gamma_{SFE}$ (mJ/m <sup>2</sup> )
Cr	BCC	2133	115	0.2498	54.8	8.61	339.1	380
Fe	BCC	1809	81.6	0.2482	58.7	8.85	239.5	180
Mo	BCC	2888	125.6	0.2725	70	9.17	464.7	
Nb	BCC	2740	37.5	0.2864	67.2	7.01	401.9	150
Ta	BCC	3253	69	0.2856	71.7	8.22	413.2	210
V	BCC	2175	46.7	0.2618	61.6	7.66	308.4	150
Ag	FCC	1234	27	0.2889	27.7	2.59	181.7	16, 23
Al	FCC	933	26.2	0.2864	33.7	1.79	126.4	166, 200,
Au	FCC	1336	27.7	0.2884	33	3.11	176.6	32, 50
Cu	FCC	1357	48.3	0.2556	47.7	4.02	203.6	45, 55, 78
Ni	FCC	1728	75	0.2492	65.1	7.26	285.1	125, 250
Pb	FCC	600	5.6	0.35	10.7	0.48	109.1	24.5
Pd	FCC	1825	43.6	0.2751	42.7	5.36	266.3	130, 180, 240
Hf	HCP	2500	56	0.3127	45.4	5.26	174.2	
Mg	HCP	922	17.3	0.3197	10.6	1.15	138.2	125
Ti	HCP	1940	45.6	0.2896	44.2	5.23	169.1	350
Zn	HCP	693	41.9	0.2665	14.3	1.09	91.7	140
Zr	HCP	2125	35	0.3179	43.3	3.94	113	220, 240

Early understanding about the SPD-induced equilibrium average grain size suggested that the steady state of SPD is the result of a balance between deformation induced grain refinement and dynamic recovery (annihilation of dislocations and destruction of GBs) [298,409–412]. Mohamed proposed a dislocation model for the minimum average grain size attainable by SPD as:

$$d_{min}/b = A_3 (e^{-(\alpha Q_{SD} - \alpha^* Q_{SD})/4RT}) (D_{PO} G b^2 / v_0 k T)^{0.25} (\gamma_{SFE} / G b)^{0.5} (G / \sigma)^{1.25} \quad (1)$$

where  $b$  is the Burgers vector,  $A_3$  is a constant (the subscript shows the trace of the formulation procedures),  $Q_{SD}$  is the self-diffusion activation energy,  $\alpha$  is the ratio between pipe diffusion activation energy and  $Q_{SD}$ ,  $\alpha^*$  is the ratio between vacancy migration activation energy and  $Q_{SD}$ ,  $R$  is the gas constant,  $T$  is the absolute temperature,  $D_{PO}$  is the frequency factor for pipe diffusion,  $G$  is the shear modulus,  $v_0$  is the ratio between lattice diffusion frequency factor and effective radius of the impurity atmosphere,  $k$  is Boltzmann's constant,  $\gamma_{SFE}$  is the SFE,  $\sigma$  is the stress generated as a result of SPD. Mohamed's dislocation model [298,412] can be a good guide for exploring the relationship between materials intrinsic properties and the minimum average grain size, and the effect of external SPD conditions on the minimum average grain size. However, Mohamed's dislocation model is not yet perfect. There are more physical parameters that are found useful by other researchers [106], which will also be discussed in the following paragraphs. A list of some relevant properties of common materials for SPD research is given in Table 3 for readers' convenience.

#### 3.6.1. Effects of atomic bond energy, specific heat capacity and self-diffusion activation energy

Mohamed's dislocation model has an energy parameter  $Q_{SD}$ , which, is defined as the energy required for the self-diffusion of one mole of atoms. It can be understood that if  $Q_{SD}$  is high, dynamic recovery would be delayed due to insufficient energy storage at medium to low strain levels [106,170,298]. Available literature reports have proven that  $d_{min}$  decreases with increasing  $Q_{SD}$  [106,152,170,298,413]. Fig. 34(a) illustrates the relationship between  $d_{min}$  and  $Q_{SD}$ . (Note: in Fig. 34,  $d_s$  is used instead of  $d_{min}$  because of different preferences of the authors, but throughout our review paper  $d_s$  and  $d_{min}$  are equivalent.) Since the stored energy in the materials increases with grain refinement [80,414,415], and the specific heat capacity  $Q_s$  represents the maximum energy that can be stored in a unit volume of solid materials, it is reasonable to assess the correlation between  $d_{min}$  and  $Q_s$ . As shown in

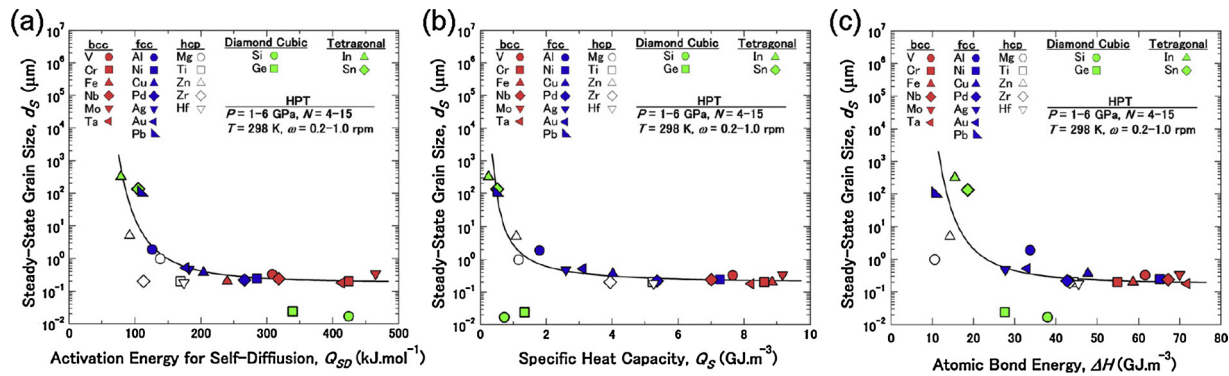


Fig. 34. A plot of steady state grain size against (a)  $Q_{SD}$ , (b)  $Q_S$  and (c)  $\Delta H$  [106].

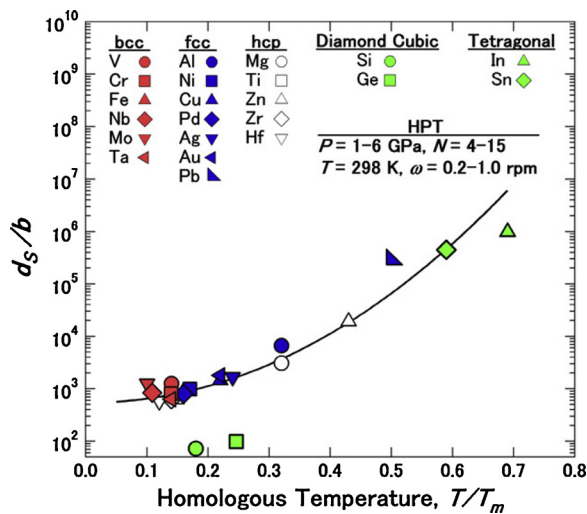


Fig. 35. A plot of steady state grain size against homologous temperature [106].

Fig. 34(b),  $d_{min}$  is also a function of  $Q_S$  that  $d_{min}$  decreases with increasing  $Q_S$ , because a material with a high  $Q_S$  is capable of storing more energy carriers (GBs and dislocations) than a material with a low  $Q_S$ . Because both  $Q_{SD}$  and  $Q_S$  are atomic bond parameters, and both parameters have effect on  $d_{min}$ , it is also necessary to consider the atomic bond energy  $\Delta H$  which is the enthalpy required to break all atomic bonds in one cubic meter of pure metal. When  $\Delta H$  is high, a high energy is required to break atomic bonds and to move atoms, therefore atomic diffusion is significantly suppressed and dynamic recovery is difficult unless there is sufficient thermal energy input (high temperature). In contrast, for the metals with low  $\Delta H$ , a significant recovery may occur after SPD at room temperature [165,381], and thus their grain sizes are more sensitive to  $Q_{SD}$  and  $Q_S$  compared with metals with high  $\Delta H$ .

### 3.6.2. The effect of temperature

Temperature affects the atomic diffusion and the microstructural evolution in multiple ways [55,105,106,127,416], and consequently affects the  $d_{min}$  in SPD. It is convenient to correlate  $d_{min}$  with homologous temperature (the temperature of a material as a fraction of its melting point temperature using the Kelvin scale) so that both processing temperature and melting temperature are considered when examining the temperature effects. According to Fig. 35, the normalized minimum grain size  $d_s/b$  (or  $d_{min}/b$ ) increases with increasing homologous temperature under comparable processing conditions [106]. This can be understood by examining the temperature effect on the two competing processes – grain refinement and grain growth. There are

numerous literatures showing that grain refinement can be enhanced by lowering the temperature [142,206,417]. For high SFE materials in which full dislocation activities governs the grain refinement, by lowering the homologous temperature the dislocation density can be increased to enhance grain refinement [142,418,419]. For materials with low SFEs in which deformation twinning plays a major role, by lowering the homologous temperature the TB-spacing can be narrowed to enhance grain refinement [105,206]. For medium SFE materials which is prone to a deformation mechanisms transition caused by processing condition variation (including changing processing temperature), the grain size can be significantly decreased if the dominant mechanism is changed from dislocation slip to deformation twinning. In other words,  $d_{min}$  of medium SFE materials is more sensitive to the variation of homologous temperature than that of other materials [105,165,417].

On the other hand, the grain coarsening/growth mechanisms such as dynamic recovery [164,413,420,421], dynamic recrystallization [408,422–424] and GB migration [425,426] are thermally activated, that can be suppressed/delayed by lowering homologous temperature. It should be aware that low temperature SPD can significantly increase the stored energy in materials. The high stored energy in the form of lattice defects decreases the activation energy and increases the rate for recrystallization [427]. Thus, fast grain growth due to recrystallization at room temperature has been found in some materials, such as high purity Al, Ag and Au, processed by cryogenic-HPT [165,427].

### 3.6.3. The effect of stacking fault energy

The effect of SFE on grain refinement has been widely investigated. It is generally agreed that materials with lower SFE can achieve smaller grain size. By decreasing the SFE, deformation twinning can be activated and TB-spacing can be reduced. Thus, grain refinement is enhanced [95,96,103,180,428]. Meanwhile, by decreasing SFE, dynamic recovery due to dislocation cross-slips can be suppressed [95,152–154]. Mohamed and Dheda plotted the normalized minimum grain size ( $d_{min}/b$ ) against the normalized SFE ( $\gamma/Gb$ ) based on the data from HPT experiments conducted by other researchers [406]. Although the increasing trend of  $d_{min}/b$  with respect to increased  $\gamma/Gb$  can be noticed, the scattering of data point is too broad. The wide scattering of data points in Fig. 36(a) is attributed to inconsistent SFE evaluation methods [405], to the significant variation of homologous temperatures and possibly to other factors [106]. Therefore, Lu et al. [405] purposely chose two limited sets of experimental data to again fit the model as shown in Fig. 36(b–c). The fitting results show much better improvements compared to Fig. 36(a).

While the majority of researchers have agreed that the steady state (minimum average) grain size processed by SPD is positively related to the SFE, Edalati and Horita argued that  $d_{min}/b$  for pure metal was almost independent of  $\gamma/Gb$  as far as the data were evaluated at a given  $T/T_m$  [106] and that  $d_{min}/b$  for single phase alloys is affected by elastic interaction, modulus interaction and SFE [429]. In fact, the dependency of the minimum average grain size on the SFE can be validated by carefully

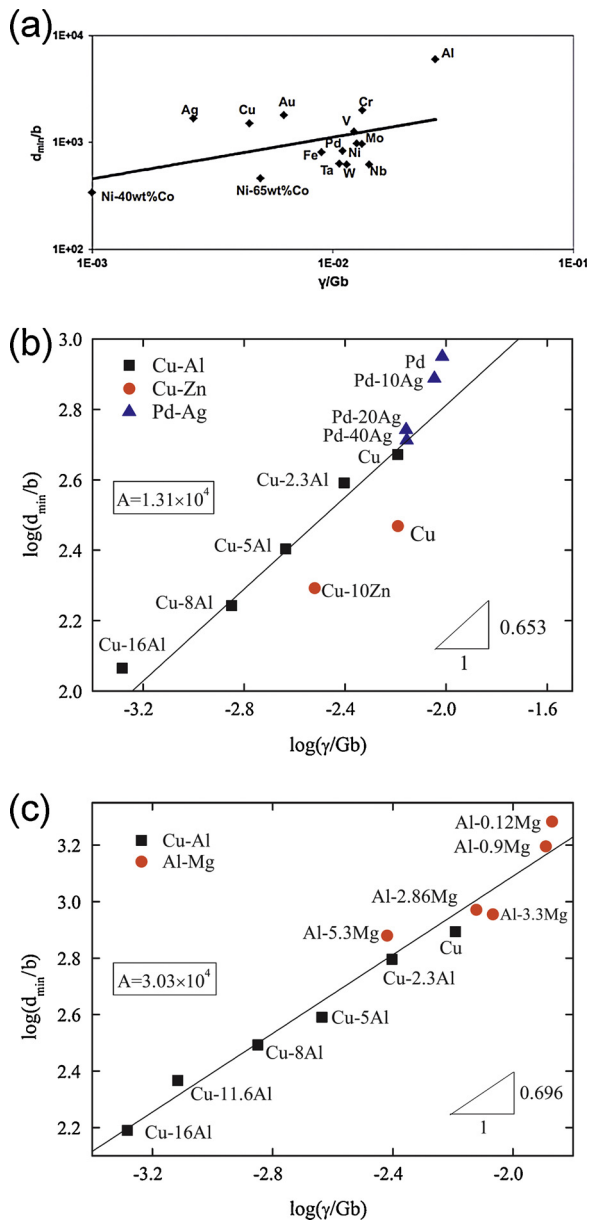


**Fig. 36.** (a) A plot of normalized minimum grain size ( $d_{\min}/b$ ) against the normalized SFE ( $\gamma/Gb$ ) based on the data from HPT experiments [406]. A logarithmic scale plot of  $d_{\min}/b$  against  $\gamma/Gb$  based on the data from (b) HPT experiments and (c) ECAP experiments, respectively [405].

reviewing relevant literatures, but the homologous temperature does have a very significant effect [89,103,105,106,176,180,184,298,430]. For the case of alloys, the problem is more complicated. The elastic interaction is attributed to atomic size mismatch between solutes and the matrix. The modulus interaction is attributed to shear modulus mismatch between solutes and the matrix. It is well-known that solute atoms exert a strong drag effect on dislocations [55,431]. Therefore, increasing solute content in single phase alloys will significantly suppress grain growth by suppressing dynamic recovery and GB migration [432,433]. Hence, it has been proposed that the significant effect of atomic size mismatch and modulus interaction on dislocation mobility and grain size should be incorporated into the model for predicting the steady state grain size attained by SPD [429].

### 3.6.4. The effect of experimental conditions

It is a convenient practice to employ the Zener–Hollomon parameter,  $Z$ , for assessing the synergetic effect of processing temperature

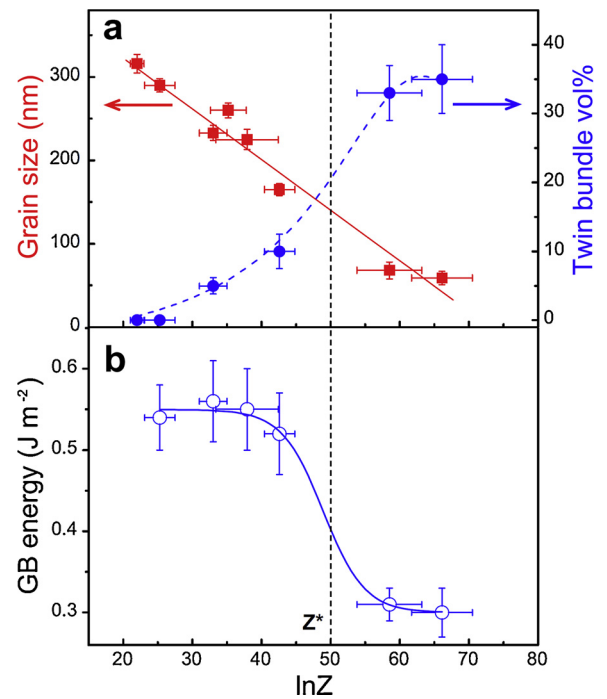


**Fig. 37.** (a) Plots of the average grain size and volume fraction of nanoscale T/M lamellae bundles against  $\ln Z$  for pure Cu; (b) a plot of the average GB energy against  $\ln Z$ . A vertical dotted line indicates the critical  $Z^*$  at which a transition from dislocation activity to deformation twinning occurs [176].

and strain rate on microstructural evolution, including the minimum average grain size [127,430]. This parameter incorporates both strain rate ( $\dot{\epsilon}$ ) and temperature ( $T$ ) as:

$$\ln Z = \ln \dot{\epsilon} + \frac{Q}{RT} \quad (2)$$

where  $Q$  is the activation energy for diffusion and  $R$  is the gas constant (8.317 kJ/mole K) [170,416]. According to Fig. 37(a), as  $Z$  increases, the grain size decreases and the tendency for twinning increases. A large fraction of deformation twins reduces the overall GB energy as shown in Fig. 37(b). There is a critical  $Z$ , referred to as  $Z^*$ , at which a transition in the dominant grain refinement mechanism from dislocation activities to deformation twinning occurs. Although, Fig. 37 is based on a particular case of Cu, recent experimental evidence implied that there may also be critical  $Z^*$ s for materials with very high SFEs and low  $T_m$  such as Al [88].

Lu et al. [405] reduced Mohamed's dislocation model into the form  $\frac{d_{\min}}{b} = A \left( \frac{\gamma}{Gb} \right)^q$ , the two fitting parameters  $A$  and  $q$  are affected by deformation conditions and possibly some other less-explored factors such as solute atoms. Lu et al. fitted the equation with some experimental data as shown in Fig. 36(b–c). Fig. 36(a) is based on data from HPT experiments, the linear fitting parameters were found to be  $A \approx 1.31 \times 10^4$  and  $q \approx 0.653$ . Fig. 36(c) is based on data from ECAP experiments, the linear fitting parameters were found to be  $A \approx 3.03 \times 10^4$  and  $q \approx 0.696$ . The major difference between HPT and ECAP is the applied pressure. Therefore, the significant variations in the fitting parameters indicate the significant effect of pressure on the steady state grain size. High pressure can enhance the accumulation of dislocations [146,434] and/or promote deformation twinning [86,210]. Meanwhile, high pressure reduces self-diffusivity by the vacancy mechanism and hence decreases the dynamic recovery rate by diffusion controlled mechanisms [156,251,407]. As a result, high pressure leads to small steady state grain size.

#### 4. SPD-induced grain growth

In recent years, deformation induced grain growth has attracted significant attention. SPD processing can lead to two opposite phenomena – SPD-induced grain refinement and grain growth. The final average grain size of materials processed by SPD is achieved through the dynamic balance between the grain refinement process and the grain growth process. For CG materials, SPD processing leads to grain refinement. Conversely, grain growth has been readily observed in nc materials that were subjected to various types of plastic deformation processes, including nanoindentation [435,436], cold rolling [437,438], uniaxial tension [439], uniaxial compression [440,441], and HPT [199,428,442,443]. In these cases, the starting grain sizes were much smaller than the final steady state grain size under the specific deformation conditions. For example, Liao et al. [442] conducted HPT on electrodeposited nc Ni with an initial grain size of ~30 nm. Grain growth occurred, reaching an average grain size of ~129 nm after HPT processing. This value is within the reported grain size ranges achieved in HPT-processed CG Ni (~105 nm [444], ~120 nm [445], and ~170 nm [146,155,446]). This suggests that there exists an upper size limit for deformation induced grain growth, and this upper limit is close to the lower grain size limit for HPT-induced grain refinement of CG Ni. The final grain size of materials processed by SPD is determined by processing parameters and material properties (more details can be seen in Section 3.6).

##### 4.1. Grain growth mechanisms

As presented in Section 3, when SPD is applied on CG materials, grains in the materials are refined mainly by dislocation slip or combined dislocation slip and deformation twinning. When SPD is applied on nc materials with a significant volume fraction of GBs, GB mediated processes including GB sliding, grain rotation, GB migration, GB diffusion and partial dislocation emission from GBs play a major role in accommodating the strain, resulting in grain growth via different mechanisms. A number of investigations have been carried out to understand the grain growth mechanisms. Results of molecular dynamic (MD) simulations [447–451], theoretical calculations [200,452], in-situ TEM investigations [201,217], and post-mortem TEM investigations [22,197,435,442,444,453] revealed two plastic deformation induced grain growth mechanisms – GB migration and grain rotation.

##### 4.1.1. GB migration

For grains larger than 100 nm, deformation-induced grain growth occurs via GB migration. By conducting in situ nanoindentation and in-situ tensile testing in TEM on UFG Al thin films, Jin et al. [436] and Legros et al. [454] observed GB migration from larger grains towards smaller grains, i.e., a grain grows at the expense of neighbouring smaller grains. Fig. 38 shows evidence of deformation-induced grain growth via GB migration in an UFG Al film during nanoindentation [436]. Fig. 38(a) presents a bright-field TEM image containing three grains numbered as 1, 2 and 3 before indentation. Fig. 38(b–d) show dark-field images of the three grains before indentation. Fig. 38(e and f–h) present bright-field and dark-field images, respectively, of these grains after indentation. It's clearly observable that the small grain 1, which existed before the indentation, was absorbed by the growth of its neighboring grains 2 and 3 during indentation [436]. Fig. 39(a–e) show a series of pictures extracted from a video recording a grain growth process during tensile testing on an Al thin film. Fig. 39(f) shows the sketch of the successive positions of a GB. The clearly observable shape change in grain A confirms the effectiveness of GB migration as a grain growth mechanism [454].

##### 4.1.2. Grain rotation

For grains much smaller than 100 nm, grain growth occurs via grain rotation and GB sliding. Both post-mortem TEM investigations on SPD-processed bulk nc materials [197,428,437,438] and in-situ deformation TEM studies on thin film nc materials [201,217] revealed the grain rotation mechanism. There was some concern that grain growth observed by in-situ TEM was caused by the thin film effect in which materials were constrained only in two dimensions. To exclude the thin film effect, Wang et al [197] applied HPT to severely deform electrodeposited bulk nc Ni-20 wt.% Fe disks. Significant grain growth occurred after 1-revolution HPT with the average grain size of the material evolving from ~22 nm to ~95 nm. As shown in Fig. 40, many sub-grains with low-angle sub-grain boundaries (as indicated by dotted lines) forming large grains were observed in HPT-processed specimens. Note that the sizes of the sub-grains were consistent with the grain sizes in the as-received sample, indicating that the large grains were formed through the rotation of the initial small grains. Furthermore, the GB of the large grain with dark contrast in Fig. 40 is of irregular shape which matches well with the boundaries of the initial small grains, indicating that no observable GB migration occurred at this stage of the grain rotation. Fig. 41(a) shows another example of a large grain with a grain

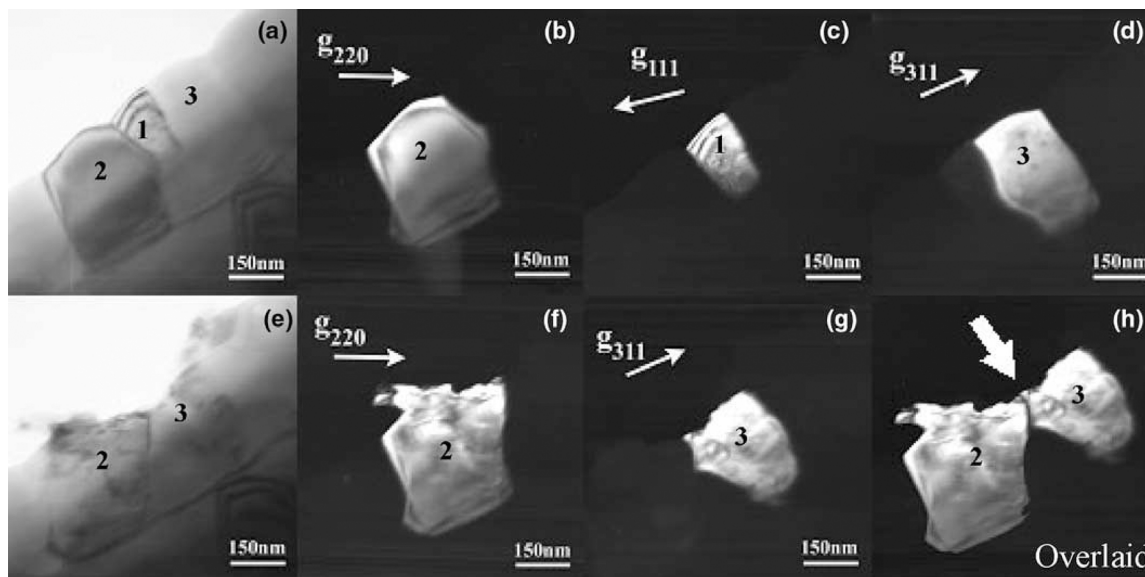


Fig. 38. Bright-field and dark-field TEM images before and after indentation, indicating indentation-induced GB migration [436].

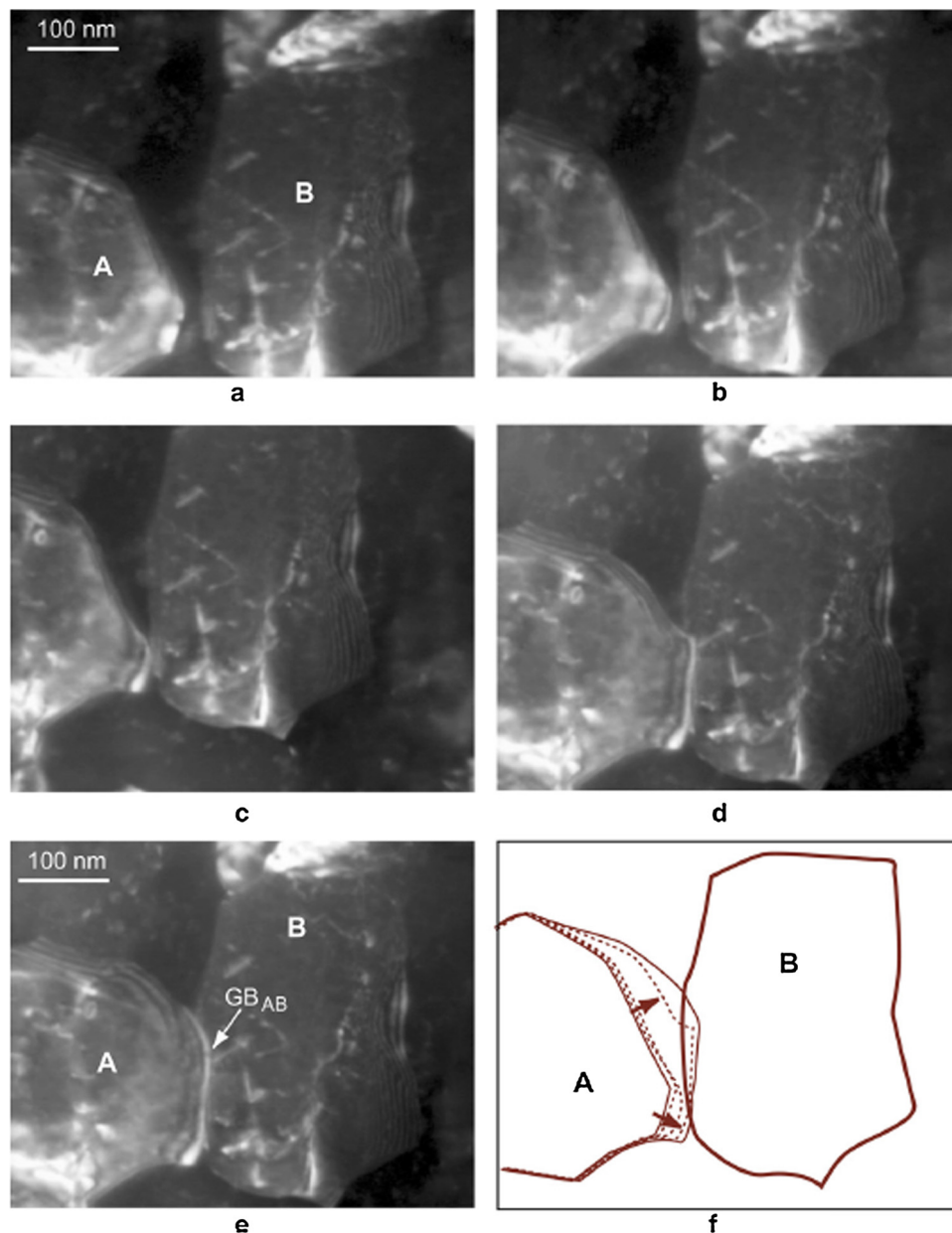


Fig. 39. Video sequence taken in dark field recording straining-induced grain growth. (a)  $t = 0$  s, (b)  $t = 1.2$  s, (c)  $t = 18.16$  s, (d)  $t = 29.01$  s, (e)  $t = 29.24$  s, and (f) a sketch of successive GB positions [454].

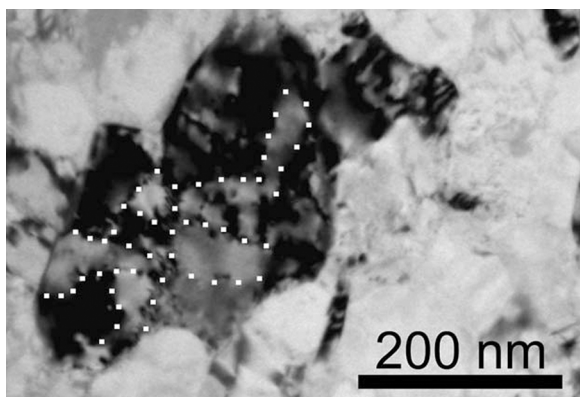


Fig. 40. A TEM image of an HPT-processed Ni-Fe nc material. The white dotted lines indicate sub-grain boundaries [197].

size of  $\sim 80$  nm formed by several sub-grains with small angle sub-grain boundaries, as highlighted by dash lines. Fig. 41(b) shows an HRTEM image of the area marked with a white rectangle in Fig. 41(a). A mis-orientation of  $\sim 6^\circ$  between the two sides of the sub-grain boundary is seen clearly. Note that the GB of the large grain is much straighter than that of the large grain in Fig. 40, part of which was marked by two black arrowheads. The smooth and straight GB indicates that both grain rotation and GB migration occurred during the grain growth process.

#### 4.1.3. Cooperation of two mechanisms for nc materials

For grains larger than 100 nm, grain rotation cannot be easily activated because the critical stress to activate the rotational deformation increases with increasing grain size [200]. Therefore, only for nc materials with grain size much smaller than 100 nm GB rotation plays a major role on deformation-induced grain growth. Notably, there exists a cooperative action of grain rotation and GB migration in deformed nc materials. MD simulations in a polycrystalline Pd with an average grain size of 15 nm revealed a close coupling between the grain rotation and

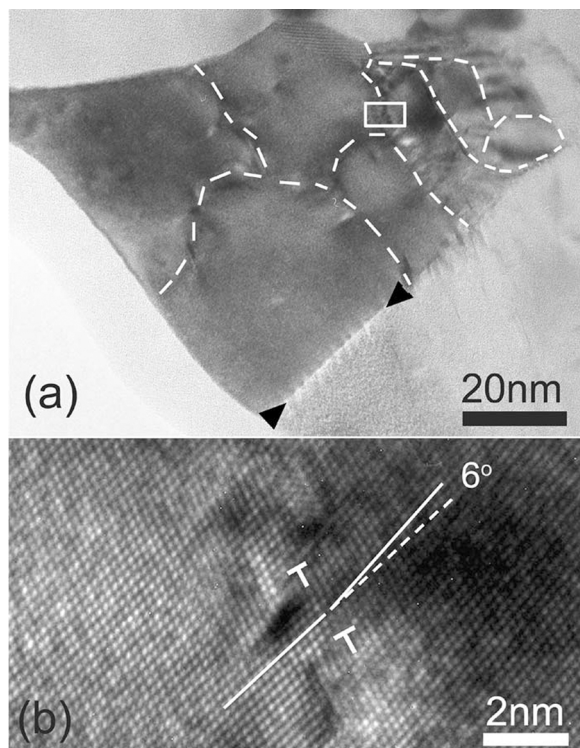


Fig. 41. (a) A TEM image of a grain consisting of several sub-grains. The sub-grain boundaries were highlighted by dash lines; (b) an HRTEM image of the area marked with a white rectangle in (a), showing a misorientation of  $\sim 6^\circ$  between the two sides of the sub-grain boundary [197].

GB migration, that is, grain rotation induced grain coalescence will always induce GB migration, and GB migration may, in turn, trigger grain rotation when the grain size is small enough [447]. Later atomistic simulations on a deformed nc aluminum indicated that the grain growth resulted from rotation of nano-grains and rotation triggered migration of GBs [449].

The coupling effect was analyzed using an atomic model based on the atomic-level shear stress acting on the interfaces during indentation [449]. Fig. 42(a) shows the contact area before indentation. Fig. 42(b–h) show the evolution of the structure of a few neighboring grains in the dashed area in Fig. 42(a). In these figures, the contact force applied by the indenter to the film was provided at the lower left corner of the images. It can be seen that, at the early state of indentation, significant rotation of grain 1 takes place due to GB sliding between grains 1 and 5, as shown in Fig. 42(c). After grain 1 rotation, the misorientation angle between grains 1 and 2 transformed from  $\sim 22^\circ$  to  $\sim 13.5^\circ$ . As the contact force increases, the boundary separating grains 1 and 2, which consists of GB dislocations, begins to migrate towards grain 4 until it is absorbed by the boundary of grain 4. The collective migration of dislocations is accompanied by local lattice rotation. In this process, grain 2 and grain 1 eventually coalesce to form one grain. The cooperative action of grain rotation and GB migration may explain the formation of the straight GBs in Fig. 41(a) [447,455].

#### 4.2. Twin density evolution during grain growth process

SPD-induced grain growth processes are accompanied with other structural evolutions, including the evolutions of twin density and dislocation density. The latter will be discussed in Session 5. Both twinning and de-twinning have been reported to occur during the deformation of nc materials. Deformation induced twinning was observed in nc Al during cryogenic ball milling [193] and ns Cu during HPT [92]. Deformation induced detwinning was observed in nc Ni-Fe alloys

during HPT [100,456], cold rolling [437] and uniaxial compression [441,457]. Ni et al [100] carried out a systematic investigation on the evolution of twin density during the HPT-induced grain growth process in a nc Ni-Fe alloy. The results indicate that de-twinning occurred at the beginning of deformation, and as the grain size increased to a certain value, deformation twinning occurred. Fig. 43(a–c) show typical bright-field TEM images of the as-deposited Ni-Fe alloy, the edge part of the 10-revolution HPT disk and the edge part of the 20-revolution HPT disk, respectively. Twins were indicated by white arrows. It can be seen that a high density of growth twins existed in the as-deposited material with an initial average grain size of  $\sim 21$  nm. This is consistent with previous results of similar materials prepared by the same method [7,215,437,438,441,458]. During HPT, continuous grain growth occurred and the twin density experienced a decreasing, then increasing and decreasing again as the number of HPT revolution increases, which indicates an optimum grain size for twinning. Few twins were seen in the 10-revolution HPT specimen, as evidenced in Fig. 43(b), while a high density of twins was seen in the 20-revolution HPT disk in Fig. 43(c).

It is clear that with increasing grain size the number of grains containing twins first decreased and then increased, which indicates that deformation induced de-twinning and twinning occurred consecutively during the grain growth process. Fig. 44 shows the statistical grain size distributions and twin distributions before and after different HPT revolutions, summarized from comprehensive TEM observations. As shown in Fig. 44(a–c), the average grain size increased and the number of grains containing twins decreased from the initial state to 5- and 10-revolution HPT. As the number of revolutions increased to 15 and 20 revolutions, as shown in Fig. 44(d–e), a significant increase in twin density accompanied with grain growth appeared. Further deforming the sample to 30 HPT revolutions increased the average grain size to 115 nm (Fig. 44(f)). However, the deformation twins exist only in smaller grains and the fraction of the twinned grains is reduced, revealing a significant de-twinning occurred during deformation from 20 to 30 HPT revolutions.

The statistic data indicate that there is an optimum grain size for twinning which is not significantly affected by the overall grain size distribution. This is consistent with the inverse grain size effect on the formation of deformation twins reported earlier [99,459]. It should be noted that this optimum grain size range for twinning is affected by intrinsic materials properties such as SF energy as well as by externally applied deformation conditions, such as stress and strain rate [99]. Outside of this grain size range, the de-twinning process dominates to annihilate existing twins. The tendency for twinning and detwinning during plastic deformation as a function of grain size is schematically illustrated in Fig. 45 [100].

## 5. SPD-induced dislocation density evolution

### 5.1. The dislocation density evolution in SPD-induced grain refinement process

It has been well investigated that deformation induced grain refinement is mainly caused by dislocation activities for materials with medium to high SFEs under low strain rates [92,145,444,460], thereby a deformation-induced grain refinement process is usually accompanied by an evolution in the dislocation density. As discussed earlier, at the early stages of an SPD process, various sub-structures including dislocation cells and cell blocks form via dislocation generation and accumulation [148,181,461,462]. With increasing strain, the misorientation between neighboring cells and cell blocks increases and the size of cell blocks becomes smaller owing to further division. Eventually, cell block boundaries become high-angle GBs, and smaller grains form inside the initially coarse grains [124,145,181,461].

The evolution of the dislocation density during ECAP process was systematically investigated using XRD peak broadening analysis, TEM

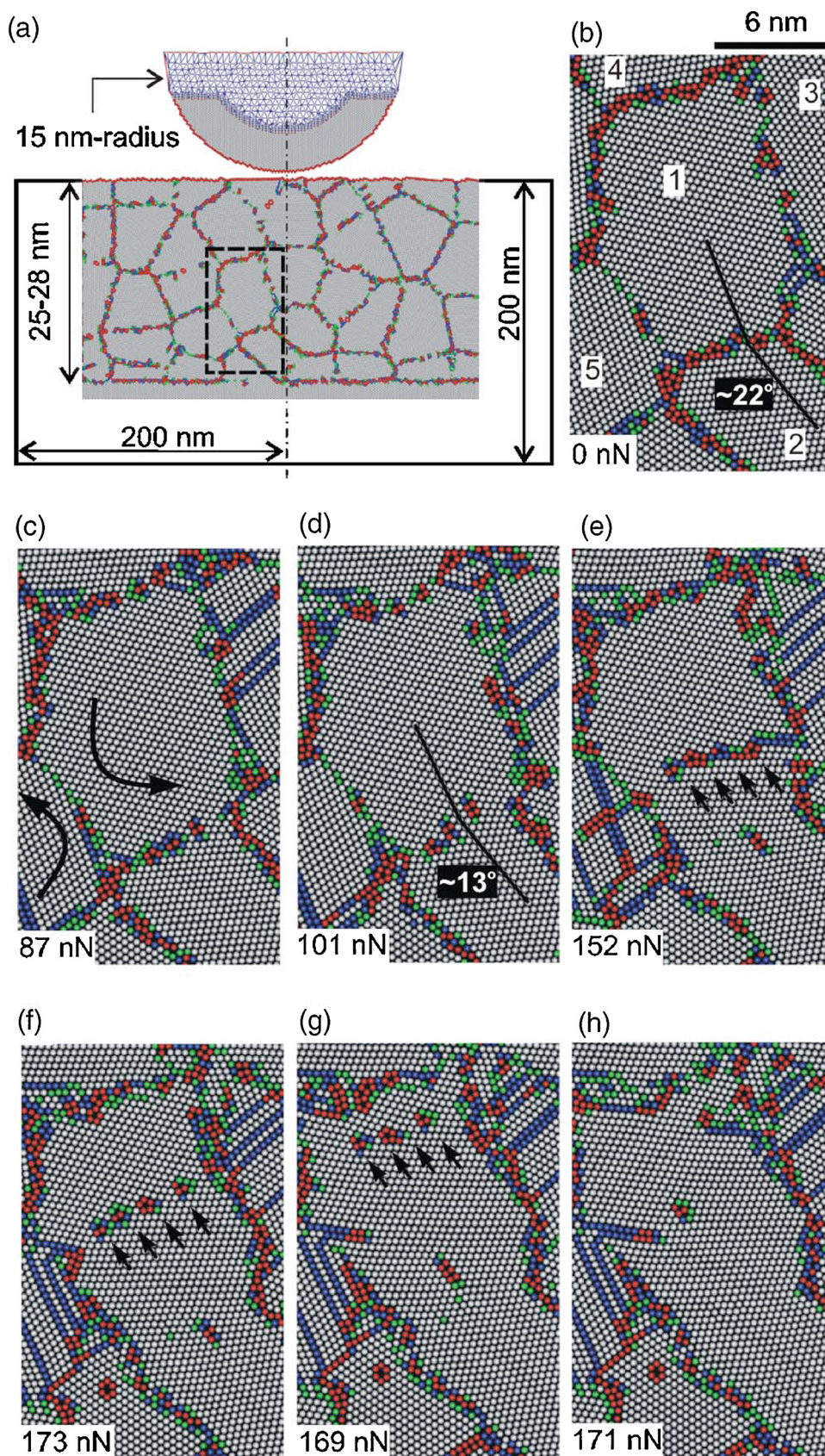


**Fig. 42.** Deformation of a cluster of grains with an average grain size of 7 nm in an Al film. (a) The contact zone before indentation; (b)-(d) Rotation of grain 1; (e)-(h) Motion of the boundary between grains 1 and 2 [449].

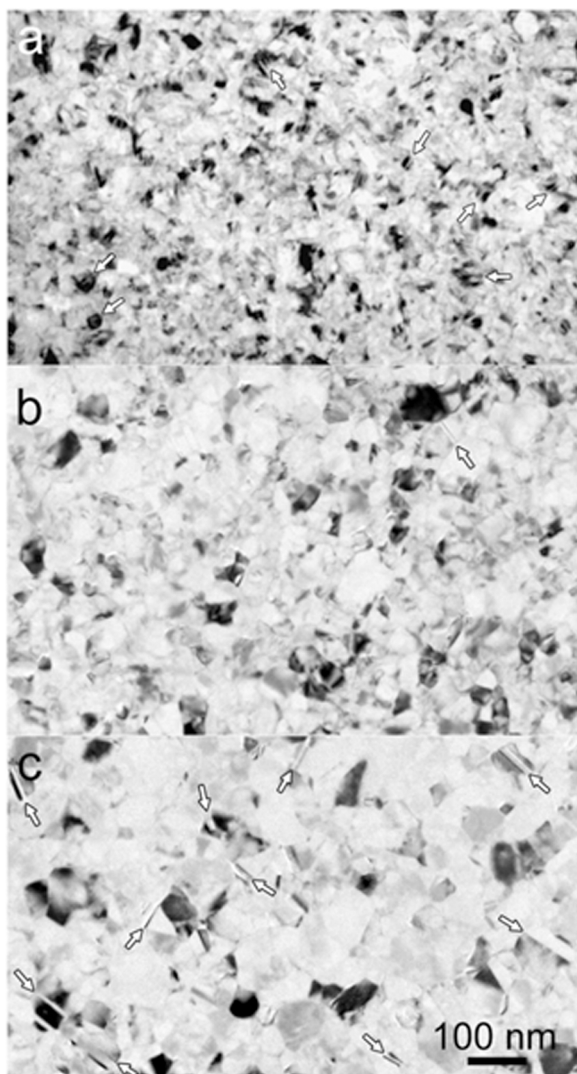


Fig. 43. Bright-field TEM images of (a) the as-deposited material, (b) the edge part of the 10-revolution HPT disk, and (c) the edge part of the 20-revolution HPT disk. Grains containing twins are indicated with white arrows [100].

analysis, the Kocks model and the Estrin model [181]. The dislocation density can be obtained from bright-field TEM images by measuring the length of the visible dislocations and dividing by the observed area multiplied by the specimen thickness [181]. The Kocks model [463] and the Estrin model [464] were based on the Taylor equation (see Eq. (3)) to evaluate the evolution of the dislocation density.

$$\hat{\sigma} = M\alpha_T Gb\sqrt{\rho} \quad (3)$$

In the Taylor equation,  $M$  is the Taylor factor accounting for a polycrystal,  $\alpha_T$  is a numerical factor,  $G$  is the shear modulus and  $b$  is the Burgers vector.  $\hat{\sigma}$  defines the flow stress at a given dislocation density. Assuming a Taylor factor of 3.06, which is valid for a randomly orientated polycrystalline material, a rough estimate of the total dislocation density can be made by replacing  $\hat{\sigma}$  with the measured yield strength  $\sigma_y$  or ultimate tensile strength (UTS). Note that the Taylor equation does not describe the microstructural evolution associated with the stresses between the yield and the ultimate tensile stress, thereby the  $\hat{\sigma}$  in the equation can be replaced by either  $\sigma_y$  or UTS.

Evaluation of the dislocation densities estimated from TEM and the two models shows that, although values of the dislocation density deduced from different ways vary, the trend of dislocation density evolution was the same: (1) the dislocation density in the copper increased

significantly at the initial stages of the ECAP process, suggesting that dislocations played a major role in grain refinement at this stage; and (2) the dislocation density reached a peak at 4-pass ECAP and then decreased. The decrease in dislocation density with further ECAP passes can be explained based on the facts that dynamic recovery occurred extensively when the dislocation density becomes high. The dislocation generation rate and annihilation rate are supposed to reach a balance at large strain values, resulting in a steady state dislocation density.

## 5.2. The dislocation density evolution in SPD-induced grain growth process

### 5.2.1. The dislocation density evolution during grain growth process

A deformation-induced grain growth process is also accompanied by an evolution in dislocation density [199,236,437,438]. Previous investigations reported a complicated dislocation density evolution during HPT-induced grain growth in nc Ni-Fe alloys. Specifically, the average dislocation density increased at the early stages of HPT processing, which is attributed to a large number of dislocations emitted from GBs to accommodate the strain [202,236]. However, the high density of dislocations in nc grains was very unstable and further deformation reduced the dislocation density [202,236]. As deformation-induced grain growth continued, a high density of Lomer-Cottrell (L-C) locks formed via interaction of dislocations gliding on different  $\{111\}$  planes (the formation of L-C locks will be reviewed in detail in session 4.2.2), leading to a subsequent increase in the dislocation density [202,236].

Fig. 46(a–b) show a typical HRTEM image of a grain at early stages of deformation and the corresponding Fourier-filtered images obtained from the area marked by white square in Fig. 46(a). Fig. 46(c–d) show a TEM image of a grain obtained at higher strain values, in which a high density of dislocations lying on different  $\{111\}$  planes were observed. Some of these dislocations met and interacted, forming L-C locks. The formation of L-C locks occurs in nc materials when two dislocations on different glide planes approach each other [221,236,465,466]. With increasing stress, the L-C locks can be dissociated when the external force is large enough to pull apart the two dislocations that form the locks. The dislocations glide and annihilate at GBs, leading to subsequent decrease in dislocation density. Further deformation did not result in significant variation on dislocation density, indicating that a balance is achieved between dislocation generation and annihilation.

Wu et al [465] reported the formation of L-C locks and the resultant increase in dislocation density in cryo-rolled nc Ni. Fig. 47 shows the dislocation density values at different rolling strains, measured from HRTEM images of individual grain and XRD analysis of a large sample, as marked by blue open circles and red solid squares, respectively. Numbers beside the blue open circles indicate the corresponding grain sizes. The results indicated that dislocation density firstly increased and then decreased with increasing rolling strain. The values of dislocation density measured by XRD analysis are comparable with those measured by HRTEM. A high density of L-C locks, as shown in Fig. 48, are primarily responsible for the dislocation accumulation and the increase on dislocation density. Dynamic recovery and the dissociation of the L-C locks are responsible for the subsequent decrease on dislocation density.

### 5.2.2. The formation and dissociation of Lomer-Cottrell locks

Both the formation and the dissociation of L-C locks have been predicted by MD simulations [467–470] and have been verified experimentally in various nc materials [236,465,471].

The formation and dissociation of L-C locks were observed in an HPT-induced grain growth process in nc Ni-Fe alloys. During the grain growth process, large grains containing a high fraction of low-angle sub-grain boundaries formed via grain rotation. High densities of misfit dislocations were located at these sub-grain boundaries to accommodate the misorientation at two sides of the boundaries [437]. With further HPT processing, the misorientation angles between neighbouring sub-grains

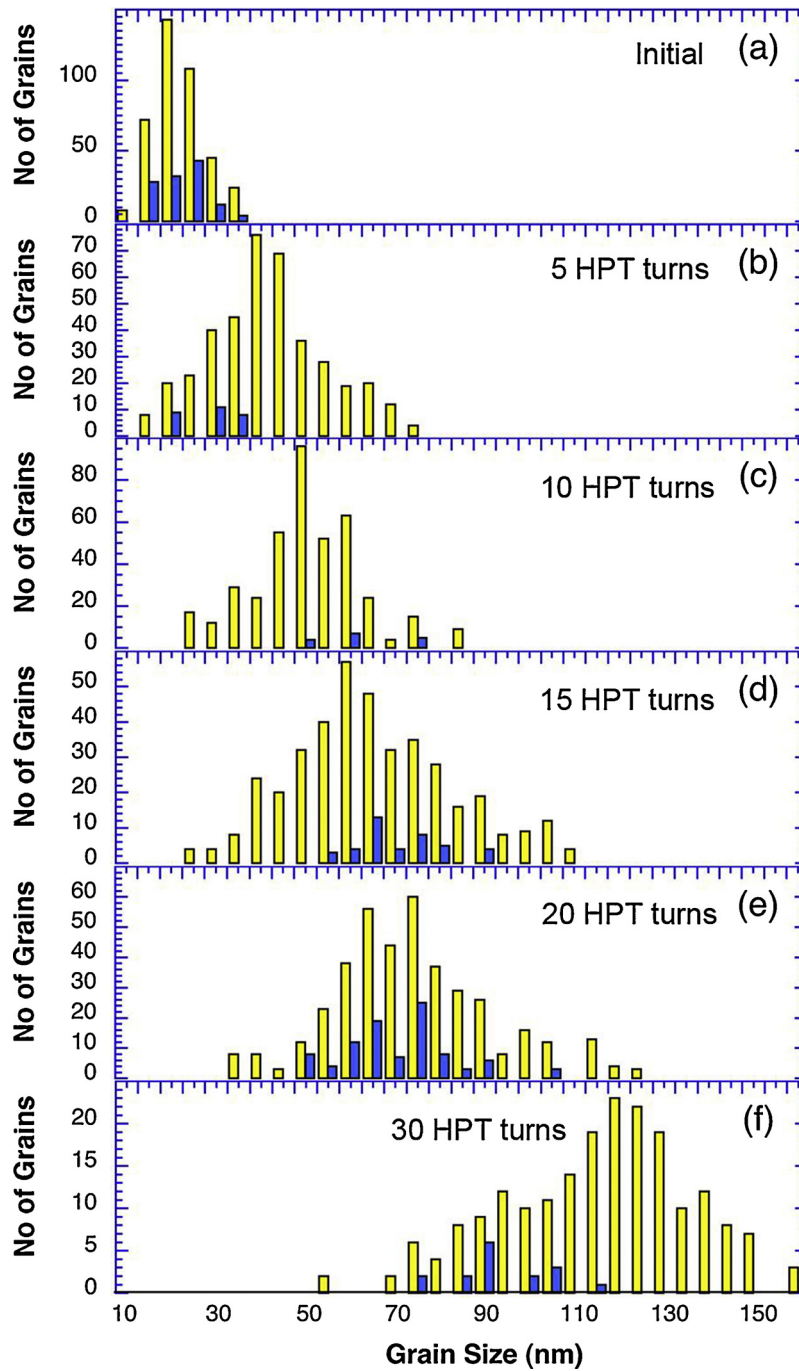


Fig. 44. The size distributions of all grains (light yellow bars) and grains containing twins (dark blue bars) with increasing HPT revolutions in an nc Ni–20 wt% Fe alloy [100] (For interpretation of the references to colour in this figure legend, the reader is referred to the web version of this article.).

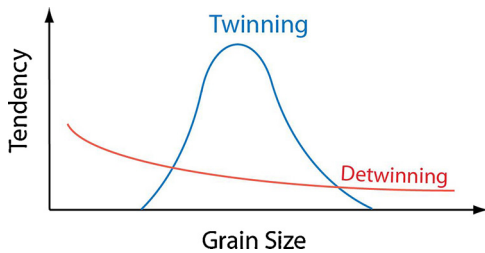
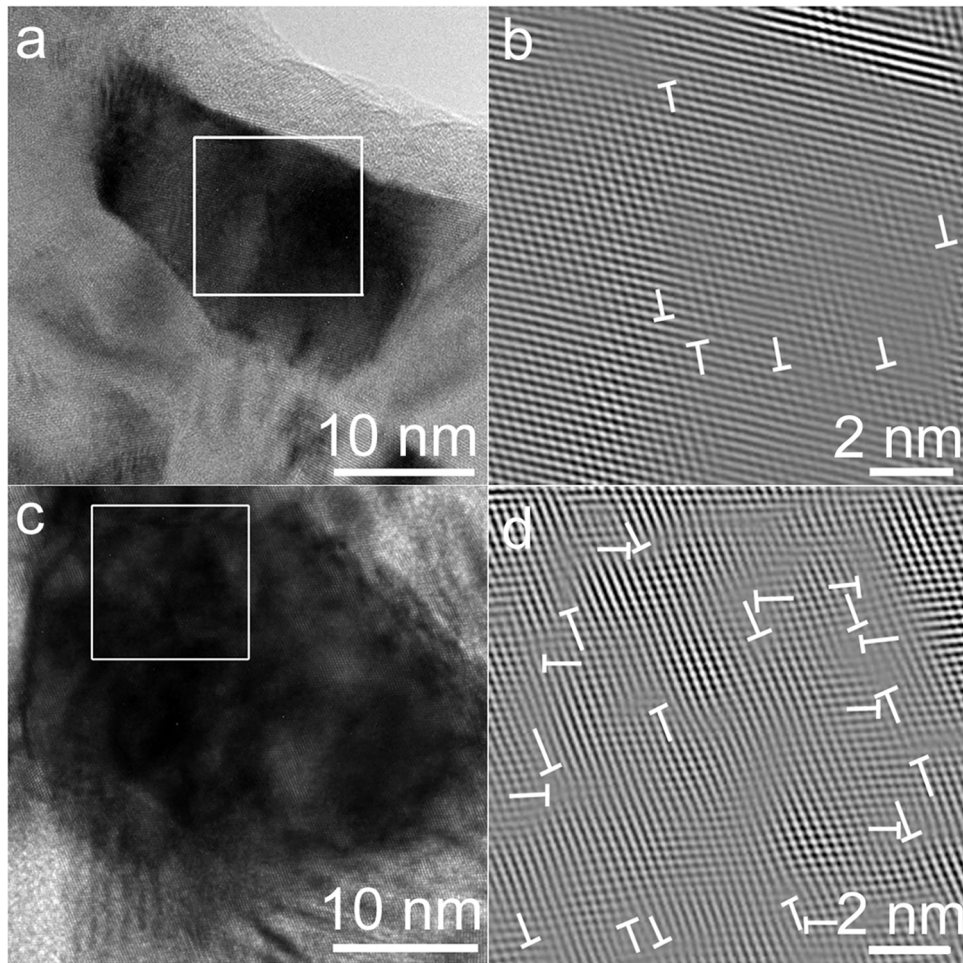


Fig. 45. Schematic representation of the grain size effect on the twinning and de-twinning tendency [100].

decreased gradually to zero and the misfit dislocations necessarily glided away [437,471]. These three-dimensional sub-grain boundary dislocations [155,437] slipping on different {111} planes may meet, interact and tangle with each other, increasing the dislocation density in the material. The existence of a high density of dislocations on two intersecting {111} planes provides a high probability for the formation of L-C locks, each of which is formed by the reaction of two leading partials from two dissociated lattice dislocations on two intersecting slip planes.

Fig. 49 shows a typical [110] HRTEM image of an HPT-processed specimen that provides evidence of L-C lock formation. The two plane



**Fig. 46.** Typical HRTEM images of grains at different deformation stages and their corresponding Fourier-filtered images obtained from the areas marked by white squares: dislocations are indicated with white “T”s. (a) and (b) are from the early stages of deformation, (c) and (d) are from deformation stages when the L-C lock formed [236].

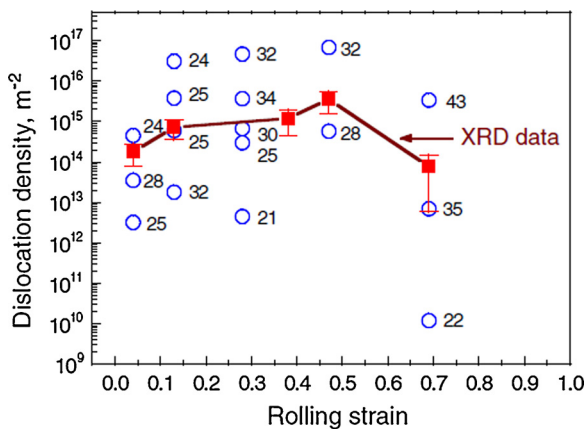


**Fig. 47.** Dislocation density as a function of rolling strain in nc Ni, measured from HRTEM images (blue unfilled circles) and XRD analysis (red solid squares) [465] (For interpretation of the references to colour in this figure legend, the reader is referred to the web version of this article.).

groups in the image can be indexed as  $(\bar{1}\bar{1}1)$  and  $(\bar{1}\bar{1}1)$ , respectively. It should be noted that a lattice dislocation in an FCC metal is normally dissociated into two  $\frac{1}{6}\langle 112 \rangle$  type partial dislocations. For example, a lattice dislocation with the Burgers vector of  $\frac{1}{2}[0\bar{1}\bar{1}]$  on  $(\bar{1}\bar{1}1)$  is dissociated into  $\frac{1}{6}[1\bar{1}\bar{2}] + \frac{1}{6}[\bar{1}\bar{2}\bar{1}]$  and a lattice dislocation with the Burgers

vector of  $\frac{1}{2}[101]$  on  $(\bar{1}\bar{1}1)$  is dissociated into  $\frac{1}{6}[211] + \frac{1}{6}[1\bar{1}2]$ . When the two lattice dislocations meet at an intersection of the  $(\bar{1}\bar{1}1)$  and  $(\bar{1}\bar{1}1)$ , the two leading partials interact, forming a stair-rod dislocation  $\frac{1}{6}[\bar{1}\bar{2}\bar{1}] + \frac{1}{6}[211] \rightarrow \frac{1}{6}[1\bar{1}0]$ . Together with the other two partial dislocations, this forms an L-C lock structure. The overall Burgers vector of the L-C lock is  $\frac{1}{2}[1\bar{1}0]$ , which is clearly evident in Fig. 49.

Because the L-C lock structure is extended on two  $\{111\}$  planes, it provides a strong barrier to dislocation glide [454] and leads to a significant accumulation of dislocations in the nc Ni-Fe alloy. Note that reactions between different combinations of partials from two slip planes can lead to various types of stair-rod dislocations. The formation of a high density of L-C locks hinders severely the motion of dislocations, which increases the dislocation density and may contribute significantly to both strength and ductility. At very high stresses, the L-C locks may be dissociated when the external force is large enough to pull apart the two dislocations that formed the locks. The dislocations glide and annihilate at GBs, leading to subsequent decrease in dislocation density.

The dissociation of L-C locks was also observed in a nc Pt ultrathin film by in-situ deformation TEM [471]. Fig. 50(a–b) show two HRTEM images taken 180 s apart during deformation. Fig. 50(c–d) present enlarged HRTEM images of the framed areas in (a) and (b), respectively. Fig. 50(e–f) display the inverse fast Fourier-filtered (IFFT) images of the framed areas in (c) and (d), respectively. The formation of L-C locks is seen in (c) and (d), and the dissociation of L-C locks in (e) and (f). With continued straining, as shown in Fig. 50(g–h), an L-C lock reformed in the same region.

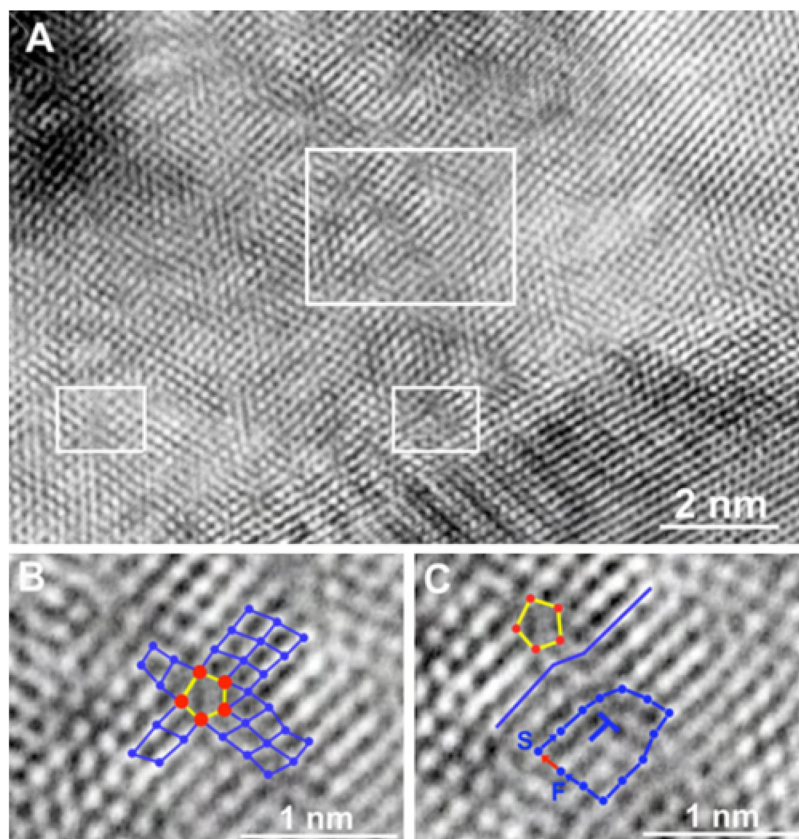


Fig. 48. (a) An HRTEM image of a cryorolled nc Ni. L-C locks were marked by three white rectangular frames; (b) enlarged image of the areas in (a), which shows a stair-rod dislocation of an L-C lock; (c) Burgers circuit enclosing a Shockley partial near an L-C lock [465].

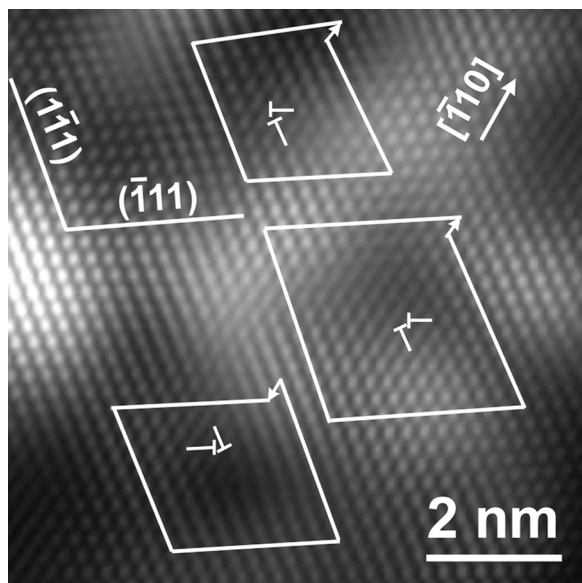


Fig. 49. A typical Fourier-filtered HRTEM image showing the formation of L-C locks: Burgers circuits are drawn in the image [236].

Fig. 51 illustrates the schematic view of the formation and dissociation process of an L-C lock under applied stress. Fig. 51(a) shows the Burgers vectors of the interacting dislocations BC and CD. Fig. 51(b–c) show the schematic view of the L-C lock formation via the interaction of the two full dislocations under applied stress. The Burgers vector of the junction segment is the sum of the initial vectors. The L-C lock can be unlocked if a critical stress is reached, as shown in Fig. 51(d).

The formation and dissociation processes can be described below. When two full dislocations meet under an applied stress on two intersecting slip planes, they react to reach a low energy configuration and thereby form a stable junction such as an L-C lock [472]. The structure of an L-C lock consists of a junction segment and four arms of the junction. With increasing stress, the two dislocations forming the junction segment are pulled apart, resulting in the decrease on the length of the junction segment [469].

## 6. SPD-induced phase transformation

Besides grain refinement and grain growth, SPD can also induce phase transformation. Both diffusive and non-diffusive (martensitic) phase transformations have been reported.

### 6.1. SPD-induced diffusive phase transformation

Diffusive phase transformations are associated with the redistribution of alloy elements and, therefore, with mass transfer. SPD-induced diffusive phase transformations include dissolution of precipitates in a matrix [473–483], decomposition of solid solutions [484–486], amorphization of crystalline phases [473,487–491], nanocrystallization of an amorphous matrix [492–498] and dissolution of multiple phases in immiscible systems to form totally new structures [499–502].

The first type of SPD-induced diffusive phase transformation is the dissolution of secondary phase/phases in alloys that results in the formation of a supersaturated solid solution or a phase transformation. For example, SPD resulted in up to 2.2 wt.% of Fe dissolved into the Al matrix although the solubility of Fe in Al is 0.05 wt.% in the Al-Fe phase diagram at room temperature [478]. Fig. 52 shows the XRD patterns for both the as-cast and the as-deformed Al-16 wt.% Fe alloy. For the as-cast alloy, peaks for Al and  $\text{Al}_{13}\text{Fe}_4$  were detected and the positions of

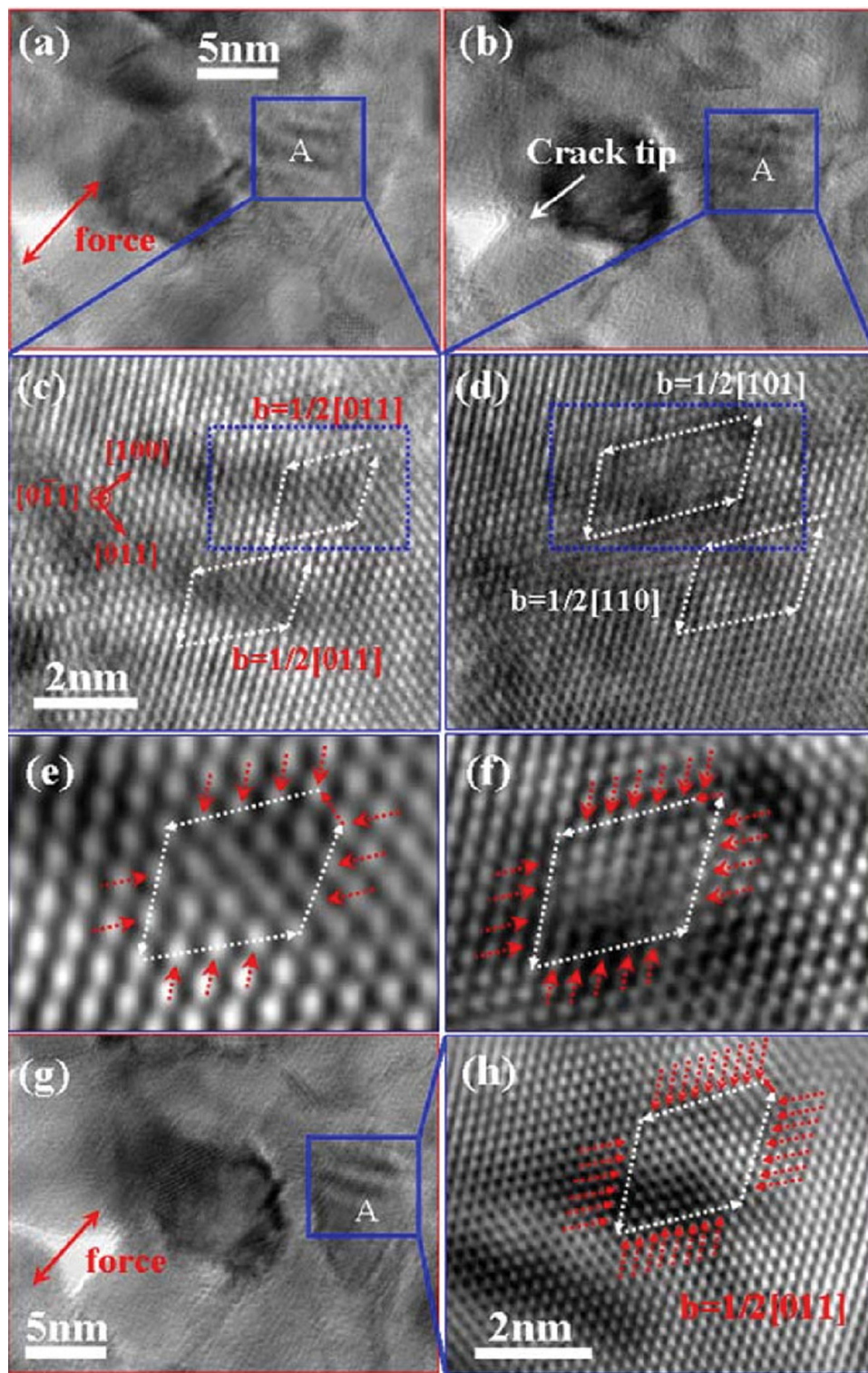


Fig. 50. In situ TEM observations of dislocation activities in a nano-grain [471].

the Al-phase peaks agree well with that of the commercial pure Al, indicating virtually no Fe in solution in the Al matrix. After SPD, the intensity of the  $\text{Al}_3\text{Fe}_4$  peaks decreased and the peaks for both Al matrix and  $\text{Al}_3\text{Fe}_4$  phase broadened significantly, indicating the dissolution of  $\text{Al}_3\text{Fe}_4$  and the formation of UFG structure in conjunction with high internal stresses. Extensive TEM and energy dispersive spectroscopy investigations revealed that deformation-induced dissolution of  $\text{Al}_3\text{Fe}_4$  phase resulted in the formation of a supersaturated solid solution of Fe in Al. SPD also produced a solid solution in the

immiscible Cu-Ag eutectic system [479]. Dissolution of cementite in carbon steels during SPD leads to the formation of supersaturated solid solutions of C in BCC ferrite [476,480] or a phase transformation from the BCC ferrite to FCC austenite [474].

The second type of SPD-induced phase transformation is the dissociation of supersaturated solid solutions into new structures/phases. This phenomenon has been found in HPT-processed Zn- and Mg- rich supersaturated (Al) solid solutions [484,485,503]. The supersaturated solid solution in the as-cast Al-30 wt.% Zn, Al-20 wt.% Zn and

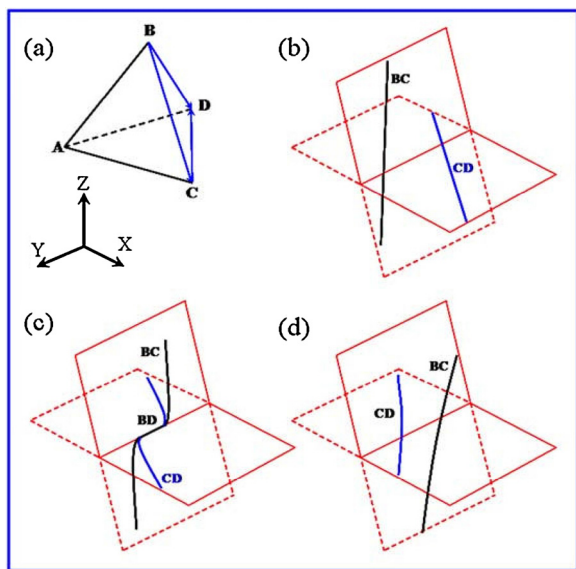


Fig. 51. (a) Thompson tetrahedron showing the Burgers vectors of the interacting dislocations. (b-d) Schematic views of the L-C lock formation and dissociation [471].

Al-10 wt.% Zn alloys contained about 15 wt.%, 7 wt.% and 3 wt.% Zn, respectively, while the equilibrium solubility of Zn in Al at room temperature is below 1 wt.% [504]. All the three supersaturated solid solutions decomposed completely after HPT, producing nano-grained Al and Zn particles simultaneously [484,485,503]. As shown in Fig. 53, the HPT process led to the formation of a phase structure that is closer to the equilibrium state than the initial undeformed material [503]. The homogenized one-phase solid solutions in the Cu-Ni alloys with 42 and 77 wt. % Ni also decomposed into Cu-rich and Ni-rich phases after HPT at room temperature [486]. HPT also separated Al from originally equilibrium single-phase Cu-Al solid solutions when the grain sizes of the materials are refined to tens of nanometers [505]. Fig. 54(a) shows a typical example of the separation, in which Al was separated from a twinned Cu nano-grain, covering the whole GB area. Fig. 54(b) shows a magnified image of the upper-right area of Fig. 54(a) [505]. The different lattice parameters and orientations measured within the grain and at the layer surrounding the grain confirmed the Al separation from the inner grain [505]. In addition, Zhang et al [506] found deformation-induced phase transformation from the BCC phase of a Co-Fe alloy to the FCC Fe and Co phases, which generally occurs at high temperatures above ~ 1150 K [507].

Recently, it has been reported that SPD-induced decomposition of (supersaturated) solid solution and SPD-induced dissociation of

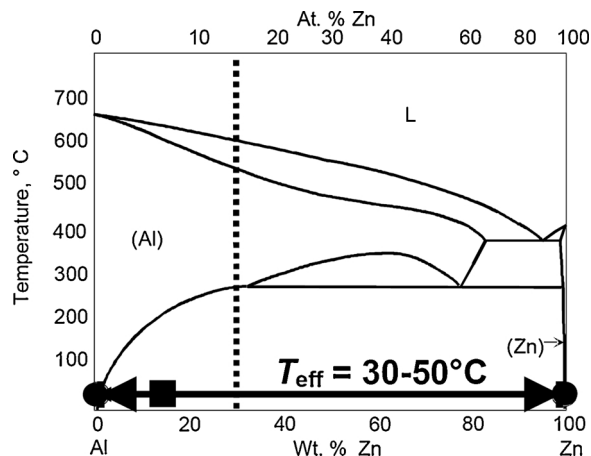


Fig. 53. The Al-Zn phase diagram. Vertical dotted line represents the composition of Al-30 wt.% Zn alloy. Filled square represents the composition of supersaturated (Al) solid solution in CG Al-30 wt.% Zn alloy before HPT. Filled circles represent the composition of phases in ultra-fine-grained Al-30 wt.% Zn alloy after HPT [503].

precipitates are not independent. The precipitation of secondary-phase particles from a solid solution and the dissolution of these secondary phase particles always take place simultaneously and compete with each other, reaching a balanced concentration of a second component in a solid solution. B.B. Straumal et al. [508] carried out HPT on an as-cast Cu-3.9 at.% Ag alloy that consists of a (Cu) solid solution with diluted 1.9at.%Ag and another 2at.%Ag as fine silver precipitates. Dissolution of precipitates occurred during deformation. HPT was also applied on an almost homogeneous (Cu) solid solution with diluted 3.9 at.%Ag, causing partial decomposition of the solid solution.

As shown in Fig. 55, the solute concentration in the matrix in both samples reached the same level (about 2.9–3.0 at.% Ag) after HPT. This value does not depend on the initial state and is higher than the equilibrium solubility limit at the HPT temperature. This concentration is equal to the solubility limit at the effective temperature of  $T_{eff} \approx 680^\circ\text{C}$ . Similar phenomenon occurred in Cu-4.9 wt. % Co alloys [482]. Alloys in two different states, Co fully dissolved in the Cu-rich matrix and Co fully precipitated from the Cu matrix, were subjected to HPT. With increasing number of rotations, the lattice parameter of the alloy in the first state decreased and that of the alloy in the second state increased. After 5 rotations, the lattice parameter in both samples becomes almost the same and agrees well with that of the solid solution of Co in Cu with 2.5 wt.%. Therefore, the initial state of the alloy prior to HPT has no relation to the composition of the solid solution after HPT.

The third type of SPD-induced diffusive phase transformation is amorphization of crystalline phases. Huang et al. [509] reported the

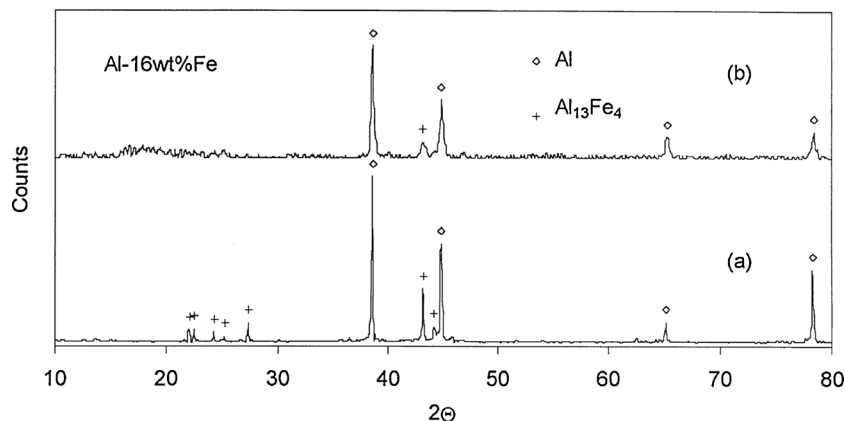


Fig. 52. XRD patterns of an Al-16 wt%Fe at the (a) as-cast and (b) as-deformed states [478].

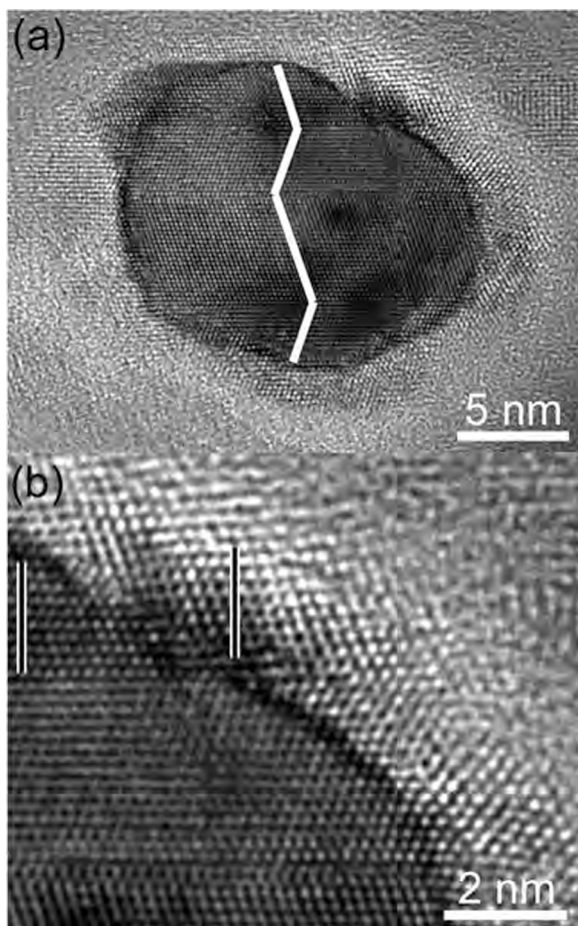


Fig. 54. (a) An HRTEM image showing Al separation surrounding the complete GB of a nano-grain. White zig-zag lines trace the  $\{111\}$  planes forming the twin relationship in different parts of the grain; and (b) an enlarged image of the upper-right part of the grain in (a). The two parallel vertical lines have equal length. The length of the lines at the grain interior roughly equals to the inter-planar distance of nine Cu  $\{111\}$  planes; the length of the lines outside the grain nearly matches the inter-planar distance of eight Al  $\{111\}$  planes [505].

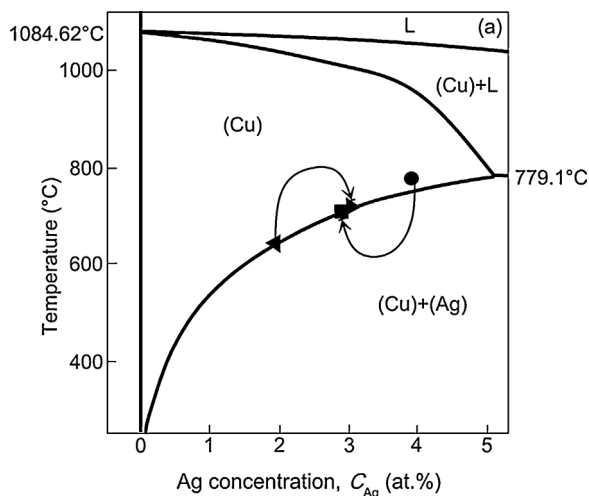


Fig. 55. The Cu-rich part of the Cu-Ag phase diagram. The full left-triangle and the full circle indicate the compositions of the as-cast alloy and the homogenized alloy, respectively, before HPT. The full right-triangle and the full square indicate the compositions of the as-cast alloy and the homogenized alloy, respectively, after HPT [508].

HPT-induced crystalline to amorphous transformation in TiNi and found that the deformation-induced amorphization initiated from dislocation core regions in the interior of grains and from GBs, as shown in Fig. 56. It is believed that the energy stored in the dislocations and the GBs contribute significantly to driving the crystalline to amorphous transformation. Cepeda-Jiménez et al. [473] reported that an Fe–20 wt. % (Nd,Pr)–5 mass % B–1.5 wt. % Cu alloy containing crystalline phases  $(\text{Nd,Pr})_2\text{Fe}_{14}\text{B}$  and Pr-rich phase transformed into a mixture of the amorphous phase and  $(\text{Nd,Pr})_2\text{Fe}_{14}\text{B}$  nano-grains after HPT. In addition, a CG as-cast Ni–20 wt. % Nb–30 wt. % Y and Ni–18 wt. % Nb–22 wt. % Y alloys containing the NiY, NbNi<sub>3</sub>, Ni<sub>2</sub>Y, Ni<sub>7</sub>Y<sub>2</sub> and Ni<sub>3</sub>Y phases transformed into a mixture of two nc NiY and Nb<sub>15</sub>Ni<sub>2</sub> phases and two different amorphous phases with one in Y-rich and the other in Nb-rich after HPT [487].

The fourth type of SPD-induced diffusive phase transformation is nanocrystallization of amorphous matrix. Shear banding-induced crystallization was reported in a  $\text{Zr}_{53}\text{Cu}_{18.7}\text{Ni}_{12}\text{Al}_{16.3}$  bulk metallic glass subjected to SPD [510]. By applying HPT on an amorphous  $\text{Cu}_{60}\text{Zr}_{30}\text{Ti}_{10}$  alloy disk sample, a gradient microstructure was obtained along the radial direction of the disk. Large and deformed grains were observed in the interior of the disk, while homogeneously dispersed nanocrystals embedded in the amorphous matrix was observed at the edge part of the disk [494]. In addition, calorimetric analysis indicated that the amorphous fraction decreased with increasing deformation. HPT on an  $\text{Al}_{85}\text{Ce}_8\text{Ni}_5\text{Co}_2$  amorphous ribbon also resulted in the formation of primary  $\alpha$ -Al nanocrystals at the edge part of the disk [495].

The fifth type of SPD-induced diffusive phase transformation is dissolution of multiple phases in immiscible systems to form totally new crystal structures, which occurred when SPD processing was applied on immiscible multi-phase materials at extremely large strains [499–502]. Edalati et al. [499,500] reported the formation of new BCC, FCC and HCP phases in Mg-Ti and Mg-Zr systems by applying HPT on Mg/Ti powder mixtures for 100 revolutions and Mg/Zr powder mixtures for 100 and 1000 revolutions, although Mg is totally immiscible in Ti and Zr even in the liquid form. Fig. 57 shows the XRD patterns for the Mg/Ti powder mixtures and for the middle and edge parts of Mg/Ti disk samples processed by HPT for 100 revolutions. It can be seen that some new phases (BCC, FCC, HCP-I, HCP-II) formed after HPT processing. Peaks for Mg and Ti were still visible at the middle part of the disk, while they totally disappeared at the edge part of the disk, confirming that the initial phases dissolved in each other under HPT processing and new phases formed. Similar phenomena were also observed in other immiscible systems, including a new BCC phase formed in Mg-V-based systems [501], a new B2 phase in Mg-Ni-Pd system [502] and a new amorphous phase in Mg-Ni-Sn system [501].

## 6.2. SPD-induced martensitic phase transformation

Stress-induced martensitic phase transformations are common in metals and alloys, including Co [511,512], Ti [336,513,514], Zr [339,381,515], Hf [516], Mo [517], Ti alloys [518–521], and shape memory alloys [522–524]. No diffusion occurred during these phase transformations. Wang et al. [518] reported HPT-induced  $\beta$  (BCC) to  $\omega$  (simple hexagonal) and  $\omega$  to  $\beta$  phase transformations in a Ti alloy and proposed that the reversible ( $\omega$  to  $\beta$ ) phase transformation was caused primarily by nc grain size. Table 4 summarize the phase transformation and microstructure at different HPT strain values. It can be seen from the table that for grain sizes larger than the submicrometer range, the  $\beta$  to  $\omega$  transformation occurred, while under the same deformation conditions when the grain sizes were less than 100 nm a reverse  $\omega$  to  $\beta$  phase transformation appeared. The reverse  $\omega$  to  $\beta$  phase transformation generally occurred under extremely high pressure or high temperature [340,518,525,526]. Reducing the grain size down to the nanometer regime reduces significantly the pressure/temperature needed for the transformation.

A shear induced HCP ( $\alpha$ ) to simple hexagonal ( $\omega$ ) plus BCC ( $\beta$ )

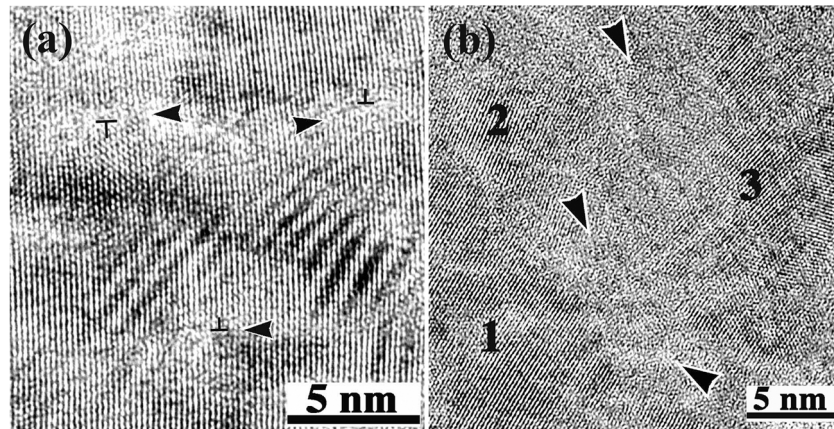


Fig. 56. (a) Amorphization initiated from dislocation cores; (b) amorphization at GBs. The numbers indicate three different grains. The arrowheads indicate the amorphous regions [509].

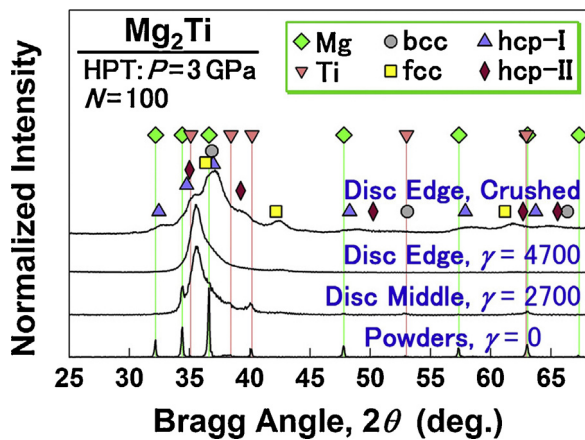


Fig. 57. XRD patterns for the Mg/Ti powder mixtures and for the middle and edge part of Mg/Ti disk samples processed by HPT [499].

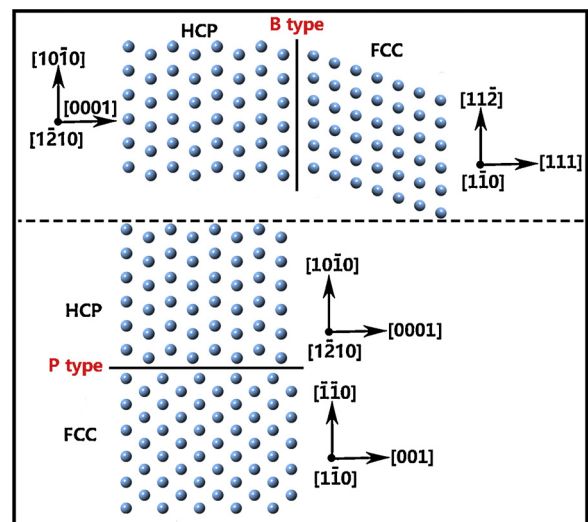


Fig. 58. Schematic diagrams show the orientation relationships of two types of phase transformation.

Table 4

Summary of phase transformation, microstructure at different HPT strain values [518].

Sample position	As-received	1/4-turn center	1/4-turn edge	1/2-turn edge	1-turn edge
Von Mises strain	0	~0.5	~4	~8	~15
Transition	N/A	$\beta \rightarrow \omega$	$\beta \rightarrow \omega$	$\beta \rightarrow \omega$	$\omega \rightarrow \beta$
Phase/s present	$\beta + \omega$	$\beta + \omega$	$\beta + \omega$	$\beta + \omega$	$\beta$
Area fraction of $\omega$	7%	24%	37%	16%	0%
$\omega$ Particle length	4 nm	40 nm	60 nm	30 nm	0
Average grain size	1.8 $\mu\text{m}$	1.8 $\mu\text{m}$	190 nm	80 nm	50 nm

transformation was reported in pure Zr under HPT [339]. The pure beta Zr fabricated was stable at room temperature and atmospheric pressure. The  $\alpha \rightarrow \omega + \beta$  transformation in Zr usually occurs under a pressure of 30 GPa [525,526], but when HPT was applied on the material the pressure required for the transformation was significantly reduced to 3 GPa. It's proposed that not only compression but also shear induced by HPT result in the pressure drop needed for transformations. This has also been predicted by first-principles calculations that the pressure needed for certain pressure-induced martensitic transformations decreases with increasing shear [527].

Recently, stress-induced HCP to FCC phase transformations have been widely observed in Ti [336,513,514], Zr [515] and Hf [516]. The HCP to FCC phase transformation typically produces two different orientation relations between the two phases: (1)  $\langle 1\bar{2}10 \rangle_{\text{HCP}} // \langle \bar{1}10 \rangle_{\text{FCC}}$  and

(2)  $\langle 0001 \rangle_{\text{HCP}} // \langle \bar{1}11 \rangle_{\text{FCC}}$ , and (2)  $\langle 0001 \rangle_{\text{HCP}} // \langle 001 \rangle_{\text{FCC}}$  and  $\langle 10\bar{1}0 \rangle_{\text{HCP}} // \langle 110 \rangle_{\text{FCC}}$ , as shown in Fig. 58(a–b), respectively. In the former case, the longitudinal boundary between two phases is parallel to the (0001) basal plane of the HCP matrix, thereby this phase transformation and the resultant orientation relationship can be denoted as the B-type phase transformation and the B-type orientation relationship. The B-type phase transformation has been observed in Ti-based alloys [528–530], Hf [516], Co [512,531], InAs nanowires [532], SiC [533] and stainless steel [534,535].

In the latter one, the longitudinal boundary between the two phases is parallel to the  $\{10\bar{1}0\}$  prism plane of the HCP matrix, thereby this phase transformation and the resultant orientation relationship can be denoted as P-type phase transformation and P-type orientation relationship. The P-type phase transformation has been observed recently in pure Ti after plastic deformation [513,514,536].

Both B-type and P-type HCP to FCC phase transformations were observed in a cold-rolled Zr recently [515]. The as-received Zr is of single HCP phase, FCC lamellas were observed after deformation. As shown in Fig. 59(a and c), FCC lamellas were embedded in the HCP matrix. The inserted SAED patterns show the orientation relationships of the two phases, revealing the B-type and P-type transformations in (a) and (c), respectively. The orientation relationships were further proved from the HRTEM images, as shown in Fig. 59(b and d). The successive gliding of Shockley partials on every other basal plane

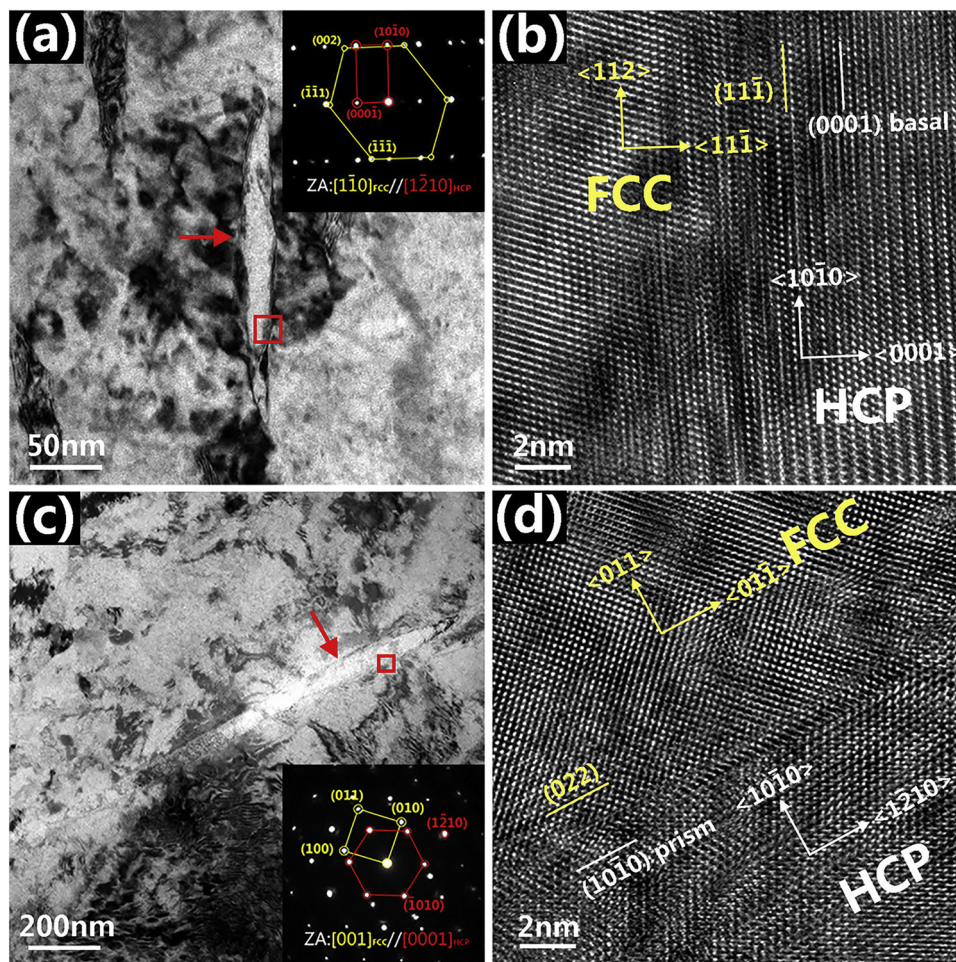


**Fig. 59.** (a) A TEM image and a corresponding SAED pattern of cold-rolled Zr with a thickness reduction of 60%; (b) an HRTEM image of the red rectangular area in (a), showing the longitudinal HCP-FCC phase interface is parallel to the (0001) basal plane; (c) another TEM image and a corresponding SAED pattern of the cold-rolled Zr; (d) an HRTEM image of the red rectangular area in (c), showing the longitudinal HCP-FCC phase interface is parallel to a {1010} prism plane [515].

triggers the B-type transformation. Those transformation-related partials are from the dissociation of  $\langle a \rangle$  full dislocations ( $60^\circ$  mixed-type  $\langle a \rangle$  and screw  $\langle a \rangle$  dislocations) [515,516]. For the P-type transformation, the formation of FCC lamellas is realized through the pure-shuffle and shear-shuffle mechanisms by successive gliding of opposite-signed 2-layer steps [515]. Interestingly, a reverse FCC to HCP phase transformation was observed in a cryogenic-deformed FeCoCrNi high-entropy alloy recently [537]. The transformation was revealed to occur via the glide of Shockley partials on every other {111} plane.

## 7. SPD-induced structural evolution in multi-phase alloys

Recently, multi-phase alloys composed of ultrafine-scale and nano-scale structures have elicited strong interest due to their remarkable enhancement of mechanical properties [9,10,538–542]. SPD, as one of the most effective microstructural refinement techniques, has been employed to tailor multi-phase alloys with nanostructures [10,543–546]. In-depth understanding of the microstructural evolution of multi-phase alloys processed by SPD is necessary. While the existence of different phases rendering the bulk materials with combined outstanding properties, it also complicates the microstructural evolution.

The major difference between single-phase alloys and multi-phase alloys is attributed to the existence of interphase interfaces (also called “phase boundaries”). Interphase interfaces are the physical linkage between phase domains and are the media through which the microstructural changes of one phase are affecting the other [547,548]. The fundamental role of interphase interfaces is very similar to GBs, i.e., an

interphase interface can act as a source, sink, and storage site of dislocations and a barrier to the motion of defects [548]. However, interphase interfaces have some unique properties that GBs do not have: (1) when a dislocation line passes through a precipitate/matrix interphase interface, an Orowan loop, which is a dislocation loop surrounding the precipitate, forms and is pinned to the interface (Orowan-like strengthening effect) [547,549–551]; (2) when a dislocation in the phase with a low elastic modulus moving towards an interphase interface, it will experience an image force from the adjacent phase with a high elastic modulus (Koehler strengthening effect) [552]; (3) dislocations could be attracted to or repelled from an interphase interface by the stresses associated with the tension or compression which sustains the lattice coherency at the interface (coherency stress) [553]; and (4) effects relate to thermodynamic properties such as heat of mixing and interfacial energies. For example, as the heat of mixing decreases from a high positive value to a low negative value, the CRSS increases and then decreases [548,554–556]; A low interfacial energy may hinder the emission of dislocations from the interface [557,558].) Consequently, interphase interfaces play a crucial role in affecting the microstructural evolution of each phase and in determining the mechanical properties of the materials [547,553].

There are in general two types of multi-phase alloys: dual-phase alloys and alloys with precipitates. Because of their distinct structural features, SPD-induced structural evolution of the two types of alloys will be discussed separately. Some representative microstructures observed during the concurrent microstructural evolution of multiple phases will be discussed to reveal the important deformation

mechanisms that are operative during SPD. The role of interphase interfaces played in the microstructural evolution at a broad length scale from the micrometer regime to the nanometer regime will be discussed.

### 7.1. Dual-phase alloys

The dual-phase alloys reviewed in this section are alloys with a comparatively large volume fraction of the secondary phase. The two phases of the starting materials are in the polycrystalline bulk state [228,544,545,559–562]. A good example of dual-phase materials is commercial grade duplex stainless steels [228]. Their grain sizes are normally a few tens micrometers or even much larger. Therefore, there is plentiful space for deformation structures such as dislocation walls and deformation twins to form in the grain interiors during deformation. In a dual-phase material, the plasticity of one phase is different from the other due to the difference in crystal structure and/or chemical composition, i.e., the two phases are not equally easy to deform. Plastic deformation starts in the soft phase while the hard phase could still be in the elastic state [563–567]. As the plastic deformation proceeds further, the soft phase is strain hardened and internal stresses at interphase interfaces drastically build up via dislocation accumulation and pile up [568,569]. Thus, there exist a stress gradient and a strain gradient from the interface to the interior of phase domains [547,554], which lead to the buildup of back stress [570]. Eventually, co-deformation of the two phases begins.

Experimental evidence [556,565] and theoretical analysis [547,554,571,572] suggested that dislocation transmission through interphase interfaces is very unlikely at micrometer length scale, due to insufficient stress and large dislocation accumulations at the interfaces. Therefore, each phase deforms by its own preferred deformation mechanisms identical to those in single-phase materials [228,565,573]. For example, in a ferrite–austenite duplex steel processed by HPT, dislocation activities were the major deformation mode in the ferritic phase (evidenced by the dislocation structures in Fig. 60(a) and the corresponding diffraction pattern in Fig. 60(b)), while deformation twinning played a significant role in the deformation of the adjacent austenitic phase with a low SFE (evidenced by a high density of twin bands in Fig. 60(a) and the corresponding diffraction pattern in

Fig. 60(c)) [228,544]. The sharp change of microstructures at interphase interfaces suggests no dislocation transmission across the interface. It is anticipated that once both phases start to yield, the strain gradient at the interface is reduced to the minimum by having characteristic microstructures in each phase [569,574]. For example, in Fig. 60, in order to achieve a similar strength with the ferritic phase the originally soft austenitic phase was strengthened with a high density of nano-twins, while the ferritic phase was only deformed to have some scattered dislocations and low-angle dislocation walls [228].

The high shear strain imposed by SPD can refine the grains in dual-phase materials down below the UFG regime. The phase domains can also be refined significantly and redistributed more homogeneously than in the unprocessed samples, as exemplified by an HPT processed Zn–22% Al eutectoid alloy shown in Fig. 61. For some dual-phase materials with outstanding plasticity such as Cu–Ag alloys, Cu–Au composites and Cu–Nb composites, the width of the phase domains can be refined down below 100 nm [538,560,575,576]. In many cases full dislocations and/or twinning partials may not encounter any obstacle when gliding from one side of the phase domain to the other side if the two phases have a favorable orientation relationship. At this length scale (interphase interface spacing  $< \sim 100$  nm) the deformation mechanisms are mainly associated with the interphase interfaces. Conventional Hall-Petch type dislocation pile-up mechanisms at GBs and at interphase interfaces begin to lose dominance, meanwhile confined layer slip (CLS), interfacial sliding and dislocation transmission through interface become active [548,549,556,572,577,578].

When the sizes of phase domains reduce to the nanometer regime, dislocation entanglement within grains are much less likely [547,580], instead CLS of individual dislocations moving on closely packed glide planes occurs frequently [565,578,581]. In the CLS deformation mechanism, the edge component of a dislocation is emitted from a dislocation node which is pinned on the interphase interface, and spreading into an “Orowan type glide loop” to glide within the domain confined by the interface. An example is shown in Fig. 62(a), the dislocations I and II were emitted and pinned to the nodes marked by white arrows. As the strain increases, the dislocation I glides to the left by the Orowan bowing process parallel to the interface and depositing misfit-type dislocations at the interface. Three new dislocations III, IV and V

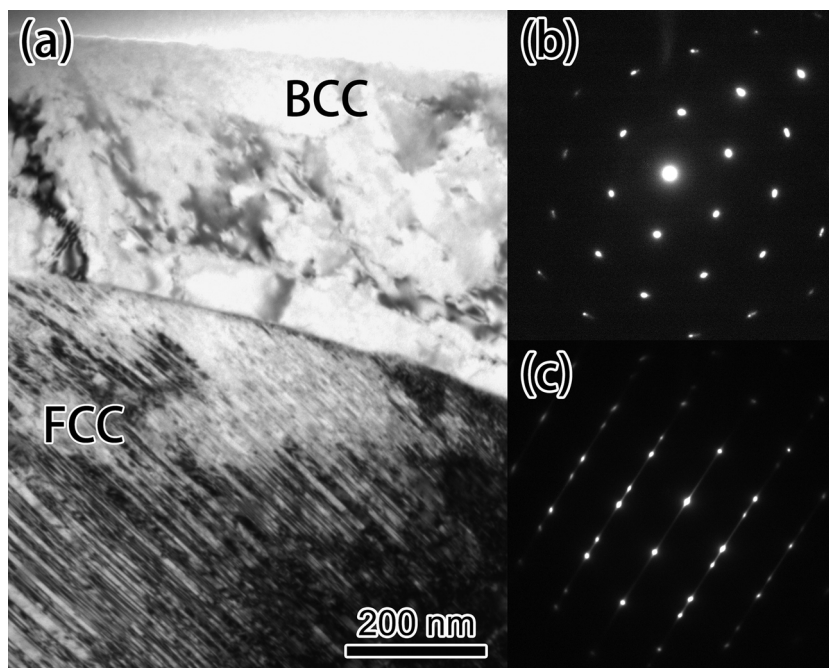


Fig. 60. (a) A TEM image showing microstructures of the austenitic phase and ferritic phase, and the interphase interface in an HPT processed duplex steel at a low strain; (b) and (c) corresponding diffraction patterns of the ferritic phase and the austenitic phase, respectively.

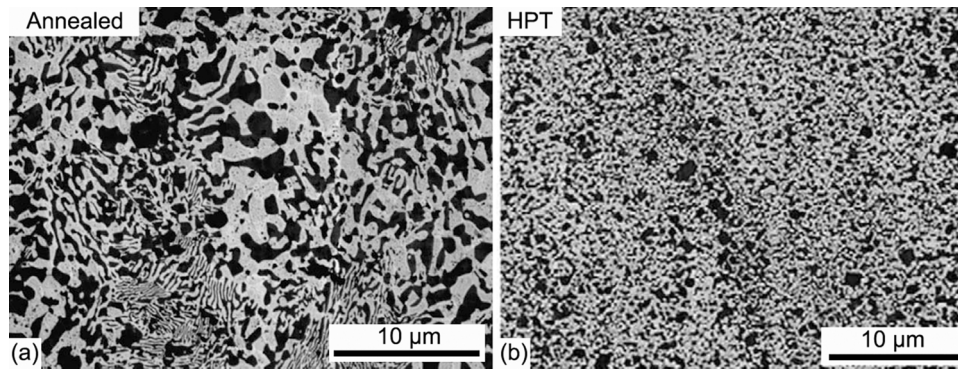


Fig. 61. Micrographs of the Zn-22% Al alloy (a) in the as-annealed condition [559] and (b) after HPT processing to 4 revolutions [579].

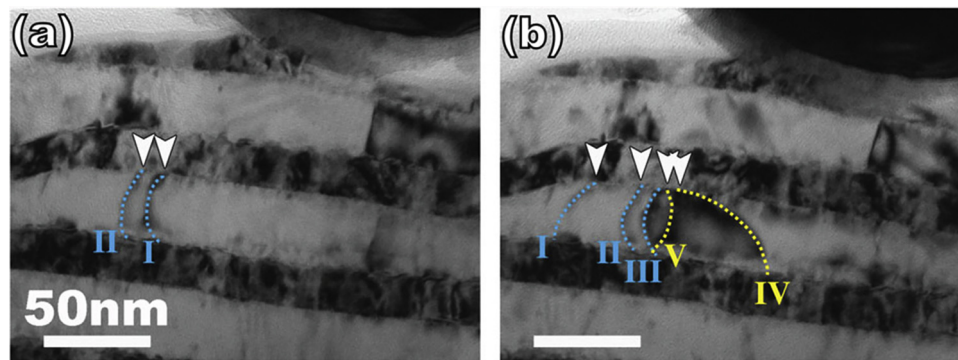


Fig. 62. TEM images showing (a) dislocations I and II nucleated at Cu-Nb interfaces, and (b) dislocation I glided to the left and IV and V nucleated and glided in the opposite direction by the CLS mechanism [578].

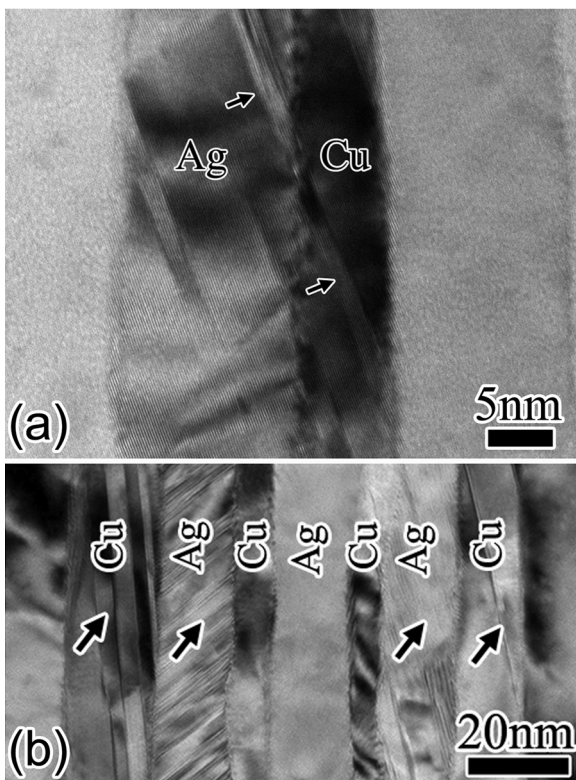


Fig. 63. (a) An HRTEM image showing the transmission of deformation twin through a Cu-Ag interface.; (b) typical microstructures of an eutectic Ag-28 wt. % Cu alloy processed by HPT to an equivalent strain of  $\sim 60$  (some deformation twins are marked by arrows) [575].

nucleate and glide parallel to the interface in different directions. More details about the CLS mechanism can be found in literatures [578,582].

Interfacial sliding and dislocation transmission through interface are competing mechanisms in dual-phase materials and they are affected by atomic misfit and both structural and chemical aspects of interfacial bonding [555,572]. There are four types of interphase interfaces: (1) coherent interfaces in which the two phases have a strict orientation relationship and the lattices at the interface match very well so that the slip planes and Burgers vectors are continuous at the interface [553]; (2) semi-coherent interfaces in which interfacial lattice parameters of the two phases have a small misfit ( $< 5\%$ ) [583]; (3) incoherent interphase interface with a large lattice misfit ( $> 5\%$ ); and (4) non-isostructural interface, e.g., an interface between a FCC and a BCC phase [572]. For dislocation transmission through coherent and semi-coherent interfaces, high stresses are required to overcome the coherency stress due to lattice mismatch, the Koehler stress due to the shear moduli mismatch and the stress associated with the changes in core structure on passing from one layer to the other [553,584].

An example of dislocation transmission through semi-coherent interface is shown in Fig. 63(a), some twinning dislocations initiated in Ag transmitted into the Cu phase, leading to deformation twinning in the Cu phase [575,585]. In fact, even partial dislocation transmission through an interphase interface is not a very common phenomenon as evidenced in Fig. 63(b) that most of the deformation twins and partial dislocations are confined within each of the phase domains.

For dislocation transmission through incoherent interfaces, there is no coherency stress, but interfacial shear strengths become another important factor. For a weak interface, slip transmission could be treated as nucleation from interfaces without preferred nucleation sites, since the incoming dislocation can be smeared out or dissociated into infinitesimal dislocations within the interface through glide and climb [580]. For a strong interface, the interface shear becomes difficult and the barrier for slip transmission will be determined by the Koehler force

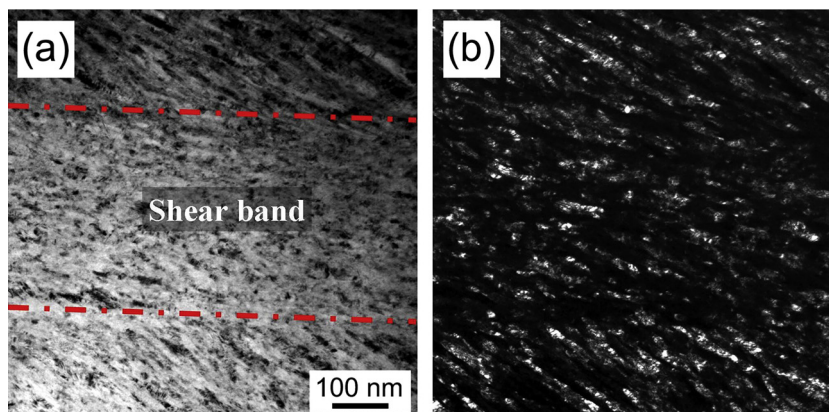


Fig. 64. (a) A bright-field TEM image and (b) the corresponding dark-field image showing a shear band structure observed in a Cu-28 wt.% Ag alloy processed by HPT for 20 revolutions [573].

and the interaction between the residual dislocation and the emitted dislocation [556,571,572]

Shear banding also plays an important role in the microstructural evolution of dual phase materials processed by SPD [573,586,587]. For example, in Fig. 64 shear banding can cause significant fragmentation of phase domains by cutting through lamellar phase bands that refines the grain structures of both phases in a localized region [573]. It is well-known that shear bands are non-crystallographic and occur when dislocation slip is strictly confined [223,241,587–590]. Therefore, it is reasonable to anticipate that the initiation of shear banding in dual phase alloys is affected by the shape and size of phase domains [590–592], resistance to slip transmission at interphase interfaces [589,593,594], the plastic strain magnitude [573,586] and the

microscopic deformation process [89,184,593,595]. In CG and UFG dual phase alloys or composites, dislocations can pile-up at GBs and interphase interfaces. The accumulation of defect structures can generate stress concentration that can potentially trigger shear banding [596–598]. In contrast, in nanolayered dual phase alloys or composites, in which the interface spacing is of the order of a few tens of nanometers or less, there is no room within the crystals to accommodate dislocation pile-ups or substructure [575,577,594]. Then the resistance to slip transmission at interphase interfaces is a crucial factor to initiate shear banding. The interface with low shear strength tends to absorb incoming dislocations, but without dislocation transmission the interface tilts gradually due to the accumulation of the non-planar component of the dislocations. Tilting of the interface reduces the angle

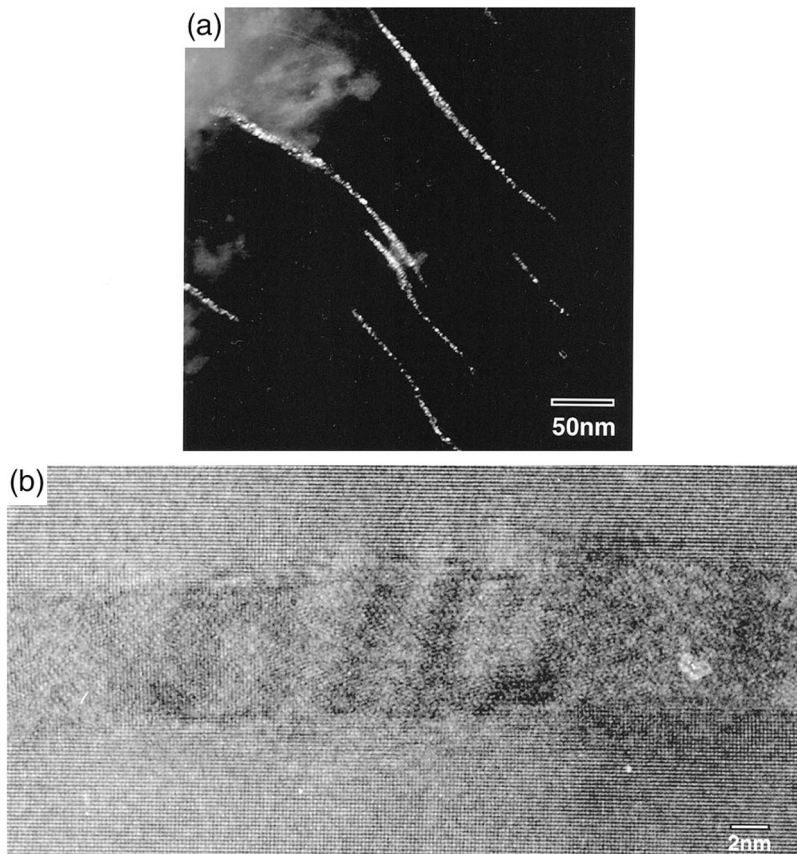


Fig. 65. (a) A dark-field TEM image taken using the (110)  $\theta'$  precipitate reflection and (b) an HRTEM image of the  $\theta'$  precipitate in the Al-1.7 at% Cu alloy after a single pass of ECAP [595].

between the interface and the global applied stress, and gradually increases the resolved shear stress parallel to the interface. Therefore, dislocation slip parallel to the interface is intensified, which eventually leads to shear banding [590,594].

## 7.2. Alloys with precipitates

Precipitates are dispersed fine particles of secondary phases within the primary phase matrix. Precipitates can be intermetallic or ceramic materials having various unique properties [9,554,599]. The type, size, morphology and number density of precipitates significantly affect the overall properties of bulk materials and are traditionally controlled by ageing treatments and alloy composition engineering [600,601]. During ageing treatments, the precipitation process usually follows a transformation sequence dominated by the precipitation kinetics and thermodynamics: Guinier–Preston (GP) zones → Metastable phase → Equilibrium phase [602,603]. As a result, precipitates generally have simple orientation relationships with the matrix and a unique morphology, such as rod or platelet shapes. In the last twenty years, there has been a growing interest in controlling the microstructures of alloys with precipitates by SPD processing [604–607]. Pronounced activities of crystalline defects during SPD substantially alter the morphology of the precipitate and structures of the matrix and significantly improve the mechanical properties of the material to a new high level [7,9,599,608].

The microstructural evolution of alloys containing precipitates is significantly affected by the dislocation-precipitate interaction [609,610], GB-precipitate interaction [611], dislocation slip [603,612] and atomic diffusion [432,613,614]. Precipitates vary by their structures [615,616], chemical stability [617,618] and mechanical properties [619]. Even for the same type of precipitates, their size, shape and density vary with thermal processing histories [603,611,620]. All these characteristics of precipitates lead to complex microstructural evolutions of precipitates and the matrix.

### 7.2.1. Evolution of precipitates during SPD processing

In practice, precipitates can form before, during or after SPD [621]. Under different circumstances, the resulting precipitation microstructures can be significantly different. Therefore, it is necessary to discuss the three different cases separately.

Some research work showed that pre-existing brittle precipitates with large aspect ratios can be fragmented and/or dissolved (i.e. in Al–4.11Cu [622–624], Al–1.7Cu–0.7Mg–0.3 Mn [625]) and solute atoms can be redistributed and segregated to GBs/dislocations, e.g. in AA7075 (Al–5.6Zn–2.5Mg–1.6Cu–0.4Si–0.5Fe–0.3 Mn–0.23Cr–0.2Ti) [9,603], AA6060 (Al–0.6Mg–0.6Si–0.5Cr–0.3Fe–0.1Mn–0.1Ti–0.15Zn) [626], AA6061 (Al–1.2Mg–0.8Si–0.4Cu–0.35Cr–0.15Mn–0.7Fe–0.25Zn–0.15Ti) [627], AA7136 (Al–9.4Zn–2.5Mg–0.12Si–0.15Fe–2.5Cu–0.2Zr–0.05Mn–0.05Cr–0.1Ti) [601,628]) under SPD processing. The fragmentation of the precipitates is exemplified in Fig. 65(a), where the originally thin and flat  $\theta'$  (Al<sub>2</sub>Cu) platelets in an Al alloy are bent and fragmented [595]. The HRTEM image in Fig. 65(b) shows that significant dislocation accumulation at the interphase interface severely distorted the coherency of the interface and caused massive cross slip to shear the large  $\theta'$  platelets into pieces [595].

Distortion of the interface can change the orientation of the precipitate and increase the interfacial energy between the precipitate and the matrix due to the change in the atomic configuration. Fragmentation of the precipitates reduces their aspect ratios. These two conditions favor thermodynamic processes such as dissolution or isotropic growth of precipitates [595,601]. However, only metastable precipitates are prone to dissolution [476,601], while stable/equilibrium precipitates tend to grow under SPD processing by attracting atoms and fragments from the dissolved precipitates [476,601,629]. As a result, the metastable precipitates will shrink in size or diminish while the stable precipitates will become more equiaxed by fragmentation and subsequent isotropic growth.

The increase in flow stress and the pronounced dislocation activities can alter the precipitation kinetics during SPD. For example, an Al–7136 alloy initially has a large amount of GP-zones and a minimal amount of  $\eta$  precipitates. Aging treatment of the alloy for 20 mins results in the

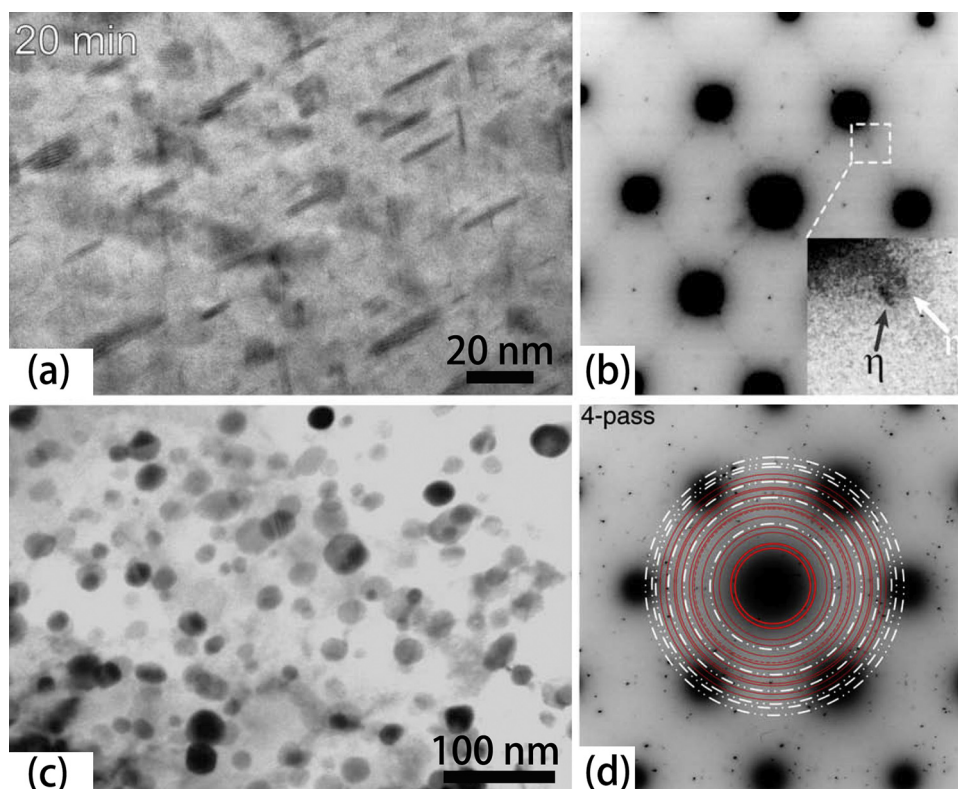


Fig. 66. (a) A bright-field TEM image and (b) a corresponding SAED pattern for the sample thermally aged at 473 K for 20 min; (c) a TEM image and (d) a corresponding SAED pattern for the sample processed by four ECAP passes [601].

formation of  $\eta$  and  $\eta'$  platelet precipitates with high aspect ratios, as shown in Fig. 66(a) [601]. The diffraction pattern in Fig. 66(b) verifies the types of precipitates. (Note that the spherical  $\text{Al}_3\text{Zr}$  particles exist before ageing.) In contrast, the precipitates formed during the ECAP processing are comparatively large and all have the spherical shape. The precipitate number density in the ECAP processed sample is lower than in the simply aged sample. The diffraction pattern in Fig. 66(d) verifies that the precipitates are  $\eta$  phase (white circles), Cu-rich  $\theta$ -phase (red circles) and  $\text{Al}_3\text{Zr}$  phase (unmarked), but  $\eta'$  precipitates are difficult to find. Because the experiment was designed that four ECAP passes corresponds to an effective thermal duration time of 20 min [601], obviously the shear strain imposed by ECAP have changed the precipitation kinetics (significantly promote the formation of equilibrium precipitates), the precipitates orientations, the precipitates shapes and even the precipitate number density.

The underlying physics is explained as follows: (1) Dislocation lines serve as fast diffusion paths for solute atoms in the matrix [630], thereby permitting rapid diffusion to the stable precipitates to assist in their growth [601]; (2) Severe local shear may bring two well-separated precipitates closer together and promote their coalescence [631]; (3) Metastable precipitates may merge with the neighboring stable precipitate, thus the stable precipitates can grow at the expense of the small metastable precipitates.

There are also numerous researches on the precipitation kinetics after SPD processing [7,595,603,608]. It is known that during SPD processing, a large number of dislocations tangled and formed walls, or were absorbed by GBs [57]. During the deformation of an alloy, a large amount of solute atoms could be driven by dislocation slip to the dislocation walls and GBs, causing solute segregation to the boundaries [432,614,628]. GBs can act as heterogeneous nucleation sites for equilibrium precipitates (such as the  $\theta$  phase in Al-Cu alloys [595] and the  $\eta$  phase in the 7075 Al alloy [603]). While a large number of heterogeneous nucleation sites is available in the UFG and nc alloys processed by SPD; During a post-deformation ageing treatment, equilibrium precipitates may heterogeneously nucleate at the GBs, diffusion of solute atoms continuously occurs from the interior of grains to the boundaries to further reduce the content of solute atoms in the grain interior. As a result, precipitation of metastable phases at grain interiors are significantly suppressed due to insufficient solute atoms, but precipitation of equilibrium phases at solute-rich boundaries [595] and nucleation of G-P zones at grain interiors are promoted [603,608]. Moreover, it was also proposed that there is a critical grain size below which the nucleation of G-P zone can also be suppressed [595].

### 7.2.2. Evolution of the matrix during SPD processing

To date, there has been numerous research work on how the precipitates affect the grain refinement of the matrix during SPD processing. Extensive literature survey on relevant work revealed critical controversy on if the existence of precipitates can speed-up or slow down the grain refinement of the matrix.

On one side, a large amount of research work supports the hypothesis that pre-existing precipitates promote matrix refinement. Large-sized (micrometer size) precipitates have large interphase interfaces, therefore precipitates can block a large amount of dislocations. Accumulation of dislocations causes stress concentration at the interface. If the precipitate is non-deformable, a localized deformation zone will be created surrounding the precipitate as a result of stress gradient originated from the interface. Within the deformation zone the rate of dislocation accumulation and GB formation increases [632]. The size of the deformation zone surrounding the precipitate is not large, normally less than the size of the precipitate [633,634]. Therefore, a sufficient high density of large non-deformable precipitates is required to significantly accelerate the grain refinement process of the matrix phase [612,632,634,635].

Some non-deformable precipitates, such as eutectic Si precipitates in the Al matrix, can be brittle [546,636–638]. They could fracture into finer pieces under sufficiently high strain. Although fracture of the particles can relax the stress concentration to a certain extent, the overall grain refinement of the matrix phase is still promoted [639]. Moreover, nano-sized precipitates are also found to promote matrix grain refinement, due to the nature that the precipitates facilitate retention of high dislocation density by pinning dislocations and promoting microband formation (please refer to section 3.1 for details about microbands) [568,640]. In addition, the pinning effect of nano-sized precipitates on GB migration can facilitate the creation of triple junctions [432,611].

On the other hand, many researchers claimed that a large portion of the energy imposed by SPD is used for the fracture, fragmentation and eventual dissolution/growth of precipitates. Therefore, the energy contributing to the grain refinement of the matrix of the alloys is significantly lowered, resulting in a lower rate of grain refinement than in single-phase materials [595,601,604,641,642]. In addition, nano-sized precipitates may retard the grain refinement in two ways: (1) nano-sized precipitates impose resistance forces on dynamic recovery (at cell walls) to delay the development of GNBs [432,643] and (2) formation of microbands are suppressed because nano-sized precipitates help to homogenize slip [612].

Although a final conclusion has not been reached on whether the pre-existing precipitates can promote matrix refinement. Some clues can be found from comparing the work by Shen et al. [611]. and Apps et al. [612]. In the work by Shen et al. [611], a precipitate-containing Al-0.2Sc-0.1 Zr alloy and a commercial pure Al deformed by accumulative continuous extrusion forming are compared. The grain size of the Al matrix is increased from  $\sim 0.8 \mu\text{m}$  to  $\sim 1.8 \mu\text{m}$  as the precipitate size is decreased from  $\sim 100 \text{ nm}$  to  $\sim 50 \text{ nm}$  under the same deformation condition, but the grain size is still smaller than the single phase Al [611].

In the work of Apps et al., the grain size of the Al matrix is larger than a single phase Al alloy with similar composition, when the size of

**Table 5**  
Some representative precipitates and corresponding characteristics.

Precipitate	Precipitate size ( $\mu\text{m}$ )	Precipitate density	Precipitate boundary coherency	Precipitate mechanical property	Precipitate chemical stability	Effect on matrix grain refinement
SiC [645,646]	$\sim 10$	High	Incoherent	Hard & Brittle	Stable	Promote
$\text{Al}_2\text{O}_3$ [637,647]	$\sim 7.5$	High	Incoherent	Hard & Brittle	Stable	Promote
$\text{Al}_{13}\text{Fe}_4$ [632]	$\sim 2$	High	Incoherent	Hard	Stable	Promote
$\text{Al}_6\text{Mn}$ [648]	$> 0.1$	High	Incoherent	Hard	Stable	Promote
$\text{Al}_3(\text{Sc}, \text{Zr})$ [611,649]	$\sim 0.05\text{--}0.1$	High	Semi-coherent Or incoherent	Hard	Stable	Promote
$\text{Al}_3\text{Sc}$ [612,648,650]	$> 0.03$	High	Coherent	Hard	Stable	Retard
$\text{Al}_2\text{Cu}$ $\theta'$ [595]	0.01-0.6	High	Coherent	Soft	Metastable	Retard
$\text{MgZn}_2$ [601,603,642]	1-40 or 100-500	High	Semi-coherent ( $\eta'$ ) or Incoherent ( $\eta$ )	Soft & Brittle	Metastable ( $\eta'$ ) or Stable ( $\eta$ )	Retard
$\text{Al}_3\text{Zr}$ [601,642]	0.01	High	Coherent	Hard	Metastable	Retard

the precipitate is as small as  $\sim 20$  nm [612]. Two brief conclusions can be drawn from these experimental results: firstly, the effect of precipitates on promoting grain refinement decreases with decreasing the size of the precipitates; secondly, there may exist a critical precipitate size below which the precipitates no longer promote grain refinement but impede grain refinement. If the effect of precipitates on grain refinement is explored in more details, it can be noticed that the characteristics of precipitates may have determinative effect on the microstructural evolution of the matrix during SPD. According to Table 5, a high density of chemically stable precipitates with large sizes and incoherent interfaces will promote grain refinement of the matrix. The chemically stable coherent precipitates with sizes below 50 nm will impede grain refinement of the matrix. For these metastable precipitates, they tend to impede matrix grain refinement while the size of the precipitates is less relevant (This might be because the concentration of alloying elements in the matrix plays a more dominant role [432,626,644]). Each of the characteristics may promote or impede the grain refinement to certain extent, but the apparent effect has to be a combination of all.

## 8. Effect of SPD on mechanical properties

SPD can impose a shear strain far beyond the strain level attainable by conventional shaping and forming methods such as rolling, drawing and extrusion. As a result, bulk metallic materials can be processed to achieve nanostructures that possess mechanical properties that expand known performance boundaries [7,9,608,651,652], as exemplified in Fig. 67 [653]. Despite of different crystalline structures, both ns Ti and ns Cu possess combined tensile strength and ductility beyond the region (the shadowed area in Fig. 67) of conventionally processed materials. The mechanical properties of SPD processed materials are governed by microstructures and the intriguing cooperation of deformation mechanisms, which are related to the intrinsic characteristic properties of materials and processing conditions. However, materials are intrinsically different due to different crystal structures, solute contents, phase contents, and starting grain structures, etc. These intrinsic differences between materials have led to obviously different microstructural evolutions, as discussed earlier. The effects of SPD processing on the mechanical properties are also expected to vary significantly from one material to another. Therefore, it is easy to realize that the outstanding combination of mechanical properties such as that exemplified in Fig. 67 is not universal to all SPD processed materials. It is therefore critical to understand the mechanisms that leads to outstanding combination of strength and ductility in some SPD processed materials. This section reviews the most important aspects of the mechanical properties of SPD processed materials in relation to materials' intrinsic characteristics and strengthening mechanisms.

### 8.1. The effect of SPD processing on strength

Four major mechanisms are frequently used for strengthening metallic materials: (1) strain hardening, which is also called work hardening; (2) GB-strengthening, which is realized through grain size reduction; (3) solid solution strengthening; and (4) precipitation strengthening [29,126,151,160,163,164,315,654]. The effects of various strengthening mechanisms are often treated additive [23,655–657], as expressed by equation [658] (for readers' convenience, the parameters used in Eqs. (4)–(12) for describing the strengthening mechanisms are summarized in Table 6):

$$\sigma_y = \sigma_0 + \Delta\sigma_d + \Delta\sigma_{HP} + \Delta\sigma_{ss} + \Delta\sigma_p \quad (4)$$

Nevertheless, factors including crystal structure and SFE of materials also have a significant impact on some of the strengthening effects. In addition, these strengthening factors could mutually affect each other, but this is not well studied and is generally ignored. Therefore, Eq. (4) should be treated as an empirical equation. This section begins

with an in-depth review on the effect of SPD processing on the strength of materials in relation to the four major mechanisms.

#### 8.1.1. The effects of strain hardening and grain size reduction

All bulk metallic materials processed by SPD underwent tremendous dislocation activities, which led to significant increase of dislocation density and subsequent grain refinement [80,127,136,150,159,162]. Thus, strain hardening and GB-strengthening (grain size reduction) are two fundamental strengthening mechanisms and are closely connected throughout the microstructural evolution process. Strain hardening from dislocation accumulation dominates at the early stages of SPD. The strength increment caused by strain hardening can be related to the total dislocation density ( $\rho_t$ ) using the Bailey–Hirsch relationship [160,162,460,664]:

$$\Delta\sigma_d = M\alpha_T b G \sqrt{\rho_t} \quad (5)$$

It is worth to mention that as the grain size is reduced to the UFG regime a dislocation source-limited hardening mechanism may be operative, thus a higher stress is required to activate alternative dislocation sources [657,665].

The strength increment caused by GB-strengthening and/or TB-strengthening can be described using the famous empirical Hall–Petch relationship [16,660,666–668]:

$$\Delta\sigma_{HP} = k_{GB} D_B^{-1/2} + k_{TB} \lambda_{TB}^{-1/2} \quad (6)$$

The two terms in Eq. (6),  $k_{GB} D_B^{-1/2}$  and  $k_{TB} \lambda_{TB}^{-1/2}$  are used to describe strength contribution due to the resistance to dislocation motion caused by the presence of GBs and TBs, respectively [16,666,669]. It has been proposed that TBs are just as effective in blocking dislocation slip as GBs are, so  $k_{GB} = k_{TB}$  is normally accepted. Thereby, if twins are not present in the microstructure (in materials with high SFEs), the term  $k_{TB} \lambda_{TB}^{-1/2}$  is then redundant. However, in materials with low SFEs where deformation twinning takes an important part and the TB-spacing is normally one order of magnitude smaller than that of GB-spacing, TB-strengthening makes the major contribution to the strengthening effect [233,668,669]. In addition, the obstacle nature of GBs increases with impurity concentration along the GBs. Therefore, the Hall–Petch coefficient  $k_{GB}$  increases with the increasing content of alloying elements [662,670].

For experimental convenience, the strengthening effect of SPD processing is often evaluated by measuring the hardness of the processed materials [126], because it is widely accepted that hardness is

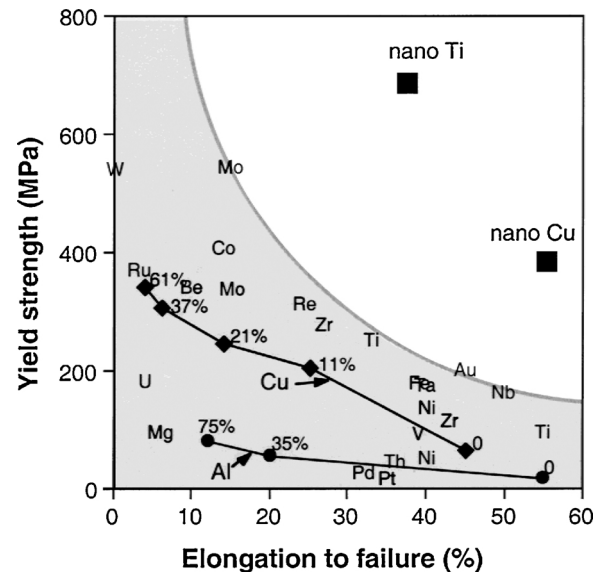
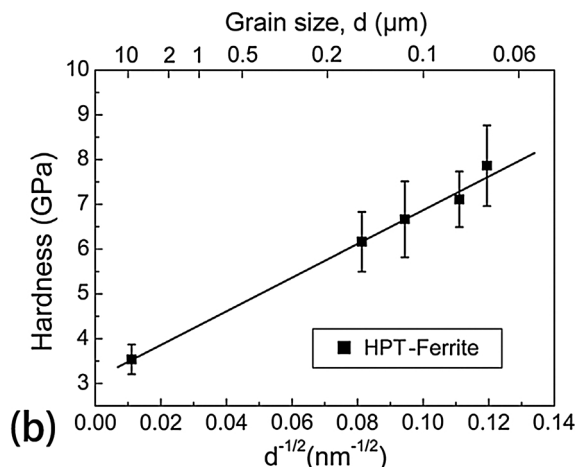
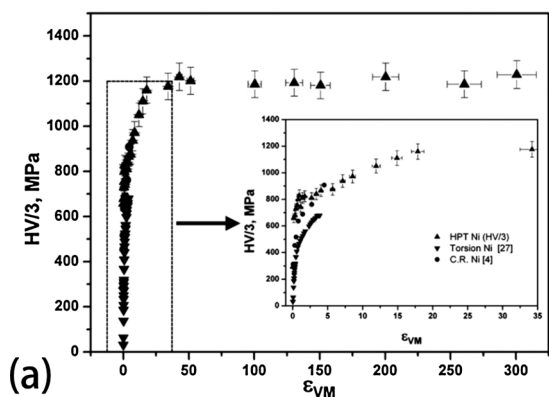


Fig. 67. Extraordinary combination of high strength and high ductility of SPD-processed ns Cu and Ti as compared with those of CG metals [653].

**Table 6**  
Physical meaning and units of different symbols used in the strengthening mechanisms [16,659–663].

Symbol	Meaning	Unit
$\sigma_y$	Yield strength (overall strength)	MPa
$\sigma_0$	The lattice friction stress	MPa
$\Delta\sigma_d$	Dislocation strengthening	MPa
$\Delta\sigma_{HP}$	GB and/or TB strengthening	MPa
$\Delta\sigma_{ss}$	Solid solution strengthening	MPa
$\Delta\sigma_p$	Precipitate strengthening	MPa
$M$	Mean orientation factor	Dimensionless
$\alpha_T$	A constant in the range of 0.3–0.5 depending on temperature	Dimensionless
$b$	Burgers vector	nm
$G$	Shear modulus	GPa
$\rho_t$	Total dislocation density	$m^{-2}$
$k_{GB}$	Hall–Petch coefficient for GB strengthening	$MPa/\sqrt{m}$
$k_{TB}$	Hall–Petch coefficient for TB strengthening	$MPa/\sqrt{m}$
$D_B$	Average grain size	nm
$\lambda_{TB}$	Average TB spacing	nm
$\epsilon_{ss}$	Interaction parameter that accounts for the local resistance to dislocation propagation	Dimensionless
$c$	Concentration of solute atoms	wt.%
$\nu$	Poisson ratio	Dimensionless
$\bar{r}$	Mean radius of a cross-section in a random plane for a precipitate	nm
$r$	Mean radius of the precipitates	nm
$\lambda_p$	Mean edge-to-edge inter-precipitate spacing	nm
$\alpha_c$	A constant between 2 and 3	Dimensionless
$\epsilon_c$	Constrained lattice parameter misfit	Dimensionless
$m$	An exponent estimated to be 0.85	Dimensionless
$f$	Volume fraction of the precipitates	Vol.%
$\gamma_{apb}$	Antiphase boundary free energy of the precipitate phase	$J/m^2$

proportional to strength [42,671]. Fig. 68(a) [126] presents the relationship between flow stress and von Mises Strain ( $\epsilon_{VM}$ ) for Ni processed by different plastic deformation methods. The flow stress was estimated to be 1/3 of its hardness [671,672]. It is seen from Fig. 68(a) that significant hardening took place at low to medium strains and quickly leveled off at high strains where the strain hardening and GB-strengthening effects diminished. Despite of different deformation methods (cold rolling, torsion and HPT) conducted, the hardening rates were very similar at low strains as shown in the insert in Fig. 68(a). Fig. 68(b) presents an example showing the Hall-Petch type hardening in the ferrite phase in an HPT processed austenite-ferrite duplex steel. The hardness (measured by nano-indentation) increased linearly as a function of  $d^{-1/2}$  from ~3.4 GPa to ~8 GPa. Therefore, one can



**Fig. 68.** (a) The estimated stress–strain relationship for a pure Ni deformed by HPT, cold-rolling and torsion [126]; (b) hardness vs. the inverse square root of grain size of ferrite [228].

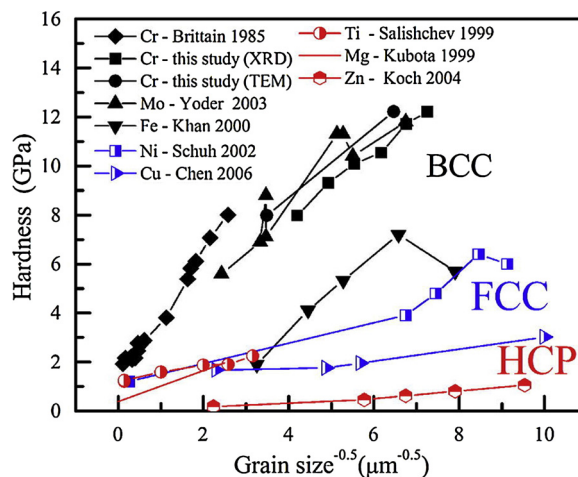


**Fig. 69.** Comparison of the Hall–Petch relationship in BCC, FCC and HCP materials [674].

conclude that different strain paths have little influence on the strain hardening and GB-strengthening effects [126].

**8.1.1.1. The influence of crystal structure on the SPD-induced strengthening.** While both strain hardening and GB-strengthening are fundamental and universal to all SPD processed metallic materials, there are also noticeable differences in the responses of materials with different crystal structures to the strain hardening and GB-strengthening effects. It was found that GBs in BCC materials are more efficient in blocking dislocation slip than that in the FCC and HCP materials [673,674]. This phenomenon is thus reflected by higher Hall–Petch coefficient (the slope of the trend line) in BCC metals (black symbols) than in FCC (blue symbols) and HCP (red symbols) metals, as shown in Fig. 69 [674]. Based on the relationship between the stress concentration and the critical shear stress for the activation of dislocation sources [666], the Hall–Petch coefficient is a function of the Taylor factor ( $m_f$ ), the shear modulus ( $G$ ), Burgers vector ( $b$ ), the Sachs orientation factor ( $m_s$ ) and Poisson’s ratio ( $\nu$ ), as expressed by equation:

$$k_1 = 3m_f \left( \frac{\pi m_s \tau_c G b}{4(1-\nu)(2-\nu)} \right)^{1/2} \quad (7)$$

Most importantly, the Hall–Petch coefficient is governed by  $\tau_c$ , which is the CRSS for dislocation nucleation from GBs or the CRSS necessary to propagate plastic flow across GBs. In general,  $\tau_c$  for BCC

metals is significantly larger than that for FCC and HCP metals [674–677]. Therefore, BCC materials tend to have larger Hall–Petch coefficients than FCC and HCP materials.

Due to the low level of symmetry of HCP structures, the strain hardening and GB-strengthening effects in HCP materials differ significantly with respect to different textures. When the majority of refined grains are oriented for hard slip (grains with basal planes nearly perpendicular to the stress direction), HCP materials would exhibit a high GB-strengthening effect (i.e., a high Hall–Petch coefficient) [383,674,678]. The significant texture effect on the strength of HCP materials leads to significant flow stress anisotropy. Although SPD processing can effectively reduce the grain size to the lower bound of the UFG regime, texture and microstructural inhomogeneity may still present due to the unique deformation mechanisms of HCP materials under shear stress [323,347,374]. Therefore, the flow stress anisotropy is still evident [372,679–681]. In addition, Meredith and Khan conducted a systematic research on the flow stress anisotropy of UFG Ti. They found that the flow stress anisotropy of HCP Ti (perhaps many other HCP materials as well) is insensitive to deformation temperature, when homologous temperature is below  $\sim 0.33$  [65,316,355].

The low symmetry of the hexagonal crystal structures and the consequent lack of an adequate number of independent slip systems significantly deteriorate the plasticity of HCP materials [64,75,76]. Even for a CG HCP material in which sufficient space seems available for dislocation accumulation, it may still quickly fail under a conventional plastic deformation process. For example, in CG Mg and Mg alloys, basal slip facilitates microscopic yielding at very low stresses. Meanwhile, strong yield anisotropy in Mg and Mg alloys prevents a large number of basal dislocations from slipping, and rapidly increases stress concentration at GBs and triple junctions to a high level [343,682]. In order to accommodate further deformation, other slip systems and deformation mechanisms have to be activated especially at GBs and triple junctions, such as  $\{10\bar{1}2\}$  tension twins, which are very common in CG Mg alloys at low strain [683,684]. When a large number of propagating twins interact with GBs, high stress concentration may develop in the nearby regions of the adjacent grains. Subsequently cracks initiate at the stress concentration sites [64,353,683]. As a result, at room temperature a CG Mg only has a very limited plasticity and quickly fail after reaching a low UTS value.

Fig. 70 shows the compressive stress–strain curves for Mg samples with different grain sizes. The Mg samples were processed by ECAP for four passes at room temperature, 100 °C, 150 °C, and 200 °C, leading to average grain sizes of 0.8  $\mu\text{m}$ , 2  $\mu\text{m}$ , 4  $\mu\text{m}$ , and 7  $\mu\text{m}$ , respectively. The as-cast Mg sample with an average grain size of  $\sim 980 \mu\text{m}$  had a very low yield strength of 13 MPa and failed at a compressive strain of  $\sim 7\%$ . When the average grain size was reduced to  $\sim 7 \mu\text{m}$ , both the strength and plasticity of Mg were improved significantly. As the grain size of Mg was reduced further to an average of  $\sim 4 \mu\text{m}$  and  $\sim 2 \mu\text{m}$ , the UTS of samples were about three times higher than that of the as-received sample but with poor ductility. Further reducing the average grain sizes to 0.8  $\mu\text{m}$  resulted in a very high yield strength, short-lived strain hardening and prolonged constant compression true stress [652,685–687].

Overall, the observed improvement of mechanical properties of the commercial purity Mg with decreasing grain size can be summarized as follows: (1) grain size reduction leads to GB-strengthening. (2) Grain size reduction leads to the increase of the number of randomly oriented grains, which helps to reduce the flow stress anisotropy. (3) Grain size reduction increases the number of GBs to help dissipate stress concentration [343,368,369,688]. (4) Grain size reduction to the UFG regime may significantly suppress deformation twinning, meanwhile the density of dislocations with c-component increases to meet the von Mises criterion [343,390,395,399,401,403,685]. (5) Mg has a low homologous temperature. As the grain size is reduced to the UFG regime, temperature sensitive deformation mechanisms such as GB sliding, GB diffusion and dynamic recrystallization can be conspicuous

even at room temperature. Thus, the combined effect of many deformation mechanisms can cause significant changes to the rate of strain hardening and the plastic instability [404,689–691].

**8.1.1.2. The influence of stacking fault energy on the SPD-induced strengthening.** SFE is a major intrinsic materials property that poses a strong effect on the deformation mechanism, SPD-induced microstructural evolution [90,95,96,102,184], and thus the mechanical properties [90,154]. Dislocation slip is the major deformation mechanism in materials with medium to high SFEs. Thus, SPD-induced microstructural evolutions follow the general pattern of grain subdivision by dislocation activities on a finer and finer scale [125–127]. Lowering SFE changes the deformation mode from full dislocation activities to extended dislocation (a stacking fault bounded by two partial dislocations) activities and deformation twinning. This leads to an increased defect (dislocation and twin) density, accelerated grain refinement and thus a higher work hardening rate than materials with high SFEs, because the deformation induced twins are normally very thin and effective in trapping dislocations [95,105,184].

As shown in Fig. 71 [418], a series of materials with different SFEs (the estimated SFEs of Al, AA 6061 (Al-1.2Mg-0.8Si-0.4Cu-0.35Cr-0.15Mn-0.7Fe-0.25Zn-0.15Ti), Cu, Cu4.6Al, Cu9Al and Cu15Al are 166 mJ/m<sup>2</sup>, 150 mJ/m<sup>2</sup>, 55 mJ/m<sup>2</sup>, 25 mJ/m<sup>2</sup>, 13 mJ/m<sup>2</sup>, and 6 mJ/m<sup>2</sup>, respectively) were plastically deformed by rolling at room temperature and cryogenic temperature. The increase in hardness with increasing strain reflects the hardening effect in the tested materials. It is noticed that the hardness and the work hardening rate of the materials increase with decreasing SFE. For the same material, if the dominant deformation mechanism changes from dislocation slip (Cu4.6Al at room temperature) to twinning (Cu4.6Al at cryogenic temperature) (low temperature promotes twinning [59,73]), the hardness and the work hardening rate increase. This indicates the important role of deformation mechanisms in affecting the mechanical properties of materials [92,169,186].

Despite of different deformation mechanisms operating during SPD processes, the hardness/strength of materials increases and eventually saturates [29,150]. Materials with low SFEs tend to have prolonged hardening stage and higher saturation hardness than materials with high SFEs, as shown in Fig. 72 [184]. It is believed that increased twinning activities are the major reason for the improved strength/hardness of FCC materials with low SFEs, because (1) TBs are effective in blocking dislocations [668]; (2) the low energy nature of coherent TBs provides a high dislocation storage capacity [91,458]; and (3) nano-twins can transform into nano-crystallites of sizes that are not achievable by sole dislocation activities [87].

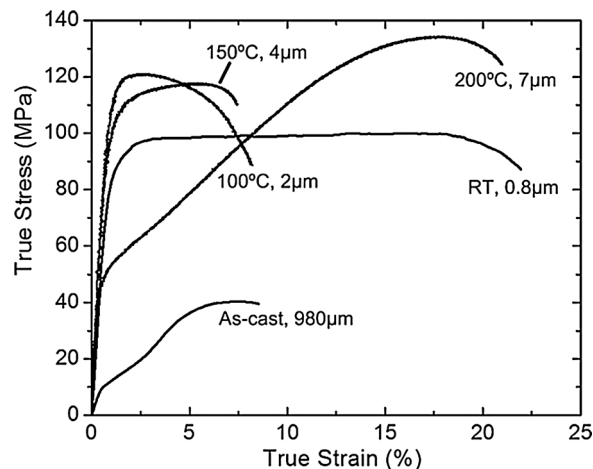


Fig. 70. Compressive true stress–true strain curves for Mg samples with different grain sizes [403].

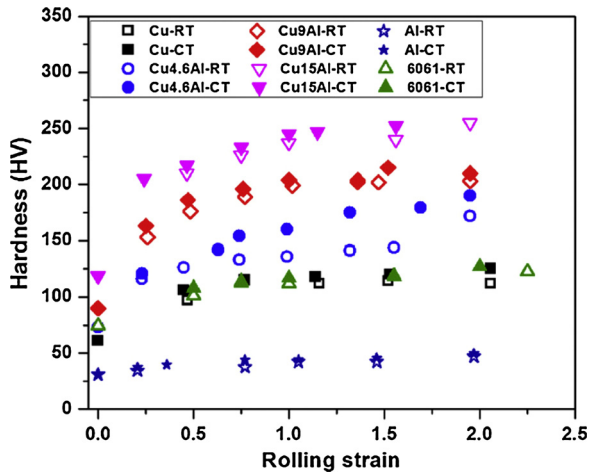


Fig. 71. A plot of hardness vs. rolling strain in Cu–Al, Al and AA-6061 alloys processed by rolling at room and cryogenic temperatures [418].

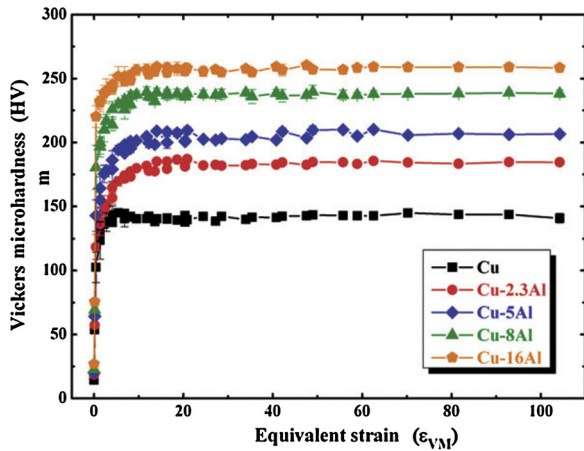


Fig. 72. A plot of microhardness vs. equivalent strain in Cu, Cu-2.3Al, Cu-5Al, Cu-8Al and Cu-16Al alloys processed by HPT [184].

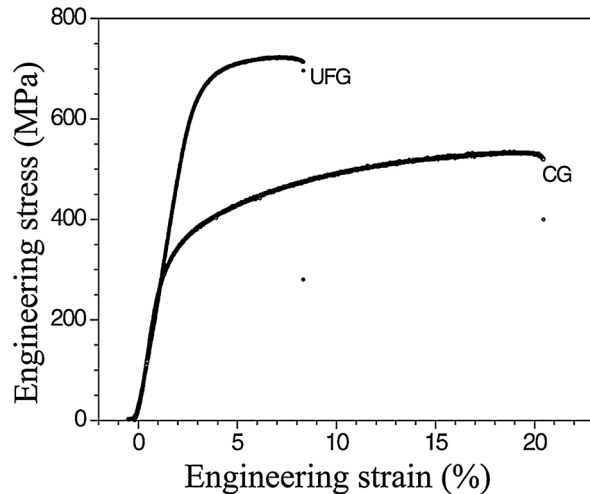
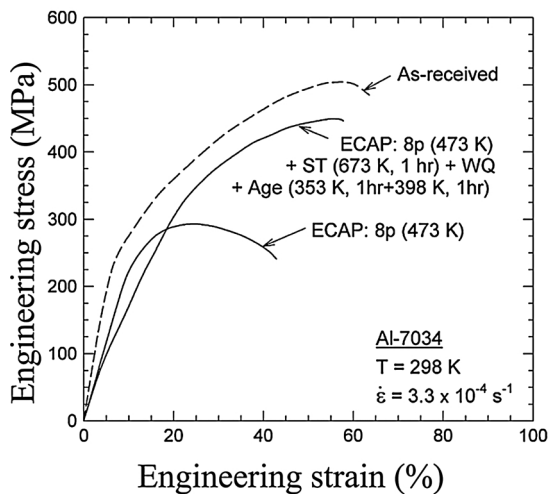


Fig. 73. (a) Tensile engineering stress-strain curves for Al-7034 in the as-received condition, after 8 ECAP passes followed by a solution treatment for 1 h at 673 K with water quenching and an ageing treatment for 1 h at 353 K and 1 h at 398 K [642]; (b) tensile engineering stress-strain curves for UFG and CG Al-7075 (Both samples were naturally aged at room temperature for one month) [603].

8.1.2. The effects of solid solution and precipitation on the strength of SPD processed materials

In alloys, the variation between the atomic radius of different elements introduces local strain fields that provide additional resistance to dislocation slip on top of the lattice friction, leading to solid solution strengthening. The solid solution strengthening effect is governed by the Fleischer equation [692,693]:

$$\Delta\sigma_{ss} = MGb\epsilon_{ss}^{3/2} \sqrt{c} \tag{8}$$

Some studies suggested change the power of  $c$  from  $\frac{1}{2}$  to 1 for ns materials with an average grain size < 30 nm [663]. Thereby, care shall be taken when using the Fleischer equation to estimate the solid solution strengthening effect of materials with extremely small grains.

Precipitates can effectively block dislocation slip by providing additional boundaries in the metal matrix. Precipitates can form in supersaturated solid solution through aging treatment. Therefore, some alloys can be further strengthened by the precipitation strengthening effect on top of the solid solution strengthening effect. Precipitation strengthening is one of the most important materials strengthening effect, and has been extensively investigated and practiced in the last 100 years. Readers are referred to the review papers on precipitation strengthening by Kelly and Nicholson [694] and by Ardell [659]. As mentioned in Section 7, dislocations may interact with precipitates in different ways depending on the atomic mismatch between precipitates and the matrix. For precipitates, e.g. the  $\eta$  phase precipitates that are incoherent with their Al matrix [601], the Orowan dislocation bypassing mechanism might govern the precipitation strengthening effect [695–697]. Thus, the strength increment ( $\Delta\sigma_{orowan}$ , governed by the Orowan dislocation bypassing mechanism) added by precipitation strengthening is expressed as [661]:

$$\Delta\sigma_p = \Delta\sigma_{orowan} = M \frac{0.4Gb}{\pi\sqrt{1-\nu}} \frac{\ln(\frac{2r}{b})}{\lambda_p} \tag{9}$$

On the other hand, for precipitates, e.g. coherent GP zones [601] and semi-coherent  $\theta'$  ( $Al_2Cu$ ) precipitates in Al alloys [595], a precipitate shearing mechanism might govern the interactions between dislocations and precipitates. The precipitation strengthening effect governed by the dislocation shearing mechanism is determined by the choice of three specific strengthening effects: (1) coherency

strengthening ( $\Delta\sigma_{cs}$ ), (2) modulus mismatch strengthening ( $\Delta\sigma_{ms}$ ) and (3) order strengthening ( $\Delta\sigma_{os}$ ).

$$\Delta\sigma_{cs} = M\alpha_c(G\varepsilon_c)^{3/2}\left(\frac{r_f}{0.5Gb}\right)^{1/2} \quad (10)$$

$$\Delta\sigma_{ms} = M0.0055(\Delta G)^{3/2}\left(\frac{2f}{G}\right)^{1/2}\left(\frac{r}{b}\right)^{\frac{3m}{2}-1} \quad (11)$$

$$\Delta\sigma_{os} = M0.81\frac{\gamma_{apb}}{2b}\left(\frac{3\pi f}{8}\right)^{1/2} \quad (12)$$

The larger of  $\Delta\sigma_{cs}$ ,  $\Delta\sigma_{ms}$  or  $\Delta\sigma_{os}$  is responsible for the strength increment from precipitation strengthening governed by the dislocation shearing mechanism [658].

Once the strength increments are evaluated by Eqs. (9)–(12), a comparison between the estimated values has to be made to determine the actual governing mechanism. When choosing between the Orowan dislocation bypassing mechanism [568,698,699] and dislocation shearing mechanism [700], the one causing a smaller strength increment is thought to be the operative mechanism [658,661].

The high shear strain and stress imposed by SPD processing can alter the solubility of alloying elements and thus change the state of solid solution of an alloy [478]. The SPD-induced variation of the solubility of impurities combined with extensive defect activities may result in the dissolution of preexisting precipitates [476,508,622,623] and segregation [475,613,614,628] or redistribution of solute atoms [476,701,702]. The increased solute content within the base materials may cause additional elastic interactions between dislocations and solute atoms, thus improve the overall solid solution strengthening effect [432,478,630]. However, the increased solid solution strengthening effect might be achieved at the expenses of preexisting precipitates [478]. Thus for alloys containing precipitates, SPD processing may or may not benefit the mechanical properties of the materials, depending on the resulting microstructures [603,642,703]. As shown in Fig. 73(a), ECAP processing of an Al-7034 alloy at 473 K reduces both the strength and ductility [642]. When the ECAP-processed sample is aged to increase the number of precipitates, both the strength and ductility can be improved. The reduction in strength by SPD processing is due to the strain induced dissolution of the hardening  $\eta$ -phase precipitates and a transformation of  $\eta$  into  $\eta$  under subsequent coalescence process [601]. The number of precipitates available to impede the motion of intragranular dislocations is significantly reduced and thus there is an inherent weakening of the material. Although additional solid solution strengthening and grain size reduction of the matrix can increase the strength, it is not enough to compensate for the strength reduction due to the reduction in the density of precipitates.

For another example shown in Fig. 73(b), the tensile yield strength and UTS of the UFG Al-7075 alloy are 650 and 720 MPa, respectively, which are ~103% and ~35% higher, respectively, than those of their CG counterparts. The elongation to failure of the UFG sample is ~8.39%, which is still adequate for many potential industrial applications. Different from the Al-7034 case in Fig. 73(a), the UFG Al-7075 alloy in Fig. 73(b) was aged to have a higher density of precipitates than the CG Al-7075 alloy. Therefore, the UFG sample has a higher strength

than the CG sample. Overall, the improved strength of the UFG 7075 Al alloy can be attributed to: (i) GB-strengthening, (ii) strain hardening (dislocation strengthening) (iii) solid solution strengthening and (iv) precipitation strengthening.

A straight forward illustration of the combined effect of the four strengthening mechanisms is exemplified in Table 7 [661]. UFG-7075-E represents a consolidated 7075 Al alloy made from as-cryomilled 7075 Al alloy powder, which went through degassing plus hot isostatically press plus extrusion. UFG7075-E-T6 represents a UFG7075-E sample subsequently treated by solution heat treatment and quenched in ice water, and then treated by artificial ageing at 120 °C in air for 24 h. CG7075-E represents a consolidated CG 7075 Al alloy made from as-received gas atomized powder, which went through degassing plus hot isostatically press plus extrusion. CG7075-E-T6 represents CG7075-E sample subsequently treated by solution heat treatment and quenched in ice water, and then treated by artificial ageing at 120 °C in air for 24 h. All four samples possess yield strengths which were attributed to the abovementioned four strengthening mechanisms. The estimated yield strength by summation of the calculated strength increments is very close to the experimental values, verifying the reliability of Eqs. (4)–(12).

It is worth to emphasize that among the four strengthening mechanisms, precipitation strengthening is unique compared to single phase alloys, because precipitates can significantly hinder dynamic recovery and block dislocation slip to provide additional strengthening effect on top of the grain refinement of the matrix [7,603].

### 8.1.3. The effect of different stages of SPD processing on the strength/hardness of nanocrystalline materials

The SPD-induced grain refinement has a limit in the achievable minimum average grain size at the steady state. This is determined by both intrinsic materials properties and extrinsic processing parameters [211,298]. The intrinsic materials properties include SFE, bulk modulus, melting temperature, and activation energy for recovery. If the starting material has an average grain size smaller than the steady state grain size, SPD can induce grain growth [437,439,440,442,443]. The SPD-induced grain growth process is accompanied with the evolutions of grain size, dislocation density and twin density, which play important roles on the mechanical properties of the materials [197,199,428,438,457,704–706] (readers can refer to section 4).

A unique hardness evolution process was revealed during the HPT-induced grain growth process of an nc Ni-Fe alloy as shown in Fig. 74 [456,707]: strain hardening occurred at the initial stages of deformation (under the increasing strain from 0 to ~20 as shown in Fig. 74(a)), followed by a strain softening (within the strain range between ~20 and ~35 as shown in Fig. 74(b)), a subsequent further strain hardening (within the strain range between ~35 and ~45 as shown in Fig. 74(b)) before a plateau was reached, and a strain softening again (as the shear strain is further increased from ~45 to ~340 as shown in Fig. 74(c)). The two strain hardening stages are accompanied by an increase in the dislocation density. The strain softening stage between the two hardening stages is associated with a decrease in the dislocation density. The effect of HPT-induced grain growth and twin density evolution on the

**Table 7**

Yield strength and estimated strength increments contributed by different strengthening mechanisms, for 7075 Al alloys processed under different conditions [661].

Strength (MPa)	UFG-7075-E	UFG-7075-E-T6	CG-7075-E	CG-7075-E-T6
$\sigma_0 + \Delta\sigma_{HP}$	242	185	127	120
$\Delta\sigma_d$	99	95	61	35
$\Delta\sigma_{ss}$	<82	<<82	<82	<<82
$\Delta\sigma_p$	45	414	102	472
Total estimated yield strength	<468	<<776	<372	<<709
Total experimental yield strength	583	734	283	613

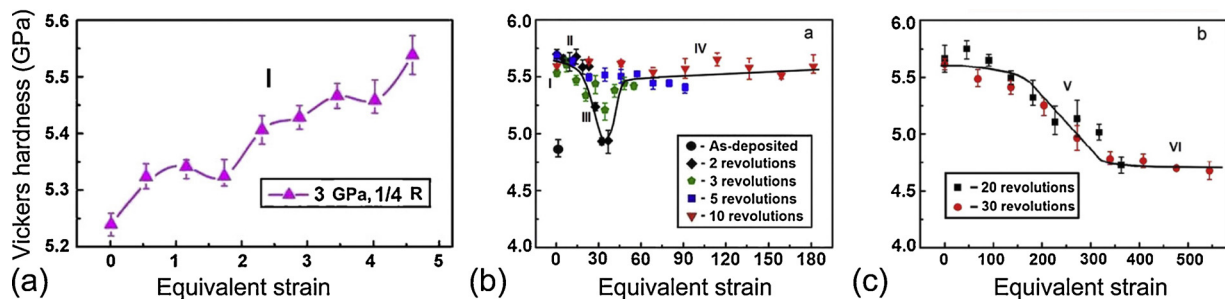


Fig. 74. Vickers hardness plotted against von Mises equivalent strain for disks processed by HPT for (a) 1/4 revolutions [456], (b) 2, 3, 5, and 10 revolutions [707], and (c) for 20 and 30 revolutions [707].

hardness is overwhelmed by the stronger role of the dislocation density at these stages [707]. However, the second strain softening stage is primarily controlled by the grain growth, while other structural evolutions play minor role on the hardness evolution [442]. Finally, a stable hardness stage is achieved, which is associated both with an average grain size at or close to the steady state grain size of an HPT-induced grain growth process and with a constant dislocation density. It is therefore proposed that the steady state achieved in this stage is the result of balance between deformation-induced grain growth and grain refinement, and between deformation-induced dislocation generation and dislocation annihilation. During the SPD-induced grain growth process, the grain size increased monotonously from  $\sim 20$  nm to  $\sim 120$  nm, while the hardness changed in an undulating manner. This indicates that the conventional Hall-Petch type strengthening effect loses dominance in the nc regime [218,667,668,708].

#### 8.1.4. The strain softening effect of SPD-processed BCC materials

The strain rate sensitivity of ns BCC materials decreases with decreasing grain size, which is opposite to the behavior of ns FCC and HCP materials [295,360,709–715]. The strain rate sensitivity  $M_s$  can be expressed using the following equation [295]:

$$\frac{1}{M_s} = \frac{\partial \ln(\rho_s v_s + \rho_e v_e)}{\partial \ln \tau} \quad (13)$$

where  $\tau$  is the flow stress;  $\rho_s$  and  $v_s$  are the density and speed of screw dislocations, respectively;  $\rho_e$  and  $v_e$  are the density and speed of dislocations with edge components (edge and mixed dislocations), respectively. Due to the non-planar nature of the core of screw dislocations in BCC materials, screw dislocations experience very high lattice friction [269]. Thus, screw dislocations have much lower mobility than edge dislocations ( $v_s \ll v_e$ ) [63]. As the grain size decreases from the CG regime to the nc regime, the deformation mechanism changes from screw dislocation dominance to edge and mixed dislocation dominance. Consequently, the strain rate sensitivity of BCC materials decreases with decreasing grain size.

It is well-known that CG BCC materials are notoriously resistant to shear banding because of the dominance of screw dislocations and the unique screw dislocation core structure. However, UFG and nc BCC materials are prone to shear banding [241,246,262], due to the lack of strain hardening and effective strain rate hardening [685]. Thus all SPD-processed BCC materials show strain softening when deformed by dynamic compression. As shown in Fig. 75, the stress–strain curves of UFG W deformed by dynamic compression revealed obvious strain softening soon after yielding. It is worth to note that CG W exhibited brittle failure. However, as shown in Fig. 75, UFG W can deform plastically without strain hardening under quasistatic loading, resulting in nearly flat true stress–strain curves after yielding [240,360].

#### 8.2. The effect of SPD processing on ductility

Most SPD-processed materials have very high strength but

unsatisfactory ductility [29,30]. Only a few materials processed by SPD are observed to have both high strength and decent ductility [7,9,608,651–653]. An increasing number of work showed that combining SPD and other processing, e.g. subsequent heat treatment of materials could lead to both high strength and good ductility [6,651,716–719]. The outstanding mechanical properties of these reported materials are attributed to some specific microstructural architectures. Therefore, it is crucial to discuss the micro/nanostructures that are beneficial to ductility.

Ductility, which is the plastic tensile strain of materials at failure, is significantly affected by microstructure. Ovid'ko et al. recently published an extensive review on the ductility of ns materials [404]. The primary reason for the low ductility is low strain hardening capability, which leads to localized plastic strain instability (necking). Thus, micro/nanostructures that provide additional strain hardening capability to delay localized plastic strain instability is critical for ductility. Another approach for improving ductility is to increase the strain rate sensitivity, but this is often negligible for most materials because their strain rate sensitivity is often very small at room temperature [404]. However, this may change for materials with low melting temperatures, where room temperature represents relatively high homologous temperature.

Thoughtful design and careful SPD processing of materials to gain hierarchical nanostructures is one way to achieve outstanding combination of strength and ductility. HPT processing of a commercial 7075 Al alloy led to a record breaking yield strength of above 1 GPa, which is about twice the strength of a standard T6 ageing treated 7075 Al alloy (note: T6 aging treatment is achieved by homogenizing the cast 7075 Al alloy at 450 °C for a designated period of time, quenching, and then aging at 120 °C for 24 h [720]), while maintaining a decent uniform elongation of  $\sim 5\%$  and ductility of  $\sim 9\%$  (Fig. 76(a)) [9]. The outstanding mechanical properties of the HPT-processed 7075 Al alloy are

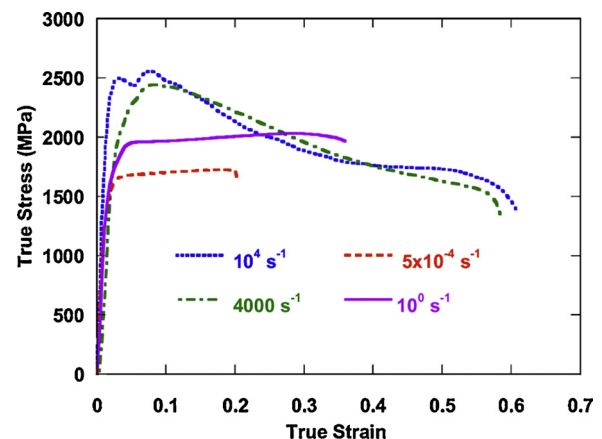
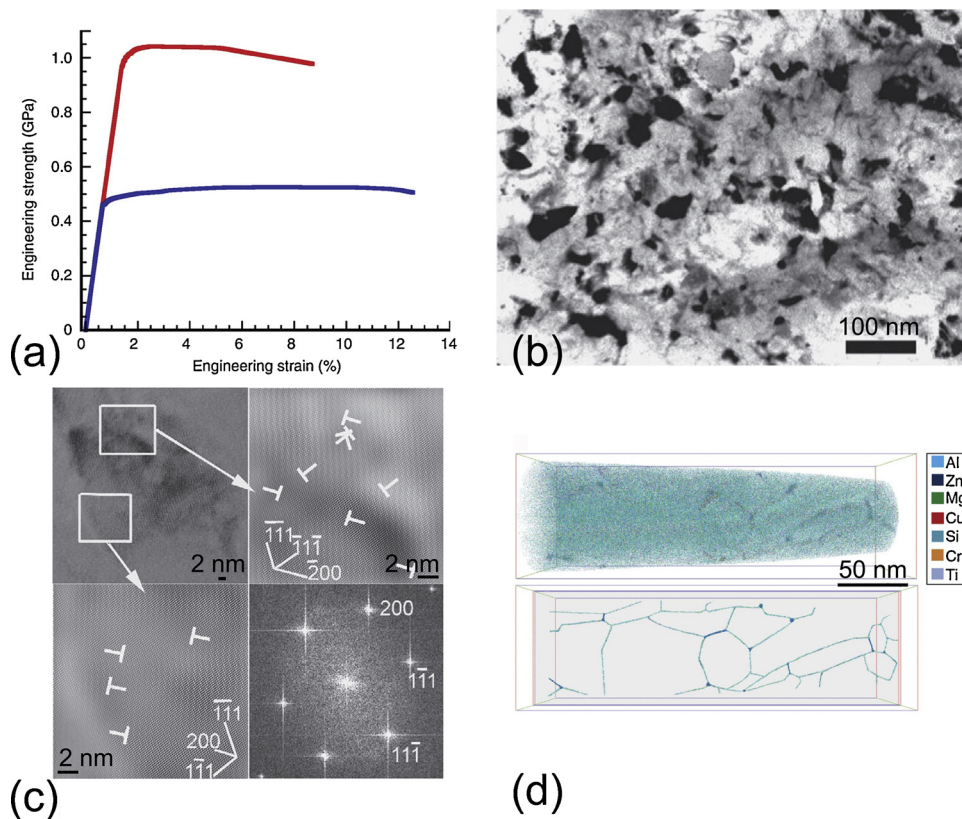


Fig. 75. True stress–strain curves of UFG W under compression. The loading rates are provided in the figure [245].



**Fig. 76.** (a) Engineering stress – strain plots for the HPT-7075 (red curve) and T6-7075 (blue curve) alloys; (b) a TEM image showing nano-grains in the HPT-7075 alloy; (c) HRTEM images showing a high density of dislocations at the interior of a nano-grain. Two magnified inverse Fourier transformation images are provided for better illustration of the dislocations marked by “T”. The diffraction pattern indicates the absence of precipitate. (d) The upper image is an atom probe tomography map of a specimen of the 7075 Al alloy with nanostructure hierarchies; The lower image reveals solute aggregation along GBs [9] (For interpretation of the references to colour in this figure legend, the reader is referred to the web version of this article.).

attributed to the resultant hierarchical nanostructure featuring (i) grain sizes of tens of nanometres (Fig. 76(b)), (ii) a high density of dislocations (Fig. 76(c)), (iii) subnanometre intragranular solute clusters (Fig. 76(d)), and (iv) two geometries of nanometre-scale intergranular solute structures [9]. It is noteworthy that in this case the high density of intragranular solute clusters were introduced to increase the dislocation storage capability of the material, and thus expand the strain hardening capacity [9,630]. Meanwhile, the intergranular solute nanostructures at GBs providing additional resistance to embrittlement and defect generation, may help the material against brittle failure [9].

Zhao et al. processed a ns 7075 Al alloy through following procedures [608]: (1) a commercial T6-treated 7075 Al alloy was solution-treated at 500 °C for 5 h then quenched into liquid nitrogen; (2) repetitive rolling of the solution-treated 7075 Al alloy at liquid nitrogen temperature was conducted to achieve nanostructures; and (3) the repetitively rolled sample was immediately aged, first at 50 °C for 5 h and then at 80 °C for 9 h in an argon atmosphere, to introduce nano-precipitates. As shown in Fig. 77(a), the ns 7075 Al alloy before age treatment (labelled NS in the figure) had a yield strength of 550 MPa which is about more than three times higher than that of the CG 7075 Al alloy (145 MPa), but the uniform elongation of the ns 7075 Al alloy is only 3.3%. However, after a series of age treatment firstly at 50 °C for 5 h and then at 80 °C for 9 h in an argon atmosphere, the yield strength further increased to 615 MPa and surprisingly the ductility also increased to 7.4% uniform elongation. SPD-processing introduced a very high density of defects/dislocations into the 7075 Al alloy, which acted as the heterogeneous nucleation sites for precipitates during subsequent ageing process. It was also found that SPD processing can accelerate the precipitation process and significantly increase the density of the nano-precipitates [603]. The improvement in ductility is attributed to the introduction of a very high density of nano-precipitates (second-phase particles) as shown in Fig. 77(b). The high density of nano-sized second-phase particles significantly hinders dynamic recovery and increases the dislocation storage capability, thus increases the strain-hardening rate [404,608].

ECAP processing of CG pure Cu (99.99%) at room temperature for 12 passes produced UFG structures with a high density of dislocations that dramatically increased the yield strength from < 50 MPa to ~410 MPa (Fig. 78(a) [7]) but significantly reduced the ductility from ~43% to ~6%. The ECAP processing led to an UFG structure (Fig. 78(b)) with the steady state grain size [172,173] and the steady state dislocation density [16,150,174]. The strain hardening capability of the UFG Cu sample was almost depleted at the equilibrium stage. Similar to most other SPD materials, although the UFG Cu sample has a very high strength, its ductility is reduced to a very low value as a trade-off. However, subsequent drawing and rolling at cryogenic temperature introduced a high density of nano-twins in the UFG structure (Fig. 78(c)), leading to both improved yield strength and ductility to 500 MPa and > 10%, respectively, compared to the ECAP-processed sample [7]. The simultaneous improvements of strength and ductility are attributed to the novel combination of an UFG structure and a high density of nano-twins [29,30,721,722]. There has been many literature reports showing that coherent TBs are very effective in blocking and storing dislocations to give an improvement in the strain-hardening rate, thus benefit both the strength and ductility of the materials [7,91,233,235,723].

Recent researches have led to a new renaissance of materials with heterostructures [11,718,719,724,725]. A heterostructured material normally possess large deviation of grain sizes from coarse grains to nano-grains. The intuitive idea is that the coarse grains mainly provide ductility and the nano-grains mainly provide strength. However, careful architecture of the heterogeneous nanostructures is necessary and can be achieved by partial SPD processing or combining SPD with a subsequent heat treatment. Inconsistent results have been reported, some of which are not repeatable.

A typical technique for partial SPD processing is the surface mechanical grinding treatment (SMGT) technique. Fang et al. [716]. used the technique to process a gradient nano-grained Cu rod which exhibited tensile yield strength of ~129 MPa (twice that of the CG sample) and ductility nearly identical to its CG counterpart, as shown in

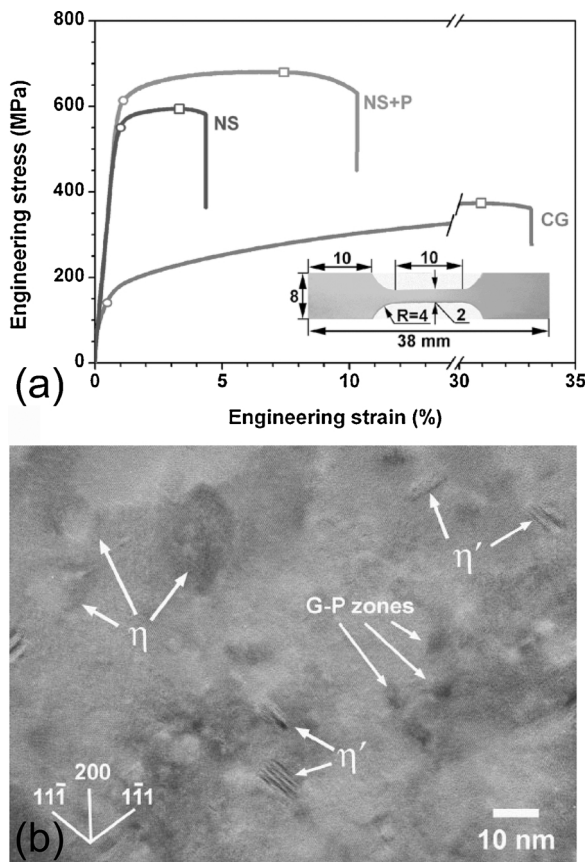


Fig. 77. (a) Tensile engineering stress–strain curves of the CG, cryogenically rolled ns, and aged ns 7075 Al alloy samples. Open circles and squares mark yield strength and uniform elongation, respectively. (b) An HRTEM image showing spherical G-P zones, plate-shaped  $\eta'$  phase, and equiaxed  $\eta$  phase in the aged ns 7075 Al alloy sample [608].

Fig. 79 [716]. The SMGT processed Cu rod sample has a gradient grain-size structure with a ns layer on the sidewall of the rod (Fig. 79(b–c)) and coarse grains at the interior of the rod. In this particular case, while the CG core deforms by conventional dislocation slip during the tensile test, the ns layer deforms by mechanically driven GB migration process [726–729]. It was later discovered by Wu et al. [719], in a gradient structured IF steel that the mutual constraint between the unstable ns surface layers and stable central core changes the stress state that helps with dislocation interaction and accumulation to produce extra strain

hardening. In addition, the mechanical incompatibility among the gradient layers produced a strong back-stress strengthening and back-stress strain hardening [570].

Wang et al. conducted severe cold rolling under liquid-nitrogen-temperature to deform a high purity Cu to 93% thickness reduction, and subsequently annealed the sample at 200 °C for 3 min [651,730]. The resulting material possesses a bimodal grain size distribution that approximately 25% volume fraction of the material is coarse grains and the rest of the material is nano-grains and ultrafine grains. The bimodal ns Cu produced a yield strength above 400 MPa and retained 30% uniform elongation. Wu et al. produced heterogeneous Ti samples with a mixture of nano-lamellar grains and equiaxed coarse grains by repetitive asymmetrical rolling and subsequent annealing at 475 °C for 5 min [718]. The Ti samples were two times or even three times stronger than conventional CG Ti while sustaining the same ductility. Both the bi-modal structured Cu and the heterogeneous lamella Ti are special types of heterostructured materials with soft domains embedded in strong matrix. During the tensile test, the strain partitioning [564,731–735] between strong matrix of nano-grains and soft coarse grains induces significant back-stress work hardening which can help prevent necking and thus improve the ductility of the material [718]. The definition and fundamental mechanisms of heterogeneous (heterostructured) materials can be found in a recent perspective paper [725].

In summary, the ductility of metallic materials can be enhanced by: (1) granting materials with additional strain hardening capability and (2) delaying localized plastic strain instability (necking). The micro/nanostructures that are beneficial to ductility include:

- (1) High density of intragranular solute clusters [9,630] and/or a high density of nano-sized second-phase particles [404,608] which can significantly hinder dynamic recovery and increase the dislocation storage capability.
- (2) A large number of coherent TBs, which possess a comparatively low energy state and are very effective in blocking and storing dislocations [7,91,233,235,723].
- (3) Gradient nanostructure with ns surface layers and CG central core [716,717,727,736,737]. The mutual constraint between the unstable ns surface layers and stable central core leads to multiaxial stress state to enhance dislocation hardening and the mechanical incompatibility leads to high back-stress work hardening during tensile deformation [719].
- (4) Heterostructure with agglomerated coarse grain domains embedded within ns or nc matrix. During the tensile test, the strain gradient near the domain boundaries need to be accommodated by geometrically necessary dislocations (GNDs), which produces strong back stress

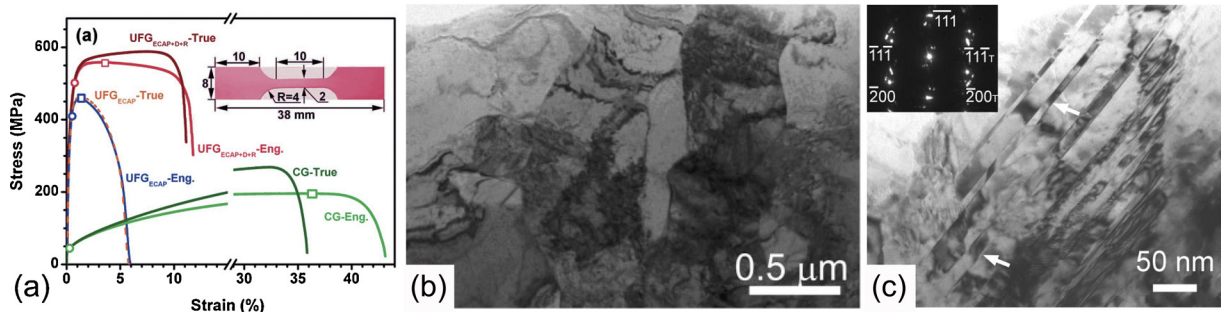


Fig. 78. (a) Stress – strain plots for the samples processed by ECAP for 12 passes (UFG<sub>ECAP</sub>) and ECAP + cryogenic drawing + cryogenic rolling (UFG<sub>ECAP+D+R</sub>), and for CG Cu samples; (b) a TEM image showing ultrafine grains in the UFG<sub>ECAP+D+R</sub> Cu sample; (c) a TEM image showing a high density of nano-twins found in an ultrafine grain [7].

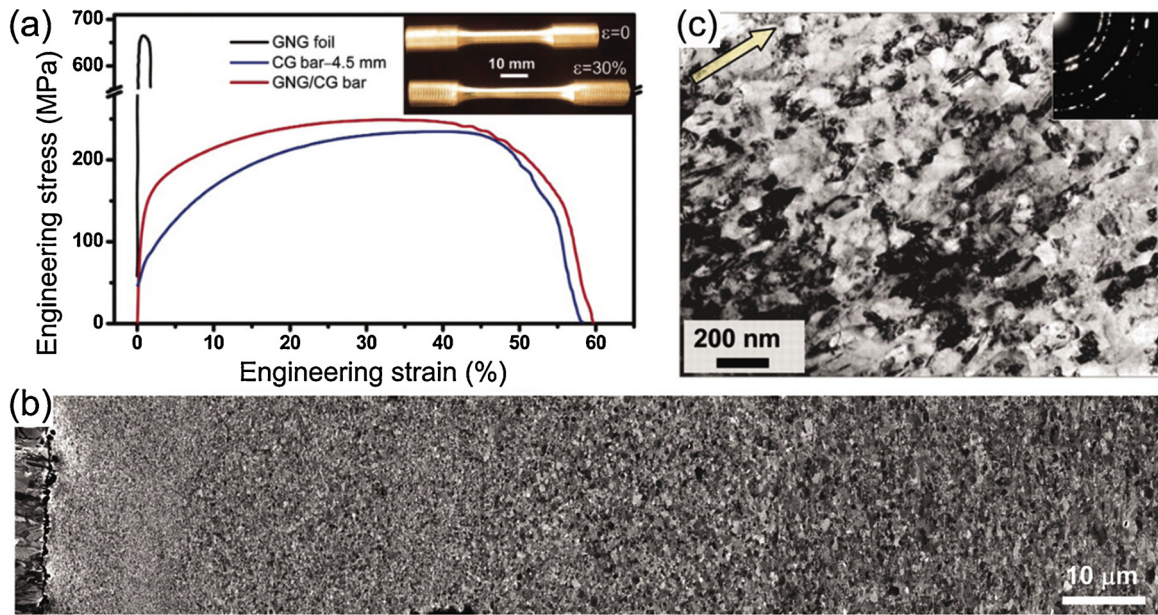


Fig. 79. (a) Tensile engineering stress–strain curves for a CG Cu sample (CG bar with a gauge diameter of 4.5 mm), the sample with a gradient nano-grained layer and a CG core (GNG/CG bar), and a free-standing gradient nano-grained foil sample (GNG foil); (b) a SEM image showing the gradient grain-size structure of a SMGT Cu sample; (c) a TEM image showing nanostructures at the location that is  $\sim 3$  mm below the SMGT processed surface [716].

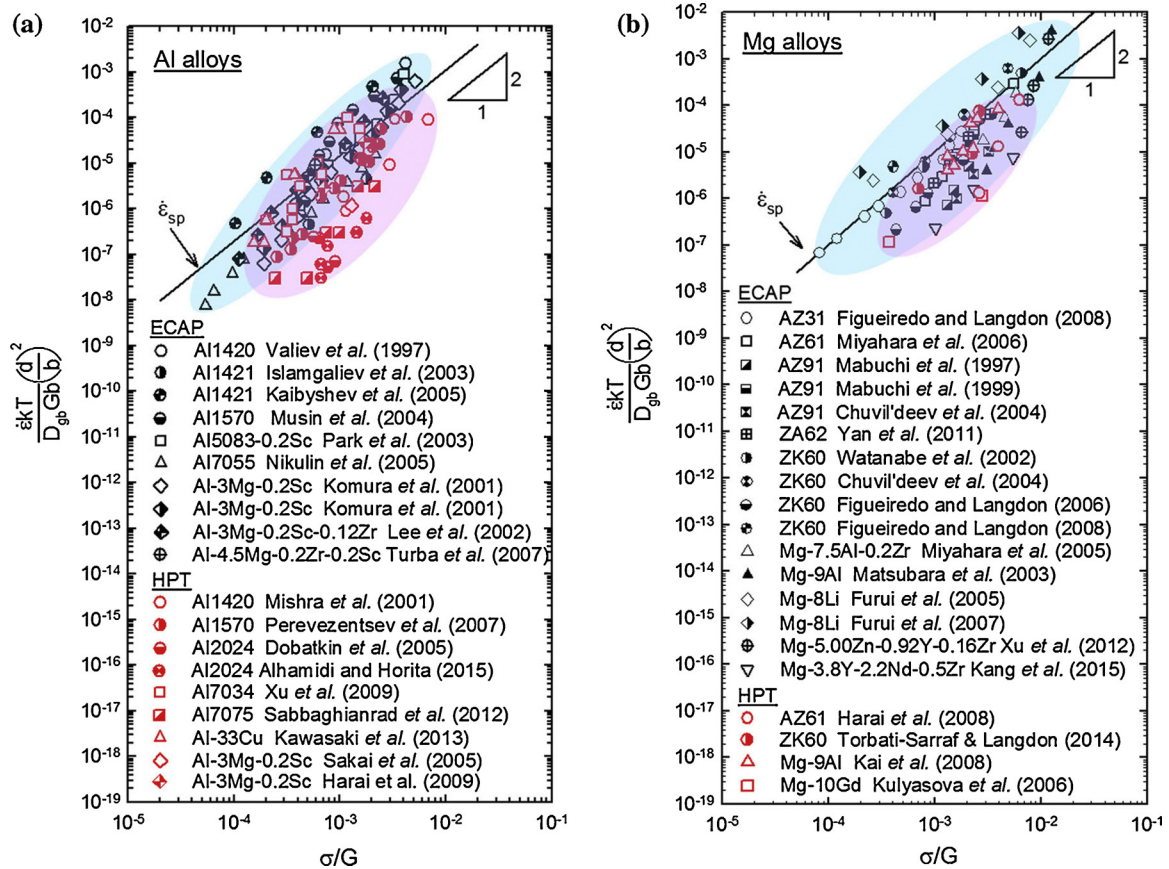


Fig. 80. Temperature and grain size compensated strain rate versus normalized stress for a serious of superplastic (a) Al alloys and (b) Mg alloys processed by SPD, respectively. A solid straight line represents a prediction of superplastic flow made by using Eq. (14). The datum points from ECAP and HPT are encircled by blue and pink ovals, respectively [742].

strengthening to improve strength and back-stress work hardening to retain/improve ductility [564,725,731–735].

### 8.3. Superplastic properties of SPD processed materials

#### 8.3.1. Achieving superplastic properties in SPD materials at elevated temperatures

Superplasticity is defined as the capacity of a material to plastically deform under tension by over 400% [738,739]. There are two fundamental requirements for achieving superplasticity in conventional polycrystalline materials: (1) a grain size smaller than 10  $\mu\text{m}$ , and (2) a homologous temperature above 0.5 Tm [740,741]. The effects of grain size and temperatures on superplasticity are correlated in the famous stress-creep rate relationship :

$$\dot{\epsilon} = \frac{AD_0Gb}{kT} \left(\frac{b}{d}\right)^p \left(\frac{\sigma_t}{G}\right)^n e^{(-Q_{GB}/RT)} \quad (14)$$

where  $\dot{\epsilon}$  is the strain rate, A is a constant,  $D_0$  is a frequency factor, G is the shear modulus, b is the Burgers vector, k is Boltzmann's constant, T is the absolute temperature, d is the grain size, p is the exponent of the inverse grain size,  $\sigma_t$  is the tensile stress, n is the exponent of the stress,  $Q_{GB}$  is the activation energy for GB diffusion and R is gas constant.

The validity of Eq. (14) for SPD processed materials has been testified in a large number of SPD processed materials, and some results are provided in Fig. 80 [742]. It is clearly seen from Fig. 80 that the prediction of the strain rates by Eq. (14) for superplastic flow in SPD processed Al alloys and Mg alloys fits very well with the experimental results. Thus, it is confirmed that the superplastic flow behavior in conventional alloys can be reasonably applied to describe the superplastic flow of UFG materials processed by SPD. Most importantly, Eq. (14) indicates that reducing grain size can expand the optimal strain rate regime for superplasticity to a faster strain rate region, and this is actually attested by extensive experiments [743,744]. This expansion in the range of strain rate implies a potential application of SPD processed materials in the field of high strain rate plastic forming, where UFG and nc materials without any contamination and/or porosity may be used to replace corresponding metal powders. For detailed reviews on the high temperature superplasticity of SPD processed materials, readers can refer to the literatures [742,744].

#### 8.3.2. Achieving superplastic properties in SPD materials at room temperature

Superplasticity typically occurs only at high homologous temperatures ( $> 0.5 T_m$ ), where the thermally activated GB sliding mechanism dominates over conventional dislocation activities [742,743]. Since Eq. (14) has been validated for UFG and nc materials, it thus implies enhanced ductility in UFG and nc materials at lower temperatures and higher strain rates than those in their microcrystalline counterparts [404]. Although it has been well documented that grain size reduction to the UFG and nc regimes can significantly enhance GB mediated deformation mechanisms [3,42,43,201,202,218,705] including GB sliding [200,219,691] and can lower the temperature for superplasticity by 100–200 K [6]. It is still unlikely for materials with medium to high melting temperatures to deform superplastically at room temperature.

Close examination of Eq. (14) reveals that low-temperature superplasticity can be possibly achieved by enhancing GB diffusion. Apart from high temperatures, GB diffusion can also be enhanced by engineering the compositions at GBs through strain induced segregation [414,745]. It is widely known that the energy and mobility of GBs can be altered through segregation of solute atoms, and segregation of selected types of atoms in certain alloys can enhance GB diffusion [628,644,746].

Recently, the hypothesis of achieving room-temperature superplasticity by segregation at GBs has been experimentally proved with SPD processed Mg-8 wt.% Li [747] and Al-30at.%Zn alloys [748]. For the SPD processed Mg-8 wt.% Li alloy, it was found that the combined

effect of segregation of Li atoms to the GBs and the increase in the fraction of Li-rich  $\alpha/\beta$  interphase boundaries led to strongly enhanced GB diffusion. Hence, the SPD processed UFG Mg-8 wt.%Li alloy could demonstrate 440% elongation at room temperature that corresponds 0.35 Tm [747]. For the SPD processed Al-30at.%Zn alloy, it was found that segregation of Zn atoms to Al/Al GBs significantly increased the diffusivity along the Al/Al GBs, making it comparable to the GB diffusivity in Zn metal. The presence of Al-rich  $\alpha$  and Zn-rich  $\eta$  phases together with significantly enhanced GB diffusion at Al/Al GBs in SPD processed ns Al-30at.%Zn alloy led to the superplasticity of 400% tensile elongation at room temperature, corresponding to a homologous temperature of 0.36 Tm [748].

It can be concluded that engineering the GB composition through SPD induced solute segregation can be an effective method for achieving room-temperature superplasticity in alloys with medium melting temperatures. This opens up a new path to enhance the deformability of structural materials at low homologous temperatures.

## 9. Concluding remarks and outstanding issues

### 9.1. Concluding remarks

We have presented a systematic review on SPD-induced grain refinement and other microstructural evolutions of metallic materials with FCC, BCC, and HCP crystalline structures and metallic materials with multiple phases, and the structural effect on mechanical properties. These are summarized below:

- (1) SFE plays a critical role in the deformation and microstructural evolution of FCC materials. For FCC materials with high SFEs, SPD-induced grain refinement occurs mainly via lattice dislocation activities including dislocation multiplication, accumulation, and annihilation via the formation of low-angle and then high-angle GBs. For FCC materials with medium SFEs, their deformation mechanisms and microstructural evolutions are sensitive to deformation condition. For SPD processing at low temperatures, under high hydrostatic pressures and/or high strain rates, deformation twinning plays an important role in the deformation. Otherwise, the microstructural evolution of materials with medium SFEs is similar to that of the materials with high SFEs. For FCC materials with low SFEs, deformation twinning is a major deformation mechanism. The grain refinement process is a combined effect of deformation twinning and the interactions between dislocations and TBs. The resulting final grain sizes are usually smaller than the grain sizes refined only by full dislocation activities and are comparable to the twin thicknesses. Depending on deformation conditions, deformation twinning may be accompanied by significant de-twinning processes and this leads to final refined grain sizes larger than the thicknesses of the primary deformation twins.
- (2) Although the SPD-induced grain refinement processes in BCC materials are similar to those of FCC materials with high SFEs, they also present some unique features. For example, slip of screw dislocations controls the mechanical behavior of CG BCC materials. Screw dislocations in BCC materials possess non-planar cores, strong lattice friction and consequently the mobility of screw dislocations is sensitive to strain rate, temperature and shear stress. When the grain size is reduced to the nc regime, edge and mixed dislocations tend to dominate the deformation, thus the strain rate sensitivity of the deformation behavior of nc BCC metals decreases with smaller grains, which is opposite to the behavior nc FCC metals.
- (3) The easiest deformation mechanism in HCP materials is either  $\langle a \rangle$  basal slip or  $\langle a \rangle$  prismatic slip, depending on whether the c/a ratio is above or below 1.6. There are not enough slip systems to meet the von Mises criterion for strain accommodation and to accommodate strain along the c-axis in HCP materials. Therefore, dislocations

with  $\langle c \rangle$  components and/or deformation twinning are necessary during deformation of HCP materials. However, both deformation mechanisms requires significantly higher stress than  $\langle a \rangle$  slip. Thus, flow stress anisotropy in HCP materials is very significant and this leads to considerably inhomogeneous grain refinement during the early stages of SPD-processing of HCP materials.

- (4) Deformation twinning is critical in HCP materials to meet the von Mises criterion for the plastic deformation of the materials. Similar to other materials, deformation twinning in HCP materials is also sensitive to temperature, stress and grain size. In addition, twinning systems in HCP materials are also material-dependent. The dominance of a single twinning mode in some HCP materials leads to high stress concentration and thus fast failure, which has been observed in Mg and many of its alloys. In contrast, cooperation of multiple twinning modes may benefit homogeneous deformation and allow HCP materials, such as Ti and Zr, to deform to a large strain without failure.
- (5) The final steady-state grain size achieved by SPD processing is affected by many factors including SFE, atomic bond energy, specific heat capacity, self-diffusion activation energy, temperature, the SPD strain path, applied pressure, and strain rate. When the starting grain size is smaller than the steady state grain size, SPD processing results in grain growth through mechanisms such as GB sliding, grain rotation, GB migration, and GB diffusion. During the SPD-induced continuous grain growth process from a much smaller grain size to the steady state grain size, formation and dissociation of L-C locks may continuously occur, leading to an obvious undulation of materials' strength.
- (6) SPD processing leads to pronounced dislocation activities and increases significantly the density of point defects including vacancies. Dislocation slip may drag and redistribute solute atoms to cause diffusive phase transformations such as dissolution of precipitates and/or decomposition of solid solutions, thus change the solubility of materials. Significant accumulation and multiplication of dislocations may cause localized amorphization in certain materials such as TiNi, Fe-B-Cu and Ni-Nb-Y alloys. On the other hand, the high energy imposed by SPD may also lead to nanocrystallization in amorphous metallic materials. High shear stress imposed by SPD may cause non-diffusive (martensitic) phase transformation in many materials including Co, Ti, Zr, Hf, Mo, Ti alloys.
- (7) Dual phase alloys have two phases of similar volume fractions. During SPD processing, each phase domain deforms by its own preferred deformation mechanisms. As the size of the phase domains reduces to the nc regime, deformation mechanisms in one phase may affect the deformation of the adjacent phase that dislocation slip or deformation twins may transmit through the interphase interface of two neighboring grains/phases that are of some specific orientation relationships. If the lattice misfit between the two phases is large, interfacial sliding occurs instead of the transmission of slip across phase boundaries.
- (8) SPD processing leads to significant increase in dislocation density and grain refinement thus strengthens materials. In many situations, SPD processing improves strength but deteriorates ductility. Other subsequent processing treatments would be necessary to acquire structures that promote ductility. Producing heterogeneous ns materials containing both nano-grains and coarse grains is a good strategy for combined high yield strength and decent ductility

## 9.2. Outstanding issues

While SPD processing of metallic materials for improved mechanical properties has been extensively investigated, there are still some outstanding issues to be explored. Details of dislocation activities in and microstructural evolution of FCC, BCC and HCP materials during plastic deformation are still not fully understood due to the lack of structural characterization capabilities. Encouragingly, recent advancement in

materials characterisation techniques may provide significant help for the task. The transmission Kikuchi diffraction (TKD) technique in the scanning electron microscope enables fast, automated orientation mapping of crystalline materials with a dramatically improved spatial resolution compared to the conventional electron backscatter diffraction technique [48,49,749]. The highest achievable spatial resolution of the TKD technique is about 2 nm. Combination of the TKD technique and in-situ straining microscopy techniques makes it possible to study the collaborative deformation processes including the evolution of the crystallographic orientations of neighbouring grains in relatively large areas, the development of dislocation substructures in individual grains during deformation processes, and the relationships between these structural evolutions with mechanical properties of UFG and nc materials. Spherical aberration ( $C_s$ )-corrected TEM with a point-to-point image resolution of smaller than 0.1 nm enables the investigation of the dislocation core structure in BCC materials. The development of in-situ straining TEM enables observation of real-time dislocation activities such as nucleation, slip, accumulation and multiplications in FCC, BCC and HCP materials [278,471,750–754].

The SFE of materials can be changed by changing the composition of the materials. This leads to the difficulty of differentiation of the contribution of SFE and alloy elements to SPD-induced structural evolution and the mechanical properties of UFG and nc materials. This issue may be more critical in materials with significant alloying elemental content such as high entropy alloys. State-of-the-art materials characterization techniques including 3D atom probe tomography, in-situ straining experiments and HRTEM imaging using  $C_s$ -corrected TEM/STEM are ideal for tackling this issue.

As mentioned in Section 3.6, the model to explain the physics behind the steady-state grain size obtainable by SPD is not complete yet, although Mohamed's dislocation model [298,406,412] could predict the minimum average grain size with some degree of accuracy. Many important factors, such deformation twinning, martensitic phase transformation, dynamic recrystallization, GB migration and grain rotation, are strongly suggested to be incorporated into the model for improving the accuracy.

The effect of precipitates on the grain refinement of matrix is affected by the characteristics of the precipitates such as the size, density, precipitate/matrix boundary coherency, chemical stability, and mechanical properties of the precipitates [611,632]. In addition, there seems to be a critical size of precipitates above which the matrix grain refinement can be promoted. Unfortunately, to date all relevant information are randomly scattered, there isn't a systematic research to correlate all these characteristics of precipitates and deformation conditions with the rate of matrix grain refinement. It is crucially important to understand the effect of precipitates on the grain refinement of the matrix, in order to manipulate the microstructures of the materials for optimum mechanical properties.

Recently, heterostructured materials are emerging as a fast-growing hot research topic. Heterostructured materials consist of domains with dramatically different strengths [725]. The domain sizes can vary from micrometers to millimeters and domain geometries can vary from equiaxed to layered. From this definition, some of the aforementioned structures can be classified as special types of heterostructured materials, including the bi-modal structure [8,651,755,756], the heterogeneous lamella structure [684], and the gradient structure [716,719,736,757,758]. A common feature of these structures is that they all have a mixture of CG domains/grains and ns/nc domains. It was noticed in many literatures that heterostructured materials can be processed through SPD processing [349,353,759] or SPD with subsequent heat treatment [8,651,755,756]. While the research in heterostructured materials is expanding its popularity, research on using SPD to manipulate the structural heterogeneity is also an interesting topic.

The ultimate goal of materials processing is to acquire structures that lead to superior mechanical properties. It is critical to have

complete understanding of the relationships between structure and mechanical properties of UFG and nc materials, and ways to achieve the optimum structures. There is still a long way to go for the ultimate goal.

## Acknowledgements

We would like to express our sincere gratitude to all researchers who have contributed to the field of SPD processing of metallic materials. We thank the technical support from the Materials Characterization Facility of Nanjing University of Science and Technology. This work is supported by the National Key R&D Program of China (2017YFA0204403), National Natural Science Foundation of China (Grant No. 51601094 (Y.C.) and Grant No. 51771229 (S.N.)), Australian Research Council (DP150101121) and U.S. Army Research Office (W911 NF-17-1-0350).

## References

- [1] Y.T. Zhu, X.Z. Liao, *Nat. Mater.* 3 (2004) 351–352.
- [2] K. Lu, *Science* 328 (2010) 319–320.
- [3] M.A. Meyers, A. Mishra, D.J. Benson, *Prog. Mater. Sci.* 51 (2006) 427–556.
- [4] R.O. Ritchie, *Nat. Mater.* 10 (2011) 817.
- [5] H. Gleiter, *Prog. Mater. Sci.* 33 (1989) 223–315.
- [6] S.X. McFadden, R.S. Mishra, R.Z. Valiev, A.P. Zhilyaev, A.K. Mukherjee, *Nature* 398 (1999) 684–686.
- [7] Y.H. Zhao, J.F. Bingert, X.Z. Liao, B.Z. Cui, K. Han, A.V. Sergueeva, A.K. Mukherjee, R.Z. Valiev, T.G. Langdon, Y.T. Zhu, *Adv. Mater.* 18 (2006) 2949–2953.
- [8] Y. Zhao, T. Topping, J.F. Bingert, J.J. Thornton, A.M. Dangelewicz, Y. Li, W. Liu, Y. Zhu, Y. Zhou, E.J. Lavernia, *Adv. Mater.* 20 (2008) 3028–3033.
- [9] P.V. Liddicoat, X.-Z. Liao, Y. Zhao, Y. Zhu, M.Y. Murashkin, E.J. Lavernia, R.Z. Valiev, S.P. Ringer, *Nat. Commun.* 1 (2010) 63.
- [10] S.J. Zheng, I.J. Beyerlein, J.S. Carpenter, K.W. Kang, J. Wang, W.Z. Han, N.A. Mara, *Nat. Commun.* 4 (2013) 1696.
- [11] Y. Wei, Y. Li, L. Zhu, Y. Liu, X. Lei, G. Wang, Y. Wu, Z. Mi, J. Liu, H. Wang, H. Gao, *Nat. Commun.* 5 (2014) 3580.
- [12] X. Wu, F. Yuan, M. Yang, P. Jiang, C. Zhang, L. Chen, Y. Wei, E. Ma, *Sci. Rep.* 5 (2015) 11728.
- [13] G. Wu, K.-C. Chan, L. Zhu, L. Sun, J. Lu, *Nature* 545 (2017) 80.
- [14] J. Hu, Y.N. Shi, X. Sauvage, G. Sha, K. Lu, *Science* 355 (2017) 1292–1296.
- [15] S.H. Jiang, H. Wang, Y. Wu, X.J. Liu, H.H. Chen, M.J. Yao, B. Gault, D. Ponge, D. Raabe, A. Hirata, M.W. Chen, Y.D. Wang, Z.P. Lu, *Nature* 544 (2017) 460.
- [16] N. Hansen, *Scr. Mater.* 51 (2004) 801–806.
- [17] R.Z. Valiev, Y. Estrin, Z. Horita, T.G. Langdon, M.J. Zehetbauer, Y.T. Zhu, *JoM* 58 (2006) 33–39.
- [18] Y.T. Zhu, T.C. Lowe, T.G. Langdon, *Scr. Mater.* 51 (2004) 825–830.
- [19] U. Erb, A.M. El-Sherik, G. Palumbo, K.T. Aust, *Nanostruct. Mater.* 2 (1993) 383–390.
- [20] G.W. Nieman, J.R. Weertman, R.W. Siegel, *Scr. Metall.* 23 (1989) 2013–2018.
- [21] C.C. Koch, Y.S. Cho, *Nanostruct. Mater.* 1 (1992) 207–212.
- [22] K.S. Kumar, S. Suresh, M.F. Chisholm, J.A. Horton, P. Wang, *Acta Mater.* 51 (2003) 387–405.
- [23] X.H. Chen, L. Lu, K. Lu, *Scr. Mater.* 64 (2011) 311–314.
- [24] J.D. Giallonardo, G. Avramovic-Cingara, G. Palumbo, U. Erb, *J. Mater. Sci.* 48 (2013) 6689–6699.
- [25] S. Van Petegem, F. Dalla Torre, D. Segers, H. Van Swyngheoven, *Scr. Mater.* 48 (2003) 17–22.
- [26] B.Z. Cui, K. Han, Y. Xin, D.R. Waryoba, A.L. Mbaruku, *Acta Mater.* 55 (2007) 4429–4438.
- [27] P.G. Sanders, J.A. Eastman, J.R. Weertman, *Acta Mater.* 45 (1997) 4019–4025.
- [28] R.Z. Valiev, R.K. Islamgaliev, I.V. Alexandrov, *Prog. Mater. Sci.* 45 (2000) 103–189.
- [29] A.P. Zhilyaev, T.G. Langdon, *Prog. Mater. Sci.* 53 (2008) 893–979.
- [30] R.Z. Valiev, T.G. Langdon, *Prog. Mater. Sci.* 51 (2006) 881–981.
- [31] K. Edalati, Z. Horita, *Mater. Sci. Eng.: A* 652 (2016) 325–352.
- [32] R.M. Imayev, V.M. Imayev, G.A. Salishchev, *J. Mater. Sci.* 27 (1992) 4465–4471.
- [33] M.A. Abdulstaar, E.A. El-Danaf, N.S. Waluyo, L. Wagner, *Mater. Sci. Eng.: A* 565 (2013) 351–358.
- [34] Y. Saito, H. Utsunomiya, N. Tsuji, T. Sakai, *Acta Mater.* 47 (1999) 579–583.
- [35] R. Jamaati, M.R. Toroghinejad, H. Edris, *Mater. Sci. Eng.: A* 578 (2013) 191–196.
- [36] T.G. Langdon, J.T. Wang, R.B. Figueiredo, T.G. Langdon (Eds.), *Nanomaterials by Severe Plastic Deformation: Nanospd5, Pts 1 and 2*, vol. 667–669, *Trans Tech Publications Ltd., Stafa-Zurich*, 2011, pp. 9–14.
- [37] Y. Estrin, A. Vinogradov, *Acta Mater.* 61 (2013) 782–817.
- [38] P.W. Bridgman, *Phys. Rev.* 48 (1935) 825–847.
- [39] K.S. Kumar, H. Van Swyngheoven, S. Suresh, *Acta Mater.* 51 (2003) 5743–5774.
- [40] D. Wolf, V. Yamakov, S.R. Phillpot, A. Mukherjee, H. Gleiter, *Acta Mater.* 53 (2005) 1–40.
- [41] M. Dao, L. Lu, R.J. Asaro, J.T.M. De Hosson, E. Ma, *Acta Mater.* 55 (2007) 4041–4065.
- [42] C.S. Pande, K.P. Cooper, *Prog. Mater. Sci.* 54 (2009) 689–706.
- [43] Y.T. Zhu, X.Z. Liao, X.L. Wu, *Prog. Mater. Sci.* 57 (2012) 1–62.
- [44] Y. Huang, T.G. Langdon, *Mater. Today* 16 (2013) 85–93.
- [45] B. Gault, F. Vurpillot, A. Bostel, A. Menand, B. Deconihout, *Appl. Phys. Lett.* 86 (2005) 094101.
- [46] A.M. Minor, S.A. Syed Asif, Z. Shan, E.A. Stach, E. Cyranowski, T.J. Wyrobek, O.L. Warren, *Nat. Mater.* 5 (2006) 697–702.
- [47] S. Patala, J.K. Mason, C.A. Schuh, *Prog. Mater. Sci.* 57 (2012) 1383–1425.
- [48] P.W. Trimby, Y. Cao, Z. Chen, S. Han, K.J. Hemker, J. Lian, X. Liao, P. Rottmann, S. Samudrala, J. Sun, J.T. Wang, J. Wheeler, J.M. Cairney, *Acta Mater.* 62 (2014) 69–80.
- [49] G.C. Sneddon, P.W. Trimby, J.M. Cairney, *Mater. Sci. Eng.: R: Rep.* 110 (2016) 1–12.
- [50] H. Razavi-Khosroshahi, K. Edalati, H. Emami, E. Akiba, Z. Horita, M. Fuji, *Inorg. Chem.* 56 (2017) 2576–2580.
- [51] K. Edalati, Z. Horita, *Scr. Mater.* 63 (2010) 174–177.
- [52] K. Edalati, T. Daio, Y. Ikoma, M. Arita, Z. Horita, *Appl. Phys. Lett.* 103 (2013) 034108.
- [53] K. Edalati, M. Arimura, Y. Ikoma, T. Daio, M. Miyata, D.J. Smith, Z. Horita, *Mater. Res. Lett.* 3 (2015) 216–221.
- [54] M. Kawasaki, Z. Horita, T.G. Langdon, *Mater. Sci. Eng.: A* 524 (2009) 143–150.
- [55] J.P. Hirth, J. Lothe, *Theory of Dislocations*, Krieger Pub. Co., Malabar, FL, 1992.
- [56] N. Hiroshi, E. David, K. Hono (Eds.), *Physical Metallurgy*, Fifth Edition, Elsevier, Oxford, 2014, pp. 561–637.
- [57] N. Hansen, C.Y. Barlow, K. Hono (Ed.), *Physical Metallurgy*, Fifth Edition, Elsevier, Oxford, 2014, pp. 1681–1764.
- [58] D. Rodney, J. Bonneville, E. David, K. Hono (Eds.), *Physical Metallurgy*, Fifth Edition, Elsevier, Oxford, 2014, pp. 1591–1680.
- [59] J.W. Christian, S. Mahajan, *Prog. Mater. Sci.* 39 (1995) 1–157.
- [60] V. Gerold, H.P. Karnthaler, *Acta Metall.* 37 (1989) 2177–2183.
- [61] Y.L. Wei, A. Godfrey, W. Liu, Q. Liu, X. Huang, N. Hansen, G. Winther, *Scr. Mater.* 65 (2011) 355–358.
- [62] G.W. Groves, A. Kelly, *Philos. Mag.* 8 (1963) 877–887.
- [63] C.R. Weinberger, B.L. Boyce, C.C. Bataille, *Int. Mater. Rev.* 58 (2013) 296–314.
- [64] M.H. Yoo, *Metall. Trans. A* 12A (1981) 409–418.
- [65] I. Kim, J. Kim, D.H. Shin, C.S. Lee, S.K. Hwang, *Mater. Sci. Eng.: A* 342 (2003) 302–310.
- [66] L. Capolungo, P.E. Marshall, R.J. McCabe, I.J. Beyerlein, C.N. Tomé, *Acta Mater.* 57 (2009) 6047–6056.
- [67] A. Serra, D.J. Bacon, R.C. Pond, *Acta Metall.* 36 (1988) 3183–3203.
- [68] A. Serra, R.C. Pond, D.J. Bacon, *Acta Metall. Mater.* 39 (1991) 1469–1480.
- [69] G. Xu, C. Zhang, *J. Mech. Phys. Solids* 51 (2003) 1371–1394.
- [70] Y. Xiang, H. Wei, P. Ming, W. E, *Acta Mater.* 56 (2008) 1447–1460.
- [71] C.R. Weinberger, W. Cai, *Proc. Natl. Acad. Sci.* 105 (2008) 14304–14307.
- [72] G. Xu, A.S. Argon, *Philos. Mag. Lett.* 80 (2000) 605–611.
- [73] M.A. Meyers, O. Vöhringer, V.A. Lubarda, *Acta Mater.* 49 (2001) 4025–4039.
- [74] I. Karaman, H. Sehitoglu, K. Gall, Y.I. Chumlyakov, H.J. Maier, *Acta Mater.* 48 (2000) 1345–1359.
- [75] R. von Mises, *Z. Angew. Math. Mech.* 8 (1928) 161.
- [76] G.I. Taylor, *J. Inst. Met.* 62 (1938) 307.
- [77] J.F.W. Bishop, R. Hill, *The London, Edinburgh Dublin Philos. Mag. J. Sci.* 42 (1951) 414–427.
- [78] D. Kuhlmann-Wilsdorf, *Mater. Sci. Eng.: A* 113 (1989) 1–41.
- [79] F. Otto, A. Dlouhý, C. Somsen, H. Bei, G. Eggeler, E.P. George, *Acta Mater.* 61 (2013) 5743–5755.
- [80] B. Bay, N. Hansen, D.A. Hughes, D. Kuhlmann-Wilsdorf, *Acta Metall. Mater.* 40 (1992) 205–219.
- [81] A.H. Cottrell, B.A. Bilby, *Philos. Mag.* 42 (1951) 573–581.
- [82] J.A. Venables, *Philos. Mag.* 6 (1961) 379–396.
- [83] J.B. Cohen, J. Weertman, *Acta Metall.* 11 (1963) 971.
- [84] M.V. Klassen-Neklyudova, *Mech. Twinn. Cryst.* (1964) p. null.
- [85] S. Mahajan, G.Y. Chin, *Acta Metall.* 21 (1973) 1353–1363.
- [86] Y. Cao, Y.B. Wang, X.Z. Liao, M. Kawasaki, S.P. Ringer, T.G. Langdon, Y.T. Zhu, *Appl. Phys. Lett.* 101 (2012) 231903.
- [87] Y.S. Li, N.R. Tao, K. Lu, *Acta Mater.* 56 (2008) 230–241.
- [88] F. Zhao, L. Wang, D. Fan, B.X. Bie, X.M. Zhou, T. Suo, Y.L. Li, M.W. Chen, C.L. Liu, M.L. Qi, M.H. Zhu, S.N. Luo, *Phys. Rev. Lett.* 116 (2016) 075501.
- [89] X.H. An, Q.Y. Lin, S. Qu, G. Yang, S.D. Wu, Z.F. Zhang, *J. Mater. Res.* 24 (2009) 3636–3646.
- [90] X.H. An, Q.Y. Lin, S.D. Wu, Z.F. Zhang, R.B. Figueiredo, N. Gao, T.G. Langdon, *Scr. Mater.* 64 (2011) 954–957.
- [91] L. Lu, X. Chen, X. Huang, K. Lu, *Science* 323 (2009) 607–610.
- [92] X.Z. Liao, Y.H. Zhao, Y.T. Zhu, R.Z. Valiev, D.V. Gunderov, *J. Appl. Phys.* 96 (2004) 636–640.
- [93] I. Gutierrez-Urrutia, S. Zaefferer, D. Raabe, *Mater. Sci. Eng.: A* 527 (2010) 3552–3560.
- [94] H. Van Swyngheoven, P.M. Derlet, A.G. Froseth, *Nat. Mater.* 3 (2004) 399–403.
- [95] L. Balogh, T. Ungár, Y. Zhao, Y.T. Zhu, Z. Horita, C. Xu, T.G. Langdon, *Acta Mater.* 56 (2008) 809–820.
- [96] Y. Zhang, N.R. Tao, K. Lu, *Scr. Mater.* 60 (2009) 211–213.
- [97] Y.T. Zhu, X.Z. Liao, S.G. Srinivasan, Y.H. Zhao, M.I. Baskes, F. Zhou, E.J. Lavernia, *Appl. Phys. Lett.* 85 (2004) 5049–5051.
- [98] Y.T. Zhu, X.Z. Liao, S.G. Srinivasan, E.J. Lavernia, *J. Appl. Phys.* 98 (2005) 034319.
- [99] X.L. Wu, Y.T. Zhu, *Phys. Rev. Lett.* 101 (2008) 025503.
- [100] S. Ni, Y.B. Wang, X.Z. Liao, H.Q. Li, R.B. Figueiredo, S.P. Ringer, T.G. Langdon,

- Y.T. Zhu, *Phys. Rev. B* 84 (2011) 235401.
- [101] Y. Cao, Y.B. Wang, X.H. An, X.Z. Liao, M. Kawasaki, S.P. Ringer, T.G. Langdon, Y.T. Zhu, *Scr. Mater.* 100 (2015) 98–101.
- [102] Z.W. Wang, Y.B. Wang, X.Z. Liao, Y.H. Zhao, E.J. Lavernia, Y.T. Zhu, Z. Horita, T.G. Langdon, *Scr. Mater.* 60 (2009) 52–55.
- [103] Y.H. Zhao, X.Z. Liao, Y.T. Zhu, Z. Horita, T.G. Langdon, *Mater. Sci. Eng.: A* 410–411 (2005) 188–193.
- [104] Y.H. Zhao, Y.T. Zhu, X.Z. Liao, Z. Horita, T.G. Langdon, *Mater. Sci. Eng.: A* 463 (2007) 22–26.
- [105] Y. Zhang, N.R. Tao, K. Lu, *Acta Mater.* 59 (2011) 6048–6058.
- [106] K. Edalati, Z. Horita, *Acta Mater.* 59 (2011) 6831–6836.
- [107] S. Lee, Z. Horita, *Mater. Trans.* 53 (2012) 38–45.
- [108] L.J. Kecskes, K.C. Cho, R.J. Dowding, B.E. Schuster, R.Z. Valiev, Q. Wei, *Mater. Sci. Eng.: A* 467 (2007) 33–43.
- [109] M.H. Yoo, J.K. Lee, *Philos. Mag.* 63 (1991) 987–1000.
- [110] D.H. Sastry, Y.V.R.K. Prasad, K.I. Vasu, *Scr. Metall.* 3 (1969) 927–929.
- [111] A. Couret, D. Caillard, *Acta Metall.* 33 (1985) 1455–1462.
- [112] R.L. Fleischer, *Scr. Metall.* 20 (1986) 223–224.
- [113] Y. Wang, L.Q. Chen, Z.K. Liu, S.N. Mathaudhu, *Scr. Mater.* 62 (2010) 646–649.
- [114] Z. Ding, S. Li, W. Liu, Y. Zhao, *Adv. Mater. Sci. Eng.* 2015 (2015) 8.
- [115] Z. Ding, W. Liu, S. Li, D. Zhang, Y. Zhao, E.J. Lavernia, Y. Zhu, *Acta Mater.* 107 (2016) 127–132.
- [116] L. Tang, W. Liu, Z. Ding, D. Zhang, Y. Zhao, E.J. Lavernia, Y. Zhu, *Comput. Mater. Sci.* 115 (2016) 85–91.
- [117] Y.F. Wu, S. Li, Z.G. Ding, W. Liu, Y.H. Zhao, Y.T. Zhu, *Scr. Mater.* 112 (2016) 101–105.
- [118] M. Muzyk, Z. Pakiel, K.J. Kurzydowski, *Scr. Mater.* 64 (2011) 916–918.
- [119] C. Brandl, P.M. Derlet, H. Van Swygenhoven, *Phys. Rev. B* 76 (2007) 054124.
- [120] I.L. Dillamore, R.E. Smallman, *Philos. Mag.* 12 (1965) 191–193.
- [121] C.B. Carter, S.M. Holmes, *Philos. Mag.* 35 (1977) 1161–1172.
- [122] I.L. Dillamore, R.E. Smallman, W.T. Roberts, *Philos. Mag.* 9 (1964) 517–526.
- [123] A. Howie, P.R. Swann, *Philos. Mag.* 6 (1961) 1215–1226.
- [124] D. Kuhlmann-Wilsdorf, N. Hansen, *Scr. Metall. Mater.* 25 (1991) 1557–1562.
- [125] D.A. Hughes, N. Hansen, *Acta Mater.* 48 (2000) 2985–3004.
- [126] H.W. Zhang, X. Huang, N. Hansen, *Acta Mater.* 56 (2008) 5451–5465.
- [127] A. Mishra, B.K. Kad, F. Gregori, M.A. Meyers, *Acta Mater.* 55 (2007) 13–28.
- [128] B. Bay, N. Hansen, D. Kuhlmann-Wilsdorf, *Mater. Sci. Eng.: A* 113 (1989) 385–397.
- [129] D. Hull, D.J. Bacon, Chapter 3 - Movement of Dislocations, *Introduction to Dislocations, Fifth Edition*, Butterworth-Heinemann, Oxford, 2011, pp. 43–62.
- [130] B. Nøst, *Philos. Mag.* 11 (1965) 183–184.
- [131] S. Howe, C. Elbaum, *Philos. Mag.* 6 (1961) 1227–1240.
- [132] Q. Liu, N. Hansen, *Scr. Metall. Mater.* 32 (1995) 1289–1295.
- [133] B. Jakobsen, H.F. Poulsen, U. Lienert, J. Almer, S.D. Shastri, H.O. Sørensen, C. Gundlach, W. Pantleon, *Science* 312 (2006) 889–892.
- [134] P. Hähner, *Acta Mater.* 44 (1996) 2345–2352.
- [135] J.Y. Huang, Y.T. Zhu, H. Jiang, T.C. Lowe, *Acta Mater.* 49 (2001) 1497–1505.
- [136] D. Kuhlmann-Wilsdorf, *Scr. Mater.* 36 (1997) 173–181.
- [137] A. Godfrey, Q. Liu, *Scr. Mater.* 60 (2009) 1050–1055.
- [138] R. Madec, B. Devincere, L.P. Kubin, *Phys. Rev. Lett.* 89 (2002) 255508.
- [139] N. Hansen, *Mater. Sci. Eng.: A* 409 (2005) 39–45.
- [140] X. Huang, G. Winther, *Philos. Mag.* 87 (2007) 5189–5214.
- [141] G. Winther, X. Huang, *Philos. Mag.* 87 (2007) 5215–5235.
- [142] Y. Huang, P.B. Prangnell, *Acta Mater.* 56 (2008) 1619–1632.
- [143] Y. Chen, Y. Li, L. He, C. Lu, H. Ding, Q. Li, *Mater. Lett.* 62 (2008) 2821–2824.
- [144] D.A. Hughes, N. Hansen, *Scr. Metall. Mater.* 33 (1995) 315–321.
- [145] D.A. Hughes, N. Hansen, *Acta Mater.* 45 (1997) 3871–3886.
- [146] A.P. Zhilyaev, G.V. Nurislamova, B.K. Kim, M.D. Baró, J.A. Szpunar, T.G. Langdon, *Acta Mater.* 51 (2003) 753–765.
- [147] Z. Horita, D.J. Smith, M. Nemoto, R.Z. Valiev, T.G. Langdon, *J. Mater. Res.* 13 (1998) 446–450.
- [148] X.Z. Liao, J.Y. Huang, Y.T. Zhu, F. Zhou, E.J. Lavernia, *Philos. Mag.* 83 (2003) 3065–3075.
- [149] X.L. Wu, Y.T. Zhu, *Appl. Phys. Lett.* 89 (2006) 031922.
- [150] N.Q. Chinh, T. Csanádi, J. Gubicza, T.G. Langdon, *Acta Mater.* 58 (2010) 5015–5021.
- [151] T. Csanádi, N.Q. Chinh, J. Gubicza, T.G. Langdon, *Acta Mater.* 59 (2011) 2385–2391.
- [152] F. Prinz, A.S. Argon, W.C. Moffatt, *Acta Metall.* 30 (1982) 821–830.
- [153] D. Raabe, K. Hono (Ed.), *Physical Metallurgy, Fifth Edition*, Elsevier, Oxford, 2014, pp. 2291–2397.
- [154] F. Hamdi, S. Asgari, *Scr. Mater.* 62 (2010) 693–696.
- [155] A.P. Zhilyaev, B.K. Kim, G.V. Nurislamova, M.D. Baró, J.A. Szpunar, T.G. Langdon, *Scr. Mater.* 46 (2002) 575–580.
- [156] M.J. Zehetbauer, H.P. Stüwe, A. Vorhauer, E. Schafner, J. Kohout, *Adv. Eng. Mater.* 5 (2003) 330–337.
- [157] C. Xu, K. Xia, T.G. Langdon, *Acta Mater.* 55 (2007) 2351–2360.
- [158] Y.T. Zhu, T.C. Lowe, *Mater. Sci. Eng.: A* 291 (2000) 46–53.
- [159] N. Hansen, R.F. Mehl, A. Medalist, *Metall. Mater. Trans. A* 32 (2001) 2917–2935.
- [160] U.F. Kocks, H. Mecking, *Prog. Mater. Sci.* 48 (2003) 171–273.
- [161] W.D. Kaplan, *Science* 349 (2015) 1059–1060.
- [162] N. Hansen, X. Huang, D.A. Hughes, *Mater. Sci. Eng.: A* 317 (2001) 3–11.
- [163] M. Zehetbauer, V. Seumer, *Acta Metall. Mater.* 41 (1993) 577–588.
- [164] M. Zehetbauer, *Acta Metall. Mater.* 41 (1993) 589–599.
- [165] K. Edalati, Z. Horita, *Mater. Sci. Eng.: A* 528 (2011) 7514–7523.
- [166] Y. Ito, Z. Horita, *Mater. Sci. Eng.: A* 503 (2009) 32–36.
- [167] Y. Iwahashi, Z. Horita, M. Nemoto, T.G. Langdon, *Metall. Mater. Trans. A* 29 (1998) 2503–2510.
- [168] P.B. Berbon, M. Furukawa, Z. Horita, M. Nemoto, T.G. Langdon, *Metall. Mater. Trans. A* 30 (1999) 1989–1997.
- [169] S. Qu, X.H. An, H.J. Yang, C.X. Huang, G. Yang, Q.S. Zang, Z.G. Wang, S.D. Wu, Z.F. Zhang, *Acta Mater.* 57 (2009) 1586–1601.
- [170] T. Sakai, A. Belyakov, R. Kaibyshev, H. Miura, J.J. Jonas, *Prog. Mater. Sci.* 60 (2014) 130–207.
- [171] A.A. Salem, T.G. Langdon, T.R. McNelley, S.R. Kalidindi, S.L. Semiatin, *Metall. Mater. Trans. A* 37 (2006) 2879–2891.
- [172] D. Moldovan, D. Wolf, S.R. Phillpot, A.J. Haslam, *Acta Mater.* 50 (2002) 3397–3414.
- [173] D. Farkas, S. Mohanty, J. Monk, *Mater. Sci. Eng. A* 493 (2008) 33–40.
- [174] N.Q. Chinh, G. Horváth, Z. Horita, T.G. Langdon, *Acta Mater.* 52 (2004) 3555–3563.
- [175] K. Wang, N.R. Tao, G. Liu, J. Lu, K. Lu, *Acta Mater.* 54 (2006) 5281–5291.
- [176] N.R. Tao, K. Lu, *Scr. Mater.* 60 (2009) 1039–1043.
- [177] S. Ogata, J. Li, S. Yip, *Science* 298 (2002) 807–811.
- [178] M.H. Loretto, L.M. Clarebrough, R.L. Segall, *Philos. Mag.* 11 (1965) 459–465.
- [179] X. Nie, W. Renhui, Y. Yiyang, Z. Yumei, W. Dingsheng, *Solid State Commun.* 96 (1995) 729–734.
- [180] C.X. Huang, W. Hu, G. Yang, Z.F. Zhang, S.D. Wu, Q.Y. Wang, G. Gottstein, *Mater. Sci. Eng. A* 556 (2012) 638–647.
- [181] F. Dalla Torre, R. Lapovok, J. Sandlin, P.F. Thomson, C.H.J. Davies, E.V. Pereloma, *Acta Mater.* 52 (2004) 4819–4832.
- [182] F.H. Dalla Torre, E.V. Pereloma, C.H.J. Davies, *Acta Mater.* 54 (2006) 1135–1146.
- [183] C.X. Huang, K. Wang, S.D. Wu, Z.F. Zhang, G.Y. Li, S.X. Li, *Acta Mater.* 54 (2006) 655–665.
- [184] X.H. An, Q.Y. Lin, S.D. Wu, Z.F. Zhang, R.B. Figueiredo, N. Gao, T.G. Langdon, *Philos. Mag.* 91 (2011) 3307–3326.
- [185] F. Wetscher, A. Vorhauer, R. Pippan, *Mater. Sci. Eng. A* 410–411 (2005) 213–216.
- [186] X.Z. Liao, Y.H. Zhao, S.G. Srinivasan, Y.T. Zhu, R.Z. Valiev, D.V. Gunderov, *Appl. Phys. Lett.* 84 (2004) 592–594.
- [187] E. El-Danaf, S.R. Kalidindi, R.D. Doherty, *Metall. Mater. Trans. A* 30 (1999) 1223–1233.
- [188] D. Lahaie, J.D. Embury, M.M. Chadwick, G.T. Gray, *Scr. Metall. Mater.* 27 (1992) 139–142.
- [189] E. Romhanji, V. Milenkovic, D. Drobnjak, *Zeitschrift für Metallkunde* 83 (1992) 110–114.
- [190] M. Meyers, U. Andrade, A. Chokshi, *Metall. Mater. Trans. A* 26 (1995) 2881–2893.
- [191] S. Mahajan, *Scr. Mater.* 68 (2013) 95–99.
- [192] R.J. Asaro, P. Krysl, B. Kad, *Philos. Mag. Lett.* 83 (2003) 733–743.
- [193] X.Z. Liao, F. Zhou, E.J. Lavernia, D.W. He, Y.T. Zhu, *Appl. Phys. Lett.* 83 (2003) 5062–5064.
- [194] M. Chen, E. Ma, K.J. Hemker, H. Sheng, Y. Wang, X. Cheng, *Science* 300 (2003) 1275–1277.
- [195] X. Wu, Y.T. Zhu, M.W. Chen, E. Ma, *Scr. Mater.* 54 (2006) 1685–1690.
- [196] Y.T. Zhu, X.L. Wu, X.Z. Liao, J. Narayan, S.N. Mathaudhu, L.J. Kecskes, *Appl. Phys. Lett.* 95 (2009) 031909.
- [197] Y.B. Wang, J.C. Ho, X.Z. Liao, H.Q. Li, S.P. Ringer, Y.T. Zhu, *Appl. Phys. Lett.* 94 (2009) 011908.
- [198] M. Ke, S.A. Hackney, W.W. Milligan, E.C. Aifantis, *Nanostruct. Mater.* 5 (1995) 689–697.
- [199] Y.B. Wang, J.C. Ho, Y. Cao, X.Z. Liao, H.Q. Li, Y.H. Zhao, E.J. Lavernia, S.P. Ringer, Y.T. Zhu, *Appl. Phys. Lett.* 94 (2009) 091911.
- [200] M.Y. Gutkin, I.A. Ovid'ko, N.V. Skiba, *Acta Mater.* 51 (2003) 4059–4071.
- [201] Z. Shan, E.A. Stach, J.M.K. Wiezorek, J.A. Knapp, D.M. Follstaedt, S.X. Mao, *Science* 305 (2004) 654–657.
- [202] V. Yamakov, D. Wolf, S.R. Phillpot, A.K. Mukherjee, H. Gleiter, *Nat. Mater.* 1 (2002) 45–49.
- [203] V. Yamakov, D. Wolf, S.R. Phillpot, A.K. Mukherjee, H. Gleiter, *Nat. Mater.* 3 (2004) 43–47.
- [204] Y.T. Zhu, X.Z. Liao, *Appl. Phys. Lett.* 86 (2005) 103112.
- [205] X.H. An, Q.Y. Lin, S.D. Wu, Z.F. Zhang, R.B. Figueiredo, N. Gao, T.G. Langdon, *Scr. Mater.* 64 (2011) 249–252.
- [206] G.H. Xiao, N.R. Tao, K. Lu, *Scr. Mater.* 59 (2008) 975–978.
- [207] M. Dao, L. Lu, Y.F. Shen, S. Suresh, *Acta Mater.* 54 (2006) 5421–5432.
- [208] X.L. Wu, Y. Qi, Y.T. Zhu, *Appl. Phys. Lett.* 90 (2007) 221911.
- [209] S. Lee, Y. Estrin, B. Cooman, *Metall. Mater. Trans. A* 45 (2014) 717–730.
- [210] R.J. McCabe, I.J. Beyerlein, J.S. Carpenter, N.A. Mara, *Nat. Commun.* 5 (2014) 3806.
- [211] Y.B. Wang, X.Z. Liao, Y.H. Zhao, E.J. Lavernia, S.P. Ringer, Z. Horita, T.G. Langdon, Y.T. Zhu, *Mater. Sci. Eng.: A* 527 (2010) 4959–4966.
- [212] H. Ikeda, Y. Qi, T. Çagin, K. Samwer, W.L. Johnson, W.A. Goddard, *Phys. Rev. Lett.* 82 (1999) 2900–2903.
- [213] M. Li, *Phys. Rev. B* 62 (2000) 13979–13995.
- [214] Y. Cao, L.C. Zhang, Y. Zhang, *Mater. Sci. Eng.: A* 658 (2016) 321–325.
- [215] L. Lu, Y.F. Shen, X.H. Chen, L.H. Qian, K. Lu, *Science* 304 (2004) 422–426.
- [216] Y.B. Wang, B. Wu, M.L. Sui, *Appl. Phys. Lett.* 93 (2008) 041906.
- [217] Y.B. Wang, B.Q. Li, M.L. Sui, S.X. Mao, *Appl. Phys. Lett.* 92 (2008) 011903.
- [218] J. Schiötz, F.D. Di Tolla, K.W. Jacobsen, *Nature* 391 (1998) 561–563.
- [219] J. Schiötz, K.W. Jacobsen, *Science* 301 (2003) 1357–1359.
- [220] Y. Cao, Y.B. Wang, Z.B. Chen, X.Z. Liao, M. Kawasaki, S.P. Ringer, T.G. Langdon, Y.T. Zhu, *Mater. Sci. Eng.: A* 578 (2013) 110–114.
- [221] Y.T. Zhu, X.L. Wu, X.Z. Liao, J. Narayan, L.J. Kecskes, S.N. Mathaudhu, *Acta Mater.* 59 (2011) 812–821.

- [222] S. Ni, Y.B. Wang, X.Z. Liao, R.B. Figueiredo, H.Q. Li, S.P. Ringer, T.G. Langdon, Y.T. Zhu, *Acta Mater.* 60 (2012) 3181–3189.
- [223] C.S. Hong, N.R. Tao, X. Huang, K. Lu, *Acta Mater.* 58 (2010) 3103–3116.
- [224] H.W. Zhang, Z.K. Hei, G. Liu, J. Lu, K. Lu, *Acta Mater.* 51 (2003) 1871–1881.
- [225] B.Q. Li, M.L. Sui, B. Li, E. Ma, S.X. Mao, *Phys. Rev. Lett.* 102 (2009) 205504.
- [226] J. Wang, N. Li, O. Anderoglu, X. Zhang, A. Misra, J.Y. Huang, J.P. Hirth, *Acta Mater.* 58 (2010) 2262–2270.
- [227] J. Wang, O. Anderoglu, J.P. Hirth, A. Misra, X. Zhang, *Appl. Phys. Lett.* 95 (2009) 021908.
- [228] Y. Cao, Y.B. Wang, X.H. An, X.Z. Liao, M. Kawasaki, S.P. Ringer, T.G. Langdon, Y.T. Zhu, *Acta Mater.* 63 (2014) 16–29.
- [229] Y. Wei, *Mater. Sci. Eng.: A* 528 (2011) 1558–1566.
- [230] Z.X. Wu, Y.W. Zhang, D.J. Srolovitz, *Acta Mater.* 59 (2011) 6890–6900.
- [231] X. Li, Y. Wei, L. Lu, K. Lu, H. Gao, *Nature* 464 (2010) 877–880.
- [232] X. Zhang, A. Misra, H. Wang, M. Nastasi, J.D. Embury, T.E. Mitchell, R.G. Hoagland, J.P. Hirth, *Appl. Phys. Lett.* 84 (2004) 1096–1098.
- [233] X.Y. Li, Y.J. Wei, L. Lu, K. Lu, H.J. Gao, *Nature* 464 (2010) 877–880.
- [234] L. Li, N.M. Ghoniem, *Phys. Rev. B* 79 (2009) 075444.
- [235] Y. Wei, *Phys. Rev. B* 83 (2011) 132104.
- [236] S. Ni, Y.B. Wang, X.Z. Liao, S.N. Alhajeri, H.Q. Li, Y.H. Zhao, E.J. Lavernia, S.P. Ringer, T.G. Langdon, Y.T. Zhu, *Scr. Mater.* 64 (2011) 327–330.
- [237] X.H. An, W.Z. Han, C.X. Huang, P. Zhang, G. Yang, S.D. Wu, Z.F. Zhang, *Appl. Phys. Lett.* 92 (2008) 201915.
- [238] V.F. Moiseev, V.I. Trefilov, *Phys. Status Solidi* 18 (1966) 881.
- [239] M.S. Duesbery, V. Vitek, *Acta Mater.* 46 (1998) 1481–1492.
- [240] Q. Wei, L.J. Kecskes, K.T. Ramesh, *Mater. Sci. Eng.: A* 578 (2013) 394–401.
- [241] D. Jia, K.T. Ramesh, E. Ma, *Acta Mater.* 51 (2003) 3495–3509.
- [242] Q. Wei, D. Jia, K.T. Ramesh, E. Ma, *Appl. Phys. Lett.* 81 (2002) 1240–1242.
- [243] Q. Wei, B.E. Schuster, S.N. Mathaudhu, K.T. Hartwig, L.J. Kecskes, R.J. Dowding, K.T. Ramesh, *Mater. Sci. Eng.: A* 493 (2008) 58–64.
- [244] N. Maury, N.X. Zhang, Y. Huang, A.P. Zhilyaev, T.G. Langdon, *Mater. Sci. Eng.: A* 638 (2015) 174–182.
- [245] Q. Wei, K.T. Ramesh, E. Ma, L.J. Kecskes, R.J. Dowding, V.U. Kazykhanov, R.Z. Valiev, *Appl. Phys. Lett.* 86 (2005) 101907.
- [246] Z. Pan, F. Xu, S.N. Mathaudhu, L.J. Kecskes, W.H. Yin, X.Y. Zhang, K.T. Hartwig, Q. Wei, *Acta Mater.* 60 (2012) 2310–2323.
- [247] A. Hohenwarter, S. Wurster, *Mater. Sci. Eng.: A* 650 (2016) 492–496.
- [248] S. Lee, K. Edalati, Z. Horita, *Mater. Trans.* 51 (2010) 1072–1079.
- [249] Y. Huang, M. Lemang, N.X. Zhang, P.H.R. Pereira, T.G. Langdon, *Mater. Sci. Eng.: A* 655 (2016) 60–69.
- [250] R. Wadsack, R. Pippan, B. Schedler, *Fusion Eng. Des.* 66–68 (2003) 265–269.
- [251] R.Z. Valiev, Y.V. Ivanisenko, E.F. Rauch, B. Baudalet, *Acta Mater.* 44 (1996) 4705–4712.
- [252] B.Q. Han, E.J. Lavernia, F.A. Mohamed, *Metall. Mater. Trans. A* 35 (2004) 1343–1350.
- [253] K. Edalati, T. Fujioka, Z. Horita, *Mater. Trans.* 50 (2009) 44–50.
- [254] Y. Fukuda, K. Oh-ishi, Z. Horita, T.G. Langdon, *Acta Mater.* 50 (2002) 1359–1368.
- [255] F. Wetscher, A. Vorhauer, R. Stock, R. Pippan, *Mater. Sci. Eng.: A* 387–389 (2004) 809–816.
- [256] B.L. Li, A. Godfrey, Q. Liu, *Scr. Mater.* 50 (2004) 879–883.
- [257] H.R.Z. Sandim, H.H. Bernardi, B. Verlinden, D. Raabe, *Mater. Sci. Eng.: A* 467 (2007) 44–52.
- [258] G.M. Cheng, H. Yuan, W.W. Jian, W.Z. Xu, P.C. Millett, Y.T. Zhu, *Scr. Mater.* 68 (2013) 130–133.
- [259] V.P. Pilyugin, L.M. Voronova, T.M. Gapontseva, T.I. Chashchukhina, M.V. Degtyarev, *Int. J. Refract. Met. Hard Mater* 43 (2014) 59–63.
- [260] Q. Wei, Z.L. Pan, X.L. Wu, B.E. Schuster, L.J. Kecskes, R.Z. Valiev, *Acta Mater.* 59 (2011) 2423–2436.
- [261] Y. Huang, N. Maury, N.X. Zhang, T.G. Langdon, B. Beausir, O. Bouaziz, E. Bouzy, T. Grosdidier, L.S. Toth (Eds.), 6th International Conference on Nanomaterials by Severe Plastic Deformation, vol. 63, IOP Publishing Ltd., Bristol, 2014.
- [262] Q. Wei, H.T. Zhang, B.E. Schuster, K.T. Ramesh, R.Z. Valiev, L.J. Kecskes, R.J. Dowding, L. Magness, K. Cho, *Acta Mater.* 54 (2006) 4079–4089.
- [263] P. Li, X. Wang, K.-M. Xue, Y. Tian, Y.-C. Wu, *Int. J. Refract. Met. Hard Mater* 54 (2016) 439–444.
- [264] P. Gumbsch, J. Riedle, A. Hartmaier, H.F. Fischmeister, *Science* 282 (1998) 1293–1295.
- [265] A. Giannattasio, Z. Yao, E. Tarleton, S.G. Roberts, *Philos. Mag.* 90 (2010) 3947–3959.
- [266] A.M. Lennon, K.T. Ramesh, *Mater. Sci. Eng.: A* 276 (2000) 9–21.
- [267] S.S. Lau, J.E. Dorn, *Phys. Status Solidi (A)* 2 (1970) 825–836.
- [268] D. Caillard, *Acta Mater.* 58 (2010) 3493–3503.
- [269] C.R. Weinberger, *Acta Mater.* 58 (2010) 6535–6541.
- [270] K. Masuda, K. Kobayashi, A. Sato, T. Mori, *Philos. Mag. B* 43 (1981) 19–28.
- [271] D. Caillard, *Acta Mater.* 58 (2010) 3504–3515.
- [272] G.M. Cheng, W.Z. Xu, W.W. Jian, H. Yuan, M.H. Tsai, Y.T. Zhu, Y.F. Zhang, P.C. Millett, *J. Mater. Res.* 28 (2013) 1820–1826.
- [273] V. Vitek, *Philos. Mag.* 84 (2004) 415–428.
- [274] A.S. Keh, *Philos. Mag.* 12 (1965) 9–30.
- [275] A. Sato, K.-I. Masuda, *Philos. Mag. B* 43 (1981) 1–17.
- [276] G. Po, Y. Cui, D. Rivera, D. Cereceda, T.D. Swinburne, J. Marian, N. Ghoniem, *Acta Mater.* 119 (2016) 123–135.
- [277] R. Gröger, A.G. Bailey, V. Vitek, *Acta Mater.* 56 (2008) 5401–5411.
- [278] J. Wang, Z. Zeng, C.R. Weinberger, Z. Zhang, T. Zhu, S.X. Mao, *Nat. Mater.* 14 (2015) 594–600.
- [279] R.F. Zhang, J. Wang, I.J. Beyerlein, T.C. Germann, *Philos. Mag. Lett.* 91 (2011) 731–740.
- [280] S. Mahajan, *Acta Metall.* 23 (1975) 671–684.
- [281] L.E. Murr, M.A. Meyers, C.S. Niou, Y.J. Chen, S. Pappu, C. Kennedy, *Acta Mater.* 45 (1997) 157–175.
- [282] J.W. Christian, *Metall. Trans. A* 14 (1983) 1237–1256.
- [283] V. Vitek, *Prog. Mater. Sci.* 36 (1992) 1–27.
- [284] S. Queyreau, G. Monnet, B. Devincere, *Int. J. Plast.* 25 (2009) 361–377.
- [285] M. Tang, L.P. Kubin, G.R. Canova, *Acta Mater.* 46 (1998) 3221–3235.
- [286] L.M. Hsiung, D.H. Lassila, *Acta Mater.* 48 (2000) 4851–4865.
- [287] S.Z. Li, X.D. Ding, J.K. Deng, T. Lookman, J. Li, X.B. Ren, J. Sun, A. Saxena, *Phys. Rev. B* 82 (12) (2010) 205435.
- [288] Y. Fukuda, K. Oh-ishi, M. Furukawa, Z. Horita, T.G. Langdon, *Acta Mater.* 52 (2004) 1387–1395.
- [289] L. Zhu, M. Seefeldt, B. Verlinden, *Acta Mater.* 61 (2013) 4504–4511.
- [290] L. Zhu, M. Seefeldt, B. Verlinden, *Acta Mater.* 61 (2013) 4490–4503.
- [291] Q. Wei, T. Jiao, S.N. Mathaudhu, E. Ma, K.T. Hartwig, K.T. Ramesh, *Mater. Sci. Eng.: A* 358 (2003) 266–272.
- [292] D. Goran, J.J. Fundenberger, E. Bouzy, W. Skrotzki, S. Suwas, T. Grosdidier, L.S. Toth, *Philos. Mag.* 91 (2011) 281–299.
- [293] Q. Wei, T. Jiao, K.T. Ramesh, E. Ma, L.J. Kecskes, L. Magness, R. Dowding, V.U. Kazykhanov, R.Z. Valiev, *Acta Mater.* 54 (2006) 77–87.
- [294] K. Edalati, Z. Horita, *Mater. Trans.* 51 (2010) 1051–1054.
- [295] G.M. Cheng, W.W. Jian, W.Z. Xu, H. Yuan, P.C. Millett, Y.T. Zhu, *Mater. Res. Lett.* 1 (2013) 26–31.
- [296] Y. Ivanisenko, R.Z. Valiev, H.J. Fecht, *Mater. Sci. Eng.: A* 390 (2005) 159–165.
- [297] A. Ojha, H. Sehitoglu, *Philos. Mag. Lett.* 94 (2014) 647–657.
- [298] F.A. Mohamed, *Acta Mater.* 51 (2003) 4107–4119.
- [299] S. Shi, L. Zhu, H. Zhang, Z. Sun, R. Ahuja, *Acta Mater.* 144 (2018) 853–861.
- [300] C.Q. Chen, G. Hu, J.N. Florando, M. Kumar, K.J. Hemker, K.T. Ramesh, *Scr. Mater.* 69 (2013) 709–712.
- [301] L.M. Hsiung, D.H. Lassila, *Scr. Mater.* 38 (1998) 1371–1376.
- [302] C.Q. Chen, J.N. Florando, M. Kumar, K.T. Ramesh, K.J. Hemker, *Acta Mater.* 69 (2014) 114–125.
- [303] L. Liu, H.C. Wu, J. Wang, S.K. Gong, S.X. Mao, *Philos. Mag. Lett.* 94 (2014) 225–232.
- [304] Y. Zhang, P.C. Millett, M. Tonks, S.B. Biner, *Acta Mater.* 60 (2012) 6421–6428.
- [305] Y. Zhang, P.C. Millett, M. Tonks, B. Biner, *Scr. Mater.* 66 (2012) 117–120.
- [306] T.M. Gapontseva, M.V. Degtyarev, V.P. Pilyugin, T.I. Chashchukhina, L.M. Voronova, A.M. Patselov, *Phys. Metals Metall.* 117 (2016) 336–347.
- [307] A. Staroselsky, L. Anand, *Int. J. Plast.* 19 (2003) 1843–1864.
- [308] A.A. Salem, S.R. Kalidindi, R.D. Doherty, *Acta Mater.* 51 (2003) 4225–4237.
- [309] S.R. Niezgoda, A.K. Kanjarla, I.J. Beyerlein, C.N. Tomé, *Int. J. Plast.* 56 (2014) 119–138.
- [310] J.C. Williams, R.G. Baggerly, N.E. Paton, *Metall. Mater. Trans. A* 33 (2002) 837–850.
- [311] G. Proust, C.N. Tomé, A. Jain, S.R. Agnew, *Int. J. Plast.* 25 (2009) 861–880.
- [312] M.H. Yoo, S.R. Agnew, J.R. Morris, K.M. Ho, *Mat. Sci. Eng.: A* 319–321 (2001) 87–92.
- [313] Z. Wu, W.A. Curtin, *Proc. Natl. Acad. Sci.* 113 (2016) 11137–11142.
- [314] Q. Yu, J. Sun, J.W. Morris Jr, A.M. Minor, *Scr. Mater.* 69 (2013) 57–60.
- [315] W.D. Callister, *Materials Science and Engineering: An Introduction*, John Wiley & Sons, 2007.
- [316] I.P. Jones, W.B. Hutchinson, *Acta Metall.* 29 (1981) 951–968.
- [317] M. Knezevic, A. Levinson, R. Harris, R.K. Mishra, R.D. Doherty, S.R. Kalidindi, *Acta Mater.* 58 (2010) 6230–6242.
- [318] J.I. Dickson, G.B. Craig, *J. Nucl. Mater.* 40 (1971) 346–348.
- [319] A. Akhtar, *Acta Metall.* 21 (1973) 1–11.
- [320] M. Knezevic, R.J. McCabe, C.N. Tomé, R.A. Lebensohn, S.R. Chen, C.M. Cady, G.T. Gray III, B. Mihaila, *Int. J. Plast.* 43 (2013) 70–84.
- [321] A.A. Salem, S.R. Kalidindi, R.D. Doherty, *Scr. Mater.* 46 (2002) 419–423.
- [322] M. Knezevic, I.J. Beyerlein, T. Nizolek, N.A. Mara, T.M. Pollock, *Mater. Res. Lett.* 1 (2013) 133–140.
- [323] V.V. Stolyarov, Y.T. Zhu, I.V. Alexandrov, T.C. Lowe, R.Z. Valiev, *Mater. Sci. Eng.: A* 299 (2001) 59–67.
- [324] J.P. Poirier, J. Antolin, J.M. Dupouy, *Can. J. Phys.* 45 (1967) 1221–1224.
- [325] D.W. Brown, I.J. Beyerlein, T.A. Sisneros, B. Clausen, C.N. Tomé, *Int. J. Plast.* 29 (2012) 120–135.
- [326] M. Knezevic, I.J. Beyerlein, D.W. Brown, T.A. Sisneros, C.N. Tomé, *Int. J. Plast.* 49 (2013) 185–198.
- [327] T.B. Britton, F.P.E. Dunne, A.J. Wilkinson, *Proc. R. Soc. A* 471 (2015) 20140881.
- [328] P. Gao, S.Q. Zhu, X.H. An, S.Q. Xu, D. Ruan, C. Chen, H.G. Yan, S.P. Ringer, X.Z. Liao, *Mater. Sci. Eng.: A* 691 (2017) 150–154.
- [329] A. Chapuis, J.H. Driver, *Acta Mater.* 59 (2011) 1986–1994.
- [330] M. Arul Kumar, I.J. Beyerlein, R.J. McCabe, C.N. Tomé, *Nat. Commun.* 7 (2016) 13826.
- [331] H. Li, D.E. Mason, T.R. Bieler, C.J. Boehlert, M.A. Crimp, *Acta Mater.* 61 (2013) 7555–7567.
- [332] L. Wang, Z. Zheng, H. Phukan, P. Kenesei, J.S. Park, J. Lind, R.M. Suter, T.R. Bieler, *Acta Mater.* 132 (2017) 598–610.
- [333] A.A. Salem, S.R. Kalidindi, S.L. Semiatin, *Acta Mater.* 53 (2005) 3495–3502.
- [334] X. Wu, S.R. Kalidindi, C. Necker, A.A. Salem, *Acta Mater.* 55 (2007) 423–432.
- [335] M. Knezevic, R.A. Lebensohn, O. Cazacu, B. Revil-Baudard, G. Proust, S.C. Vogel, M.E. Nixon, *Mater. Sci. Eng.: A* 564 (2013) 116–126.
- [336] Y. Todaka, J. Sasaki, T. Moto, M. Umamoto, *Scr. Mater.* 59 (2008) 615–618.
- [337] M.T. Pérez-Prado, A.A. Gimazov, O.A. Ruano, M.E. Kassner, A.P. Zhilyaev, *Scr. Mater.* 58 (2008) 219–222.

- [338] K. Edalati, Z. Horita, Y. Mine, *Mater. Sci. Eng.: A* 527 (2010) 2136–2141.
- [339] M.T. Pérez-Prado, A.P. Zhilyaev, *Phys. Rev. Lett.* 102 (2009) 175504.
- [340] S.K. Sikka, Y.K. Vohra, R. Chidambaram, *Prog. Mater. Sci.* 27 (1982) 245–310.
- [341] J. Gong, A.J. Wilkinson, *Acta Mater.* 59 (2011) 5970–5981.
- [342] J.F. Stohr, J.P. Poirier, *Philos. Mag.* 25 (1972) 1313–1329.
- [343] S. Biswas, S. Singh Dhinwal, S. Suwas, *Acta Mater.* 58 (2010) 3247–3261.
- [344] D.C. Foley, M. Al-Maharbi, K.T. Hartwig, I. Karaman, L.J. Kecskes, S.N. Mathaudhu, *Scr. Mater.* 64 (2011) 193–196.
- [345] T. Benjamin Britton, A.J. Wilkinson, *Acta Mater.* 60 (2012) 5773–5782.
- [346] J. Gong, A.J. Wilkinson, *Acta Mater.* 57 (2009) 5693–5705.
- [347] P. Šedá, A. Ostapovets, A. Jäger, P. Lejček, *Philos. Mag.* 92 (2012) 1223–1237.
- [348] R.B. Figueiredo, T.G. Langdon, *Mater. Sci. Eng.: A* 501 (2009) 105–114.
- [349] Y.B. Wang, M. Louie, Y. Cao, X.Z. Liao, H.J. Li, S.P. Ringer, Y.T. Zhu, *Scr. Mater.* 62 (2010) 214–217.
- [350] M.R. Barnett, *Mater. Sci. Eng.: A* 464 (2007) 8–16.
- [351] R.B. Figueiredo, P.R. Cetlin, T.G. Langdon, *Acta Mater.* 55 (2007) 4769–4779.
- [352] S.R. Agnew, P. Mehrotra, T.M. Lillo, G.M. Stoica, P.K. Liaw, *Acta Mater.* 53 (2005) 3135–3146.
- [353] E. Dogan, M.W. Vaughan, S.J. Wang, I. Karaman, G. Proust, *Acta Mater.* 89 (2015) 408–422.
- [354] S.L. Semiatin, V.M. Segal, R.E. Goforth, N.D. Frey, D.P. DeLo, *Metall. Mater. Trans. A* 30A (1999) 1425–1435.
- [355] C.S. Meredith, A.S. Khan, *Int. J. Plast.* 30–31 (2012) 202–217.
- [356] S.Q. Zhu, H.G. Yan, X.Z. Liao, S.J. Moody, G. Sha, Y.Z. Wu, S.P. Ringer, *Acta Mater.* 82 (2015) 344–355.
- [357] S.Q. Zhu, S.P. Ringer, *Acta Mater.* 144 (2018) 365–375.
- [358] J.L. Sun, P.W. Trimby, F.K. Yan, X.Z. Liao, N.R. Tao, J.T. Wang, *Acta Mater.* 79 (2014) 47–58.
- [359] S.D. Antolovich, R.W. Armstrong, *Prog. Mater. Sci.* 59 (2014) 1–160.
- [360] Q. Wei, L. Kecskes, T. Jiao, K.T. Hartwig, K.T. Ramesh, E. Ma, *Acta Mater.* 52 (2004) 1859–1869.
- [361] F. Kang, J.T. Wang, Y. Peng, *Mater. Sci. Eng.: A* 487 (2008) 68–73.
- [362] X. Zhao, W. Fu, X. Yang, T.G. Langdon, *Scr. Mater.* 59 (2008) 542–545.
- [363] J.A. del Valle, F. Carreño, O.A. Ruano, *Acta Mater.* 54 (2006) 4247–4259.
- [364] C.M. Cepeda-Jiménez, J.M. Molina-Aldareguia, F. Carreño, M.T. Pérez-Prado, *Acta Mater.* 85 (2015) 1–13.
- [365] I. Kim, J. Kim, D.H. Shin, X.Z. Liao, Y.T. Zhu, *Scr. Mater.* 48 (2003) 813–817.
- [366] D.-H. Kang, T.-W. Kim, *Mater. Des.* 31 (Suppl. 1) (2010) S54–S60.
- [367] V.V. Stolyarov, Y.T. Zhu, T.C. Lowe, R.Z. Valiev, *Mater. Sci. Eng.: A* 303 (2001) 82–89.
- [368] S.R. Agnew, P. Mehrotra, T.M. Lillo, G.M. Stoica, P.K. Liaw, *Mater. Sci. Eng.: A* 408 (2005) 72–78.
- [369] B. Beausir, S. Suwas, L.S. Tóth, K.W. Neale, J.-J. Fundenberger, *Acta Mater.* 56 (2008) 200–214.
- [370] C.M. Cepeda-Jiménez, J.M. Molina-Aldareguia, M.T. Pérez-Prado, *Acta Mater.* 88 (2015) 232–244.
- [371] K. Xia, J.T. Wang, X. Wu, G. Chen, M. Gurvan, *Mater. Sci. Eng.: A* 410–411 (2005) 324–327.
- [372] R.B. Figueiredo, T.G. Langdon, *Mater. Sci. Eng.: A* 528 (2011) 4500–4506.
- [373] Y.B. Wang, D.D. Qu, X.H. Wang, Y. Cao, X.Z. Liao, M. Kawasaki, S.P. Ringer, Z.W. Shan, T.G. Langdon, J. Shen, *Acta Mater.* 60 (2012) 253–260.
- [374] A. Jäger, V. Gärtnerova, K. Tesař, *Mater. Sci. Eng.: A* 644 (2015) 114–120.
- [375] X. Zhao, X. Yang, X. Liu, X. Wang, T.G. Langdon, *Mater. Sci. Eng.: A* 527 (2010) 6335–6339.
- [376] Y. Xirong, Z. Xicheng, F. Wenjie, *Rare Metal Mater. Eng.* 38 (2009) 955–957.
- [377] G.G. Yapici, I. Karaman, H.J. Maier, *Mater. Sci. Eng.: A* 434 (2006) 294–302.
- [378] Z. Zeng, S. Jonsson, H.J. Roven, *Acta Mater.* 57 (2009) 5822–5833.
- [379] Y.J. Chen, Y.J. Li, J.C. Walmsley, S. Dumoulin, P.C. Skaret, H.J. Roven, *Mater. Sci. Eng.: A* 527 (2010) 789–796.
- [380] Z. Horita, K. Matsubara, K. Makii, T.G. Langdon, *Scr. Mater.* 47 (2002) 255–260.
- [381] K. Edalati, Z. Horita, S. Yagi, E. Matsubara, *Mater. Sci. Eng.: A* 523 (2009) 277–281.
- [382] V.V. Stolyarov, Y.T. Zhu, I.V. Alexandrov, T.C. Lowe, R.Z. Valiev, *Mater. Sci. Eng.: A* 343 (2003) 43–50.
- [383] K. Edalati, A. Yamamoto, Z. Horita, T. Ishihara, *Scr. Mater.* 64 (2011) 880–883.
- [384] N. Munroe, X. Tan, H. Gu, *Scr. Mater.* 36 (1997) 1383–1386.
- [385] Y.J. Li, Y.J. Chen, J.C. Walmsley, R.H. Mathinsen, S. Dumoulin, H.J. Roven, *Scr. Mater.* 62 (2010) 443–446.
- [386] D.H. Shin, I. Kim, J. Kim, Y.S. Kim, S.L. Semiatin, *Acta Mater.* 51 (2003) 983–996.
- [387] A. Ghaderi, M.R. Barnett, *Acta Mater.* 59 (2011) 7824–7839.
- [388] D.H. Shin, I. Kim, J. Kim, Y.T. Zhu, *Mater. Sci. Eng.: A* 334 (2002) 239–245.
- [389] G. Proust, C.N. Tomé, G.C. Kaschner, *Acta Mater.* 55 (2007) 2137–2148.
- [390] J.L. Sun, P.W. Trimby, X. Si, X.Z. Liao, N.R. Tao, J.T. Wang, *Scr. Mater.* 68 (2013) 475–478.
- [391] Y.B. Chun, S.H. Yu, S.L. Semiatin, S.K. Hwang, *Mater. Sci. Eng.: A* 398 (2005) 209–219.
- [392] Q. Yu, J. Wang, Y. Jiang, R.J. McCabe, N. Li, C.N. Tomé, *Acta Mater.* 77 (2014) 28–42.
- [393] J.P. Hirth, J. Wang, C.N. Tomé, *Prog. Mater. Sci.* 83 (2016) 417–471.
- [394] M. Gong, J.P. Hirth, Y. Liu, Y. Shen, J. Wang, *Mater. Res. Lett.* 5 (2017) 449–464.
- [395] P. Molnár, A. Jäger, P. Lejček, *Scr. Mater.* 67 (2012) 467–470.
- [396] M. Zecevic, M. Knezevic, I.J. Beyerlein, C.N. Tomé, *Mater. Sci. Eng.: A* 638 (2015) 262–274.
- [397] H. Wang, P.D. Wu, J. Wang, C.N. Tomé, *Int. J. Plast.* 49 (2013) 36–52.
- [398] J. Wang, L. Liu, C.N. Tomé, S.X. Mao, S.K. Gong, *Mater. Res. Lett.* 1 (2013) 81–88.
- [399] J.L. Sun, P.W. Trimby, F.K. Yan, X.Z. Liao, N.R. Tao, J.T. Wang, *Scr. Mater.* 69 (2013) 428–431.
- [400] Q. Yu, Z.-W. Shan, J. Li, X. Huang, L. Xiao, J. Sun, E. Ma, *Nature* 463 (2010) 335.
- [401] Q. Yu, R.K. Mishra, A.M. Minor, *JOM* 64 (2012) 1235–1240.
- [402] X.L. Wu, K.M. Youssef, C.C. Koch, S.N. Mathaudhu, L.J. Kecskes, Y.T. Zhu, *Scr. Mater.* 64 (2011) 213–216.
- [403] J. Li, W. Xu, X. Wu, H. Ding, K. Xia, *Mater. Sci. Eng.: A* 528 (2011) 5993–5998.
- [404] I.A. Ovid'ko, R.Z. Valiev, Y.T. Zhu, *Prog. Mater. Sci.* 94 (2018) 462–540.
- [405] S. Lu, Q.-M. Hu, E.K. Delczeg-Czirjak, B. Johansson, L. Vitos, *Acta Mater.* 60 (2012) 4506–4513.
- [406] F.A. Mohamed, S.S. Dheda, *Mater. Sci. Eng.: A* 558 (2012) 59–63.
- [407] M.J. Zehetbauer, J. Kohout, E. Schafner, F. Sachslehner, A. Dubravina, *J. Alloys Compd.* 378 (2004) 329–334.
- [408] U. Andrade, M.A. Meyers, K.S. Vecchio, A.H. Chokshi, *Acta Metall. Mater.* 42 (1994) 3183–3195.
- [409] J. Eckert, J.C. Holzer, C.E. Krill III, W.L. Johnson, *J. Mater. Res.* 7 (1992) 1751–1761.
- [410] D. Oleszak, P.H. Shingu, *J. Appl. Phys.* 79 (1996) 2975–2980.
- [411] H.J. Fecht, *Nanostruct. Mater.* 6 (1995) 33–42.
- [412] F.A. Mohamed, *Mater. Sci. Eng.: A* 527 (2010) 2157–2162.
- [413] T. Yu, N. Hansen, X. Huang, *Acta Mater.* 61 (2013) 6577–6586.
- [414] X. Sauvage, G. Wilde, S.V. Divinski, Z. Horita, R.Z. Valiev, *Mater. Sci. Eng.: A* 540 (2012) 1–12.
- [415] P.R. Cantwell, M. Tang, S.J. Dillon, J. Luo, G.S. Rohrer, M.P. Harmer, *Acta Mater.* 62 (2014) 1–48.
- [416] C. Zener, J.H. Hollomon, *J. Appl. Phys.* 15 (1944) 22–32.
- [417] Y. Estrin, N.V. Isaev, S.V. Lubenets, S.V. Malykhin, A.T. Pugachov, V.V. Pustovalov, E.N. Reshetnyak, V.S. Fomenko, L.S. Fomenko, S.E. Shumilin, M. Janecek, R.J. Hellmig, *Acta Mater.* 54 (2006) 5581–5590.
- [418] V.S. Sarma, J. Wang, W.W. Jian, A. Kauffmann, H. Conrad, J. Freudenberger, Y.T. Zhu, *Mater. Sci. Eng.: A* 527 (2010) 7624–7630.
- [419] L.H. Su, C. Lu, L.Z. He, L.C. Zhang, P. Guagliardo, A.K. Tieu, S.N. Samarín, J.F. Williams, H.J. Li, *Acta Mater.* 60 (2012) 4218–4228.
- [420] T. Yu, D.A. Hughes, N. Hansen, X. Huang, *Acta Mater.* 86 (2015) 269–278.
- [421] E.I. Galindo-Nava, P.E.J. Rivera-Díaz-del-Castillo, *Mater. Sci. Eng.: A* 558 (2012) 641–648.
- [422] H. Paul, J.H. Driver, Z. Jasiński, *Acta Mater.* 50 (2002) 815–830.
- [423] T. Hebesberger, H.P. Stüwe, A. Vorhauer, F. Wetscher, R. Pippan, *Acta Mater.* 53 (2005) 393–402.
- [424] E.I. Galindo-Nava, C.M.F. Rae, *Mater. Sci. Eng.: A* 636 (2015) 434–445.
- [425] R.B. Godiksen, Z.T. Trautt, M. Upmanyu, J. Schiotz, D.J. Jensen, S. Schmidt, *Acta Mater.* 55 (2007) 6383–6391.
- [426] C. Günster, D.A. Molodov, G. Gottstein, *Acta Mater.* 61 (2013) 2363–2375.
- [427] K. Edalati, J.M. Cubero-Sesin, A. Alhamidi, I.F. Mohamed, Z. Horita, *Mater. Sci. Eng.: A* 613 (2014) 103–110.
- [428] Y. Ivanisenko, L. Kurmanaeva, J. Weissmueller, K. Yang, J. Markmann, H. Rösner, T. Scherer, H.J. Fecht, *Acta Mater.* 57 (2009) 3391–3401.
- [429] K. Edalati, D. Akama, A. Nishio, S. Lee, Y. Yonenaga, J.M. Cubero-Sesin, Z. Horita, *Acta Mater.* 69 (2014) 68–77.
- [430] Y.S. Li, Y. Zhang, N.R. Tao, K. Lu, *Acta Mater.* 57 (2009) 761–772.
- [431] G.P.M. Leyson, L.G. Hector, W.A. Curtin, *Acta Mater.* 60 (2012) 3873–3884.
- [432] Y. Lin, H. Wen, Y. Li, B. Wen, W. Liu, E.J. Lavernia, *Acta Mater.* 82 (2015) 304–315.
- [433] E. Bruder, P. Braun, H.u. Rehman, R.K.W. Marceau, A.S. Taylor, R. Pippan, K. Durst, *Scr. Mater.* 144 (2018) 5–8.
- [434] D.J. Lee, E.Y. Yoon, D.-H. Ahn, B.H. Park, H.W. Park, L.J. Park, Y. Estrin, H.S. Kim, *Acta Mater.* 76 (2014) 281–293.
- [435] K. Zhang, J.R. Weertman, J.A. Eastman, *Appl. Phys. Lett.* 87 (2005) 061921–061923.
- [436] M. Jin, A.M. Minor, E.A. Stach, J.W. Morris Jr, *Acta Mater.* 52 (2004) 5381–5387.
- [437] L. Li, T. Ungár, Y.D. Wang, G.J. Fan, Y.L. Yang, N. Jia, Y. Ren, G. Tichy, J. Lendvai, H. Choo, P.K. Liaw, *Scr. Mater.* 60 (2009) 317–320.
- [438] L. Li, T. Ungár, Y.D. Wang, J.R. Morris, G. Tichy, J. Lendvai, Y.L. Yang, Y. Ren, H. Choo, P.K. Liaw, *Acta Mater.* 57 (2009) 4988–5000.
- [439] G.J. Fan, L.F. Fu, H. Choo, P.K. Liaw, N.D. Browning, *Acta Mater.* 54 (2006) 4781–4792.
- [440] G.J. Fan, Y.D. Wang, L.F. Fu, H. Choo, P.K. Liaw, Y. Ren, N.D. Browning, *Appl. Phys. Lett.* 88 (2006) 171914.
- [441] S. Cheng, Y.H. Zhao, Y.Z. Guo, Y. Li, Q.M. Wei, X.L. Wang, Y. Ren, P.K. Liaw, H. Choo, E.J. Lavernia, *Adv. Mater.* 21 (2009) 5001–5004.
- [442] X.Z. Liao, A.R. Kilmametov, R.Z. Valiev, H. Gao, X. Li, A.K. Mukherjee, J.F. Bingert, Y.T. Zhu, *Appl. Phys. Lett.* 88 (2006) 021909.
- [443] A.P. Zhilyaev, A.A. Gimazov, E.P. Soshnikova, Á. Révész, T.G. Langdon, *Mater. Sci. Eng.: A* 489 (2008) 207–212.
- [444] F. Dalla Torre, P. Spätig, R. Schäublin, M. Victoria, *Acta Mater.* 53 (2005) 2337–2349.
- [445] N. Krasilnikov, W. Lojkowski, Z. Pakiel, R. Valiev, *Mater. Sci. Eng. A* 397 (2005) 330–337.
- [446] A.P. Zhilyaev, S. Lee, G.V. Nurislamova, R.Z. Valiev, T.G. Langdon, *Scr. Mater.* 44 (2001) 2753–2758.
- [447] A.J. Haslam, S.R. Phillpot, H. Wolf, D. Moldovan, H. Gleiter, *Mater. Sci. Eng. A* 318 (2001) 293–312.
- [448] J. Schiotz, *Mater. Sci. Eng. A* 375 (2004) 975–979.
- [449] F. Sansoz, V. Dupont, *Appl. Phys. Lett.* 89 (2006) 111901.
- [450] J. Monk, D. Farkas, *Phys. Rev. B* 75 (2007) 045414.
- [451] D. Farkas, S. Mohanty, J. Monk, *Phys. Rev. Lett.* 98 (2007) 165502.
- [452] D. Moldovan, V. Yamakov, D. Wolf, S.R. Phillpot, *Phys. Rev. Lett.* 89 (2002)

- 206101.
- [453] D.S. Gianola, S. Van Petegem, M. Legros, S. Brandstetter, H. Van Swygenhoven, K.J. Hemker, *Acta Mater.* 54 (2006) 2253–2263.
- [454] M. Legros, D.S. Gianola, K.J. Hemker, *Acta Mater.* 56 (2008) 3380–3393.
- [455] A.J. Haslam, D. Moldovan, V. Yamakov, D. Wolf, S.R. Phillpot, H. Gleiter, *Acta Mater.* 51 (2003) 2097–2112.
- [456] S. Ni, Y.B. Wang, X.Z. Liao, S.N. Alhajeri, H.Q. Li, Y.H. Zhao, E.J. Lavernia, S.P. Ringer, T.G. Langdon, Y.T. Zhu, *Mater. Sci. Eng.: A* 528 (2011) 3398–3403.
- [457] S. Cheng, Y. Zhao, Y. Wang, Y. Li, X.-L. Wang, P.K. Liaw, E.J. Lavernia, *Phys. Rev. Lett.* 104 (2010) 255501.
- [458] K. Lu, L. Lu, S. Suresh, *Science* 324 (2009) 349–352.
- [459] J.Y. Zhang, G. Liu, R.H. Wang, J. Li, J. Sun, E. Ma, *Phys. Rev. B* 81 (2010) 172104.
- [460] N. Hansen, X. Huang, *Acta Mater.* 46 (1998) 1827–1836.
- [461] Q. Liu, D.J. Jensen, N. Hansen, *Acta Mater.* 46 (1998) 5819–5838.
- [462] T. Ungar, J. Gubicza, G. Ribarik, A. Borbely, *J. Appl. Crystallogr.* 34 (2001) 298–310.
- [463] U.F. Kocks, *J. Eng. Mater. Technol.* 98 (1976) 76–85.
- [464] Y. Estrin, H. Mecking, *Acta Metall.* 32 (1984) 57–70.
- [465] X.L. Wu, Y.T. Zhu, Y.G. Wei, Q. Wei, *Phys. Rev. Lett.* 103 (2009) 205504.
- [466] Y.T. Zhu, J. Narayan, J.P. Hirth, S. Mahajan, X.L. Wu, X.Z. Liao, *Acta Mater.* 57 (2009) 3763–3770.
- [467] V. Bulatov, F.F. Abraham, L. Kubin, B. Devincere, S. Yip, *Nature* 391 (1998) 669–672.
- [468] V.B. Shenoy, R.V. Kukta, R. Phillips, *Phys. Rev. Lett.* 84 (2000) 1491–1494.
- [469] D. Rodney, R. Phillips, *Phys. Rev. Lett.* 82 (1999) 1704–1707.
- [470] M.J. Buehler, A. Hartmaier, M.A. Duchaineau, F.R. Abraham, H.J. Gao, *Acta Mech. Sin.* 21 (2005) 103–111.
- [471] L.H. Wang, X.D. Han, P. Liu, Y.H. Yue, Z. Zhang, E. Ma, *Phys. Rev. Lett.* 105 (2010) 135501.
- [472] R. Madec, B. Devincere, L. Kubin, T. Hoc, D. Rodney, *Science* 301 (2003) 1879–1882.
- [473] C.M. Cepeda-Jimenez, J.M. Garcia-Infanta, A.P. Zhilyaev, O.A. Ruano, F. Carreno, *J. Alloys Compd.* 509 (2011) 636–643.
- [474] Y. Ivanisenko, I. MacLaren, X. Sauvage, R.Z. Valiev, H.J. Fecht, *Acta Mater.* 54 (2006) 1659–1669.
- [475] X. Sauvage, Y. Ivanisenko, *J. Mater. Sci.* 42 (2007) 1615–1621.
- [476] Y. Ivanisenko, W. Lojkowski, R.Z. Valiev, H.J. Fecht, *Acta Mater.* 51 (2003) 5555–5570.
- [477] B.B. Straumal, A.A. Mazilkin, S.G. Protasova, S.V. Dobatkin, A.O. Rodin, B. Baretzky, D. Goll, G. Schutz, *Mater. Sci. Eng. A* 503 (2009) 185–189.
- [478] O.N. Senkov, F.H. Froes, V.V. Stolyarov, R.Z. Valiev, J. Liu, *Scr. Mater.* 38 (1998) 1511–1516.
- [479] H. Shen, Z. Li, B. Gunther, A.V. Korznikov, R. Valiev, *Nanostruct. Mater.* 6 (1995) 385–388.
- [480] Y.V. Ivanisenko, K. Korznikov, L. Safarov, R. Valiev, *Nanostruct. Mater.* 6 (1995) 433–436.
- [481] S. Ohsaki, S. Kato, N. Tsuji, T. Ohkubo, K. Hono, *Acta Mater.* 55 (2007) 2885–2895.
- [482] X. Sauvage, W. Lefebvre, C. Genevois, S. Ohsaki, K. Hono, *Scr. Mater.* 60 (2009) 1056–1061.
- [483] X. Sauvage, C. Genevois, G. Da Costa, V. Pantisyrny, *Scr. Mater.* 61 (2009) 660–663.
- [484] A.A. Mazilkin, B.B. Straumal, E. Rabkin, B. Baretzky, S. Enders, S.G. Protasova, O.A. Kogtenkova, R.Z. Valiev, *Acta Mater.* 54 (2006) 3933–3939.
- [485] B.B. Straumal, B. Baretzky, A.A. Mazilkin, F. Philipp, O.A. Kogtenkova, M.N. Volkov, R.Z. Valiev, *Acta Mater.* 52 (2004) 4469–4478.
- [486] B.B. Straumal, S.G. Protasova, A.A. Mazilkin, E. Rabkin, D. Goll, G. Schutz, B. Baretzky, R.Z. Valiev, *J. Mater. Sci.* 47 (2012) 360–367.
- [487] A.A. Mazilkin, G.E. Abrosimova, S.G. Protasova, B.B. Straumal, G. Schutz, S.V. Dobatkin, A.S. Bakai, *J. Mater. Sci.* 46 (2011) 4336–4342.
- [488] S.D. Prokoshkin, I.Y. Khmelevskaya, S.V. Dobatkin, I.B. Trubitsyna, E.V. Tatyamin, V.V. Stolyarov, E.A. Prokofiev, *Acta Mater.* 53 (2005) 2703–2714.
- [489] A.V. Sergueeva, C. Song, R.Z. Valiev, A.K. Mukherjee, *Mater. Sci. Eng. A* 339 (2003) 159–165.
- [490] V.V. Stolyarov, D.V. Gunderov, A.G. Popov, V.S. Gaviko, A.S. Ermolenko, *J. Alloys Compd.* 281 (1998) 69–71.
- [491] A. Revesz, S. Hobor, J.L. Labar, A.P. Zhilyaev, Z. Kovacs, *J. Appl. Phys.* 100 (2006) 103522.
- [492] A.M. Glezer, M.P. Plotnikova, A.V. Shalimova, S.V. Dobatkin, *Bull. Russ. Acad. Sci. Phys.* 73 (2009) 1233–1239.
- [493] S. Hobor, Z. Kovacs, A.P. Zhilyaev, L.K. Varga, P.J. Szabo, A. Revesz, W. Skrotzki, C.G. Oertel, H. Biermann, M. Heilmaier (Eds.), 15th International Conference on the Strength of Materials, vol. 240, Iop Publishing Ltd., Bristol, 2010.
- [494] S. Hobor, A. Revesz, P.J. Szabo, A.P. Zhilyaev, V.K. Kis, J.L. Labar, Z. Kovacs, *J. Appl. Phys.* 104 (2008) 033525.
- [495] Z. Kovacs, P. Henits, A.P. Zhilyaev, A. Revesz, *Scr. Mater.* 54 (2006) 1733–1737.
- [496] A. Revesz, E. Schafner, Z. Kovacs, *Appl. Phys. Lett.* 92 (2008) 011910.
- [497] P. Henits, A. Revesz, A.P. Zhilyaev, Z. Kovacs, *J. Alloys Compd.* 461 (2008) 195–199.
- [498] Z. Kovacs, P. Henits, A.P. Zhilyaev, N.Q. Chinh, A. Revesz, W.J. Poole, M.A. Wells, D.J. Lloyd (Eds.), *Aluminium Alloys 2006*, Pts 1 and 2, vol. 519–521, Trans Tech Publications Ltd., Stafa-Zurich, 2006, pp. 1329–1334.
- [499] K. Edalati, H. Emami, A. Staykov, D.J. Smith, E. Akiba, Z. Horita, *Acta Mater.* 99 (2015) 150–156.
- [500] K. Edalati, H. Emami, Y. Ikeda, H. Iwaoka, I. Tanaka, E. Akiba, Z. Horita, *Acta Mater.* 108 (2016) 293–303.
- [501] K. Edalati, R. Uehiro, K. Fujiwara, Y. Ikeda, H.-W. Li, X. Sauvage, R.Z. Valiev, E. Akiba, I. Tanaka, Z. Horita, *Mater. Sci. Eng.: A* 701 (2017) 158–166.
- [502] K. Edalati, R. Uehiro, Y. Ikeda, H.-W. Li, H. Emami, Y. Filinchuk, M. Arita, X. Sauvage, I. Tanaka, E. Akiba, Z. Horita, *Acta Mater.* 149 (2018) 88–96.
- [503] B.B. Straumal, O.A. Kogtenkova, R.Z. Valiev, P. Zieba, B. Baretzky, *Diffus. Found.* 5 (2015) 95–108.
- [504] A.A. Mazilkin, B.B. Straumal, M.V. Borodachenkova, R.Z. Valiev, O.A. Kogtenkova, B. Baretzky, *Mater. Lett.* 84 (2012) 63–65.
- [505] Y.B. Wang, X.Z. Liao, Y.H. Zhao, J.C. Cooley, Z. Horita, Y.T. Zhu, *Appl. Phys. Lett.* 102 (2013) 231912.
- [506] L.C. Zhang, M. Calin, F. Paturaud, C. Mickel, J. Eckert, *Appl. Phys. Lett.* 90 (2007) 201908.
- [507] Y. Ustinovshikov, S. Tresheva, *Mater. Sci. Eng. A* A248 (1998) 238–244.
- [508] B.B. Straumal, V. Pontikis, A.R. Kilmametov, A.A. Mazilkin, S.V. Dobatkin, B. Baretzky, *Acta Mater.* 122 (2017) 60–71.
- [509] J.Y. Huang, Y.T. Zhu, X.Z. Liao, R.Z. Valiev, *Philos. Mag. Lett.* 84 (2004) 183–190.
- [510] D.D. Qu, Y.B. Wang, X.Z. Liao, J. Shen, *Scr. Mater.* 67 (2012) 332–335.
- [511] K. Edalati, S. Toh, M. Arita, M. Watanabe, Z. Horita, *Appl. Phys. Lett.* 102 (2013) 181902.
- [512] X. Wu, N. Tao, Y. Hong, G. Liu, B. Xu, J. Lu, K. Lu, *Acta Mater.* 53 (2005) 681–691.
- [513] H.C. Wu, A. Kumar, J. Wang, X.F. Bi, C.N. Tome, Z. Zhang, S.X. Mao, *Sci. Rep.* 6 (2016) 8.
- [514] D.H. Hong, T.W. Lee, S.H. Lim, W.Y. Kim, S.K. Hwang, *Scr. Mater.* 69 (2013) 405–408.
- [515] H.L. Zhao, X.Y. Hu, M. Song, S. Ni, *Scr. Mater.* 132 (2017) 63–67.
- [516] H.L. Zhao, M. Song, S. Ni, S. Shao, J. Wang, X.Z. Liao, *Acta Mater.* 131 (2017) 271–279.
- [517] S.J. Wang, H. Wang, K. Du, W. Zhang, M.L. Sui, S.X. Mao, *Nat. Commun.* 5 (2014) 3433.
- [518] Y.B. Wang, Y.H. Zhao, Q. Lian, X.Z. Liao, R.Z. Valiev, S.P. Ringer, Y.T. Zhu, E.J. Lavernia, *Scr. Mater.* 63 (2010) 613–616.
- [519] H. Xing, J. Sun, *Appl. Phys. Lett.* 93 (2008) 031908.
- [520] R.J. Talling, R.J. Dashwood, M. Jackson, D. Dye, *Acta Mater.* 57 (2009) 1188–1198.
- [521] Y. Yang, G.P. Li, G.M. Cheng, Y.L. Li, K. Yang, *Appl. Phys. Lett.* 94 (2009) 061901.
- [522] Y. Qiu, M.L. Young, X. Nie, *Metall. Mater. Trans. A* 46A (2015) 4661–4668.
- [523] F.D. Bubani, M. Sade, V. Torra, F. Lovey, A. Yawny, *Mater. Sci. Eng. A* 583 (2013) 129–139.
- [524] Y. Liu, I. Karaman, H. Wang, X. Zhang, *Adv. Mater.* 26 (2014) 3893–3898.
- [525] X. Hui, S.J. Duclos, A.L. Ruoff, Y.K. Vohra, *Phys. Rev. Lett.* 64 (1990) 204–207.
- [526] G.K. Dey, R. Tewari, S. Banerjee, G. Jyoti, S.C. Gupta, K.D. Joshi, S.K. Sikka, *Acta Mater.* 52 (2004) 5243–5254.
- [527] K.J. Caspersen, A. Lew, M. Ortiz, E.A. Carter, *Phys. Rev. Lett.* 93 (2004) 115501.
- [528] R. Jing, C.Y. Liu, M.Z. Ma, R.P. Liu, *J. Alloys Compd.* 552 (2013) 202–207.
- [529] R. Jing, S.X. Liang, C.Y. Liu, M.Z. Ma, R.P. Liu, *Mater. Sci. Eng. A* 559 (2013) 474–479.
- [530] Y. Koizumi, T. Fujita, Y. Minamino, S. Hata, *Acta Mater.* 58 (2010) 1104–1115.
- [531] G.P. Zheng, Y.M. Wang, M. Li, *Acta Mater.* 53 (2005) 3893–3901.
- [532] H. Zheng, J. Wang, J.Y. Huang, J.B. Wang, Z. Zhang, S.X. Mao, *Nano Lett.* 13 (2013) 6023–6027.
- [533] B. Chen, J. Wang, Y.W. Zhu, X.Z. Liao, C.S. Lu, Y.W. Mai, S.P. Ringer, F.J. Ke, Y.G. Shen, *Acta Mater.* 80 (2014) 392–399.
- [534] X.S. Yang, S. Sun, X.L. Wu, E. Ma, T.Y. Zhang, *Sci. Rep.* 4 (2014) 7.
- [535] X.S. Yang, S. Sun, T.Y. Zhang, *Acta Mater.* 95 (2015) 264–273.
- [536] J.Q. Ren, Q.Y. Sun, L. Xiao, X.D. Ding, J. Sun, *Comput. Mater. Sci.* 92 (2014) 8–12.
- [537] Q. Lin, J. Liu, X. An, H. Wang, Y. Zhang, X. Liao, *Mater. Res. Lett.* 6 (2018) 236–243.
- [538] S.B. Lee, J.E. LeDonne, S.C.V. Lim, I.J. Beyerlein, A.D. Rollett, *Acta Mater.* 60 (2012) 1747–1761.
- [539] W.Z. Han, E.K. Cerreta, N.A. Mara, I.J. Beyerlein, J.S. Carpenter, S.J. Zheng, C.P. Trujillo, P.O. Dickerson, A. Misra, *Acta Mater.* 63 (2014) 150–161.
- [540] A. Ma, K. Suzuki, Y. Nishida, N. Saito, I. Shigematsu, M. Takagi, H. Iwata, A. Watazu, T. Imura, *Acta Mater.* 53 (2005) 211–220.
- [541] X.P. Li, X.J. Wang, M. Saunders, A. Suvorova, L.C. Zhang, Y.J. Liu, M.H. Fang, Z.H. Huang, T.B. Sercombe, *Acta Mater.* 95 (2015) 74–82.
- [542] H.-W. Yen, S.W. Ooi, M. Eizadjou, A. Breen, C.-Y. Huang, H.K.D.H. Bhadeshia, S.P. Ringer, *Acta Mater.* 82 (2015) 100–114.
- [543] C. Xu, M. Furukawa, Z. Horita, T.G. Langdon, *Acta Mater.* 51 (2003) 6139–6149.
- [544] A. Belyakov, Y. Kimura, K. Tsuzaki, *Acta Mater.* 54 (2006) 2521–2532.
- [545] Y.I. Son, Y.K. Lee, K.T. Park, C.S. Lee, D.H. Shin, *Acta Mater.* 53 (2005) 3125–3134.
- [546] J.M. Garcia-Infanta, S. Swaminathan, A.P. Zhilyaev, F. Carreno, O.A. Ruano, T.R. McNelley, *Mater. Sci. Eng. A* 485 (2008) 160–175.
- [547] J.D. Embury, J.P. Hirth, *Acta Metall.* 42 (1994) 2051–2056.
- [548] J. Wang, A. Misra, *Curr. Opin. Solid State Mater. Sci.* 15 (2011) 20–28.
- [549] H.M. Zbib, C.T. Overman, F. Akasheh, D. Bahr, *Int. J. Plast.* 27 (2011) 1618–1639.
- [550] L. Provaille, B. Bakó, *Acta Mater.* 58 (2010) 5565–5571.
- [551] S.R. Macewen, P.B. Hirsch, V. Vitek, *Philos. Mag.* 28 (1973) 703–723.
- [552] J.S. Koehler, *Phys. Rev. B* 2 (1970) 547–551.
- [553] R.G. Hoagland, T.E. Mitchell, J.P. Hirth, H. Kung, *Philos. Mag.* A 82 (2002) 643–664.
- [554] G.S. Was, T. Foecke, *Thin Solid Films* 286 (1996) 1–31.
- [555] X.Y. Liu, R.G. Hoagland, J. Wang, T.C. Germann, A. Misra, *Acta Mater.* 58 (2010) 4549–4557.
- [556] X. Liu, R. Hao, S. Mao, S.J. Dillon, *Scr. Mater.* 130 (2017) 178–181.
- [557] R.F. Zhang, I.J. Beyerlein, S.J. Zheng, S.H. Zhang, A. Stukowski, T.C. Germann,

- Acta Mater. 113 (2016) 194–205.
- [558] R.F. Zhang, J. Wang, I.J. Beyerlein, A. Misra, T.C. Germann, *Acta Mater.* 60 (2012) 2855–2865.
- [559] M. Kawasaki, B. Ahn, T.G. Langdon, *Acta Mater.* 58 (2010) 919–930.
- [560] Y.Z. Tian, X.H. An, S.D. Wu, Z.F. Zhang, R.B. Figueiredo, N. Gao, T.G. Langdon, *Scr. Mater.* 63 (2010) 65–68.
- [561] J.M. García-Infanta, A.P. Zhilyaev, F. Carreño, O.A. Ruano, J.Q. Su, S.K. Menon, T.R. McNelley, *J. Mater. Sci.* 45 (2010) 4613–4620.
- [562] T. Mungole, N. Nadammal, K. Dawra, P. Kumar, M. Kawasaki, T.G. Langdon, *J. Mater. Sci.* 48 (2013) 4671–4680.
- [563] W. Wang, M. Yang, D. Yan, P. Jiang, F. Yuan, X. Wu, *Mater. Sci. Eng.: A* 702 (2017) 133–141.
- [564] M.X. Yang, F.P. Yuan, Q.G. Xie, Y.D. Wang, E. Ma, X.L. Wu, *Acta Mater.* 109 (2016) 213–222.
- [565] L. Thilly, M. Véron, O. Ludwig, F. Lecouturier, J.P. Peyrade, S. Askénazy, *Philos. Mag.* A 82 (2002) 925–942.
- [566] N. Jia, R. Lin Peng, D.W. Brown, B. Clausen, Y.D. Wang, *Metall. Mater. Trans. A* 39 (2008) 3134.
- [567] N. Jia, R. Lin Peng, Y.D. Wang, S. Johansson, P.K. Liaw, *Acta Mater.* 56 (2008) 782–793.
- [568] M.F. Ashby, *Philos. Mag.* 21 (1970) 399–424.
- [569] N. Jia, R.L. Peng, Y.D. Wang, G.C. Chai, S. Johansson, G. Wang, P.K. Liaw, *Acta Mater.* 54 (2006) 3907–3916.
- [570] M. Yang, Y. Pan, F. Yuan, Y. Zhu, X. Wu, *Mater. Res. Lett.* 4 (2016) 145–151.
- [571] J. Wang, R.G. Hoagland, J.P. Hirth, A. Misra, *Acta Mater.* 56 (2008) 3109–3119.
- [572] J. Wang, A. Misra, R.G. Hoagland, J.P. Hirth, *Acta Mater.* 60 (2012) 1503–1513.
- [573] Y.Z. Tian, S.D. Wu, Z.F. Zhang, R.B. Figueiredo, N. Gao, T.G. Langdon, *Acta Mater.* 59 (2011) 2783–2796.
- [574] N. Jia, R. Lin Peng, G.C. Chai, S. Johansson, Y.D. Wang, *Mater. Sci. Eng.: A* 491 (2008) 425–433.
- [575] X.H. An, S.M. Zhu, Y. Cao, M. Kawasaki, X.Z. Liao, S.P. Ringer, J.F. Nie, T.G. Langdon, Y.T. Zhu, *Appl. Phys. Lett.* 107 (2015) 011901.
- [576] X. Li, T. Kreuter, X.M. Luo, R. Schwaiger, G.P. Zhang, *Mater. Res. Lett.* 5 (2017) 20–28.
- [577] A. Misra, J.P. Hirth, R.G. Hoagland, *Acta Mater.* 53 (2005) 4817–4824.
- [578] N. Li, J. Wang, A. Misra, J.Y. Huang, *Microsc. Microanal.* 18 (2012) 1155–1162.
- [579] Y. Cao, M. Kawasaki, Y.B. Wang, S.N. Alhajeri, X.Z. Liao, W.L. Zheng, S.P. Ringer, Y.T. Zhu, T.G. Langdon, *J. Mater. Sci.* 45 (2010) 4545–4553.
- [580] N. Li, J. Wang, J.Y. Huang, A. Misra, X. Zhang, *Scr. Mater.* 63 (2010) 363–366.
- [581] M. Damadam, S. Shao, I. Salehinia, G. Ayoub, H.M. Zbib, *Mater. Res. Lett.* 5 (2017) 306–313.
- [582] A. Misra, J.P. Hirth, H. Kung, *Philos. Mag.* A 82 (2002) 2935–2951.
- [583] W.P. Vellinga, J.T.M. De Hosson, V. Vitek, *Acta Mater.* 45 (1997) 1525–1534.
- [584] J. McKeown, A. Misra, H. Kung, R.G. Hoagland, M. Nastasi, *Scr. Mater.* 46 (2002) 593–598.
- [585] J. Wang, I.J. Beyerlein, N.A. Mara, D. Bhattacharyya, *Scr. Mater.* 64 (2011) 1083–1086.
- [586] Y. Cao, Y.B. Wang, R.B. Figueiredo, L. Chang, X.Z. Liao, M. Kawasaki, W.L. Zheng, S.P. Ringer, T.G. Langdon, Y.T. Zhu, *Acta Mater.* 59 (2011) 3903–3914.
- [587] N. Jia, F. Roters, P. Eisenlohr, D. Raabe, X. Zhao, *Acta Mater.* 61 (2013) 4591–4606.
- [588] D. Bhattacharyya, N.A. Mara, P. Dickerson, R.G. Hoagland, A. Misra, *J. Mater. Res.* 24 (2011) 1291–1302.
- [589] N.A. Mara, D. Bhattacharyya, J.P. Hirth, P. Dickerson, A. Misra, *Appl. Phys. Lett.* 97 (2010) 021909.
- [590] J.W. Yan, X.F. Zhu, B. Yang, G.P. Zhang, *Phys. Rev. Lett.* 110 (2013) 155502.
- [591] D. Wang, T. Kups, J. Schawohl, P. Schaaf, *J. Mater. Sci.: Mater. Electron.* 23 (2012) 1077–1082.
- [592] Y.P. Li, X.F. Zhu, J. Tan, B. Wu, W. Wang, G.P. Zhang, *J. Mater. Res.* 24 (2011) 728–735.
- [593] Y.P. Li, J. Tan, G.P. Zhang, *Scr. Mater.* 59 (2008) 1226–1229.
- [594] S.J. Zheng, J. Wang, J.S. Carpenter, W.M. Mook, P.O. Dickerson, N.A. Mara, I.J. Beyerlein, *Acta Mater.* 79 (2014) 282–291.
- [595] M. Murayama, Z. Horita, K. Hono, *Acta Mater.* 49 (2001) 21–29.
- [596] H. Paul, A. Morawiec, J.H. Driver, E. Bouzy, *Int. J. Plast.* 25 (2009) 1588–1608.
- [597] P.S. Steif, *Int. J. Solids Struct.* 22 (1986) 195–207.
- [598] L. Anand, W.A. Spitzig, *J. Mech. Phys. Solids* 28 (1980) 113–128.
- [599] Y. Chen, N. Gao, G. Sha, S.P. Ringer, M.J. Starink, *Acta Mater.* 109 (2016) 202–212.
- [600] S.P. Ringer, B.T. Sofyan, K.S. Prasad, G.C. Quan, *Acta Mater.* 56 (2008) 2147–2160.
- [601] G. Sha, Y.B. Wang, X.Z. Liao, Z.C. Duan, S.P. Ringer, T.G. Langdon, *Acta Mater.* 57 (2009) 3123–3132.
- [602] S.P. Ringer, K. Hono, *Mater. Charact.* 44 (2000) 101–131.
- [603] Y.H. Zhao, X.Z. Liao, Z. Jin, R.Z. Valiev, Y.T. Zhu, *Acta Mater.* 52 (2004) 4589–4599.
- [604] G. Sha, Y.B. Wang, X.Z. Liao, Z.C. Duan, S.P. Ringer, T.G. Langdon, *Mater. Sci. Eng.: A* 527 (2010) 4742–4749.
- [605] P. Minárik, R. Král, M. Janeček, *Appl. Surf. Sci.* 281 (2013) 44–48.
- [606] K.D. Ralston, N. Birbilis, *Corrosion* 66 (2010) 075005–075005–075013.
- [607] R.Z. Valiev, M.Y. Murashkin, I. Sabirov, *Scr. Mater.* 76 (2014) 13–16.
- [608] Y.H. Zhao, X.Z. Liao, S. Cheng, E. Ma, Y.T. Zhu, *Adv. Mater.* 18 (2006) 2280–2283.
- [609] B.G. Clark, I.M. Robertson, L.M. Dougherty, D.C. Ahn, P. Sofronis, *J. Mater. Res.* 20 (2005) 1792–1801.
- [610] Y. Chen, N. Gao, G. Sha, S.P. Ringer, M.J. Starink, *Mater. Sci. Eng.: A* 627 (2015) 10–20.
- [611] Y.F. Shen, R.G. Guan, Z.Y. Zhao, R.D.K. Misra, *Acta Mater.* 100 (2015) 247–255.
- [612] P.J. Apps, M. Berta, P.B. Prangnell, *Acta Mater.* 53 (2005) 499–511.
- [613] X. Sauvage, N. Enikeev, R. Valiev, Y. Nasedkina, M. Murashkin, *Acta Mater.* 72 (2014) 125–136.
- [614] S.K. Samudrala, P.J. Felfel, V.J. Araullo-Peters, Y. Cao, X.Z. Liao, J.M. Cairney, *Ultramicroscopy* 132 (2013) 158–163.
- [615] W.Z. Zhang, G.C. Weatherly, *Prog. Mater. Sci.* 50 (2005) 181–292.
- [616] D.J. Chakrabarti, D.E. Laughlin, *Prog. Mater. Sci.* 49 (2004) 389–410.
- [617] C.M. Allen, K.A.Q. O'Reilly, B. Cantor, P.V. Evans, *Prog. Mater. Sci.* 43 (1998) 89–170.
- [618] E.A. Marquis, J.M. Hyde, *Mater. Sci. Eng. R-Rep.* 69 (2010) 37–62.
- [619] S.C. Tjong, Z.Y. Ma, *Mater. Sci. Eng. R-Rep.* 29 (2000) 49–113.
- [620] Y. Yuan, A. Ma, J. Jiang, F. Lu, W. Jian, D. Song, Y.T. Zhu, *Mater. Sci. Eng.: A* 588 (2013) 329–334.
- [621] J. Gubicza, I. Schiller, N.Q. Chinh, J. Illy, Z. Horita, T.G. Langdon, *Mater. Sci. Eng.: A* 460 (2007) 77–85.
- [622] Z. Liu, X. Chen, X. Han, Y. Gu, *Mater. Sci. Eng.: A* 527 (2010) 4300–4305.
- [623] Z. Liu, S. Bai, X. Zhou, Y. Gu, *Mater. Sci. Eng.: A* 528 (2011) 2217–2222.
- [624] W. Huang, Z. Liu, M. Lin, X. Zhou, L. Zhao, A. Ning, S. Zeng, *Mater. Sci. Eng.: A* 546 (2012) 26–33.
- [625] W. Lechner, W. Puff, B. Mingler, M.J. Zehetbauer, R. Würschum, *Scr. Mater.* 61 (2009) 383–386.
- [626] G. Sha, K. Tugcu, X.Z. Liao, P.W. Trimby, M.Y. Murashkin, R.Z. Valiev, S.P. Ringer, *Acta Mater.* 63 (2014) 169–179.
- [627] G. Nurislamova, X. Sauvage, M. Murashkin, R. Islamgaliev, R. Valiev, *Philos. Mag. Lett.* 88 (2008) 459–466.
- [628] G. Sha, L. Yao, X. Liao, S.P. Ringer, Z. Chao Duan, T.G. Langdon, *Ultramicroscopy* 111 (2011) 500–505.
- [629] S.V. Dobatkin, E.N. Bastarache, G. Sakai, T. Fujita, Z. Horita, T.G. Langdon, *Mater. Sci. Eng.: A* 408 (2005) 141–146.
- [630] M. Kuzmina, M. Herbig, D. Ponge, S. Sandlöbes, D. Raabe, *Science* 349 (2015) 1080–1083.
- [631] G. Sha, A. Cerezo, *Acta Mater.* 53 (2005) 907–917.
- [632] P.J. Apps, J.R. Bowen, P.B. Prangnell, *Acta Mater.* 51 (2003) 2811–2822.
- [633] F.J. Humphreys, *Acta Metall.* 27 (1979) 1801–1814.
- [634] F.J. Humphreys, M.G. Ardakani, *Acta Metall. Mater.* 42 (1994) 749–761.
- [635] J. Michael Shockey, C. Desrayaud, R.R. Chromik, S. Descartes, *Mater. Sci. Eng.: A* 684 (2017) 510–516.
- [636] Y. Wang, R. Guan, D. Hou, Y. Zhang, W. Jiang, H. Liu, J. Mater. Sci. 52 (2017) 1137–1148.
- [637] Y. Li, T.G. Langdon, *J. Mater. Sci.* 35 (2000) 1201–1204.
- [638] Y. Cao, L.C. Zhang, Y. Zhang, *Mater. Sci. Eng. A* 658 (2016) 321–325.
- [639] W. Xi, W. Sun, G.D. Han, L.L. Liu, S. Xue, L.R. Li, *Mater. Sci. Eng.: A* 628 (2015) 247–251.
- [640] F.J. Humphreys, P.B. Hirsch, *Philos. Mag.* 34 (1976) 373–390.
- [641] G. Sha, J.H. Li, W. Xu, K. Xia, W.Q. Jie, S.P. Ringer, *Mater. Sci. Eng.: A* 527 (2010) 5092–5099.
- [642] C. Xu, M. Furukawa, Z. Horita, T.G. Langdon, *Acta Mater.* 53 (2005) 749–758.
- [643] Y. Lin, H. Wen, Y. Li, B. Wen, W. Liu, E.J. Lavernia, *Metall. Mater. Trans. A* 45 (2014) 2673–2688.
- [644] R. Kirchheim, *Acta Mater.* 50 (2002) 413–419.
- [645] D.J. Lloyd, *Acta Metall. Mater.* 39 (1991) 59–71.
- [646] A. Erman, J. Groza, X. Li, H. Choi, G. Cao, *Mater. Sci. Eng.: A* 558 (2012) 39–43.
- [647] M. Habibnejad-Korayem, R. Mahmudi, W.J. Poole, *Mater. Sci. Eng.: A* 567 (2013) 89–94.
- [648] I. Nikulin, A. Kipelova, S. Malopheyev, R. Kaibyshev, *Acta Mater.* 60 (2012) 487–497.
- [649] M. Schöbel, P. Pongratz, H.P. Degischer, *Acta Mater.* 60 (2012) 4247–4254.
- [650] Y. Buranova, V. Kulitskiy, M. Peterlechner, A. Mogucheva, R. Kaibyshev, S.V. Divinski, G. Wilde, *Acta Mater.* 124 (2017) 210–224.
- [651] Y. Wang, M. Chen, F. Zhou, E. Ma, *Nature* 419 (2002) 912–915.
- [652] Z. Zeng, J.-F. Nie, S.-W. Xu, C.H.J. Davies, N. Birbilis, *Nat. Commun.* 8 (2017) 972.
- [653] R.Z. Valiev, I.V. Alexandrov, Y.T. Zhu, T.C. Lowe, *J. Mater. Res.* 17 (2002) 5–8.
- [654] Y. Estrin, L.S. Tóth, A. Molinari, Y. Bréchet, *Acta Mater.* 46 (1998) 5509–5522.
- [655] L. Balogh, R.B. Figueiredo, T. Ungár, T.G. Langdon, *Mater. Sci. Eng.: A* 528 (2010) 533–538.
- [656] J.S. Wang, M.D. Mulholland, G.B. Olson, D.N. Seidman, *Acta Mater.* 61 (2013) 4939–4952.
- [657] N. Kamikawa, X. Huang, N. Tsuji, N. Hansen, *Acta Mater.* 57 (2009) 4198–4208.
- [658] H. Wen, T.D. Topping, D. Isheim, D.N. Seidman, E.J. Lavernia, *Acta Mater.* 61 (2013) 2769–2782.
- [659] A.J. Ardell, *Metall. Trans. A* 16 (1985) 2131–2165.
- [660] L.E. Murr, E. Moïn, F. Greulich, K.P. Staudhammer, *Scr. Metall.* 12 (1978) 1031–1035.
- [661] K. Ma, H. Wen, T. Hu, T.D. Topping, D. Isheim, D.N. Seidman, E.J. Lavernia, *J.M. Schoening, Acta Mater.* 62 (2014) 141–155.
- [662] B. Cao, S.P. Joshi, K.T. Ramesh, *Scr. Mater.* 60 (2009) 619–622.
- [663] T.J. Rupert, J.C. Trenkle, C.A. Schuh, *Acta Mater.* 59 (2011) 1619–1631.
- [664] J.E. Bailey, P.B. Hirsch, *Philos. Mag.* 5 (1960) 485–497.
- [665] X. Huang, N. Hansen, N. Tsuji, *Science* 312 (2006) 249–251.
- [666] R.W. Armstrong, R.M. Douthwaite, *Grain Size and Mechanical Properties - Fundamentals and Applications, Symposium, (1995), pp. 41–47.*
- [667] J.R. Weertman, *Mater. Sci. Eng.: A* 166 (1993) 161–167.
- [668] L.L. Shaw, A.L. Ortiz, J.C. Villegas, *Scr. Mater.* 58 (2008) 951–954.
- [669] Y.F. Shen, L. Lu, Q.H. Lu, Z.H. Jin, K. Lu, *Scr. Mater.* 52 (2005) 989–994.
- [670] S.P. Joshi, C. Eberl, B. Cao, K.T. Ramesh, K.J. Hemker, *Exp. Mech.* 49 (2009)

- 207–218.
- [671] P. Zhang, S.X. Li, Z.F. Zhang, *Mater. Sci. Eng.: A* 529 (2011) 62–73.
- [672] U.F. Kocks, *Philos. Mag.* 13 (1966) 541–566.
- [673] M. Zhang, B. Yang, J. Chu, T.G. Nieh, *Scr. Mater.* 54 (2006) 1227–1230.
- [674] D. Wu, J. Zhang, J.C. Huang, H. Bei, T.G. Nieh, *Scr. Mater.* 68 (2013) 118–121.
- [675] L. Wang, H. Bei, T.L. Li, Y.F. Gao, E.P. George, T.G. Nieh, *Scr. Mater.* 65 (2011) 179–182.
- [676] H. Van Swygenhoven, P.M. Derlet, A. Hasnaoui, *Phys. Rev. B* 66 (2002) 024101.
- [677] R.W. Armstrong, P. Rodriguez, *Philos. Mag.* 86 (2006) 5787–5796.
- [678] R. Ding, C. Chung, Y. Chiu, P. Lyon, *Mater. Sci. Eng.: A* 527 (2010) 3777–3784.
- [679] B.J. Bonarski, E. Schafner, B. Mingler, W. Skrotzki, B. Mikulowski, M.J. Zehetbauer, *J. Mater. Sci.* 43 (2008) 7513.
- [680] C.T. Wang, A.G. Fox, T.G. Langdon, *J. Mater. Sci.* 49 (2014) 6558–6564.
- [681] A.V. Podolskiy, C. Mangler, E. Schafner, E.D. Tabachnikova, M.J. Zehetbauer, *J. Mater. Sci.* 48 (2013) 4689–4697.
- [682] R.B. Figueiredo, T.G. Langdon, *J. Mater. Sci.* 45 (2010) 4827–4836.
- [683] I.J. Beyerlein, R.J. McCabe, C.N. Tomé, *J. Mech. Phys. Solids* 59 (2011) 988–1003.
- [684] J. Koike, T. Kobayashi, T. Mukai, H. Watanabe, M. Suzuki, K. Maruyama, K. Higashi, *Acta Mater.* 51 (2003) 2055–2065.
- [685] D. Jia, Y.M. Wang, K.T. Ramesh, E. Ma, Y.T. Zhu, R.Z. Valiev, *Appl. Phys. Lett.* 79 (2001) 611–613.
- [686] H.J. Choi, Y. Kim, J.H. Shin, D.H. Bae, *Mater. Sci. Eng.: A* 527 (2010) 1565–1570.
- [687] S. Hwang, C. Nishimura, P.G. McCormick, *Scr. Mater.* 44 (2001) 1507–1511.
- [688] A. Yamashita, Z. Horita, T.G. Langdon, *Mater. Sci. Eng.: A* 300 (2001) 142–147.
- [689] I.A. Ovid'ko, A.G. Sheinerman, *Appl. Phys. Lett.* 90 (2007) 171927.
- [690] I.A. Ovid'ko, A.G. Sheinerman, *Phys. Rev. B* 77 (2008) 054109.
- [691] I.A. Ovid'ko, A.G. Sheinerman, *Acta Mater.* 57 (2009) 2217–2228.
- [692] R.L. Fleischer, *Acta Metall.* 10 (1962) 835–842.
- [693] R.L. Fleischer, *Acta Metall.* 11 (1963) 203–209.
- [694] A. Kelly, R.B. Nicholson, *Prog. Mater. Sci.* 10 (1963) 151–391.
- [695] M.E. Fine, *Metall. Trans. A* 6 (1975) 625.
- [696] D. Richard, P.N. Adler, *Metall. Trans. A* 8 (1977) 1177–1183.
- [697] G. Fribourg, Y. Bréchet, A. Deschamps, A. Simar, *Acta Mater.* 59 (2011) 3621–3635.
- [698] T. Mori, T. Mura, *Acta Metall.* 26 (1978) 1199–1204.
- [699] P.M. Hazzledine, P.B. Hirsch, *Philos. Mag.* 30 (1974) 1331–1351.
- [700] J.J. Bhattacharyya, F. Wang, N. Stanford, S.R. Agnew, *Acta Mater.* 146 (2018) 55–62.
- [701] O.N. Senkov, F.H. Froes, V.V. Stolyarov, R.Z. Valiev, J. Liu, *Nanostruct. Mater.* 10 (1998) 691–698.
- [702] V.V. Stolyarov, L.O. Shestakova, Y.T. Zhu, R.Z. Valiev, *Nanostruct. Mater.* 12 (1999) 923–926.
- [703] I. Gutierrez-Urrutia, M.A. Muñoz-Morris, D.G. Morris, *Mater. Sci. Eng.: A* 394 (2005) 399–410.
- [704] L. Wang, P. Liu, P. Guan, M. Yang, J. Sun, Y. Cheng, A. Hirata, Z. Zhang, E. Ma, M. Chen, X. Han, *Nat. Commun.* 4 (2013) 2413.
- [705] L. Wang, J. Teng, P. Liu, A. Hirata, E. Ma, Z. Zhang, M. Chen, X. Han, *Nat. Commun.* 5 (2014) 4402.
- [706] P. Liu, S.C. Mao, L.H. Wang, X.D. Han, Z. Zhang, *Scr. Mater.* 64 (2011) 343–346.
- [707] S. Ni, Y.B. Wang, X.Z. Liao, R.B. Figueiredo, H.Q. Li, Y.H. Zhao, E.J. Lavernia, S.P. Ringer, T.G. Langdon, Y.T. Zhu, *Mater. Sci. Eng.: A* 528 (2011) 4807–4811.
- [708] J.S.C. Jang, C.C. Koch, *Scr. Metall. Mater.* 24 (1990) 1599–1604.
- [709] T.R. Malow, C.C. Koch, *Metall. Mater. Trans. A* 29 (1998) 2285–2295.
- [710] Q. Wei, S. Cheng, K.T. Ramesh, E. Ma, *Mater. Sci. Eng.: A* 381 (2004) 71–79.
- [711] Q. Wei, *J. Mater. Sci.* 42 (2007) 1709–1727.
- [712] C. Gu, J. Lian, Z. Jiang, Q. Jiang, *Scr. Mater.* 54 (2006) 579–584.
- [713] C.D. Gu, J.S. Lian, Q. Jiang, W.T. Zheng, *J. Phys. D: Appl. Phys.* 40 (2007) 7440.
- [714] H. Li, Y. Liang, L. Zhao, J. Hu, S. Han, J. Lian, *J. Alloys Compd.* 709 (2017) 566–574.
- [715] Z. Jiang, X. Liu, G. Li, Q. Jiang, J. Lian, *Appl. Phys. Lett.* 88 (2006) 143115.
- [716] T.H. Fang, W.L. Li, N.R. Tao, K. Lu, *Science* 331 (2011) 1587–1590.
- [717] X.C. Liu, H.W. Zhang, K. Lu, *Science* 342 (2013) 337–340.
- [718] X.L. Wu, M.X. Yang, F.P. Yuan, G.L. Wu, Y.J. Wei, X.X. Huang, Y.T. Zhu, *Proc. Natl. Acad. Sci. U. S. A.* 112 (2015) 14501–14505.
- [719] X. Wu, P. Jiang, L. Chen, F. Yuan, Y.T. Zhu, *Proc. Natl. Acad. Sci. U. S. A.* 111 (2014) 7197–7201.
- [720] J.K. Park, A.J. Ardell, *Metall. Trans. A* 14 (1983) 1957–1965.
- [721] J.J. Beyerlein, L.S. Tóth, *Prog. Mater. Sci.* 54 (2009) 427–510.
- [722] J. Gil Sevillano, P. van Houtte, E. Aernoudt, *Prog. Mater. Sci.* 25 (1980) 69–134.
- [723] J. Zhang, Y. Wei, T. Sun, A. Hartmaier, Y. Yan, X. Li, *Phys. Rev. B* 85 (2012) 054109.
- [724] E. Ma, T. Zhu, *Mater. Today* 20 (2017) 323–331.
- [725] X. Wu, Y. Zhu, *Mater. Res. Lett.* 5 (2017) 527–532.
- [726] T.J. Rupert, D.S. Gianola, Y. Gan, K.J. Hemker, *Science* 326 (2009) 1686–1690.
- [727] T.H. Fang, N.R. Tao, K. Lu, *Scr. Mater.* 77 (2014) 17–20.
- [728] K. Zhang, J.R. Weertman, J.A. Eastman, *Appl. Phys. Lett.* 85 (2004) 5197–5199.
- [729] S. Brandstetter, K. Zhang, A. Escudero, J.R. Weertman, H. Van Swygenhoven, *Scr. Mater.* 58 (2008) 61–64.
- [730] Y.M. Wang, E. Ma, *Acta Mater.* 52 (2004) 1699–1709.
- [731] Z.H. Cong, N. Jia, X. Sun, Y. Ren, J. Almer, Y.D. Wang, *Metall. Mater. Trans. A* 40A (2009) 1383–1387.
- [732] K. Park, M. Nishiyama, N. Nakada, T. Tsuchiyama, S. Takaki, *Mater. Sci. Eng. A* 604 (2014) 135–141.
- [733] C.C. Tasan, M. Diehl, D. Yan, C. Zambaldi, P. Shanthraj, F. Roters, D. Raabe, *Acta Mater.* 81 (2014) 386–400.
- [734] Q. Han, A. Asgari, P.D. Hodgson, N. Stanford, *Mater. Sci. Eng.: A* 611 (2014) 90–99.
- [735] M.M. Wang, C.C. Tasan, D. Ponge, A.C. Dippel, D. Raabe, *Acta Mater.* 85 (2015) 216–228.
- [736] K. Lu, *Science* 345 (2014) 1455–1456.
- [737] H.W. Huang, Z.B. Wang, X.P. Yong, K. Lu, *Mater. Sci. Technol.* 29 (2013) 1200–1205.
- [738] T.G. Langdon, *Acta Metall. Mater.* 42 (1994) 2437–2443.
- [739] T.G. Langdon, *J. Mater. Sci.* 44 (2009) 5998.
- [740] T.G. Langdon, *Metall. Trans. A* 13A (1982) 689–701.
- [741] A.H. Chokshi, A.K. Mukherjee, T.G. Langdon, *Mater. Sci. Eng.: R: Rep.* 10 (1993) 237–274.
- [742] M. Kawasaki, T.G. Langdon, *J. Mater. Sci.* 51 (2016) 19–32.
- [743] R.Z. Valiev, D.A. Salimonenko, N.K. Tsenev, P.B. Berbon, T.G. Langdon, *Scr. Mater.* 37 (1997) 1945–1950.
- [744] M. Kawasaki, N. Balasubramanian, T.G. Langdon, *Mater. Sci. Eng.: A* 528 (2011) 6624–6629.
- [745] S. Zhang, O.Y. Kontsevoi, A.J. Freeman, G.B. Olson, *Acta Mater.* 59 (2011) 6155–6167.
- [746] R. Kirchheim, *Acta Mater.* 55 (2007) 5129–5138.
- [747] K. Edalati, T. Masuda, M. Arita, M. Furui, X. Sauvage, Z. Horita, R.Z. Valiev, *Sci. Rep.* 7 (2017) 2662.
- [748] K. Edalati, Z. Horita, R.Z. Valiev, *Sci. Rep.* 8 (2018) 6740.
- [749] P.W. Trimby, *Ultramicroscopy* 120 (2012) 16–24.
- [750] L. Wang, K. Zheng, Z. Zhang, X. Han, *Nano Lett.* 11 (2011) 2382–2385.
- [751] Y. Yue, P. Liu, Z. Zhang, X. Han, E. Ma, *Nano Lett.* 11 (2011) 3151–3155.
- [752] K. Zheng, X. Han, L. Wang, Y. Zhang, Y. Yue, Y. Qin, X. Zhang, Z. Zhang, *Nano Lett.* 9 (2009) 2471–2476.
- [753] L. Wang, P. Guan, J. Teng, P. Liu, D. Chen, W. Xie, D. Kong, S. Zhang, T. Zhu, Z. Zhang, E. Ma, M. Chen, X. Han, *Nat. Commun.* 8 (2017) 2142.
- [754] X.D. Han, Y.F. Zhang, K. Zheng, X.N. Zhang, Z. Zhang, Y.J. Hao, X.Y. Guo, J. Yuan, Z.L. Wang, *Nano Lett.* 7 (2007) 452–457.
- [755] B.Q. Han, J.Y. Huang, Y.T. Zhu, E.J. Lavernia, *Acta Mater.* 54 (2006) 3015–3024.
- [756] B.Q. Han, Z. Lee, D. Witkin, S. Nutt, E.J. Lavernia, *Metall. Mater. Trans. A* 36A (2005) 957–965.
- [757] X.L. Wu, P. Jiang, L. Chen, J.F. Zhang, F.P. Yuan, Y.T. Zhu, *Mater. Res. Lett.* 2 (2014) 185–191.
- [758] A.Y. Chen, J.B. Liu, H.T. Wang, J. Lu, Y.M. Wang, *Mater. Sci. Eng. A* 667 (2016) 179–188.
- [759] M. Furukawa, Z. Horita, M. Nemoto, R.Z. Valiev, T.G. Langdon, *J. Mater. Res.* 11 (1996) 2128–2130.